Two-layer flow behaviour and the effects of granular dilatancy in dam-break induced sheet-flow

BENOIT SPINEWINE

DÉCEMBRE 2005

Thèse présentée en vue de l'obtention du grade
de docteur en sciences appliquées

Faculté des sciences
appliquées

Université catholique de Louvain

This thesis was supervised by :

Prof. Y. Zech	Université catholique de Louvain (Belgium)

Members of the Jury :

Prof. D. Vanderburgh, President	Université catholique de Louvain (Belgium)
Prof. J. Berlamont, co-advisor	Katholieke Universiteit Leuven (Belgium)
Prof. V. Guinot, co-advisor	Université Montpellier-2 (France)
Prof. M.H. Chaudhry	University of South Carolina (USA)
Prof. E. Deleersnijder	Université catholique de Louvain (Belgium)

Two-layer flow behaviour and the effects of granular dilatancy in dam-break induced sheet-flow

Thesis presented for the degree of Doctor in Applied Sciences

by

Benoit SPINEWINE

December 2005

Abstract

In case of exceptional floods induced by the failure of a dam or flood-defence structure, huge amounts of sediments may be eroded. This results in large-scale modifications of the valley morphology and drastically increases the resulting damages to mankind and infrastructure.

The objective of the present research is to advance the understanding of sediment erosion and transport under dam-break flows. For such highly erosive and transient floods, it seems crucial to account explicitly for sediment inertia, and therefore traditional modelling approaches based on "clear-water" flood routing supplemented with some "passive" sediment transport predictor are largely inappropriate. The present approach relies on a two-layer idealisation of the flow behaviour. Separating a clear-water flow region from the underlying sediment bed, the transported sediments are confined in a flow layer of finite thickness, endowed with its proper inertia, density and velocity. In addition, the thesis pinpoints granular dilatancy as being an essential mechanism of interaction between this "sheet-flow" layer, the bed substrate and the upper clear-water layer. When passing from a solid-like to a fluid-like behaviour as they are entrained by the flow, the eroded sediment grains dilate along the vertical, and this dilation generates vertical exchanges of mass and momentum between the flow layers that should also be accounted for.

The thesis proceeds first with experimental investigations. Laboratory dam-break waves have been reproduced in a dedicated flume, exploring different bed configurations and sediment densities. Digital imaging observations are used to support the proposed phenomenological description of the flow. Within a shallow-water framework, theoretical and numerical endeavours are then developed to investigate the implications on the flow dynamics of the two essential contributions of the proposed description, i.e. the two-layer flow behaviour, and the effects of granular dilatancy.

To Isabelle, with love,

to Pablo & Jonas,

to him or her, still to be named

that will join us soon

Acknowledgements

Rather than a personal accomplishment and a nice textbook, a thesis is a process, an adventure largely grounded on a network of influences and relationships, that provided motivation, inspiration and help in profusion. Special thanks should be addressed to a series of people that guided or accompanied me during the thesis.

I first wish to deeply thank Professor Yves Zech, the supervisor of this work, for his expertise, for giving me the opportunity to conduct this research with a great freedom, though providing guidance and precise feedback in abundance. The confidence and enthusiasm he devotes to his research team, and his great openness to international collaborations and networking, is greatly appreciated. Special thanks are also extended to the advise committee of the thesis: Professor Vincent Guinot (Université Montpellier-2), whose friendship dates back to my first research contract at Unesco-IHE in Delft, for his feedback on numerical curiosities and his advice on implementation; Professor Jean Berlamont (Katholieke Universiteit Leuven), for his kind encouragement and confidence since my exchange stay at KUL during my graduate studies.

The participation of Professor M. Hanif Chaudhry (University of South Carolina) and Professor Eric Deleersnijder (UCL) to the thesis jury, as well as the presidency of Professor David Vanderburgh, is greatly acknowledged. Besides his willingness to travel such a distance across the Atlantic, the judicious comments of the first to improve the English of the manuscript were very much appreciated.

This work could not even have started without the never-ending support, advice and friendship of Professor Hervé Capart (National Taiwan University). Since my student BS thesis done under his guidance, he was both the source of inspiration and motivation that distance and time could not attenuate. Early joint stays in Trento or at the Saint-Oyen Summer School on Geomorphological Fluid Mechanics, and later research stays in Taipei during the thesis, were a very profitable experience at both personal and professional levels. His admiration of the "small is beautiful" adage, both in the lab and in nature during our geomorphological "motorbike diaries" along the eastern coast of Taiwan, will long last in my memory. His belief in the "simple is beautiful" principle helped me to design theoretical and numerical frameworks that tend to maximize the underlying physics though minimizing the recourse to empiricism and adjustable coefficients. The developments of the present thesis do largely rely upon his preceding works. The enthusiasm of his research team at the NTU is also acknowledged.

The pleasure of working in the laboratory owes much to the good time spent during the collaborative works on imaging characterisation of uniform liquid-granular flows with the Università degli Studi di Trento. Dr. Michele Larcher, under the guidance of Professors Aronne Armanini and Luigi Fraccarollo, is greatly acknowledged for his hospitality during my stays in Trento, and for recommending the World Champion *Giro Pizza* and *Pizza a la rucola.* In addition, the enthusiasm of all the partners involved in the EU IMPACT project on dam-break modelling and sediment movement, provided a rich platform for discussions and exchanges among researchers, among others with Rui Ferreira, Joao Leal (Instituto Superior Tecnico, Lisboa), and Kamal el Kadi (Cemagref).

Thanks are also extended to Gerrit Klaassen (UNESCO-IHE Institute for Water Education, Delft). Working with him, at first during a one-year period and now on an occasional basis for help in teaching activities, was a great pleasure.

The enthusiastic work atmosphere at the Unité de Génie Civil et Environnemental of UCL made working in research a joy on a daily basis. It relies much upon its academics: Professors Jean-Francois Remacle, Alain Holeymann, Jean-Francois Thimus and Yves Zech; and on intimate contacts and a good team spirit in passionate and desperate moments with the co-workers of the hydraulics research team: at first Céline Savary with whom I share the office, and Dr. Sandra Soares Frazão, Nicolas le Grelle, Mourad Bellal, Christine Dal Cin, Robens Aimable; as well as previous colleagues: Didier Bousmar, Pierre-Henri Vancaster, Christophe Adriaensen, Marc Poncin, Djamal Abderrahim and Benjamin Noël. Sharing the office in the past with Didier for five years initiated a profound friendship that persists through family links and professional collaboration with the Hydraulic Laboratory of Châtelet (Ministry of Public Works, Walloon Region).

The help and good-humour of Viviane and Marie-Rose at the secretariat was warmly appreciated. The support of the team at the Laboratoire de Génie Civil was essential to the success of the laboratory work performed during the thesis. I am especially thankful to Alex Bertholet, André Renard, Eric Dupuis, Vincent and Stéphane, Hassan and all the rest of the team, as well as their directors Albert Mertens and Guy Henriet. Many student investigators provided enthusiasm and great help during their degree thesis which I had the opportunity to be associated with: Valery, Marc, Antoine, Olivier, Evrard, Nicolas, Marie, Emilie, Francois-David, Arnaud, Laurent, Didier, Francois, Pedro, Silvia, Corrado, and especially Dimitri and Antoine for helping in building the flume, as well as Jean and Quentin for helping in performing dam-break experiments. Thanks are also addressed to colleagues from the TELE laboratory, and especially Damien Douxchamps and Xavier Wielemans.

Support from the Fonds pour la Recherche dans l'Industrie et l'Agriculture through a PhD fellowship and a travel grant for a research stay at the National Taiwan University, as well as support from the Fonds Spécial pour la Recherche, Université catholique de Louvain, is gratefully acknowledged.

Finally, the thesis is dedicated to Isabelle, for her patience and love; to Pablo, Jonas and the one to come, my beloved musketeers.

Table of Contents

Chapter 1
Introduction

In a number of ancient and recent catastrophes, floods have induced severe soil movements in various forms. A variety of natural hazards involve the movement of bulked solid-liquid mixtures. They differ in triggering mechanisms, flow characteristics and sediment properties. Examples range from stony debris surges in steep torrents (Iverson 1997) or glacial-lake outburst floods (Kershaw *et al.*, 2005; Roberts *et al.*, 2003), to mudflows and lahars (Waythomas 2001) or submarine landslides (Hampton, 1996). The present research examines the case of geomorphic floods induced by the failure of a dam, dyke or flood-defence structure.

A strong example of well-documented recent catastrophe from a dyke failure is the flood in the Saguenay region of Quebec in July 1996. The failure of a dike at Lake Ha! Ha! resulted in a complete reshaping of the 35 kilometres of the downstream valley leading to the Ha!Ha! Bay (Figs. 1.1 and 1.2). Geomorphic changes included a newly scoured lake outlet, alternate reaches of intense erosion (down to 20 m in some reaches) and widespread deposition, a large-scale channel avulsion, and major channel widening (locally up to 700 %) (Brooks and Lawrence, 1999; Lapointe *et al.*, 1998; Capart, Spinewine *et al.*, submitted).

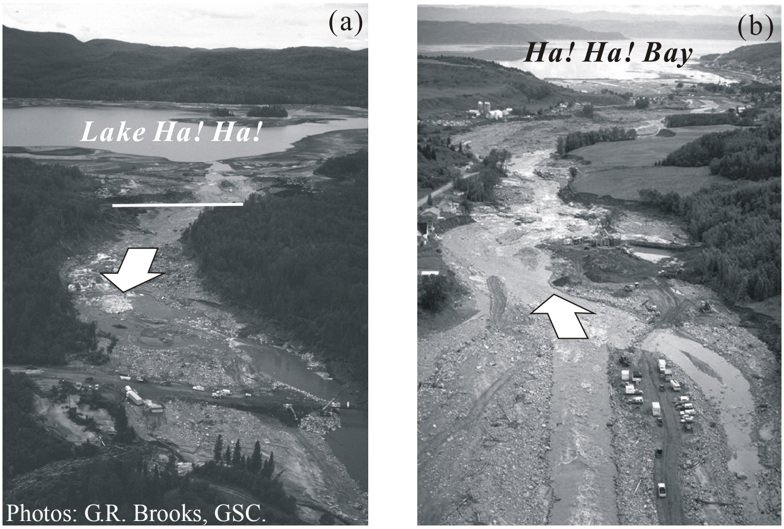

Figure 1.1. Helicopter views of the geomorphic impacts of 1996 Lake Ha! Ha! dam-break flood: (a) breached dyke and drained Lake Ha! Ha! (original dyke shown in white); (b) major widening in the lower reaches of Ha! Ha! river.

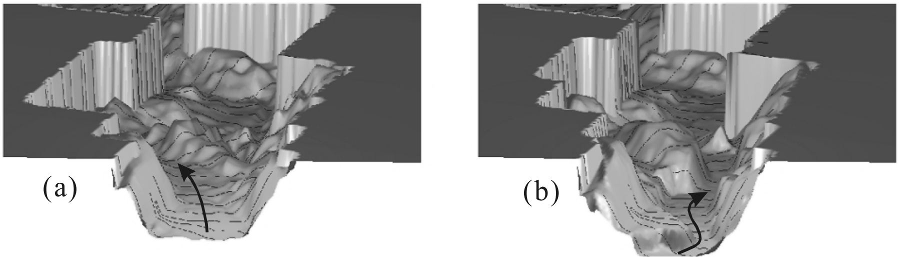

Figure 1.2. Downstream view of the geomorphic impacts at Chute-à-Perrons large scale avulsion: (a) before; (b) after the flood. Topography reconstructed based on pre- and post-flood DTMs kindly provided by INRS-Eau, University of Quebec (see Capart, Spinewine *et al.*, submitted). Channel cross-sections superimposed in black are distant of 100 m each. Vertical scale is distorted.

Even when they involve comparatively small volumes of material, geomorphic interactions can lead to severe consequences because of localized changes or adverse secondary effects. In the 1980 Pollalie Creek event, Oregon, the material entrained by a debris flow deposited in a downstream reach, forming a temporary dam that ultimately failed and caused severe flooding (Gallino and Pierson, 1985). A similar case was recorded for the Lawn Lake dam failure along the Roaring River, Colorado (Jarrett and Costa 1993). Another cascade of events was that of the 1996 Biescas flood, Spain, where a series of flood-control dams failed (Benito et al., 1998).

Since by nature, such geomorphic floods are not frequent and usually not very well documented, laboratory experiments offer an interesting complement to the analysis of real catastrophes. They provide idealized clear-cut situations and allow to investigate the mechanisms of sediment entrainment and movement in very intense and transient conditions, far from the uniform conditions for which traditional sediment transport theories have originally been developed. They may also serve as a basis for the first stage of validation of numerical models, in view of applying them to large real-life situations at a later stage, e.g. in the framework of risk assessment studies.

The preparation and realization of such an experimental investigation of dam-break waves over movable beds is the topic of Chapter 2. A new flume was designed for this purpose, based on experience gathered from previous laboratory tests, with the objective to provide initial conditions that approach as precisely as possible the idealization of an instantaneous dam collapse. Experiments were carried out for a range of initial bed configurations, obtained by changing the upstream and downstream levels of bed and water, and for two distinct granular materials (sand and PVC pellets), differing in density and grain size. A precise characterisation of the observed wave was obtained by digital imaging through the transparent flume sidewalls. Besides the evolution of the free surface and bed levels, particle-tracking techniques were used to identify and track the movement of neutrally-buoyant tracers dispersed in the water and of the individual sediment grains themselves.

The remainder of the thesis then builds a theoretical framework for the simulation of dam-break induced geomorphic floods. The experiments are utilized both at the initial and final stages of the process, at first for motivating and supporting the proposed flow description and in the end for validating the resulting numerical model by comparing its predictions with experimental observations.

Available theories in open-channel hydraulics allow to deal reasonably well with two types of flow: alluvial flows on one hand, and transient flows with rigid boundaries on the other. Alluvial geomorphic flows are such that the bed geometry evolves under the flow action, but with a sediment load small enough to play no dynamic role. The transported sediments can be treated barely as a passive tracer, and it is sufficient to handle the relation between solid transport and pure water hydrodynamics. Studies of this type are currently restricted to slowly evolving flows. On the other hand, it is now possible to deal with debris flows and rapid transients involving water, dry grains, or liquid-granular mixtures of complex rheology, as long as these flows take place in fixed geometries.

The problem with dam-break induced geomorphic flows is that they combine the difficulties of these two types of flow. They involve such rapid changes and intense rates of transport that the granular component plays an active role in the flow dynamics, and that inertia exchanges between the bed and the flow become significant (Capart, 2000). Under the heavy attack of rushing waters, the eroded sediments are fluidised and join the flow in the form of a heavier liquid-granular mixture, which may fill a substantial portion of the flow depth. The behaviour of this mixture, similar to debris-flows, can significantly affect the flow dynamics, in such a way that traditional, purely hydrodynamic modelling approaches may substantially fail to simulate the flow correctly.

To account for sediment inertia while still adopting relatively simple assumptions, Capart (2000) proposed to tackle the problem by using an extended shallow-water description: the flow is divided into three separate layers, namely the motionless sediment bed substrate and two flowing layers: a pure-water layer, and a transport layer of finite thickness, or sheet-flow layer, formed by a mixture of water and sediments globally behaving as a fluid of larger density. The layers are separated by sharp interfaces, and the erosion of the sediment bed is viewed as a phase change of the bed material, undergoing a transition from solid-like to fluid-like behaviour as it is entrained by the flow. His approach further assumed that water and moving grains moved at one and the same velocity, and that the eroded sediments were set in motion at the same granular packing as in the bed, so that the density of the flowing sediment mixture is essentially assumed equal to that of the saturated bed. Notwithstanding those simplifying assumptions, the description was found to adequately capture some major features of the flow.

The main contribution of the present thesis is to show that, departing from this idealized flow structure, a number of assumptions may be relaxed without making the resulting description intractable, but yielding new insights into the mechanisms of sediment erosion and bulking into the flow. In particular, two major extensions are examined, which consist in allowing the two flowing layers to move at distinct velocities, and in considering the effect of granular dilatancy associated with erosion. A detailed inspection of their implications on dam-break wave modelling under a two-layer, shallow-water framework forms the core of chapters 3 and 4 of the thesis, respectively.

In Chapter 3, the two-layer flow analogy will be pushed to its limits, by considering a full portion of the granular bed to be instantaneously and permanently fluidised. The conditions are thus basically those of a dam-break of a “light” fluid propagating over a substrate made of a “heavy” fluid. At this point, no account is made for the possible change of state of the granular material, passing from a solid-like to a fluid-like behaviour or vice versa. This simplified description, however, will allow to evidence some essential characteristics of a two-layer shallow water framework, and to investigate its behaviour in dam-break conditions. In particular, the chapter will devote a substantial part to examine the influence of the density of the “heavy” fluid on the wave structure, and the implications of allowing the two layers to flow at distinct velocities. Numerical simulations pursued until convergence will reveal the existence of self-similar solutions, with the emergence of a peculiar wave pattern that does not seem to have been examined before, and that is referred to as the “Ritter pinch-off”. Considerations will be made about the range of flow conditions possibly leading to the emergence of instabilities at the interface between the layers.

Limitations of the above highly simplified approach are then highlighted, the most prominent being the absence of any physical argument for determining when, and to which extent, the granular material may be fluidised and incorporated in the flow, thus behaving as a fluid rather than as a solid-like granular skeleton. Chapter 4, forming the core of the thesis, precisely deals with this issue. It is devoted to the derivation and testing of an original set of equations governing vertical exchanges between the bed and the flow. A sharp view of the evolving bed profile is adopted (Capart, 2000), by which erosion or deposition results from a downward or upward displacement of the interface separating the solid-like bed from the fluid-like moving sediment mixture. A major contribution of the proposed description, as opposed to former formulations (Capart, 2000; Fraccarollo and Capart, 2002), is to account for the effect of granular dilatancy associated with erosion. It relies on the postulate that the mobilisation of bed material is associated with an expansion of the granular matrix so that the volumetric sediment concentration in the moving layer, though still assumed constant in time, is lower than in the static bed. The importance of incorporating such a mechanism will be motivated on the basis of experimental observations. Its various implications on the flow dynamics are then discussed. In particular, dilatation of eroded sediment grains incorporated in the sheet-flow layer comes with an associated transfer of water from the top clear-water layer, required to "fill the gaps" and counterbalance the deficit in interstitial water created within the sheet flow. Momentum transfer results also, and if the layer velocities are distinct, usually greater in the clear-water layer than in the sheet flow, this may boost up the velocity of the sheet-flow. It is demonstrated that granular dilatancy provides an important mechanism of coupling between the two flow layers, which may be even more significant than friction for the highly transient flows like the geomorphic dam-break waves under study.

Ultimately, in Chapter 5 the behaviour of laboratory dam-break waves is investigated for cases where the bed profile exhibits a level discontinuity across the dam. This may for example provide a rough analogue to the configuration of a reservoir that has been partially filled with sediments which may be re-mobilized upon failure of the dam and drainage of the lake. In the experiments, at the first instants of wave formation, it is observed that mass soil movements occur in the vicinity of the bed discontinuity, that may not be explained solely on the basis of flow-induced erosion. Geotechnical considerations must be invoked, and a simple mechanism that accounts for mass failure and fluidisation of the bed step is proposed. The incorporation of such a mechanism is shown to significantly improve the agreement between simulations and observations in the neighbourhood of the dam.

Chapter 2

Laboratory experiments of idealised dam-break waves over loose granular beds.

“Remember, when discoursing about water, to induce first experience, then reason.” ”Although nature commences with reason and ends in experience it is necessary for us to do the opposite, that is to commence with experience and from this to proceed to investigate the reason.”

Leonardo da Vinci, Notebook H 90(42)r.

1. Introduction

An experimental program for investigating the erosional behaviour of dam-break waves propagating over loose granular beds is presented. In the broad sense, dam-break type experiments involve the sudden release of an idealised vertical “dam” separating two distinct regions of space. In general, the regions on both sides of the “dam” may consist in a single horizontal “layer” or a succession of “layers” at rest, usually made of fluid or granular material, each having homogeneous properties and extending infinitely. After removal of the “dam”, the two distinct regions are set in contact and a “dam-break” wave results. Most commonly, the physical mechanism responsible for the initiation of movement is gravity, transforming potential energy accumulated behind the dam into kinetic energy of the propagating wave.

Small-scale dam-break type experiments reported in the literature have been conducted in a variety of different configurations, in direct relation with at least four distinct areas of research: (i) density currents and the physics of stratified fluids, typically with laboratory experiments of multi-fluid lock-exchange flows (Gladstone *et al.*, 2004; Zhu and Lawrence, 2001; Sutherland 2002; Shin *et al.*, 2004, Simpson 1987); (ii) dry granular flows, with experiments involving the slumping of granular columns or the release of dry avalanches (Gray *et al.* 2003; Lajeunesse *et al.*, submitted; McElwaine and Nishimura, 2001); (iii) shallow-water transients, with dam-break experiments involving a single liquid of possibly varying rheology (Stansby *et al.*, 1998; Janosi *et al.*, 2004; Nsom, 2002); (iv) fluid-granular transients, like the present dam-break experiments over loose granular beds (Capart and Young, 1998; Fraccarollo and Capart, 2002; Spinewine and Zech, 2002; Leal *et al.*, 2002).

Besides their physical interest of gaining insights into the flow mechanisms within their respective fields of research, such idealised experiments have also a computational interest, as they provide clear-cut situations ideally suited for the validation and testing of numerical models. For this purpose, it is important that the experiments be designed with care, to ensure that the test conditions approximate as closely as possible the idealization of an instantaneous “dam” collapse, while minimising initial perturbations during the removal.

Experimental investigations of the geomorphic impacts of a dam-break date back to the pioneering work of Chen and Simons (1979), who examined the backward erosional rarefaction wave induced by the sudden removal of a submerged barrage in a steady flow (Fig. 2.1). The first idealised experiments in a typical dam-break configuration were performed by Capart and Young (1998), with a horizontal sediment bed extending on both sides of the dam, and a body of water initially at rest in the upstream reservoir. They used a very light sediment to amplify bed movements, and they recorded the surge of water and eroded sediments by means of fast digital cameras (Fig. 2.2).

Leal *et al.* (2002) performed experiments with granular material of two distinct densities, sand and pumice. They also investigated the variety of flow patterns observed when changing the initial conditions, by varying the bed levels and water levels on both sides of the gate.

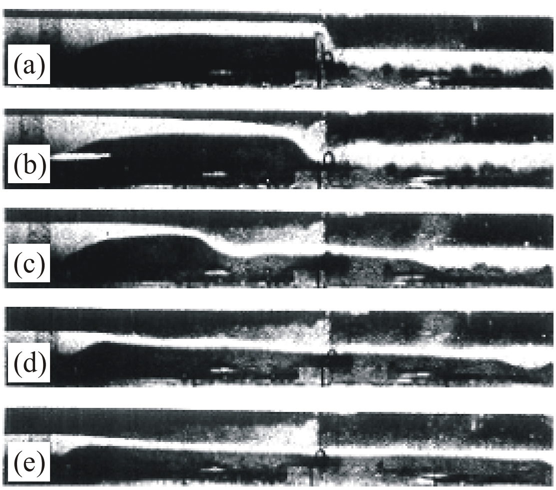

Figure 2.1. Early experiments of the morphodynamics induced by the removal of a dam, (a)-(e) respectively at instants $t = 0$, 1, 10, 120 and 180 s after gate release. Reproduced from Chen and Simons (1979)

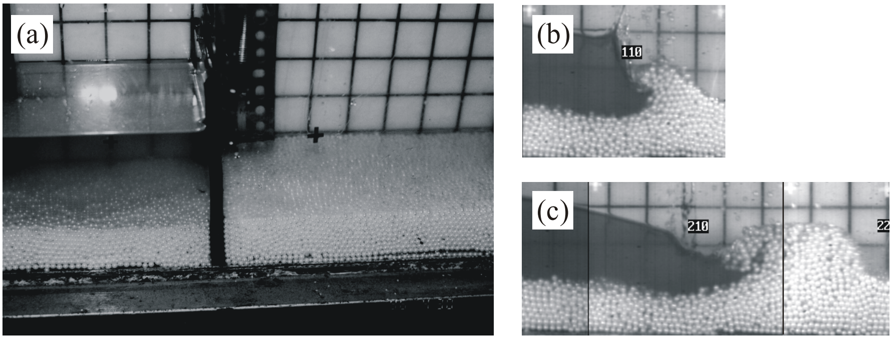

Figure 2.2. Idealised dam-break experiments with a light sediment analogue. (a) Set-up and initial configuration; (b) and (c) side-view snapshots at instants $t = 1$ and 2 s respectively. Reproduced from Capart and Young (1998)

At the laboratory of the Civil Engineering department of UCL, dam-break experiments have previously been performed by Capart (2000), Spinewine (Spinewine and Zech, 2002), and by a series of graduate students for their degree theses on the subject (Soler Salles, 2000; Van Goethem and Villers, 2000). The experiments have been conducted in a multi-purpose tilting flume, adapted for the purpose, and equipped with a rising gate simulating the dam-break. The flume was found to have several limitations, that altered the quality of the attainable experimental conditions. For the present work, it was thus chosen to build a novel experimental flume, whose design took into consideration the experience gained from previous tests. This is the purpose of Section 2 of the present chapter. In Section 3 the test conditions of the experiments are then described. Sections 4 and 5 focus on flow instrumentation by means of digital imaging techniques, used to obtain a precise visualisation of the flow processes at play, and high-quality images amenable to quantitative measurements. Finally, Section 6 presents some results. Experimental observations are restricted here to a relatively general presentation of the flow behaviour, while more detailed aspects of the experiments will be considered in later chapters when motivating the proposed theoretical framework and validating the overall approach by comparing the experiments with numerical simulations.

2. A novel dam-break flume

2.1. Flume structure

The flume designed for the present dam-break experiments is illustrated in Fig. 2.3. It has an overall length of 6 meters, i.e. 3 meters on both sides of a central gate simulating the idealized dam. The flume is mounted on an array of horizontal crossbeams, with dimension 6 meters by 1.6 meter, designed such that the deformation in the horizontal plane is less than 1 mm over the flume length. Each sidewall is made of two juxtaposed steel frames fitted with transparent glass panes, with respective lengths of 4 and 2 meters, and a height of 70 cm. They are adjusted vertically and connected with outer oblique legs to the lower structure for increased stiffness in the lateral direction.

The width of the channel in each of the two sections may be freely adjusted by displacing one or two side frames along the supporting beams. Any of the configurations shown in Fig. 2.4 may thus easily be reproduced. The prismatic configuration of Fig. 2.4a, with a channel width of 25 cm, was used for the main experimental program, utilised in chapters 3, 4 and 5 of the present thesis. The asymmetric sudden enlargement of Fig. 2.4c, from a width of 25 to 50 cm, has been utilised more recently. Results are included as perspectives for further work in chapter 6.

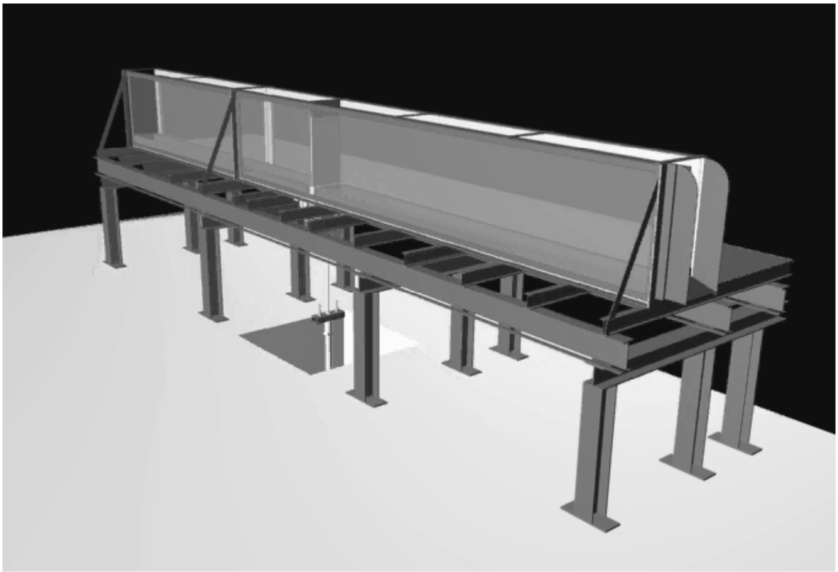

Figure 2.3. Overall view of the newly-designed dam-break flume used in the present work (CAD-drawing courtesy of Dimitri Bailly)

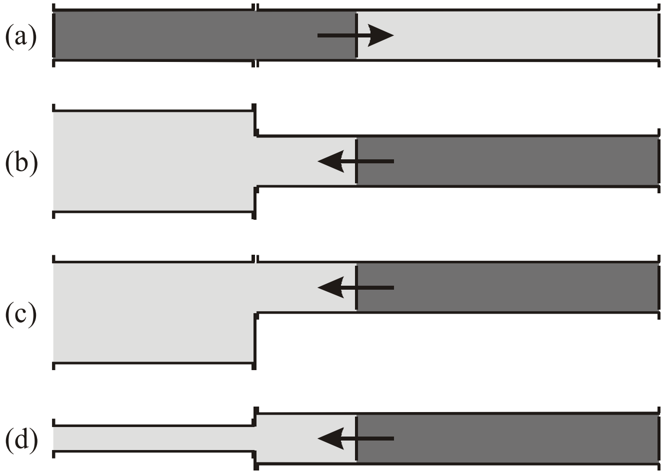

Figure 2.4. Schematic plan-views of the attainable flume configurations: (a) prismatic; (b) sudden enlargement; (c) asymmetric enlargement; (d) sudden narrowing.

The bottom of the channel is a lined wood plane sealed to the transparent sidewalls. The upstream and downstream reaches of the channel may be filled with sediments. Horizontal beds of sediments are obtained by first pouring sediments in excess, compacting them if required, and profiling them at desirable heights by conveying a scrapper plate along the channel to gradually remove layers of excess sediments. Water is then added cautiously, at a slow rate to ensure that the bed gets fully saturated and that residual air pockets are not entrapped within the pores. At the upstream end of the flume is a steel panel equipped with a narrow-crested weir with adjustable level, for a precise regulation of the water table. Level regulation at the downstream end is achieved by inserting steel plates of various heights into a slot fitted with a watertight joint around the cross-section, depending on the desired level of water and sediments in the channel. Overflow is conveyed by a gully into a settling tank.

2.2. Gate design

A dam-break wave is initiated by the sudden removal of a narrow vertical gate at the middle of the flume. Special attention was devoted to the design of this gate, with the ambition to reach initial test conditions that approach as much as possible the idealization of an instantaneous dam collapse, while minimising perturbations to the sediments and water during the removal of the gate. Conflicting design criteria appear essential in this regard: rapidity of removal, thinness, reduced frictional resistance, watertightness. In the context of density-current experiments, for example, Gladstone *et al.* (2004) insist on the significant spurious flow circulations that may be induced during the gate removal process. Furthermore, in order to allow unhindered propagation and visual observation of the resulting dam-break wave through the continuous glass walls, no fixed apparatus may be attached to the sidewalls.

Preceding dam-break experiments documented in the literature (Capart and Young, 1998; Fraccarollo and Capart, 2002; Spinewine and Zech, submitted; Leal *et al.*, 2002) were performed with a rising gate. This alternative was found to show evidence of several disadvantages: 1) the effect of gate removal is felt first in the bed region, where the pressure is maximal, and piping is initiated below the gradually rising gate, inducing severe soil movements; 2) friction along the gate tends to mobilise bed sediments; 3) the strong depression created by the void left over under the rising gate, induces an effect of suction that further eases the mobilisation of substantial lumps of sediments, entrained vertically and following the gate movement even above the water surface; 4) water droplets and remaining sediments dripping from the emerged gate perturb the water surface during the whole duration of the experiment. These drawbacks are qualitatively sketched in Fig. 2.5, and illustrated on the images of Fig. 2.6.

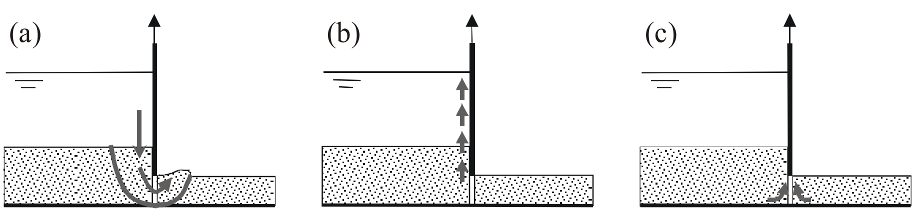

Figure 2.5. Drawbacks of a rising gate system, inducing spurious soil movements during gradual lifting as a result of (a) mass failure; (b) friction; (c) depression and suction.

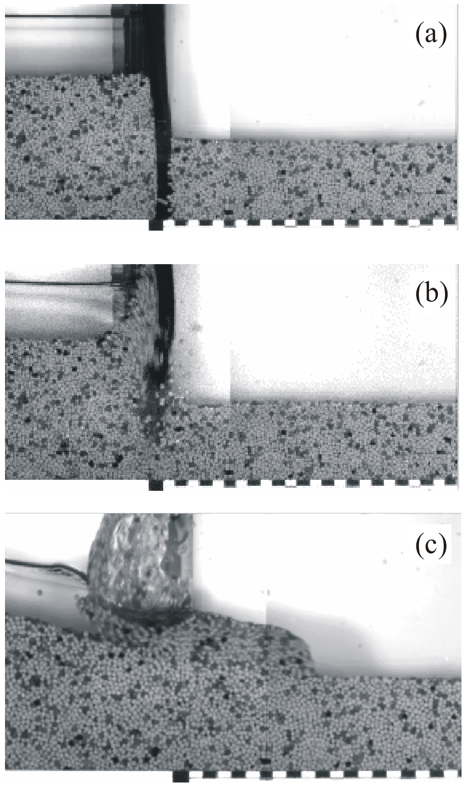

Figure 2.6. Spurious soil movements induced by a rising gate system. (a) initial conditions; (b) grain mobilisation during lift-off; (c) grains and water dropping off the released gate at a later instant. Reproduced from Soller Sales (2000)

The chosen design thus turned to a lowering of the gate. The idea of a lowering gate was first suggested by Professor A. Armanini from the University of Trento, where a first prototype was built at a smaller scale. Doing so, the above drawbacks are avoided, but a lowering gate posed also some tricky design challenges, notably to ensure watertightness of the flume while reducing the friction for a maximum acceleration.

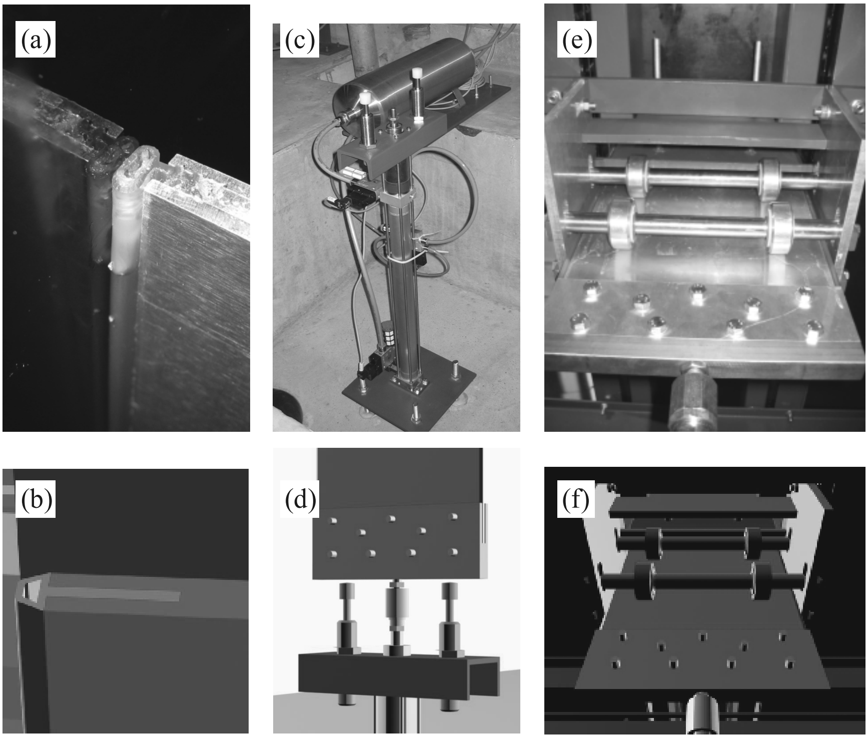

Figure 2.7. Details of the lowering gate design. (a)-(b) PVC joint along the circumference of the gate; (c) pneumatic jack, hydraulic shock absorbers, and compressed air circuit; (d) details on coupling system between gate and cylinder rod; (e)-(f) low angle views on the guiding roller bearings (photos and CAD-drawing courtesy of Dimitri Bailly)

For the present experiments the gate is made of a layered aluminium structure, 7 mm thick, and is fitted on its circumference with a hollow PVC seal ensuring watertightness against the sidewalls (Fig. 2.7a-b). A special transparent silicon oil sprayed on the sidewalls before inserting the gate reduced substantially the friction. Ensuring watertightness at the bottom of the flume was more delicate. Best performance was achieved by compressing neoprene bands below the wooden bottom plates, and covering them with lubricant oil to reduce friction during gate movement. The slenderness of the gate comes at cost of a reduced resistance to deformation. In closed position, the top of the gate is thus maintained upright and chocked up against a steel stopper on top of the flume, hampering lateral movement and bending due to the water pressure in the upstream reservoir.

The downward movement of the gate is controlled by the rapid action of a pneumatic jack (Fig. 2.7c). For maximum acceleration, the compressed air tank was placed as close as possible to the jack. A tie-rod system on the cylinder allows to pre-inflate the upper jack chamber at a pressure of 8 bars so that the full pressure is available instantaneously upon release of the rod. To avoid askew movement and blockage, the descending motion is guided by a system of roller bearings (Fig. 2.7e-f). When reaching its lower position, the gate is rapidly decelerated over a distance of less than two centimetres by two external hydraulic dampers (Fig. 2.7c-d) and a pneumatic damper in the lower chamber of the cylinder, and does not rebound.

3. Test conditions

3.1. Material properties

The apparatus allows experiments to be conducted with various sediment materials. The two materials used in the present work are coarse crushed sand and extruded PVC pellets. The sand has the following properties: particle sizes ranging from 1.2 to 2.4 mm, with $d_{50} = 1.82$ mm, an intrinsic density $\rho_M =$ 2683 kg/m³, a friction angle $\varphi = 30°$ and negligible cohesion. Before bed profiling the sand was compacted in place to reach a reproducible solid packing $c_b = 53$ %. The PVC pellets are slightly cylindrical in shape, with an equivalent spherical diameter d of 3.9 mm, have a specific density ρ_M of 1580 kg/m³, a friction angle φ of 38° and no cohesion, and are set in place at the random close packing c_b equal to 58 %.

3.2. Initial conditions

Except from the asymmetric sudden enlargement case of Fig. 2.4c for which results at an exploratory stage for two-dimensional effects are presented in chapter 6, the analysis will concentrate on prismatic configurations only. Different initial conditions are then obtained by adjusting the upstream and downstream water and sediment depths. Even in the absence of a clear-water layer on the downstream side of the gate, the bed of both the sand and PVC materials is carefully saturated with water. The configurations explored in the present work are shown in Fig. 2.8. The basic case consists in a flat sediment bed extending at the same level on both sides of the gate (Fig. 2.8a). Variations from this basic case differ primarily in the level of the sediment bed in the upstream reach, so that the bed profile presents a discontinuous step at the gate position. An upward step (Fig. 2.8b) and two downward steps (Figs. 2.8c and 2.8d) are explored, and provide rough analogues to the case of a dam partially filled or dredged with sediments. Two more specialized configurations are also examined: the case of a reservoir almost entirely filled with sediments (Fig. 2.8e), and the case of a downward bed step combined with an initial still layer of clear-water in the downstream reach (Fig. 2.8f). Finally, to investigate scaling effects, the basic case of Fig. 2.8a is also reproduced with a lower water depth upstream, i.e. 25 cm instead of 35 cm. (not shown in Fig. 2.8).

The reference scale for all the experiments is taken as the depth H separating the upstream water level and the downstream sediment level. It is equal to $H = 35$ cm for all the configurations of Figs. 2.8.

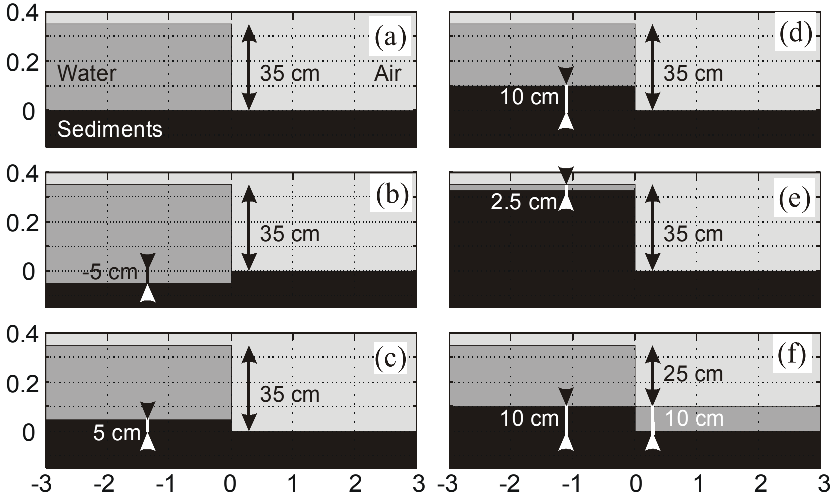

Figure 2.8. Initial experimental dam-break configurations. (a) a flat sediment bed; (b) an upward bed step of 5 cm; (c) a downward bed step of 5 cm; (d) a downward bed step of 10 cm; (e) a reservoir almost filled with sediments; (f) a downward bed step combined with an initial layer of clear water downstream. Dimensions are in meters.

4. Imaging apparatus and flow measurement

A major benefit of the flume design is to allow unperturbed observation of the flood wave through the full 4 meters of the main lateral sidewall, i.e. from 1 meter upstream of the gate till the flume outlet. Fast digital cameras were used to acquire image sequences at a frame rate of 200 images per second. For the sand tests, two synchronised Dalsa® CAD1 CCD cameras were set side by side, with a combined resolution of 512x256 pixels. For the PVC tests, a single Dalsa® DS-21-001M0150 CMOS camera was used, operating at the same frequency but with a resolution of 1024x512 pixels. All the cameras provide images with 8-bit digital output, or 256 grey levels.

Given the limited resolution of the cameras, covering the entire flume with a single image would have produced large image distortion and a pixel size of 8 (resp. 4) mm, which does not allow to derive precise measurements and detailed observations. Instead of using a panel of synchronised cameras, which were not available, several identical tests were thus repeated by displacing the camera(s) in successive steps to cover the entire flume (Fig. 2.9). Repeated identical tests performed with the camera(s) at the same location revealed a high degree of reproducibility of the experiment, supporting the procedure. To ensure the same viewing angle for each individual sequence, the camera(s) were mounted on a camera head which was simply translated along a steel rail, adjusted horizontally at a fixed distance of the flume sidewall. They are placed in such a way that the bed profile is always seen slightly from below, to avoid ambiguities that would result if both the front and back interfaces outlines were seen on the images. The focal distance of the lens(es) used with the camera(s) was chosen to cover a field of view of 60 cm for the sand tests and 80 cm for the PVC tests. The cameras were then moved in steps of 55 cm (resp. 75 cm), with a 5 cm overlap used to check the reproducibility of the tests and the alignment of the flow profiles on successive viewing windows. At the end, the attained spatial resolution for one pixel amounts to approximately 1.2 mm for the sand tests and 0.8 mm for the PVC tests.

Lighting is provided by several frontal spot heads, with a combined power of 5000 Watts, positioned to guarantee uniform illumination of the scene and avoid direct reflections of light towards the cameras. The back sidewall was covered with an external black sheet to provide a uniform background. The overall apparatus is schematised in Fig. 2.9.

A ruler on the sidewall provides scaling and reference positions for the different images. The time reference is obtained by placing a Xenon flash lamp behind the black sheet on the opposite sidewall. The lamp emits a short pulse of light when the gate is at mid-course during opening, triggered by a magnetic contact reed placed along the shaft of the jack. The flash produces a white halo through the back-sheet, clearly visible on the image recordings.

After a full sequence of repeated tests corresponding to the same configuration, the individual images pertaining to the same instants are assembled to form wide image mosaics over the entire flume length, with approximate resolution of 5000x500 pixels.

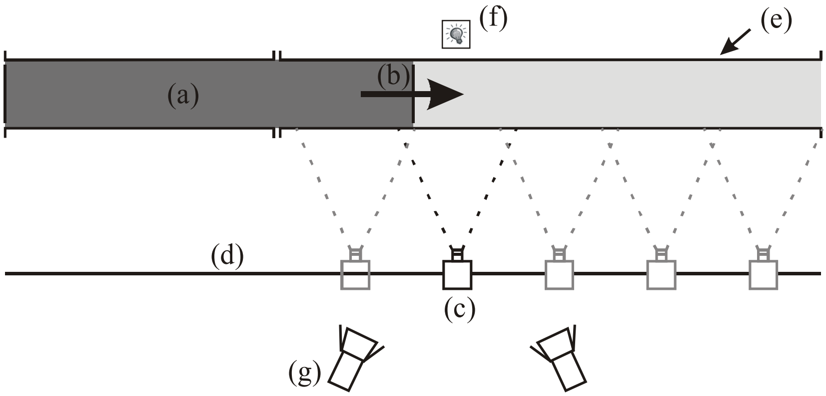

Figure 2.9. Side-view imaging apparatus. (a) flume; (b) gate; (c) digital camera; (d) guiding rail for camera displacement; (e) dark back sheet; (f) flash lamp for time synchronisation; (g) spot heads.

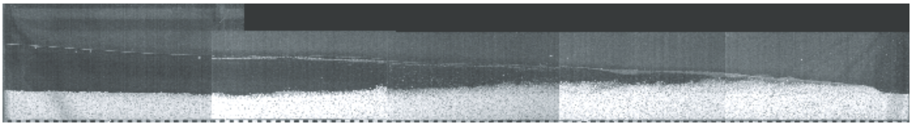

Figure 2.10. Typical mosaic image assembled from different runs; obtained for the initial configuration of Fig. 2.8a.

A typical mosaic image obtained using the above approach is illustrated in Fig. 2.10. The water is seen as a black mass with a visible upper free surface, while the sediment grains stand out saliently as bright blobs. Reasonably seamless transitions are seen between the internal images composing the mosaics, giving confidence in the reproducibility of the tests.

In a subset of the tests, the water was seeded with additional tracer particles to visualise the flow field. These are Pliolite® particles, white and about 1 to 2 mm in size, with a specific density of 1.03. Prior to being dispersed in water they are mixed for half an hour in a solution with a wetting agent (typically washing-up liquid) to remove surface tension and make them neutrally-buoyant in fresh water.

Besides side-view imaging, flow measurement included also the collection of eroded bed material in a permeable net at the flume outlet. The total amount of eroded sediments reaching the flume outlet throughout the experiment gives a rough indication on the intensity of geomorphic changes that occurred in the channel. The collected sediments were dried before being weighted precisely.

5. Imaging methods

Besides a qualitative visual interpretation, the image sequences were analysed quantitatively with two broad classes of imaging methods: the first class aims to obtain a general description by dividing the flow into a series of representative regions, and to identify the interfaces separating them; the second seeks to derive local velocity measurements by tracking the movements of the Pliolite® tracers dispersed in water, or of the individual sediments themselves.

5.1. Interface identification

Following Capart (2000), three characteristic flow regions can be identified: a pure water layer, a transport layer made of a mixture of water and moving grains, and the motionless sediment bed. These flow regions are separated by relatively sharp interfaces, that can be identified on the assembled mosaics.

The interfaces are positioned using a semi-manual procedure. The interface between air and water draws a well-defined profile that may be identified directly from the raw image mosaics without ambiguity. The interface between the clear-water layer and the sheet-flow layer is usually well defined too, except in regions where some grains depart from the main transport layer and are transported into suspension for a while. Such short-term suspension mode of transport, however, was found to occur for very restricted space and time windows of the flood wave propagation, as the range of density and sizes of the sediment particles do not allow sustained suspension. The positioning of the interface thus follows the main sheet-flow layer and avoids to incorporate isolated grains.

Finally, the interface between the layer of moving grains and the static granular bed below may not be obtained using a single image mosaic only. Information related to the flow dynamics is required to distinguish between moving and static grains. Two alternatives were explored: the first relies on a composed image obtained by superimposing multiple successive images. Each pixel value is taken as the maximum of pixel values on the sequence. The result, shown in Figs. 2.11b and 2.11f, is similar to what would be obtained from a digital camera operating at a long exposure time. The region of the static bed appears sharp, while the region of moving grains appears smeared out and blurred. The procedure was used with slow flows by Perng *et al.* (accepted) to detect coherent granular motions in uniform flows driven by an inclined conveyer belt, and by Tsorng *et al.* (submitted) to obtain long-standing trajectories of diluted particulate dispersions within lid-driven cavity flows. In the present context, it yields a qualitative feeling of the overall movement, but the procedure requires to sum up a lot of images which results in a substantial loss of spatial resolution, especially near the fast-moving wavefront. Instead, a different principle is adopted, by subtracting a mosaic pixel-by-pixel from the subsequent mosaic, and then taking the absolute value to create a differentiated image. Doing this, the regions with constant (the static bed) or homogeneous (the ambient air and clear-water layer) pixel values appear black, whereas the fluctuating region of the sheet-flow layer appears brighter. The resulting image is slightly smoothed off by applying a low-pass binomial filter with a filter scale of a few pixels, in order to remove high-frequency noise in the dark regions (Figs. 2.11c and 2.11g). The bed interface is then pinpointed using the same procedure as for the other two flow interfaces obtained previously.

In previous experimental analyses (Spinewine and Zech, 2002), automated detection procedures were used to obtain the three interfaces. Here, the guided manual procedure is preferred. Though endowed with some degree of subjectivity, it benefited from the experimented eye of the observer and was more robust. In Fig. 2.11d the three identified interfaces are superimposed on the mosaic image.

5.2. Particle-tracking velocimetry

The second class of imaging methods utilized for the present dam-break experiments with a PVC bed pertain to the broad family of Particle Tracking

Velocimetry (PTV) techniques. Their common characteristic is to identify "particles" on a sequence of digital images, and to track their positions from frame to frame to deliver particle trajectories and velocities. The term "particle" should be taken in the broad sense, as any image feature that may be abstracted to a point-like object. It may equally stand for real stand-alone particles or for salient feature-points of a larger object.

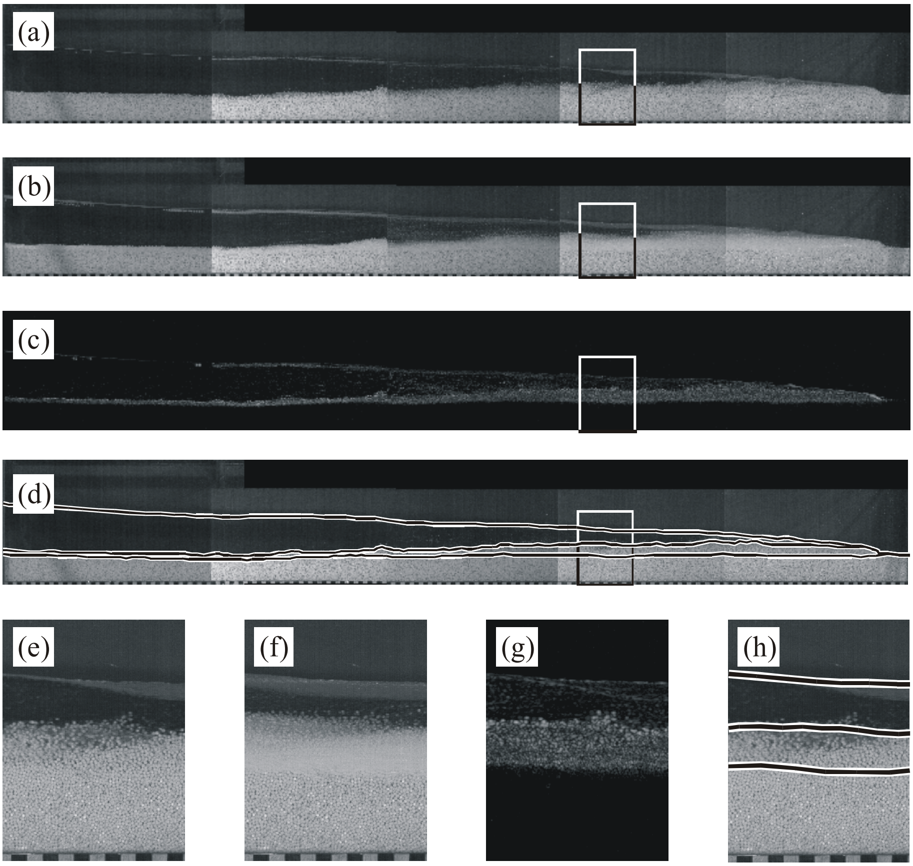

Figure 2.11. Detection of sharp flow interfaces on the experimental mosaic of Fig. 2.10. (a) original mosaic; (b) long exposure image; (c) differentiated image; (d) detected flow interfaces in superimposition; (e)-(h) zooms on the rectangle insets of panels (a)-(d) respectively.

The use of digital imaging for qualitative and quantitative characterisation of fluid flows is not new. In recent years however, with the rapid development of powerful digital cameras at affordable prices and the advances in robust and fast image processing techniques, this tool has become very popular. There has been a tremendous development of particle imaging methods in the last decade, and the methods have been used in a wide variety of applications, ranging from fluid dynamics applications to astronomy, traffic control or biology. The large majority of applications, however, used to be restricted to relatively dilute particle dispersions.

The category of Particle Tracking Velocimetry (PTV) methods typically rely on two main steps for the analysis: (i) the identification algorithm, whose objective is to abstract the image into a set of discrete positions of "particle" centroids; and (ii) the matching algorithm, performing the correspondence between sets of particle positions at two distinct instants. They differ substantially from another class of imaging velocimetry methods, usually referred to as Particle Image Velocimetry (PIV). The latter does not identify nor track individual particles, but relies directly on the image and performs image cross-correlation to identify the average flow field. Its spatial resolution is linked to the size of the interrogation window utilized in the cross-correlation algorithm, and is typically one order of magnitude larger than the pixel size of an individual particle. The advantage of PTV over PIV is that individual particle motions are resolved, and that full sets of particle trajectories can be reconstructed by following one and the same particle over many successive frames, information that might be crucial for granular flow applications (Larcher, 2002) or fluid applications involving small-scale features (vortices, turbulence), for which Lagrangian information is needed. On the other hand, its drawback is the difficulty of designing a tracking algorithm that is robust and performs well even in very dense and fluctuating particulate flows, for which the displacement of particles between two successive frames may be larger than the distance separating neighbouring particles on a single image. The current concern of dense, dam-break induced granular flows constitutes a challenging application in this regard.

The simplest tracking algorithms rely on minimum-displacement or path-coherence criteria. For these traditional algorithms, however, the probability of “mismatches”, i.e. of pairing particles that do not correspond to each other, grows dramatically as the density of particles and the fluctuations of particle movements increase. Capart *et al.* (2002) have proposed an original pattern-based tracking algorithm for the measurements of fluid-granular flows. They rely on the geometrical properties of Voronoï diagrams, built around the sets of particle positions, to perform a robust matching, even for dense and rapidly sheared granular dispersions.

Stereoscopic imagery is used to extend the methodology to three space dimensions, and substantial work was performed to validate the Voronoï method in a series of various applications: fluidised granular beds (Spinewine *et al.*, 2000; Spinewine *et al.*, 2002a), flow in granular silos (Spinewine and Zech, 2001), characterisation of 3D vortices induced by submerged jets and velocimetry and 3D free surface topography of dam-break waves past a sudden enlargement, a 90° bend or an isolated obstacle (Douxchamps *et al.*, 2003; Soares Frazao *et al.* 2001, 2003), flow over antidunes (Douxchamps *et al.*, 2005), breaching of a sand dike (Spinewine *et al.*, 2004). The method was also extended to estimate solid concentrations, and to account for several classes of particles with differing grain sizes, brightness and/or velocity fields. Current endeavours using this extension are made in collaboration with the University of Trento to characterize the segregation mechanisms in uniform debris flows of binary mixtures (Larcher *et al.*, 2005). The extension to several particle classes was useful in the present context to distinguish between the movements of the Pliolite® tracer particles and the bed sediments themselves.

The method and results are presented in Spinewine *et al.* (2003), a paper closely related to the current doctoral research and whose abstract is provided as the Appendix I of the present manuscript. The following paragraphs restrict to a brief presentation of the principles of the Voronoï methods, along with some illustrative examples in the context of dam-break experiments. The reader may refer to Capart *et al.* (2002) and Spinewine *et al.* (2003, Appendix I of this thesis) for more details on the methods.

5.2.1. Essentials of the Voronoï imaging methods

A typical set-up of a particulate flow is as presented in Fig. 2.12; a flow of particles is imaged from above or through a transparent side-wall. The particles are roughly identical and appear brighter than the surrounding fluid on the digital images. The flow is imaged from a single camera (Fig. 2.12a) or from two cameras in a stereoscopic arrangement (Fig. 2.12b).

In most of these situations, the individual elements of the disperse phase (bubbles, grains or tracers) can be approximated as rigid bodies undergoing distinct motions. The dynamic system can thus be abstracted into an evolving configuration of particle positions. The measurements to be made include 2D and/or 3D positioning of the visible grains, tracking of 2D and/or 3D particle motions, and reconstruction of full sets of particle trajectories.

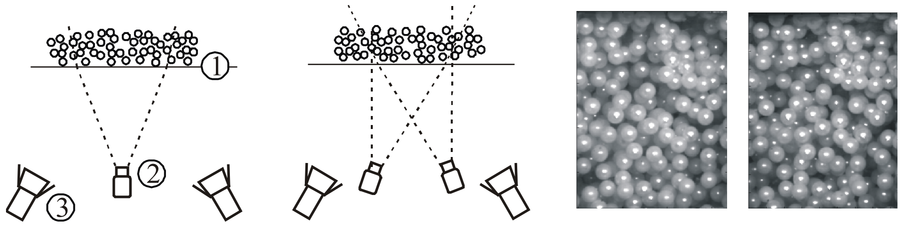

(a) (b) (c)

Figure 2.12. Typical measurement set-up of a flow of particles imaged through a side-wall, using: (a) a single camera; (b) two cameras in a stereoscopic arrangement. (1) side-wall; (2) digital camera; (3) lighting system. (c) sample images in a stereoscopic arrangement.

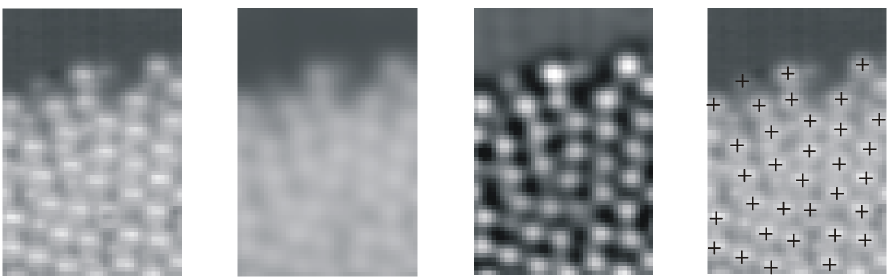

(a) (b) (c) (d)

Figure 2.13. Particle identification procedure (after Capart et al., 2002). (a) image fragment; (b) image (a) after low pass filtering; (c) image (b) after high pass filtering; (d) particle positions at brightness maxima of (c).

The first step of the analysis consists in the localisation of particle centroids on individual images. For each instant at which an image is acquired, one seeks to identify the set of particle image positions $\{\mathbf{R}_i\}$, where $\mathbf{R}_i = [X_i\ Y_i]^T$ is the 2D position of the *i*-th particle (with superscript T designating the matrix transpose). Particle images show up on the acquired frames as white blobs of a certain size against a dark, relatively noisy background (see Fig. 2.13 a). An image neighbourhood associated with a particle can be approximated by a Gaussian grey-level function centred on the particle centroid, with a diameter *D* that scales with the pixel diameter of the particles. Such bell-like regions are first highlighted by convoluting the image with a Laplacian-of-Gaussian (Mexican hat) filter of width *D* (Jähne, 1995). This effectively suppresses high frequency noise and low frequency variations in illumination (Fig. 2.13b, c). Local maxima of the highlighted images are then sought. This is done by a "dish-clearing" iterative algorithm: a global maximum is found, then a Gaussian bell of diameter *D* is subtracted from the neighbourhood grey level values; a new global maximum is found, and so on. The position of each maximum is finally refined to sub-pixel accuracy by way of a second-degree interpolation surface fitted around the discrete pixel position. These various steps are shown in Fig. 2.13a-d, with details given in Capart *et al.* (2002). The expected root-mean-square accuracy on the *X* and *Y* image co-ordinates obtained with such a procedure is of the order of 0.25 pixel (Veber *et al.*, 1997).

Besides particle positions, particle velocities are obtained as inter-frame displacements of the particle positions. Whereas the application of traditional PTV algorithms (minimum displacement, path coherence, …) is restricted to relatively coherent flows with diluted particle tracers, Capart *et al.* (2002) have proposed a more robust set of methods that allow to reconstruct full sets of particle trajectories even in extreme conditions as for very dense, intensively sheared dispersions. As for the 3D method discussed in Spinewine *et al.* (2003), the geometrical properties of the Voronoï diagram are used to track particle neighbourhoods from frame to frame. The Voronoï diagram (Fig. 2.14) is a geometrical construction that divides the space into a set of polytopes, or cells, surrounding each feature point. Each Voronoï cell V_i (in 2D) or v_i (in 3D) encompasses the region which lies closer to $\mathbf{R}_i$ (respectively $\mathbf{r}_i$) than to any other feature-point of the set. The Voronoï construction presents many useful properties, discussed in a general context in Okabe *et al.* (1992).

Sets of 2D particle positions at successive times have first been acquired by repeated application of the above positioning methods to each frame of a movie sequence. Let $\{\mathbf{r}_{i,m}\}$ and $\{\mathbf{r}_{j,m+1}\}$ be two such sets of particle positions sampled at successive times t_m and $t_{m+1} = t_m + \Delta t$. Particle velocities $\mathbf{v}_i$ ($t_{m+1/2}$) can be estimated by expression

$$\mathbf{v}_{i,m+1/2} = \frac{\mathbf{r}_{j(i),m+1} - \mathbf{r}_{i,m}}{\Delta t}, \tag{2.1}$$

provided one can first "connect the dots" and establish a pairing $j(i)$ between positions $\mathbf{r}_{i,m}$ and $\mathbf{r}_{j(i),m+1}$ belonging to the same physical particle. When dealing with a moving dispersion of many identical particles, the main problem consists in establishing this correspondence; i.e., finding which particle on one snapshot corresponds to which one on the next. This particle tracking problem can be seen as a time-domain variant of the stereo matching problem addressed in Spinewine *et al.* (2003).

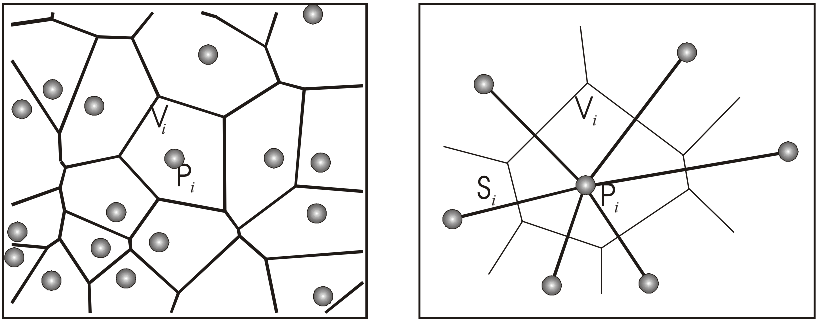

(a) (b)

Figure 2.14. Definition of the Voronoï diagram. (a) planar Voronoï diagram V_i (thick lines); (b) Voronoï vertex star S_i (thick lines) surrounding P_i.

For dilute particle dispersions or slow motion, the correspondence problem can be solved easily by simply pairing together the particles on one frame and the next which are nearest to each other (see e.g. Guler *et al.* 1999). For dense dispersions or rapid motion, however, legitimate pairing candidates may travel further away on successive frames and the minimum displacement criterion breaks down. An alternative approach derives from the following observation: while individual particles are identical to each other, the local arrangements that they form with their neighbours are unique and may be preserved by the flow long enough to serve as basis for tracking. Particle pairing can then be performed based on pattern similarity.

Capart *et al.* (2002) resort to the Voronoï diagram to implement such pattern-based tracking. Nearby particles are paired according to the geometrical similarity of their Voronoï cells. This similarity is estimated as follows: "stars" are first constructed by connecting a given particle centre to its Voronoï neighbours (i.e. the particles with which it shares a cell face), as illustrated on Fig. 2.14b. The stars belonging to two pairing candidates can then be compared based on a distance measure, defined by making their centres coincide and measuring the distances between the star extremities. Once these indicators are available for all possible pair candidates, a global optimum problem can be defined and solved that maximizes the "goodness-of-fit" of matched particles. For two dimensions, the overall method is illustrated on Fig. 2.15a-c for a plane granular flow. While graphical representation is harder in 3D, the algorithms themselves generalize straightforwardly to the third dimension (Appendix I).

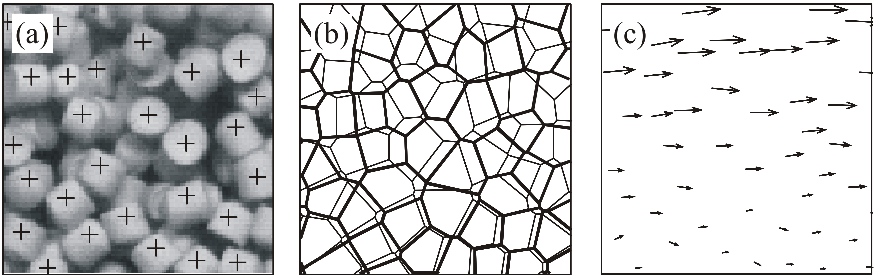

Figure 2.15. Pattern-based velocimetric tracking (Capart et al., 2002). (a) original image fragment and particle positions; (b) Voronoï diagrams built on sets of particle positions at two successive time instants; (c) velocity vectors built by matching the local Voronoï patterns.

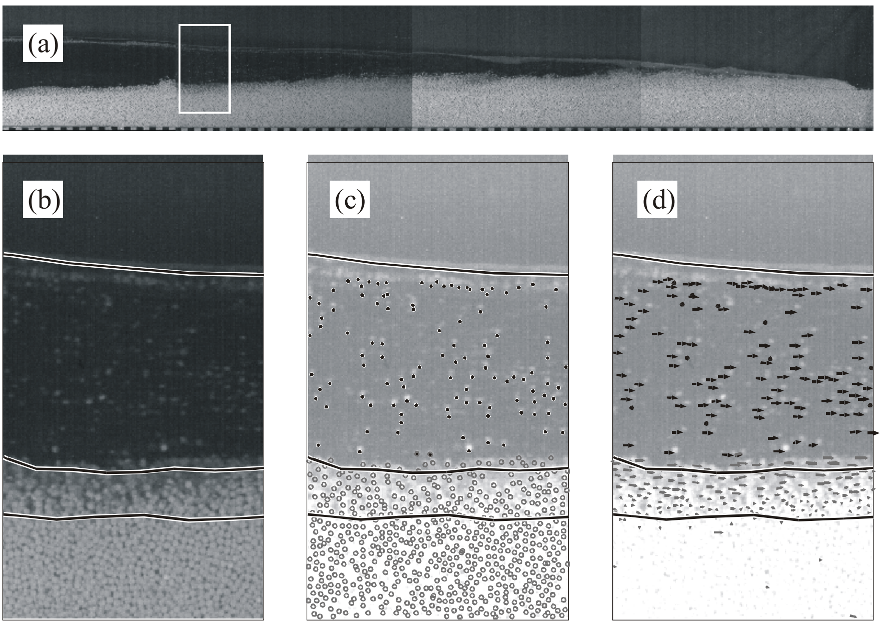

Figure 2.16. Overall Voronoï particle-tracking methodology applied to the dam-break experiments, successively to the sediment grains and to the Pliolite® tracers. (a) general flow mosaic; (b) zoom on the rectangle inset of (a), along with the three flow interfaces; (c) identified positions of sediment grains (grey hollow symbols) and Pliolite® tracers (black symbols); (d) displacement vectors between two successive mosaics.

Successive application of the overall detection and matching procedures to the granular and clear-water regions of the typical dam-break mosaic of Fig. 2.10, with filter parameters customised for the two classes of particles (Pliolite® tracers and PVC sediments) yields the particle positions and velocity vectors as highlighted in Fig. 2.16, magnified over a rectangular portion of the wave for better visualisation.

6. Experimental observations

In this section, experimental observations are presented based on the analysis of the image sequences for both the sand and PVC tests. The description restrict to general considerations of the observed flow behaviour. The experiments will be further utilised in the next Chapters for the formulation of the proposed shallow-water model and its validation.

6.1. Flume and gate performance

The gate constructed according to the design described in Section 2.2 was found to perform well. The gate drops from the upstream water level to the downstream level (a maximal distance of 35 cm for the tests of Fig. 2.8a-e) in less than 0.1 s, or 20 images. This is as fast as what was obtained previously over a much lower depth (10 cm) with a rising gate and a system of pulleys and counterweight (Spinewine and Zech, 2002). Snapshots of the free-surface in the immediate instants surrounding the gate opening are shown in Fig. 2.17. After detaching from the upper stopper, the gate bends slightly to the downstream side due to the water pressure, but the deflection is limited by the guiding roller bearings in the lower portion of the gate.

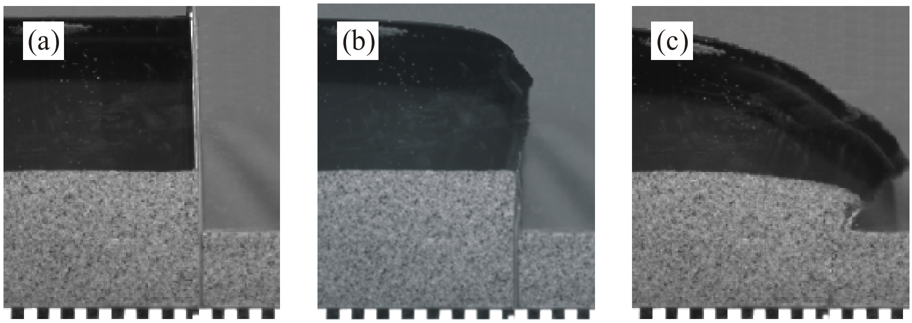

Figure 2.17. Flow snapshots at instants immediately following gate opening. (a) initial conditions with gate in raised position; (b) nearly unperturbed wall of water immediately after gate withdrawal; (c) wave formation at a later instant.

The most notable differences with the rising gate lies in the sharpness of the initial conditions and the initiation of movement. The rapidly lowering gate leaves a nearly unperturbed standing wall of water. The collapse of the water body was seen to be initiated both in the upper and lower regions. A plunging feature develops near the free surface, where the water was released at first. A mushroom-like feature emerges from the lower portion, near the sediment bed, where water pressure is initially maximum. This mushroom feature was, however, not observed in the case of a downward bed discontinuity, hence it is not visible in Fig. 2.17. Issues about the initial formation of the dam-break wave and the observed near-field features will be discussed more in details in Chapter 3, Section 2.2, and in Chapter 5.

6.2. The sand tests

Figure 2.18 shows reconstructed flow mosaics at selected instants for the sand tests on a flat bed with 35 cm of water in the upstream reservoir (configuration of Fig. 2.8a).

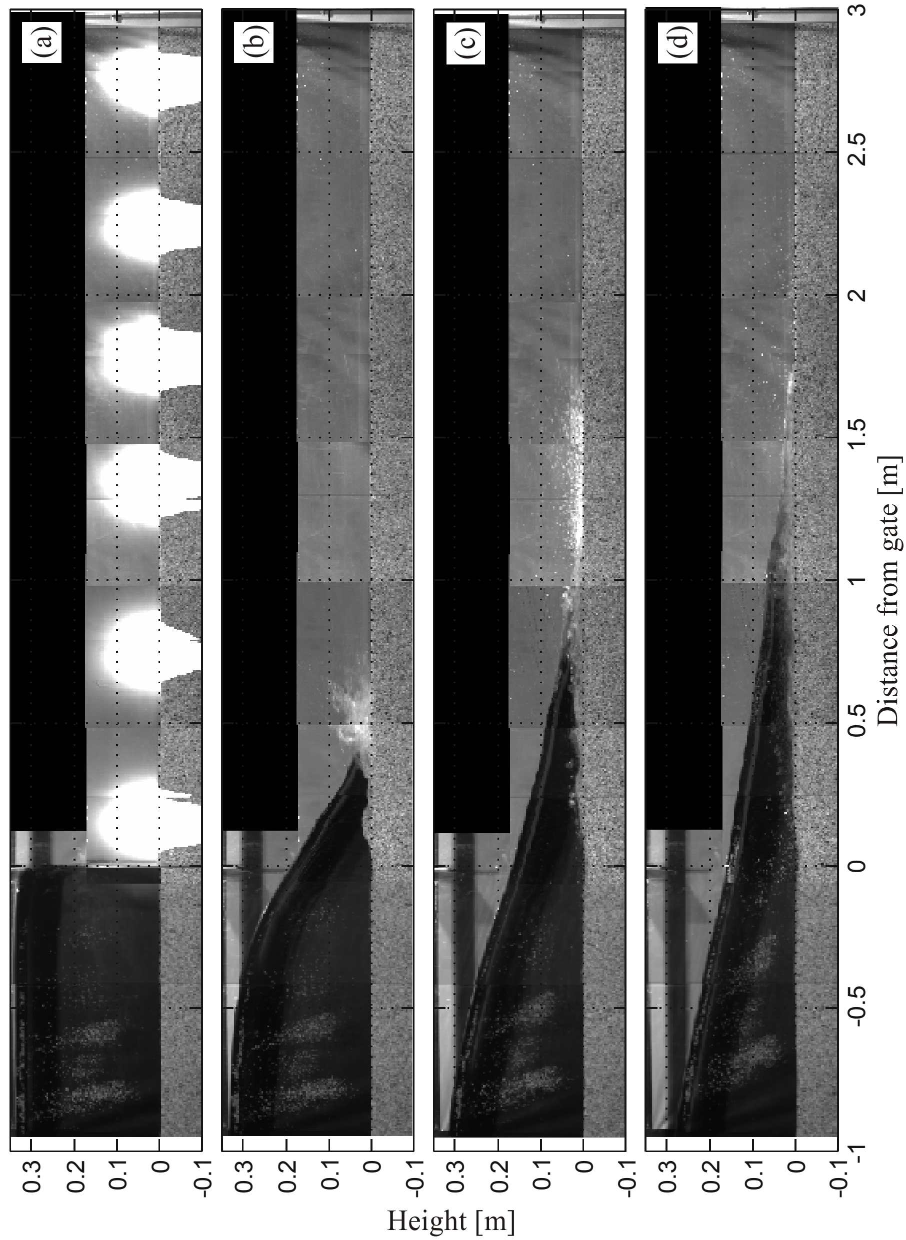
(a)
(b)
(c)
(d)
Height [m]
Distance from gate [m]
0.3
0.2
0.1
0
-0.1
-1
-0.5
0
0.5
1
1.5
2
2.5
3

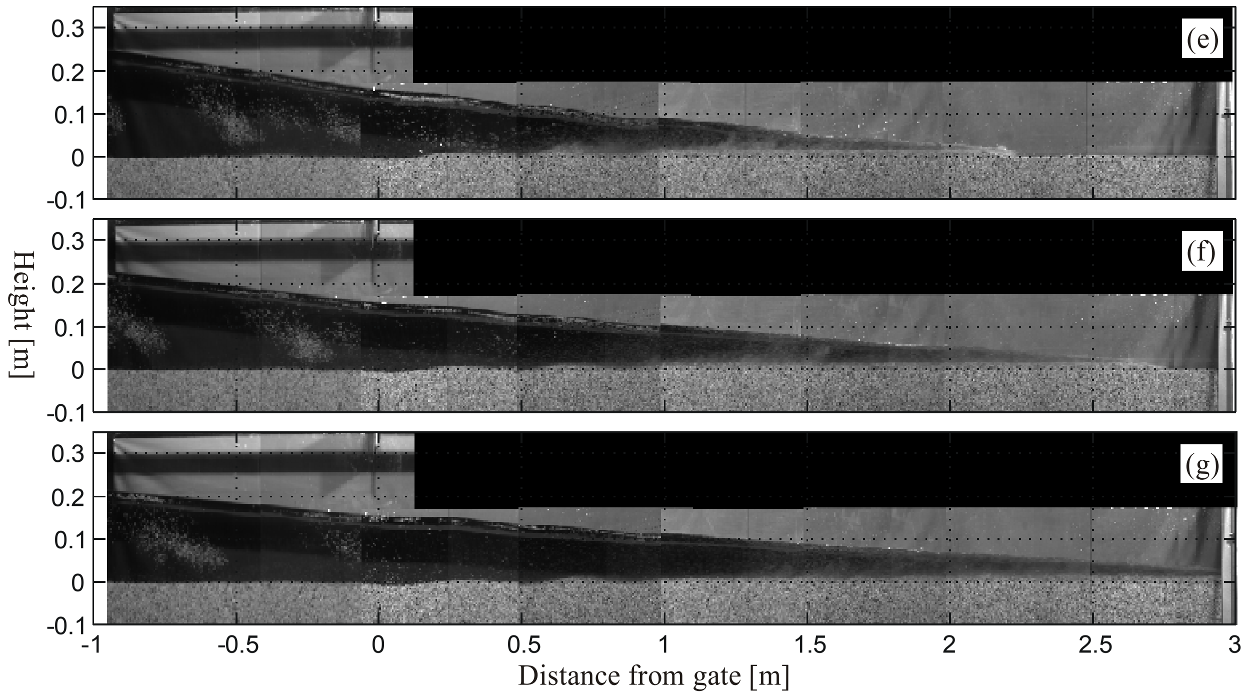

Figure 2.18. (2 pages) Flow sequence for the sand tests with a flat sediment bed (configuration of Fig. 2.8a), at instants $t = 0$, 0.25, 0.5, 0.75, 1, 1.25 and 1.5 s, respectively; vertical scale is distorted, stretched by a factor 1.5.

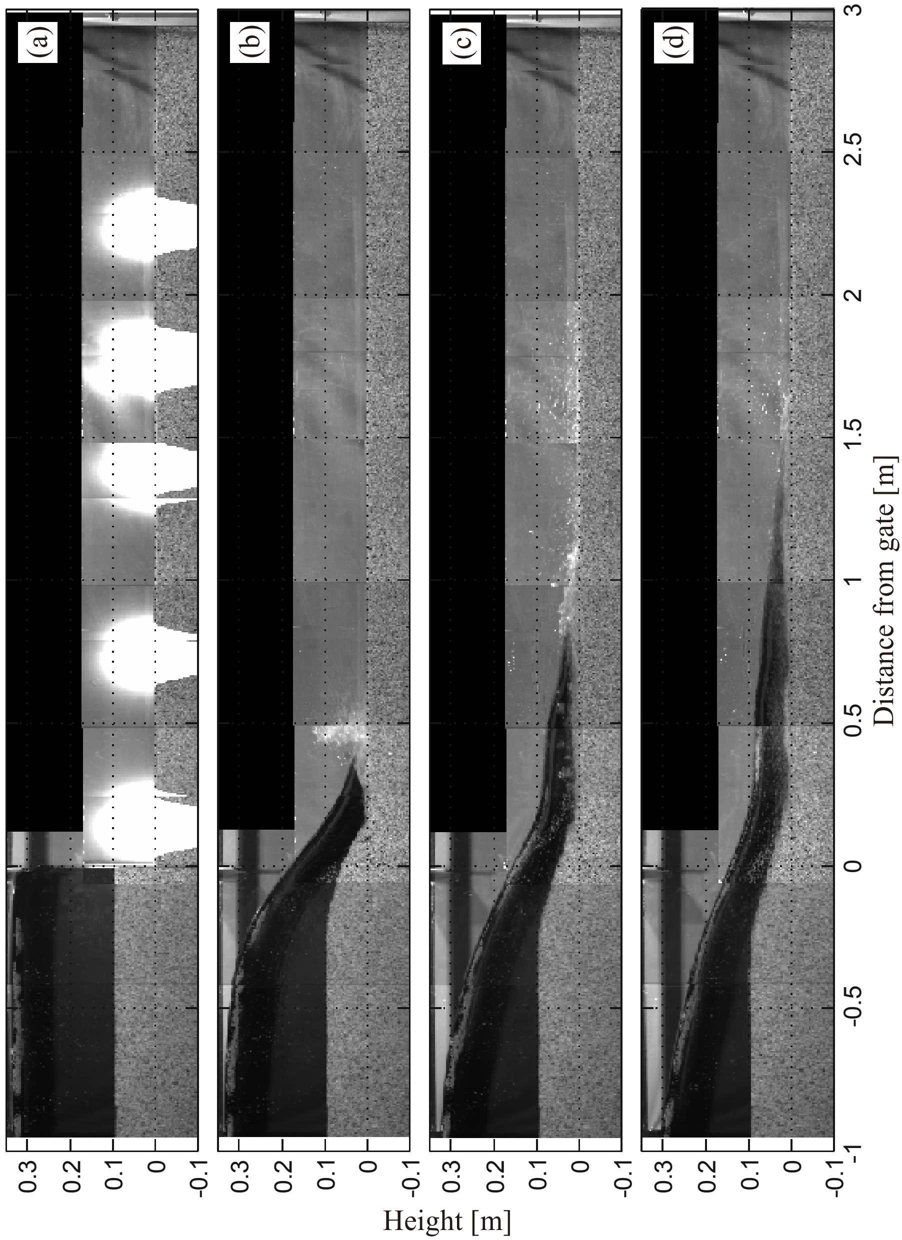
(a)
(b)
(c)
(d)
Height [m]
Distance from gate [m]
0.3
0.2
0.1
0
-0.1
-1
-0.5
0
0.5
1
1.5
2
2.5
3

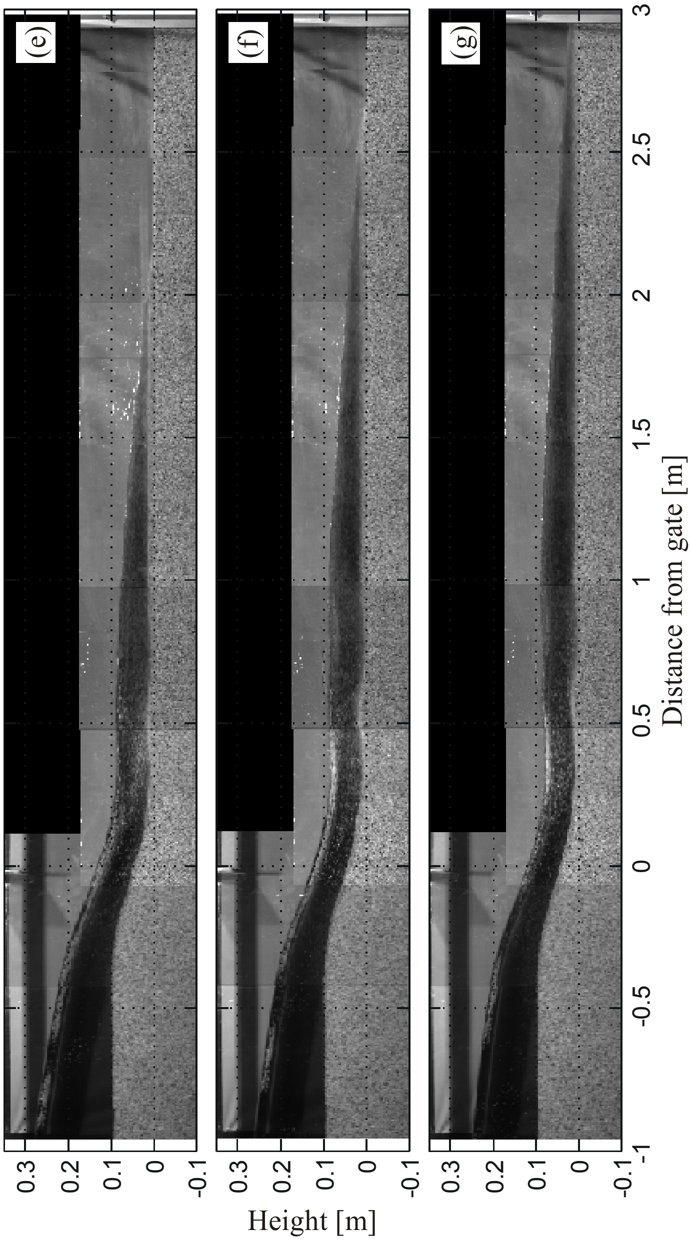

Figure 2.19. (2 pages) Flow sequence for the sand tests with a downward bed step of 10 cm (configuration of Fig. 2.8d), at instants $t = 0$, 0.25, 0.5, 0.75, 1, 1.25 and 1.5 s, respectively; vertical scale is distorted, stretched by a factor 1.5.

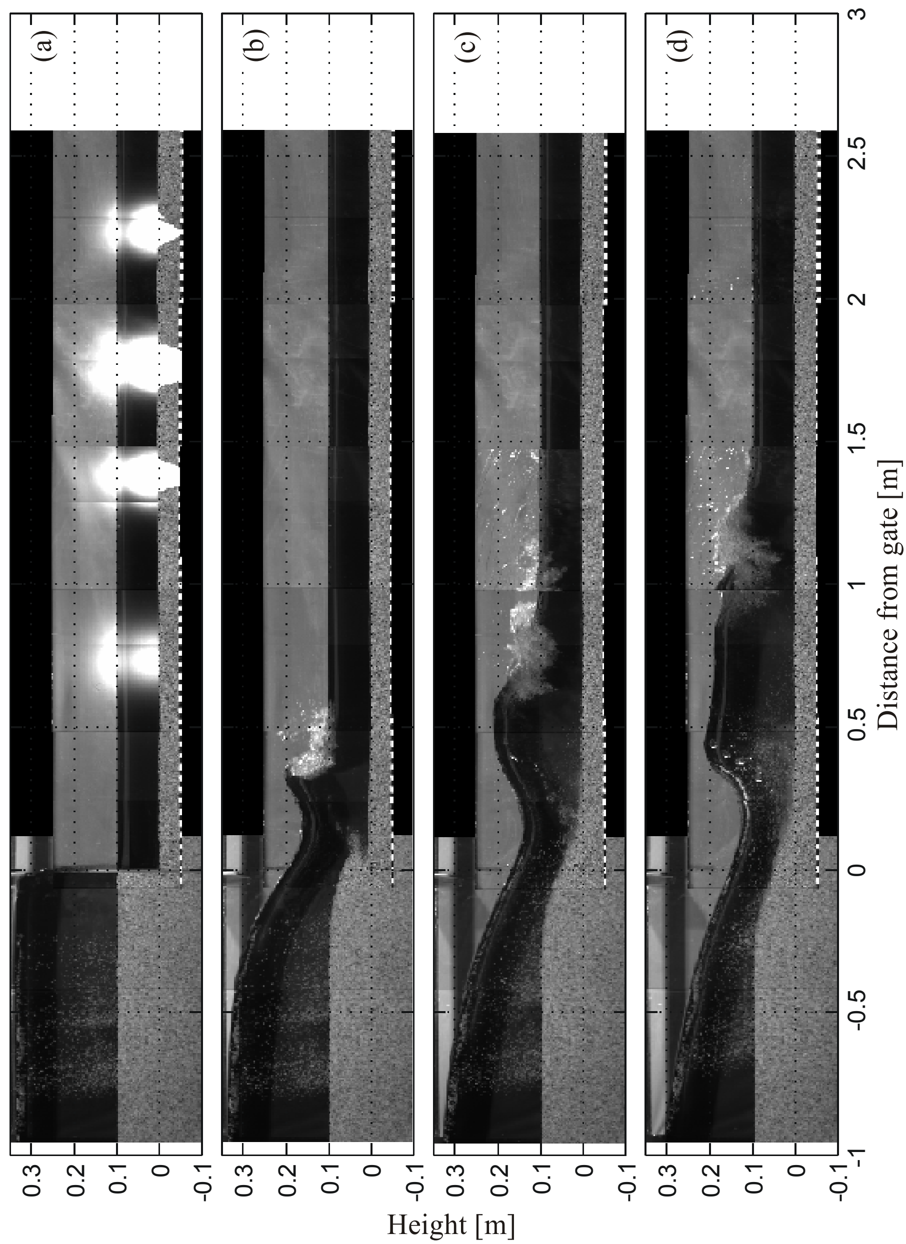
(a)
(b)
(c)
(d)
Distance from gate [m]
Height [m]
-1
-0.5
0
0.5
1
1.5
2
2.5
3
0.3
0.2
0.1
0
-0.1

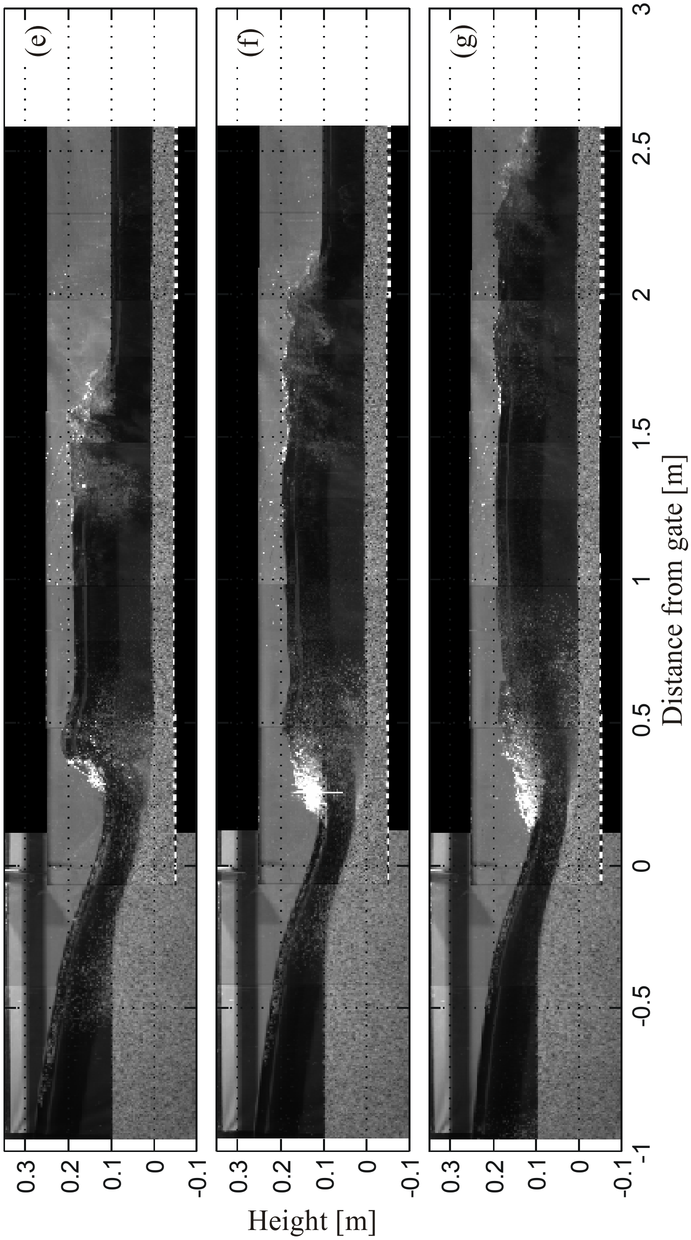

Figure 2.20. (2 pages) Flow sequence for the sand tests with a downward bed step of 10 cm and a downstream layer of water (configuration of Fig. 2.8f), at instants $t = 0$, 0.25, 0.5, 0.75, 1, 1.25 and 1.5 s, respectively; vertical scale is distorted, stretched by a factor 1.5.

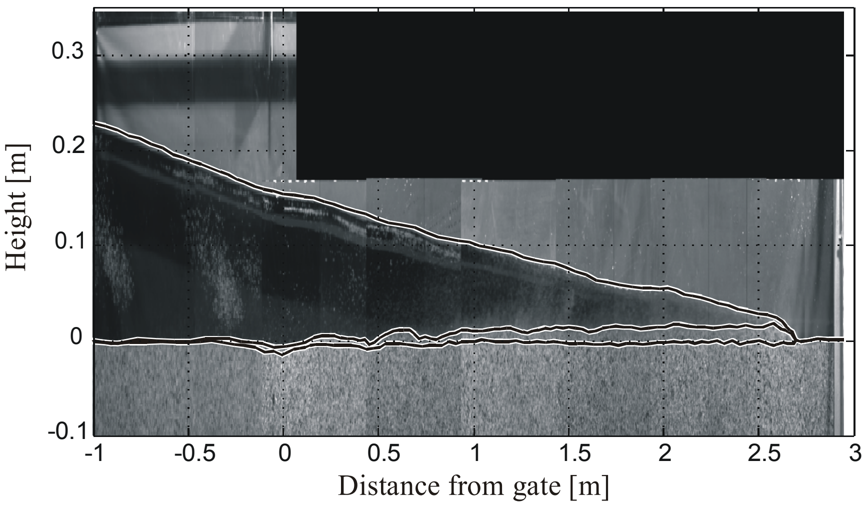

Figure 2.21. Highly distorted flow mosaic of Fig. 2.18 at instant $t = 1.25$ s; vertical scale is stretched by a factor 5.

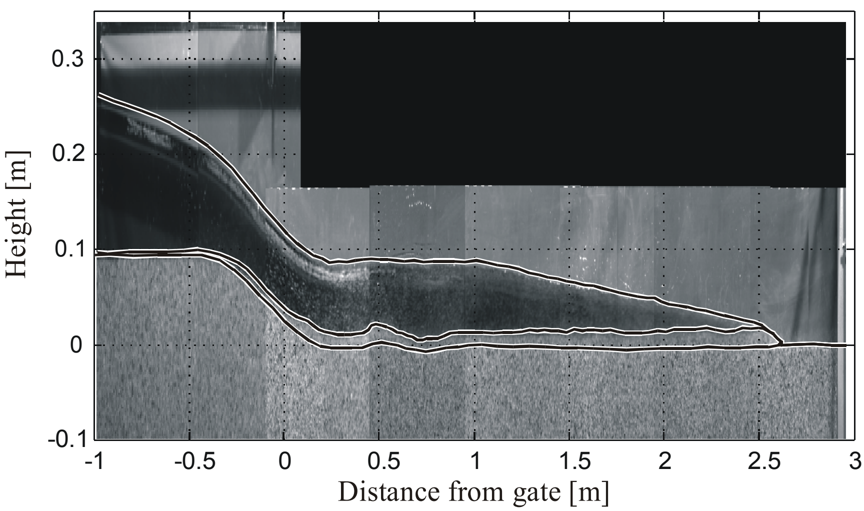

Figure 2.22. Highly distorted flow mosaics of Fig. 2.19 at instant $t = 1.25$ s; vertical scale is stretched by a factor 5.

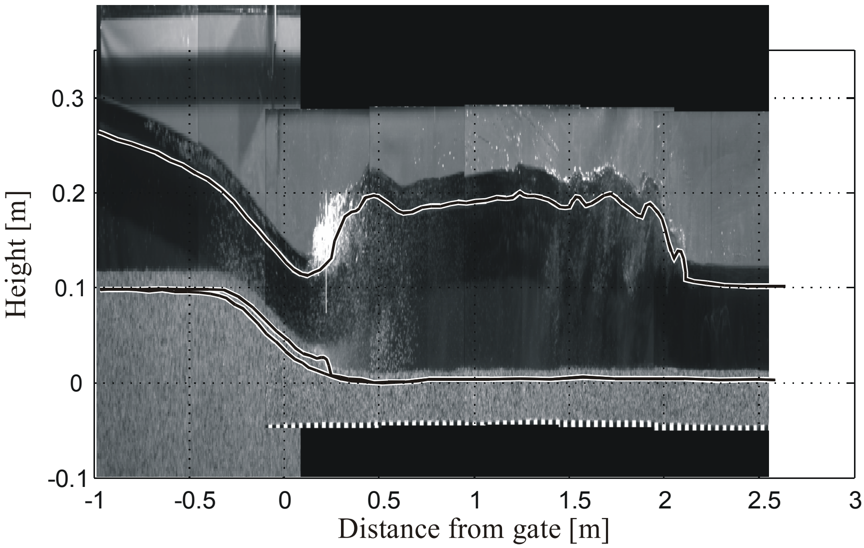

Figure 2.23. Highly distorted flow mosaics of Fig. 2.20 at instant $t = 1.25$ s; vertical scale is stretched by a factor 5.

Two other configurations are shown in Figs. 2.19 and 2.20. They correspond respectively to a downward bed step (Fig. 2.8d) and to a downward bed step combined with a downstream water layer (Fig. 2.8f). Flow mosaics for the remaining configurations (Figs. 2.8b, 2.8c and 2.8e) may be found in Appendix II.

The sequence of Fig. 2.18 highlights the behaviour of the dam-break wave. It is seen to be qualitatively comparable with the case of a classical dam-break wave over a fixed bed except for two important aspects. Those are better visualised in Fig. 2.21 where the vertical scale was distorted by a factor 5 for a better visualisation: (i) near the wavefront the depth does not approach smoothly towards zero; the wave rather forms a sharp bore of substantial thickness; (ii) all along the wave, and especially near the wavefront, the portion of flow depth filled by transported sediments is substantial. This bulking of sediments will later be seen to affect notably the celerity of the wave and the maximum attained flood levels, two parameters of utmost importance when designing emergency strategies and assessing risk associated with the potential failure of real dams or flood-defence structures.

The case of a downward bed discontinuity (Figs. 2.19 and 2.22) shows a similar behaviour near the wavefront. The initial bed step is rapidly smoothed out by the flood wave into a gradual transition. Downstream of the latter, a uniform region forms with a horizontal free surface, before the decrease towards the wavefront. The profiles of Figs. 2.20 and 2.23 in case of a bed discontinuity combined with a downstream layer of water show a very different behaviour: a downstream bore propagates at the free surface, and a hydraulic jump forms in the downstream vicinity of the gate. The bed discontinuity is first smoothed out, but then evolves into a sedimentation shock-wave located below the hydraulic jump, separating a region with active sediment transport upstream and a region with hardly no sediment transport downstream. The hydraulic jump and sedimentation shock wave then slowly propagate downstream but stay tighten together.

The different configurations may be compared in terms of wavefront celerity and interface levels. Figure 2.24 plots non-dimensional characteristic paths of the wavefront for the three cases discussed above and the other three found in Appendix II. Except for the two special configurations (Figs. 2.8e and 2.8f) where the front is much slower, the four remaining curves concentrate in a very narrow range. The height of the initial bed discontinuity is seen to have only a moderate influence, the celerity being only slightly lower for the cases with higher bed levels on the upstream side. The dashed grey line features the theoretical characteristic of the wavefront for the Ritter solution, i.e. a dam-break propagating over a rigid and frictionless dry bed at speed $u = 2\sqrt{g H_0}$, with H_0 the initial water depth. Compared to the latter, the erosional waves are significantly slowed down by the action of friction and the incorporation of bed material.

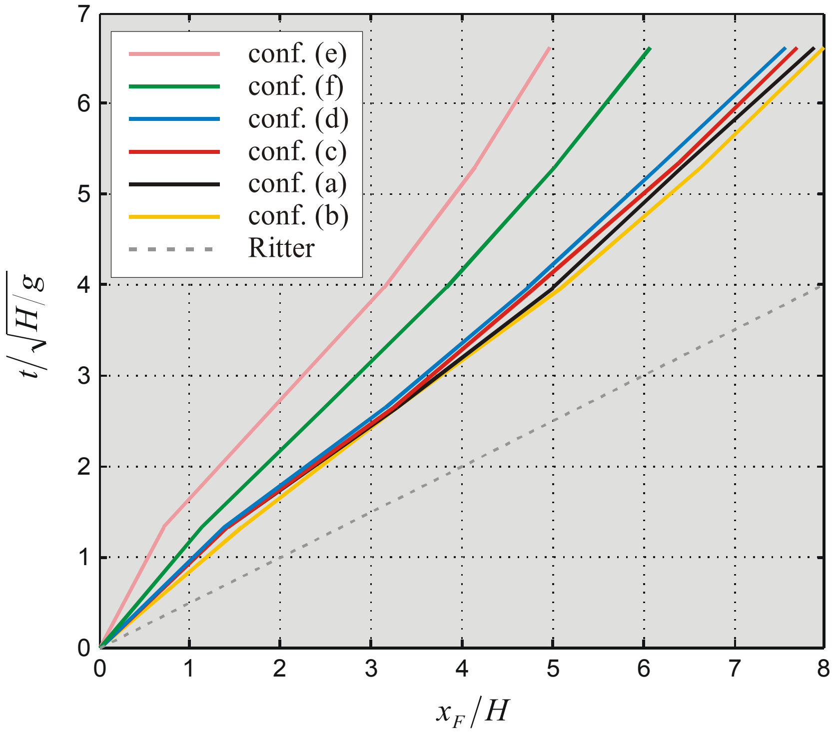

Figure 2.24. Characteristic paths of the wave front x_F for the sand tests in the various configurations. Legend refers to the configurations as defined in Fig. 2.8: (a) flat bed (black); (b) upward bed step (yellow); (c) downward bed step of 5 cm (red); (d) downward bed step of 10 cm (blue); (e) reservoir nearly filled with sediments (pink); (f) downward bed step and downstream layer of water (green); path of the Ritter wavefront on a rigid frictionless bed plotted as a grey dotted line. Axis made dimensionless by plotting x_F/H versus $t/\sqrt{H/g}$.

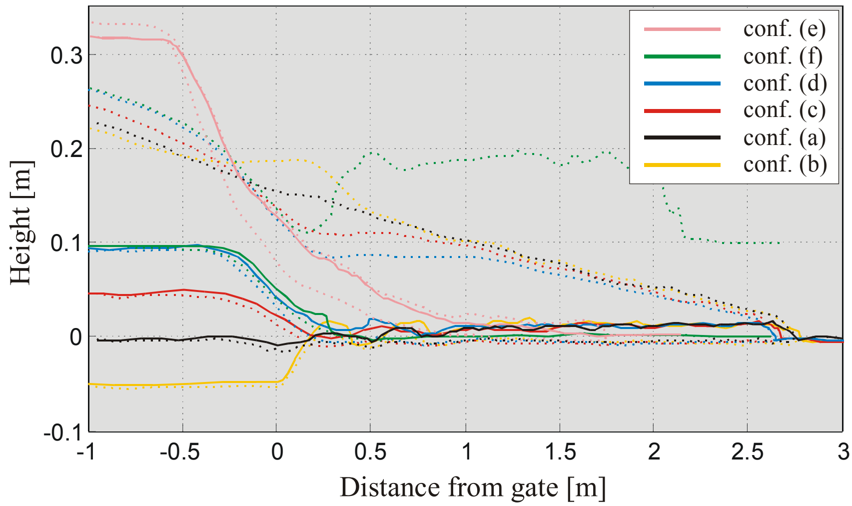

Figure 2.25. Comparison of interface levels at $t = 1.25$ s for the sand tests in the various configurations of Fig. 2.8. Colours as in Fig. 2.24; solid line: sheet-flow profile; upper dotted line: water profile; lower dotted line: bed profile. Vertical scale is stretched by a factor 5.

Comparisons of interface levels are provided in Fig. 2.25 for the same time, $t = 1.25$ s after gate release. Bed and water profiles are plotted as dashed lines, and the top of the sediment transport layer as a solid line. Again, the green and pink profiles of the two special configurations show a peculiar behaviour. The other configurations are surprisingly similar in the region of the wavefront, both in terms of the free surface profiles and of the thickness of the sediment transport layers. In the immediate vicinity of the gate, the bed discontinuity affects the free surface, creating a hump for an upward bed step (yellow curve) and a trough for a downward one (red and blue curves).

6.3. The PVC tests

Mosaics for the case of a flat bed made of PVC pellets are presented in Fig. 2.26, with a vertically distorted image reproduced in Fig. 2.27 for a better visualisation. Having in mind the corresponding images of Fig. 2.18 for sand, the PVC wave differs from its sand equivalent in three major aspects: (i) since the density of PVC is lower, erosion is much more intense, and a thicker sediment transport layer results. Near the extremity, bulking of sediment material into the flow is so intense that it saturates the full flow depth, forming a debris-flow like wavefront; (ii) the wave propagation is substantially slower, and consequently the maximum attained free surface elevations behind the front are higher. This may be a combined effect of increased friction and more intense erosion; (iii) the free surface profile does not decrease monotonously, but rather exhibits a series of humps and troughs. Similar oscillations are also observed at the top of the sediment transport layer, and are approximately in phase with the free surface undulations. These features are reminiscent of antidune bedforms observed on steep-sloped river beds or beach runnels in supercritical regime. They appear in the present context to result from a mechanism of instability between the clear-water layer and the sediment transport layer. Clues to why such instabilities are more prone to emerge in the PVC tests than in the sand tests will be given in Chapter 3.

Similar observations are derived for the other initial configurations, for which sequences of assembled mosaics are provided in Appendix II. In Fig. 2.28 corresponding flow profiles are compared for the six configurations at time $t = 1.25$ s. Very similar profiles are observed near the wavefront for the "standard" configurations (i.e. excluding the green and pink peculiar configurations). Initial bed steps seem to favour oscillations of a larger amplitude than the initially flat bed. As for the sand tests, an upward bed step creates a local rise of the free surface in the vicinity of the gate, while a downward bed step creates a local drop-down.

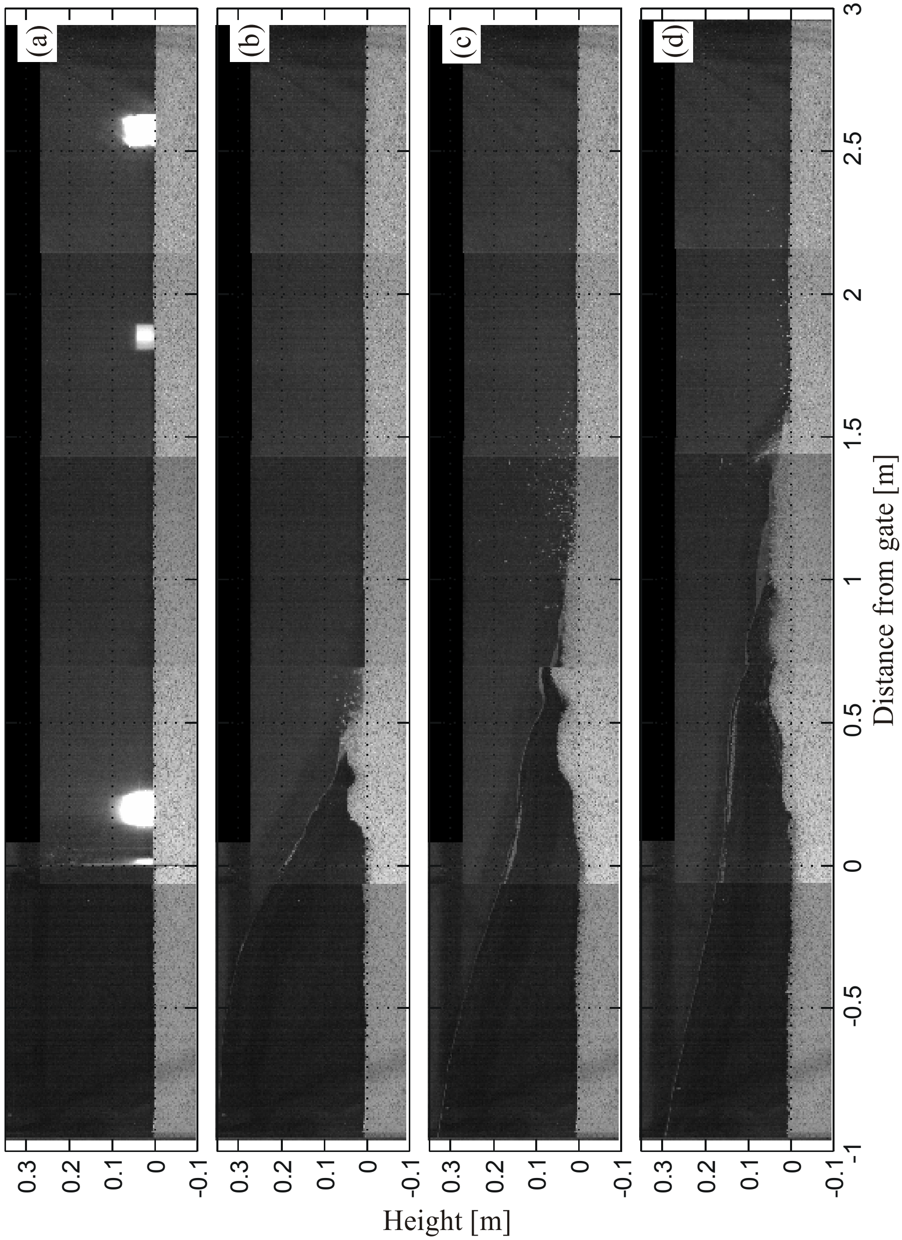
(a)
(b)
(c)
(d)
Distance from gate [m]
Height [m]
3
2.5
2
1.5
1
0.5
0
-0.5
-1
0.3
0.2
0.1
0
-0.1

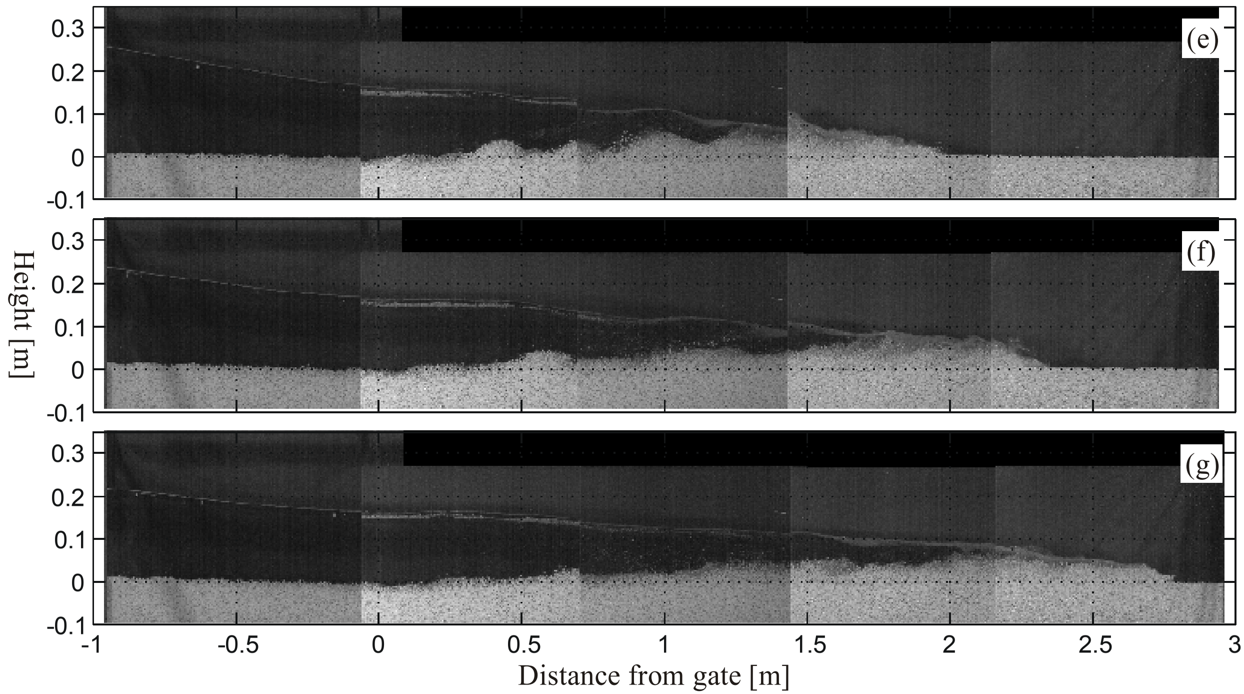

Figure 2.26. (2 pages) Flow sequence for the PVC tests with a flat sediment bed (configuration of Fig. 2.8a), at instants $t = 0$, 0.25, 0.5, 0.75, 1, 1.25 and 1.5 s, respectively; vertical scale is distorted, stretched by a factor 1.5.

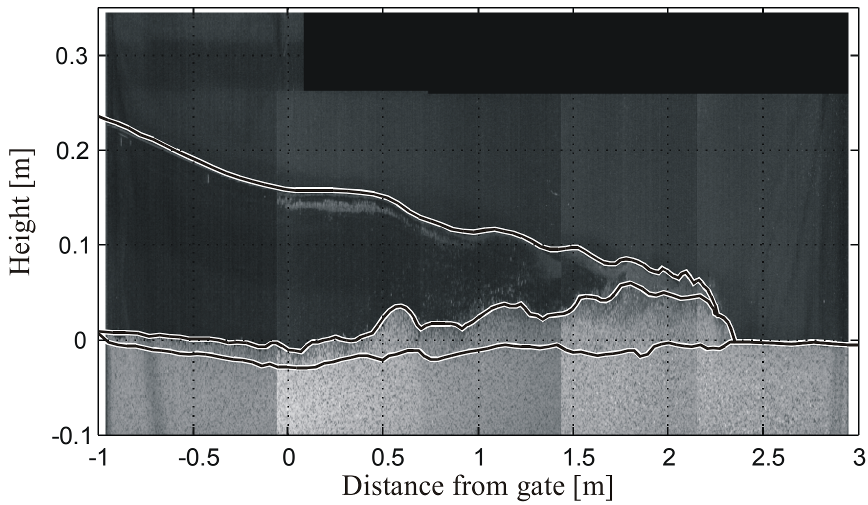

Figure 2.27. Highly distorted flow mosaic of Fig. 2.26 at instant $t = 1.25$ s; the vertical scale is stretched by a factor 5.

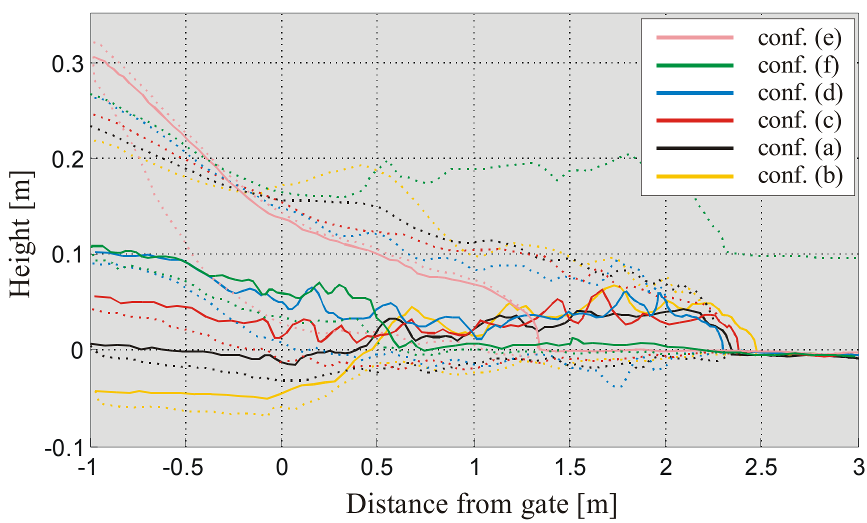

Figure 2.28. Comparison of interface levels at $t = 1.25$ s for the PVC tests in the various configurations of Fig. 2.8. Colours as in Fig. 2.24; solid line: sheet-flow profile; upper dotted line: water profile; lower dotted line: bed profile. The vertical scale is stretched by a factor 5.

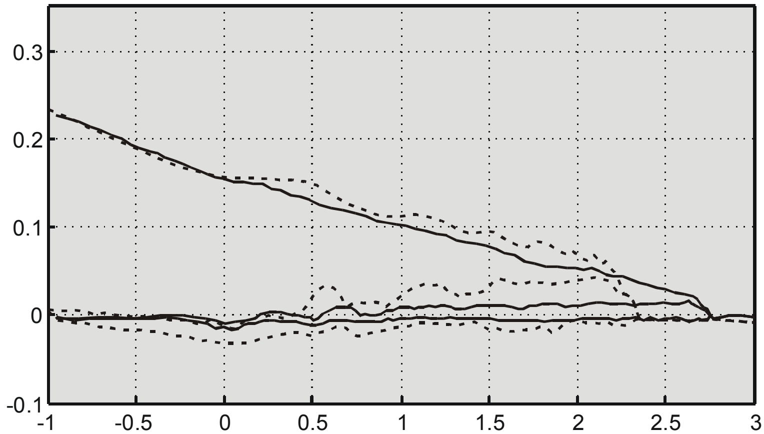

Figure 2.29. Comparison of PVC (dotted line) and sand (solid line) flow profiles for the same flat bed configuration, at the same instant $t = 1.25$ s. Dimensions in meters, vertical scale stretched by a factor 5.

If the initial bed configuration has only a moderate influence on the downstream wave celerity and shape, the density of the granular material, on the contrary, is very influential. In exactly the same initial configurations, profiles for the sand bed are compared in Fig. 2.29 with equivalents for the lighter PVC bed. For the PVC bed, the wave mobilizes a much greater volume of bed material than that for the sand, whose inertial resistance is greater. The incorporation into the flow of material initially at rest requires flow momentum, and the celerity of the wave is affected accordingly.

PVC tests were also performed with a lower initial depth of water, $H_0 = 25$ cm, in order to investigate scaling effects and similarity laws. The full sequence of flow mosaics for this case is given in Appendix II. In Fig 2.30a, the two configurations are compared at the same instant. Obviously the wave of larger depth propagates faster, and erodes the bed more actively. But when set in dimensionless form according to Froude similarity, by plotting $x/(t\sqrt{g H_0})$ on the horizontal axis and z/H_0 on the vertical axis (Fig. 2.30b), the two sets of profiles look amazingly similar (even the oscillations are approximately in phase with each other). Froude scaling thus apparently seems to be preserved even for erosional dam-break waves over granular beds, an important argument when seeking to jump, later on, from small laboratory experiments to real-life studies, and apply at large scales the same modelling strategy as the one that was validated at small scales.

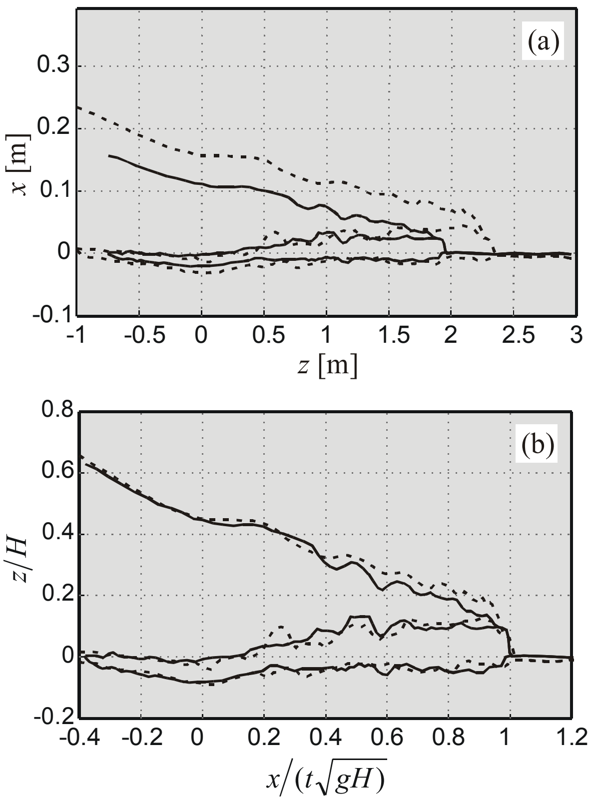

Figure 2.30. Comparison of PVC flow profiles over a flat bed for two initial depths in the upstream reservoir $H = 35$ cm (dotted line) and $H = 25$ cm (solid line). (a) dimensional plot; (b) dimensionless plot

Chapter 3

Two-layer flow behaviour of dam-break waves over granular beds

1. Introduction

The experimental studies presented in Chapter 2 allowed to examine with unprecedented details the dynamics of intense sediment mobilisation and entrainment by dam-break flood waves, in the near field close to the gate and at later instants in the region of the developed wavefront. Sediment transport intensities were seen to spread over a very wide range, from the slow grain-by-grain rolling mode in the upstream reaches to the highly concentrated sheet-flow mode near the downstream bore, where the mobilised sediments may invade the whole flow depth, moving as a dense suspension with apparently homogeneous properties. In view of reproducing these various modes of transport that are at places far from equilibrium conditions, it appears to be crucial for any geomorphic model to adequately account for sediment inertia, i.e. for the required transmission of flow momentum from the water to the sediment grains in order to set them in motion. Experimental observations have also shown that the ratio of depth-averaged velocities in the water region and in the region of mobilised sediments may vary substantially as a function of transport intensity. As a result, the two layers may not be assumed to flow at a single depth-averaged velocity. In contrast, they should be allowed to flow at distinct velocities, which should derive from the actual flow dynamics rather than from an *a priori* postulated velocity profile along the vertical.

The mobilized sediments shall be regarded as an equivalent fluid, materialised by an independent shallow flow layer endowed with its proper density, velocity and momentum. Such a two-layer shallow flow description was proposed by Capart and Young (2002), and previously applied to dam-break conditions in Spinewine et al. (2002b) and Chen et al. (submitted).

In this chapter, this fluid-like analogy is pushed to its limits, by considering a portion of the granular bed to be instantaneously and permanently fluidised, so that the conditions are basically those of a dam-break of a “light” fluid propagating over a substrate made of a “heavy” fluid. Thus, the possible change of state of the granular material, passing from a solid-like to a fluid-like behaviour or vice versa, is not accounted for at this stage. This essential mechanism, though, will be discussed later in Chapter 4, which constitutes the core of the present thesis and where a more elaborate model is derived that accounts for erosion and deposition of granular material.

The present simplified description, however, will allow to consider some essential characteristics of a two-layer shallow water framework, and to investigate its behaviour in dam-break conditions. In particular, the chapter will devote a substantial part to examine the influence of the density of the “heavy” fluid on the wave structure, and the implications of allowing the two layers to flow at distinct velocities. Considerations will also be made about the range of flow conditions possibly leading to the emergence of instabilities at the interface between the layers.

The chapter is organised as follows: Section 2 will have a closer view at the experimental flow mosaics introduced in Chapter 2. Comparison in the near field with actual two-fluids dam-break experiments found in the literature will allow to build up and motivate a two-fluid analogy of dam-break waves over granular beds. In Section 3, the two-layer shallow-flow equations are derived and their properties are examined, notably the eigenstructure of the system and its hyperbolic character. A numerical model is then built and validated in Section 4 by scrutinizing its behaviour in a series of limiting cases for which exact analytical solutions are either available in the literature or developed here. In Section 5, the simulations are compared to actual dam-break experiments performed over granular beds of three different densities, with the secret hope that the comparisons will be rich in information and insights, but poor enough to motivate the need for the more elaborate model presented in Chapter 4, that accounts for erosion and deposition and for the related phase change of granular material from a solid- to a fluid-like behaviour.

2. Imaging observations

2.1. Overall view

Figure 3.1 reproduces a typical sequence of mosaic images of dam-break experiments over a granular bed of PVC pellets. For a reason that will be apparent more clearly later on, the selected case has a bed profile presenting an initial discontinuity at the gate such that the upstream level is lower than its downstream counterpart. The observation of Fig. 3.1 allows to recall the general behaviour of the wave. After the rapid release of the gate, the upstream reservoir collapses and a wave is initiated in the downstream direction. The wave rapidly induces strong erosion by incorporating material from the underlying bed. Bulking of bed material into the flow is so intense that the moving sediments occupy a substantial portion of the flow depth, forming a dense liquid/granular mixture. In the vicinity of the downstream edge of the wave, the thickness of this mixture further grows to fill the whole depth, so that the flow in this region is fully saturated with moving grains. The corresponding wavefront gradually evolves into a well-defined snout. As it progresses downstream, this snout continues to be erosive, picking up sediments from the bed and incorporating them into the flow.

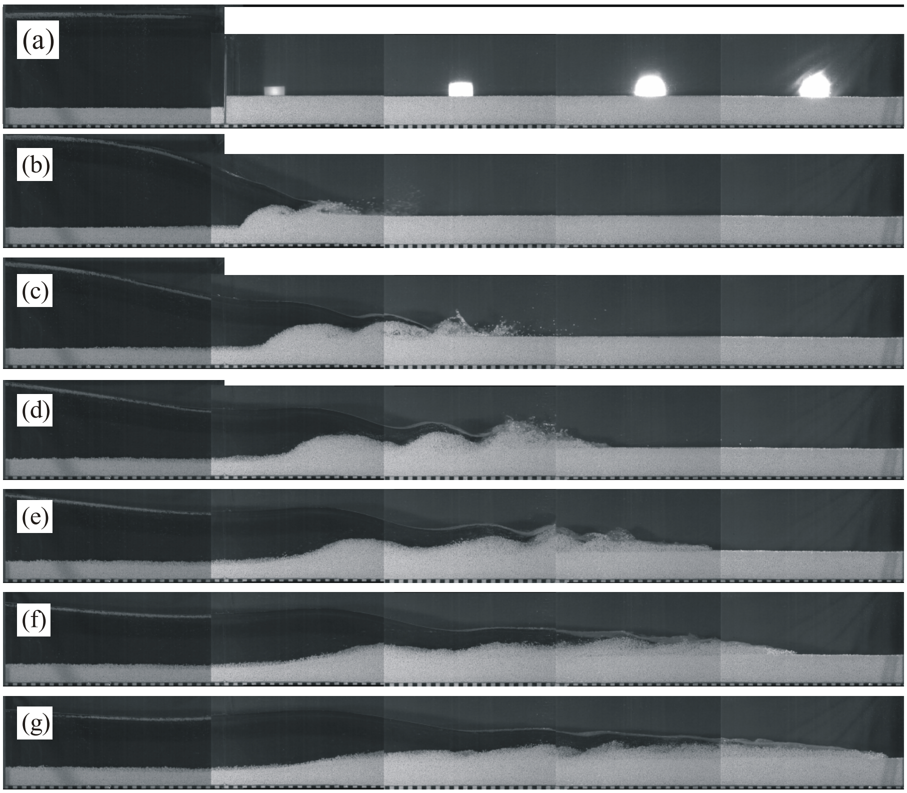

Figure 3.1. Sequence of mosaic images for the PVC test with an upward bed step, at instants $t = 0$, 0.25, 0.5, 0.75, 1, 1.25 and 1.5 s, respectively.

2.2. Plunging breakers in the short-time near field

For dam-break waves over a rigid dry bed, the free surface profile is well-known and decreases monotonously from upstream to downstream. For the dam-break wave over granular bed depicted in Fig. 3.1, a very different behaviour is recorded. Rather than decreasing monotonously, the free surface exhibits strong undulations. Such undulations are observed as well for the boundary between water and the moving grains, and evolve in phase with the free surface. For the same experiment as in Fig. 3.1, Fig. 3.2 shows space-time plots of the free-surface and sediment interfaces. Profiles every 0.1 s are staggered along the vertical at fixed intervals. The undulations are clearly seen to migrate downstream, and do first grow in amplitude before vanishing progressively at later instants. These in-phase patterns are reminiscent of the antidune bedforms of alluvial flows. Their development starts right after the wave release, in the region located immediately downstream of the gate.

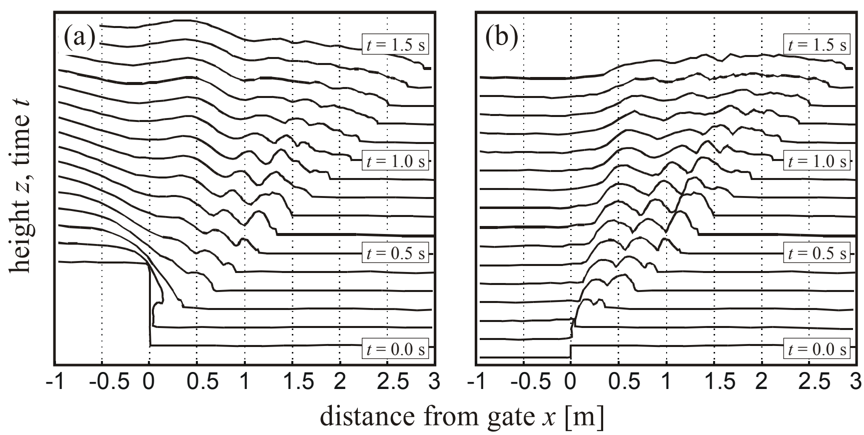

Figure 3.2. *x-z-t* staggered flow profiles for the experiment of Fig. 3.1 (PVC with an upward bed step), obtained by piling up *x-z* profiles at 0.1 s time intervals. (a) free surface elevation; (b) top of the sheet-flow layer.

Figure 3.3 provides a zoom on this region for the first few instants. The initial collapse of the water column is initiated in the upper part, where a protuberant region first appears (see Fig. 3.3b). As it further evolves towards breaking, the water body adopts a curved profile. At the same time, a second protuberance develops from the lowermost part. The latter contains sediments that are lifted up from the granular bed. Both waves reach the downstream bed at similar times (Fig. 3.3e), but the first wave originating from the upper part reaches the bed at a more downstream location. Air from the initial ambient is entrapped below the breaking waves. Collision against the bed heavily attacks the grains, and a substantial chunk of the bed is incorporated in the flow, while some grains are ejected in the air as ballistic projectiles. Rebounding of the wave then occurs, and a second breaker is initiated (Fig. 3.3f). These observations are strongly reminiscent of plunging breakers observed as a mechanism of wave breaking on steep coasts.

Plunging breakers of a strikingly similar kind have recently been observed in pure liquid dambreak wave experiments by Stansby *et al.* (1998) and Janosi *et al.* (2004), although the mechanism of gate removal was notably different. The experiments of Janosi *et al.* are especially useful as a guide for the present purposes because they were conducted with a combination of clear and coloured liquids, which illustrate the internal deformation of the flow.

For purposes of comparison, the profiles from the Janosi *et al.* experiments are plotted in Fig. 3.4 against the corresponding profiles of the PVC experiments introduced in Section 2.1. The Janosi *et al.* profiles have been digitised from the original images. Their experiments involved the release of a 15 cm upstream layer of pure water over a 1.5 cm downstream layer of coloured water with the same properties. The corresponding reference depth,

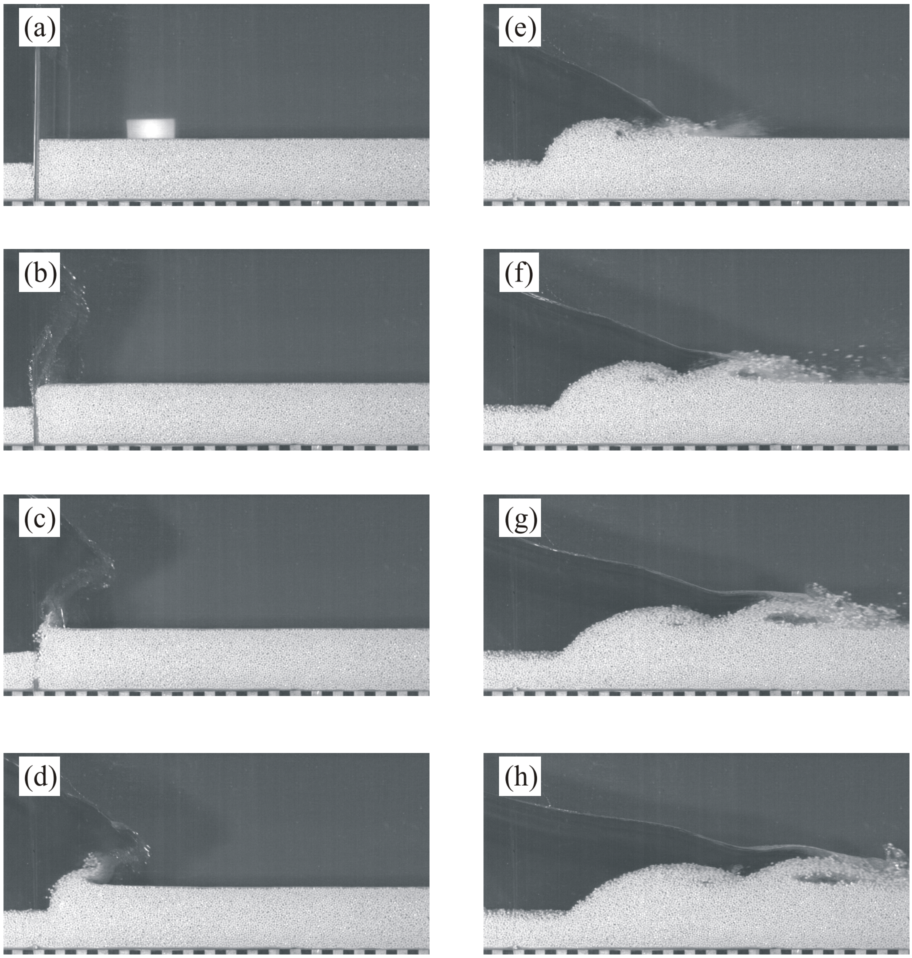

Figure 3.3. Details in the vicinity of the gate, highlighting the plunging breakers observed in the first instants. Time for panels (a)-(h) spans from $t = 0$ s to $t = 0.35$ s in steps of 0.05 s.

as defined in Chapter 2, is H_{Janosi} = 15 - 1.5 = 13.5 cm. Flow snapshots were provided by the authors at times $t =$ 0.131, 0.196, 0.261, 0.327, 0.392, 0.457 and 0.522 s, corresponding to dimensionless times $t\sqrt{g/H}$ = 1.12, 1.67, 2.22, 2.79, 3.34, 3.90 and 4.45. All but the first profile were digitised and stretched to the scale of the PVC experiments according to Froude similarity, using $z_{Janosi,stretched} = z_{Janosi}\, H_{PVC} / H_{Janosi}$ for the vertical scaling and $x_{Janosi,stretched} = x_{Janosi} \cdot (t_{PVC}\sqrt{g\, H_{PVC}}) / (t_{Janosi}\sqrt{g\, H_{Janosi}})$ for the horizontal scaling, with $H_{PVC} = 35\,\mathrm{cm}$. Profiles for the PVC experiments were prepared at the same dimensionless instants. The configuration chosen for the comparison is the same as previously depicted in Figs. 3.1, 3.2 and 3.3, namely with an initial upward bed step of 5 cm at the gate (see Fig. 2.8b), providing a rough analogue to the initially vertical internal interface of the Janosi *et al.* experiments.

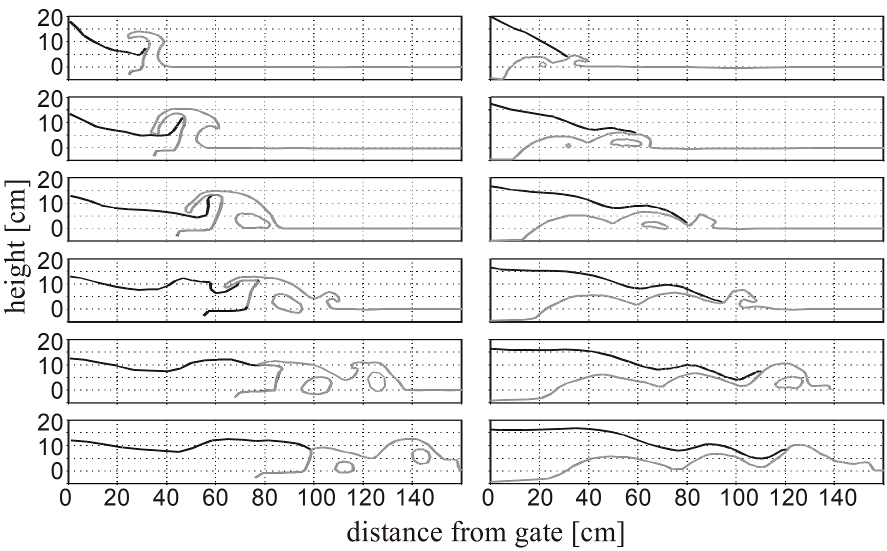

Figure 3.4. Comparison of the coloured-liquid dam-break experiments of Janosi *et al.* (2004) on the left, and the granular dam-break experiments of Fig. 3.1 on the right. The profiles digitised from the images of Janosi *et al.*, whose experiments were performed at a different scale, have been stretched to the scale of the PVC experiments according to Froude similarity. From top to bottom, profiles correspond to dimensionless instants $t\sqrt{g/H}$ = 1.67, 2.22, 2.79, 3.34, 3.90, and 4.45.

Surprising similarities between the two sets of profiles are observed. Multiple plunging breakers are seen to develop and rebound in a comparable way, with similar wavelengths and free surface undulations. Pockets of ambient air entrapped during wave breaking are visible on both configurations. The propagating bore at the wavefront is fully composed of material incorporated from the initial downstream reach. In the far-field, wavefront celerities are amazingly similar.

Significant differences may also be noticed. The most evident is the internal deformation of the “coloured” interface. For the pure liquid experiments of Janosi *el al.* the interface remains sharp and the whole coloured reach is pushed downstream, almost uniformly over the entire flow depth. During the granular PVC experiments, in contrast, the internal interface is stretched over a longer distance, producing a gradual transition between the pure water region and the flow region fully saturated with moving grains. This distinct behaviour will later be related to the increased density of the granular bed, and to the associated difference in longitudinal velocity in the two flow layers.

The above similarities lead to the analogy that is the core of the present chapter, and that will be tested further in sections 4 and 5: for dam-break waves over movable beds, the solid-like granular substrate will be considered as a fluid-like equivalent extending over an effective fluidised layer. This granular fluid will have the same density as the saturated granular assembly. The wave development of this two-fluids system will be looked at without considering erosion or deposition.

3. Shallow two-layer flow model

3.1. Governing equations

3.1.1. Phenomenological description and vertical flow structure

The idealized two-layer flow structure depicted in Fig. 3.5 is adopted. The upper layer of depth h_1 is composed of a light fluid of density ρ_1. The lower layer of depth h_2 is the heavy fluid with density $\rho_2 > \rho_1$. In the case of granular dam-break waves, the upper layer would be pure water, and the lower layer a homogeneous fluid-like granular analogue, which would be assigned a constant density ρ_s equal to the saturated bulk density of the granular bed. The lower rigid boundary of the flow Γ_r , at level z_r, is assumed horizontal and frictionless. Both layers are allowed to flow at distinct depth-averaged velocities u_1 and u_2, respectively. The two layers are immiscible.

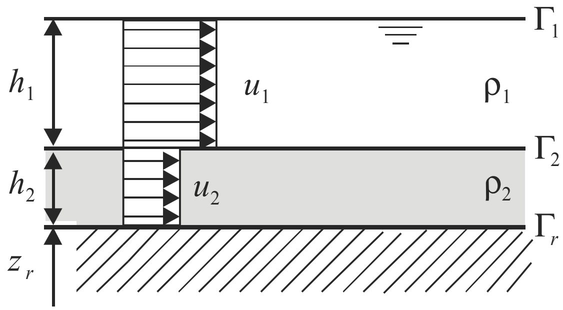

Figure 3.5. Definition sketch of a two-layer shallow-water flow over a fixed horizontal bottom

The classical shallow-water framework is adopted for each layer, assuming that vertical dimensions are small compared to the horizontal length scale, that slopes of the free surface Γ_1 and internal interface Γ_2 are small, and that pressure distribution is hydrostatic. Frictional resistance is neglected, both at the rigid interface Γ_r and at the internal interface Γ_2.

3.1.2. Least action derivation of governing equations

The resulting set of two-layer shallow-water equations are relatively classical, and have been properly derived e.g. by Abbott (1979), by expressing conservation of mass and longitudinal momentum on control volumes built around the two layers. Here an alternative original derivation is presented, showing that the equations of motion may be conveniently derived in a simple manner without considering control volumes. Hamilton's principle of least action is applied (Capart, 2004), stating that any mechanical system evolves in such a way as to minimize the Lagrangian of the system, defined as the difference between its kinetic energy and potential energy.

Let $q_k(t), k = 1,...,N$ be coordinates representing the *N* degrees of freedom of the mechanical system. Hamilton's principle holds that the system evolves so that

$$\partial S = \partial \int_{t_1}^{t_2} L(q_k(t), \dot{q}_k(t), t)\, dt = 0 \qquad (3.1)$$

where $L = T - U = (\text{kinetic energy}) - (\text{potential energy})$ is the *Lagrangian* of the system. In the present context the system has four degrees of freedom $h_1(x,t), h_2(x,t), u_1(x,t), u_2(x,t)$. The flow kinetic and potential energy densities per unit length are obtained as

$$T=\int_0^{h_2+h_1}\tfrac{1}{2}m(z)u^2(z)\,dz=\tfrac{1}{2}\rho_1 h_1 u_1^2+\tfrac{1}{2}\rho_2 h_2 u_2^2\ , \tag{3.2}$$

$$\begin{aligned}U&=\int_0^{h_2+h_1}m(z)g\,z\,dz=\left[\tfrac{1}{2}\rho_2 g\,z^2\right]_0^{h_2}+\left[\tfrac{1}{2}\rho_1 g\,z^2\right]_{h_2}^{h_2+h_1}\\&=\tfrac{1}{2}\rho_2 g\,h_2^2+\tfrac{1}{2}\rho_1 g\,h_1^2+\rho_1 g\,h_1 h_2\end{aligned} \tag{3.3}$$

The Lagrangian of the system is

$$\mathbf{L}=\mathbf{T}-\mathbf{U}+\lambda_1\left(\frac{\partial h_1}{\partial t}+\frac{\partial}{\partial x}(h_1u_1)\right)+\lambda_2\left(\frac{\partial h_2}{\partial t}+\frac{\partial}{\partial x}(h_2u_2)\right) \tag{3.4}$$

where λ_1 and λ_2 are Lagrange multipliers introduced to deal with the continuity constraints of both layers

$$\frac{\partial h_1}{\partial t}+\frac{\partial}{\partial x}(h_1u_1)=0 \quad \text{and} \quad \frac{\partial h_2}{\partial t}+\frac{\partial}{\partial x}(h_2u_2)=0\ . \tag{3.5a,b}$$

The “action” in the sense of Hamilton is

$$S=\int_{t_1}^{t_2}\int_{x_1}^{x_2}L\left(h_1,u_1,\lambda_1,h_2,u_2,\lambda_2,\frac{\partial h_1}{\partial t},\frac{\partial h_2}{\partial t},\frac{\partial h_1}{\partial x},\frac{\partial h_2}{\partial x},\frac{\partial u_1}{\partial t},\frac{\partial u_2}{\partial t},\frac{\partial u_1}{\partial x},\frac{\partial u_2}{\partial x}\right)dx\,dt$$

The principle of least action imposes (3.6)

1) $$\frac{\partial \mathbf{S}}{\partial h_1}=0 \;\Rightarrow\; \frac{\partial \mathbf{L}}{\partial h_1}-\frac{\partial}{\partial t}\left(\frac{\partial \mathbf{L}}{\partial\left(\frac{\partial h_1}{\partial t}\right)}\right)-\frac{\partial}{\partial x}\left(\frac{\partial \mathbf{L}}{\partial\left(\frac{\partial h_1}{\partial x}\right)}\right)=0 \tag{3.7}$$

Evaluating
$$\left\{\begin{aligned}&\frac{\partial \mathbf{L}}{\partial h_1}=\tfrac{1}{2}\rho_1 u_1^2-\rho_1 g(h_1+h_2)+\lambda_1\frac{\partial u_1}{\partial x}\\&\frac{\partial \mathbf{L}}{\partial\left(\frac{\partial h_1}{\partial t}\right)}=\lambda_1\\&\frac{\partial \mathbf{L}}{\partial\left(\frac{\partial h_1}{\partial x}\right)}=\lambda_1 u_1\end{aligned}\right. \tag{3.8}$$

one obtains $\frac{1}{2}\rho_1 u_1^2 - \rho_1 g(h_1 + h_2) - \frac{\partial \lambda_1}{\partial t} - u_1 \frac{\partial \lambda_1}{\partial x} = 0$ (3.9)

$$2)\ \frac{\partial \mathbf{S}}{\partial h_2} = 0 \quad \Rightarrow \quad \frac{\partial \mathbf{L}}{\partial h_2} - \frac{\partial}{\partial t}\left(\frac{\partial \mathbf{L}}{\partial\left(\frac{\partial h_2}{\partial t}\right)}\right) - \frac{\partial}{\partial x}\left(\frac{\partial \mathbf{L}}{\partial\left(\frac{\partial h_2}{\partial x}\right)}\right) = 0\,. \tag{3.10}$$

In a similar way,

$$\frac{1}{2}\rho_2 u_2^2 - \rho_2 g\left(h_2 + \frac{\rho_1}{\rho_2} h_1\right) - \frac{\partial \lambda_2}{\partial t} - u_2 \frac{\partial \lambda_2}{\partial x} = 0 \tag{3.11}$$

$$3)\ \frac{\partial \mathbf{S}}{\partial u_1} = 0 \quad \Rightarrow \quad \frac{\partial \mathbf{L}}{\partial u_1} - \frac{\partial}{\partial t}\left(\frac{\partial \mathbf{L}}{\partial\left(\frac{\partial u_1}{\partial t}\right)}\right) - \frac{\partial}{\partial x}\left(\frac{\partial \mathbf{L}}{\partial\left(\frac{\partial u_1}{\partial x}\right)}\right) = 0\,,$$

leading to $\frac{\partial \lambda_1}{\partial x} = \rho_1 u_1$ (3.12)

$$4)\ \frac{\partial \mathbf{S}}{\partial u_2} = 0 \quad \Rightarrow \quad \frac{\partial \mathbf{L}}{\partial u_2} - \frac{\partial}{\partial t}\left(\frac{\partial \mathbf{L}}{\partial\left(\frac{\partial u_2}{\partial t}\right)}\right) - \frac{\partial}{\partial x}\left(\frac{\partial \mathbf{L}}{\partial\left(\frac{\partial u_2}{\partial x}\right)}\right) = 0\,,$$

leading to $\frac{\partial \lambda_2}{\partial x} = \rho_2 u_2$ (3.13)

Substitution of (3.12) in (3.9) yields

$$\frac{\partial \lambda_1}{\partial t} + \rho_1 g(h_1 + h_2) + \frac{1}{2}\rho_1 u_1^2 = 0 \tag{3.14}$$

Substitution of (3.13) in (3.11) yields

$$\frac{\partial \lambda_2}{\partial t} + \rho_2 g\left(h_2 + \frac{\rho_1}{\rho_2} h_1\right) + \frac{1}{2}\rho_2 u_2^2 = 0 \tag{3.15}$$

Derivation with respect to *x* yields the equations of motion

$$\frac{\partial u_1}{\partial t}+\frac{\partial}{\partial x}\left(\tfrac{1}{2}u_1^2+g\left(h_1+h_2\right)\right)=0 \tag{3.16}$$

$$\frac{\partial u_2}{\partial t}+\frac{\partial}{\partial x}\left(\tfrac{1}{2}u_2^2+g\left(h_2+\tfrac{\rho_1}{\rho_2}h_1\right)\right)=0 \tag{3.17}$$

Those are weak formulations of the conservation laws of the two-layer shallow-water system introduced above. They remain valid in continuous flow regions, but do not lead to physical constraints of conservation across discontinuities. In order to deal with discontinuities, the governing equations should be written in terms of the conserved variables $h_1 u_1$ and $h_2 u_2$. Therefore, it suffices to combine the continuity equations with the above equations of motion.

$$\frac{\partial h_1}{\partial t}+\frac{\partial (h_1 u_1)}{\partial x}=0\,, \tag{3.18}$$

$$\frac{\partial h_2}{\partial t}+\frac{\partial (h_2 u_2)}{\partial x}=0\,, \tag{3.19}$$

Multiplying.(3.18) by u_1 and.(3.16) by h_1, and adding the two, one obtains

$$\frac{\partial \left(h_1 u_1\right)}{\partial t}+\frac{\partial}{\partial x}\left(h_1 u_1^2+\frac{g h_1^2}{2}\right)+g h_1\frac{\partial h_2}{\partial x}=0 \tag{3.20}$$

Similarly, $$\frac{\partial \left(h_2 u_2\right)}{\partial t}+\frac{\partial}{\partial x}\left(h_2 u_2^2+\frac{g h_2^2}{2}\right)+g h_2\frac{\rho_1}{\rho_2}\frac{\partial h_1}{\partial x}=0 \tag{3.21}$$

3.2. Eigenstructure and hyperbolicity

The above equations express conservation of mass and balance of longitudinal momentum, under the assumptions that the pressure is hydrostatic, and that the density and horizontal velocity are vertically uniform in each layer. The equations for each layer are very similar in form to the Saint-Venant equations governing the flow of a single shallow layer, but feature additional terms due to the pressure exerted by each layer on the other. These are the third terms on the left hand sides of equations (3.20)-(3.21), and can be seen to be non-conservative in nature (i.e. they cannot be fully transferred inside the partial differential operator $\partial / \partial x$).

It is useful to cast equations (3.18)-(3.21) in a vector form. This is obtained by rewriting the spatial derivatives in terms of the conserved variables, using

$$\frac{\partial}{\partial x}\left(h_i u_i^2 + \frac{g h_i^2}{2}\right) = \frac{\partial}{\partial x}\left(\frac{(h_i u_i)^2}{h_i} + \frac{g h_i^2}{2}\right) = 2u_i \frac{\partial(h_i u_i)}{\partial x} + \left(-u_i^2 + g h_i\right)\frac{\partial h_i}{\partial x} \qquad (3.22)$$

The vector formulation is

$$\frac{\partial \mathbf{U}}{\partial t} + \mathbf{A}(\mathbf{U})\frac{\partial \mathbf{U}}{\partial x} = 0 \qquad (3.23)$$

where vector $\mathbf{U}$ and coefficient matrix $\mathbf{A}$ are given by

$$\mathbf{U} = \begin{bmatrix} h_1 \\ h_2 \\ h_1 u_1 \\ h_2 u_2 \end{bmatrix}, \quad \mathbf{A}(\mathbf{U}) = \begin{bmatrix} 0 & 0 & 1 & 0 \\ 0 & 0 & 0 & 1 \\ -u_1^2 + g h_1 & g h_1 & 2u_1 & 0 \\ g h_2 \dfrac{\rho_1}{\rho_2} & -u_2^2 + g h_2 & 0 & 2u_2 \end{bmatrix}. \qquad (3.24)$$

This constitutes a homogeneous system of first order quasi-linear equations, the behaviour of which is well-known to be controlled by the eigenstructure of matrix **A**. The eigenvalues are the roots of equation

$$\det\left(\mathbf{A}-\lambda\mathbf{I}\right)=0\,. \tag{3.25}$$

Developing the determinant yields the characteristic polynomial (Abbott, 1979)

$$\{(\lambda-u_1)^2-gh_1\}\{(\lambda-u_2)^2-gh_2\}-\frac{\rho_1}{\rho_2}g^2h_1h_2=0\,. \tag{3.26}$$

Exact expressions of the four roots of this quartic polynomial may be obtained analytically, but the derivation is relatively arduous, and the eigenvalues may not be related through simple expressions to the primary variables **U**, so their interpretation must be performed with care. A step-by-step procedure is described in Lawrence (1990), and a short derivation is given in Appendix III. Nevertheless, two special cases are of interest. When $u_1=u_2=u$, (3.26) takes the form of a bi-quadratic, and simple analytical expressions of the four roots can be found in two steps by invoking a change of variables of the type $(\lambda-u_1)^2=\alpha$. The four eigenvalues are real and given by

$$\lambda_{\text{ext}}^{\pm}=u\pm\sqrt{g(h_1+h_2)}\sqrt{\frac{1+\sqrt{1-4(1-\rho_2/\rho_1)h_1h_2/(h_1+h_2)^2}}{2}}\,, \tag{3.27}$$

$$\lambda_{\text{int}}^{\pm}=u\pm\sqrt{g(h_1+h_2)}\sqrt{\frac{1-\sqrt{1-4(1-\rho_2/\rho_1)h_1h_2/(h_1+h_2)^2}}{2}}\,. \tag{3.28}$$

The exterior eigenvalues are the celerities of the so-called barotropic wave modes, representing fast outward propagation (with respect to an observer moving with the current) of small perturbations along the upper surfaces of each layer. The interior eigenvalues, on the other hand, are the celerities of the so-called baroclinic modes, representing slow outward propagation of perturbations at the interface between the two layers (Cushman-Roisin, 1994).

Another special case arises when the densities of the two layers are the same, i.e. $\rho_1 = \rho_2$, and the velocity difference $u_1 - u_2$ is assumed to be small. In that case, first-order approximations of the four eigenvalues are given by (Audusse, 2005)

$$\lambda_{\mathrm{ext}}^{\pm} \approx \frac{h_1 u_1 + h_2 u_2}{h_1 + h_2} \pm \sqrt{g(h_1 + h_2)}\,, \tag{3.29}$$

$$\lambda_{\mathrm{int}}^{\pm} \approx \frac{h_1 u_1 + h_2 u_2}{h_1 + h_2} \pm i\,\frac{u_1 - u_2}{2}\sqrt{1 - \left(\frac{h_1 - h_2}{h_1 + h_2}\right)^2}\,. \tag{3.30}$$

The external eigenvalues remain real, but any velocity difference between the two layers leads to non-vanishing imaginary components for the internal eigenvalues. The generation of such imaginary celerities is not restricted to the homogeneous case $\rho_1 = \rho_2$, but may occur as well for layers of different densities. For the general case involving both a density contrast and a velocity difference, one can evaluate the discriminant

$$\prod_{\substack{i,j=1 \\ i<j}}^{4} (\lambda_i - \lambda_j)^2 = D \tag{3.31}$$

which changes sign when roots $\lambda_{\text{int}}^{\pm}$ switch from being purely real to being partly imaginary. An algebraic expression for the discriminant may again be found in Appendix III. Invoking Galilean invariance and dimensional analysis, the discriminant D is a function of only three dimensionless products

$$D = D\left(\frac{u_1 - u_2}{\sqrt{g(h_1 + h_2)}}, \frac{h_1}{h_1 + h_2}, \frac{\rho_1}{\rho_2}\right). \tag{3.32}$$

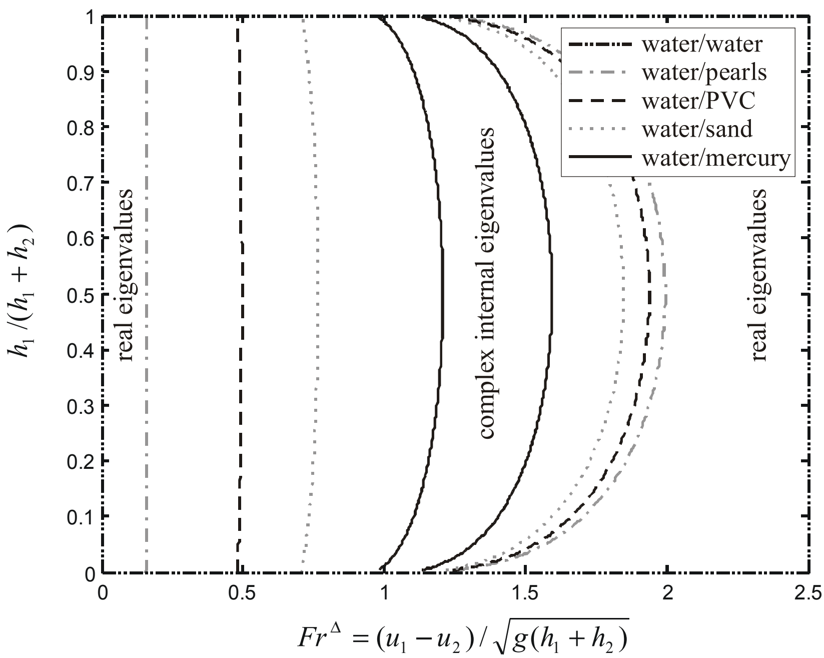

Figure 3.6. Domains of partly imaginary eigenvalues for different density ratios $\rho_1/\rho_2 = 1$ (dash-dot-dot), 0.98 (dash-dotted), 0.8 (dashed), 0.55 (dotted) and 0.07 (solid), corresponding approximately to the three granular materials exploited hereafter (pearls, PVC and sand, at a granular packing of 0.5) and to mercury. Internal eigenvalues are complex inside the band defined by the left and right curves, and real outside of it.

As shown on Fig. 3.6, the locus $D = 0$ can thus be plotted as a series of curves, traced in a plane spanned by the first two products, $(u_1 - u_2)/\sqrt{g(h_1 + h_2)}$ and $h_1/(h_1 + h_2)$, and parameterised by the density contrast ρ_1/ρ_2. Each of the resulting curves represents, for a given density ratio ρ_1/ρ_2, the boundary of the domain inside which eigenvalues $\lambda_{\mathrm{int}}^{\pm}$ are partly imaginary. When the density ratio moves away from unity, imaginary components are found to be restricted to a band of finite width. The band is located away from $u_1 - u_2 = 0$, implying that when the two layers have different densities, the velocity difference must reach a finite value before imaginary components are generated. The imaginary band is further found to shrink as the density ratio decreases, becoming crescent-shaped for low density ratios $\rho_1/\rho_2 << 1$. The crescents found in this limit are located in the neighbourhood of $Fr^{\Delta} = (u_1 - u_2)/\sqrt{g(h_1 + h_2)} \approx 1$. Except for very low density ratios, this latter value lies always inside the imaginary band, and thus constitutes a kind of critical Froude number for the velocity difference. Nevertheless this Froude number does not suffice to characterize the flow state, and in order to determine the precise left and right bounds of the imaginary band the depth ratio $h_1/(h_1 + h_2)$ must also be known. The value of this Froude number at the left bound of the imaginary band is referred to as the stability Froude number of two-layer flows, and the left contours of Fig. 3.6 indeed correspond to the critical stability curves presented in Lawrence (1990). However, Fig. 3.6 reveals another region of flow state inside which the eigenvalues of the two-layer system are real, corresponding to larger velocity differences, beyond the right bound of the imaginary band. This constitutes a significant result that will be corroborated in Section 5 for dam-break experiments.

An important consequence of the above discussion is that the quasi-linear system (3.23) is not guaranteed to be hyperbolic. Loss of hyperbolicity will be encountered whenever the velocity difference places the flow state inside the imaginary bands outlined in Fig. 3.6. Many properties taken for granted in the case of hyperbolic equations (e.g. the existence of wavelike solutions) may thus be lost, an observation which does not seem to have been much appreciated by previous authors using the two-layer shallow flow equations.

3.3. Numerical scheme

Due to the above complications, analytical solutions for non-trivial problems involving two layer flows seem largely out of reach. The present work will therefore resort to numerical computations. A difficulty in this regard is that numerical solvers developed to solve quasi-linear equations of the form (3.23) have until now been built on the assumption that the equations are strictly hyperbolic. It is unclear whether or not, or to what extent they are applicable to problems in which partial loss of hyperbolicity may be encountered. Here the ambition is not to resolve this open question. Instead, a finite volume solver is selected and used to construct solutions on the optimistic assumption that the possible loss of hyperbolicity will not invalidate the results.

The specific solver chosen is based on the HLL scheme of Harten, Lax and Van Leer (1983), a scheme which is attractive because it does not require the full system eigenstructure to be explicitly known. Instead, only outer (real) bounds for the eigenvalues must be specified. In the present case, computations will be performed based on outer bounds for the exterior eigenvalues (both of which are always real)

$$\lambda_{\min} \le \lambda_{\text{ext}}^{\pm} \le \lambda_{\max} , \tag{3.33}$$

where the lower and upper bounds are given by

$$\lambda_{\min} = \min\left(\min\,(u_1, u_2) - \sqrt{g(h_1 + h_2)}\,, 0\right), \tag{3.34}$$

and
$$\lambda_{\max} = \max\left(\max\,(u_1, u_2) + \sqrt{g(h_1 + h_2)}\,, 0\right). \tag{3.35}$$

Figure 3.7 illustrates the adopted finite volume discretisation. The primitive variables are discretised within numerical cells $x_{i-1/2} < x < x_{i+1/2}$ of constant length Δx, and at each time step numerical fluxes $\mathbf{F}$ of mass, $q_\alpha = h_\alpha u_\alpha$, and momentum, $\sigma_\alpha = h_\alpha u_\alpha^2 + ½\, g\, h_\alpha^2$, are evaluated at the interfaces $x_{i+1/2}$ separating neighbouring cells. Integrating across a time step Δt, the primitive variables are updated according to the balance of incoming and outgoing fluxes across the finite volumes.

The layer continuity equations (3.18) and (3.19) are easily dealt with. They are written in full conservation form, and may be straightforwardly incorporated in the original HLL scheme:

$$h_{\alpha,i}^{t+\Delta t} = h_{\alpha,i}^{t} + \frac{\Delta t}{\Delta x}\left(q_{\alpha,i-½} - q_{\alpha,i+½}\right), \tag{3.36}$$

where $\alpha = 1,2$ stand for the considered layer, and the mass fluxes $q_\alpha = h_\alpha u_\alpha$ at the interfaces are evaluated with the HLL statement:

$$q_{\alpha,i+½} = \frac{\lambda_{\max}}{\lambda_{\min} - \lambda_{\max}}\, q_{\alpha,i}^{t} - \frac{\lambda_{\min}}{\lambda_{\min} - \lambda_{\max}}\, q_{\alpha,i+1}^{t} + \frac{\lambda_{\min}\lambda_{\max}}{\lambda_{\min} - \lambda_{\max}}\left(h_{\alpha,i+1}^{t} - h_{\alpha,i}^{t}\right). \tag{3.37}$$

Here, the celerities $\lambda_{\min}$ (resp. $\lambda_{\max}$) are taken as the minimum (resp. maximum) of expressions (3.34) (resp. (3.35)) evaluated at x_i and x_{i+1}.

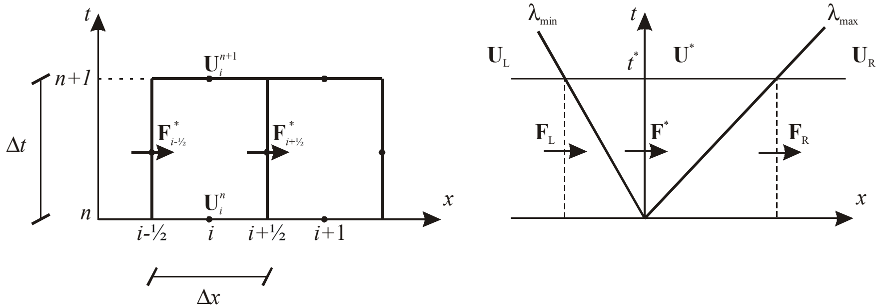

Figure 3.7. Finite volume discretisation and approximate Riemann solver.

The momentum equations (3.20) and (3.21) are treated similarly for their conservative part, but a special treatment is required to deal with the non-conservative product related to the pressure interaction between the two layers. Therefore, the scheme relies on the lateralised treatment proposed by Fraccarollo *et al.* (2003). Their LHLL scheme was originally developed to account robustly for the non conservative terms associated with bottom slope, but extends straightforwardly to the present case. It accounts for non-conservative products as lateralised corrections to the standard HLL fluxes. Centred momentum fluxes $\sigma_\alpha = h_\alpha u_\alpha^2 + \frac{1}{2} g h_\alpha^2$ are first evaluated at each interface using the standard HLL statement:

$$\sigma_{\alpha,i+\frac{1}{2}} = \frac{\lambda_{\max}}{\lambda_{\min} - \lambda_{\max}} \sigma_{\alpha,i}^t - \frac{\lambda_{\min}}{\lambda_{\min} - \lambda_{\max}} \sigma_{\alpha,i+1}^t + \frac{\lambda_{\min}\lambda_{\max}}{\lambda_{\min} - \lambda_{\max}} \left(q_{\alpha,i+1}^t - q_{\alpha,i}^t \right) \tag{3.38}$$

Left and right lateralised corrections are then introduced on both sides of the interface. For the upper layer, they write:

$$\sigma_{1,i+\frac{1}{2}}^L = \sigma_{1,i+\frac{1}{2}} - \frac{\lambda_{\min}}{\lambda_{\min} - \lambda_{\max}} \frac{g\,(h_{1,i}^t + h_{1,i+1}^t)}{2} \left(h_{2,i+1}^t - h_{2,i}^t \right). \tag{3.39}$$

$$\sigma_{1,i+\frac{1}{2}}^R = \sigma_{1,i+\frac{1}{2}} - \frac{\lambda_{\max}}{\lambda_{\min} - \lambda_{\max}} \frac{g\,(h_{1,i}^t + h_{1,i+1}^t)}{2} \left(h_{2,i+1}^t - h_{2,i}^t \right). \tag{3.40}$$

For the lower layer, they write:

$$\sigma^L_{2,i+½} = \sigma_{2,i+½} - \frac{\lambda_{\min}}{\lambda_{\min} - \lambda_{\max}} \frac{g\,(h^t_{2,i} + h^t_{2,i+1})}{2} \frac{\rho_1}{\rho_2} \left(h^t_{1,i+1} - h^t_{1,i}\right). \tag{3.41}$$

$$\sigma^R_{2,i+½} = \sigma_{2,i+½} - \frac{\lambda_{\max}}{\lambda_{\min} - \lambda_{\max}} \frac{g\,(h^t_{2,i} + h^t_{2,i+1})}{2} \frac{\rho_1}{\rho_2} \left(h^t_{1,i+1} - h^t_{1,i}\right). \tag{3.42}$$

The difference between the two lateralised estimates, interrelated through $\rho_1\left(\sigma^R_{1,i+1/2} - \sigma^L_{1,i+1/2}\right) = \rho_2\left(\sigma^R_{2,i+1/2} - \sigma^L_{2,i+1/2}\right)$, represent the exchange of momentum between the two layers as a result of pressure interaction.

The updated layer momentum is then obtained as:

$$q^{t+\Delta t}_{\alpha,i} = q^t_{\alpha,i} + \frac{\Delta t}{\Delta x}\left(\sigma^R_{\alpha,i-½} - \sigma^L_{\alpha,i+½}\right). \tag{3.43}$$

A Courant-Friedrichs-Levy condition is enforced to keep the computations stable:

$$Cr = \frac{\max(|\lambda_{\min}|,|\lambda_{\max}|)}{\Delta x / \Delta t} \leq 1, \tag{3.44}$$

and a constant Courant number $Cr = 0.5$ is used for all the computations reported hereafter.

Finally, in order to reduce numerical dissipation and obtain numerical solutions that are close to convergence with internal wave structures that appear as clear and sharp as possible, the scheme is extended to second order accuracy in space and time. The methodology is described in Capart and Young (2002). Second-order in space is achieved using the MUSCL approach of Van Leer (1977), i.e. with linear reconstruction of the primitive variables within each cell, and a minmod slope limiter. Left and right interface variables are then obtained as extrapolations of the central variables according to the limited slopes. Second order in time is achieved with a predictor-corrector procedure.

The resulting two-layer shallow water numerical code was originally developed by H. Capart at the National Taiwan University (Capart and Young 2002; Chen *et al.*, submitted), and was kindly made available for the present work. The reader may refer to the above publications for more details regarding the numerical scheme and its background.

Given the uncertainties surrounding the applicability of hyperbolic solvers to partially non-hyperbolic problems, it is clear that the computational results must be subject to close scrutiny. Accordingly, the next section is devoted to a systematic examination of the solution behaviour. The approach adopted will proceed in two steps: 1) first, check that the correct behaviour is retrieved for limiting cases in which hyperbolicity is guaranteed and analytical solutions are available; 2) next, probe the change of behaviour obtained when moving away from these limiting cases towards the more realistic conditions of the actual dam-break experiments.

4. Model validation

4.1. Single density (colour) validation

To validate the scheme, tests are first performed for a dam-break problem involving two layers of identical density $\rho_2 = \rho_1$. To facilitate comparisons, the initial conditions correspond to the experiments by Janosi *et al.* (2004) discussed earlier (see Fig. 3.8):

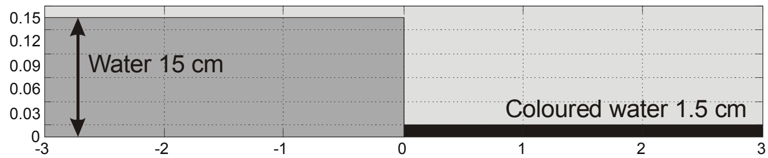

Figure 3.8. Initial conditions corresponding to the dam-break experiments by Janosi *et al.* (2004) with clear and coloured water.

$$x<0: \begin{pmatrix} h_1 \\ h_2 \\ u_1 \\ u_2 \end{pmatrix} = \begin{pmatrix} h_{1L} \\ h_{2L} \\ u_{1L} \\ u_{2L} \end{pmatrix} = \begin{pmatrix} \frac{10}{9}H \\ 0 \\ 0 \\ 0 \end{pmatrix}, \quad x>0: \begin{pmatrix} h_1 \\ h_2 \\ u_1 \\ u_2 \end{pmatrix} = \begin{pmatrix} h_{1R} \\ h_{2R} \\ u_{1R} \\ u_{2R} \end{pmatrix} = \begin{pmatrix} 0 \\ \frac{1}{9}H \\ 0 \\ 0 \end{pmatrix} \tag{3.45}$$

Here depths h_1 and h_2 correspond respectively to the clear water and coloured water regions of the Janosi experiments. The level difference $H = h_{1L} + h_{2L} - (h_{1R} + h_{2R})$ between the left and right sides of the dam is taken as basic scale for the problem.

For identical densities $\rho_2 = \rho_1$, the velocities of the two layers should be the same ($u_2 = u_1 = u$), so that the four degrees of freedom of system (3.23) reduce to three. The ratio $h_2/(h_1 + h_2)$ is passively advected with the flow, as if it was a colour concentration. The total depth $h = h_1 + h_2$ and the single velocity $u_2 = u_1 = u$ remain described by the classical Stoker solution for single layer dam-break. The wave consists of a gradually expanding self-similar profile composed of a smooth rarefaction upstream, a central uniform region of depth h_C and velocity u_C, and a shock propagating downstream at speed v_S (see e.g. Liggett, 1994). In the rarefaction, the profile is governed by

$$u - c = x/t\,, \quad u + 2c = 2c_{\mathrm{L}}\,, \tag{3.46}$$

where $c = \sqrt{g(h_1 + h_2)}$. Across the shock, the following compatibility relations apply:

$$h_C u_C = (h_C - h_R) v_S \,, \quad h_C = \tfrac{1}{2} h_R \{\sqrt{1 + 8 v_S^2 / (g h_R)} - 1\} \,. \qquad (3.47)$$

The colour component does not affect the depth and velocity, but leads to the presence of a new elementary wave inside the central region. This additional wave is a contact discontinuity which moves at speed u_C and splits the flow into upstream and downstream zones having distinct colours. This composite solution is presented in Leveque (2002), and was used earlier by Chen *et al.* (submitted) to validate two-layer shallow flow computations.

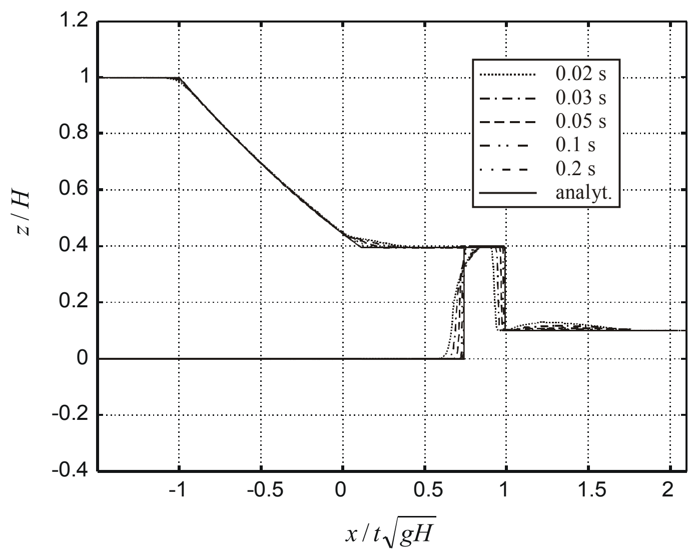

Figure 3.9. Comparison of numerical and analytical results for coloured dam-break, with two layers of identical densities, and the initial conditions of Fig. 3.8.

Figure 3.9 compares computed profiles with the reference analytical solution. Both the computed and analytical profiles are plotted in dimensionless similarity coordinates z/H versus $x/t\sqrt{gH}$. The computed profiles are shown for various values of dimensionless ratio $t\sqrt{gH}/\Delta x$ = 115, 175, 290, 575 and 1150. They indicate convergence of the numerical solutions as $t \to \infty$ for a fixed value of the spatial step Δx, or equivalently as $\Delta x \to 0$ for a fixed value of the comparison time *t*.

Thanks to the second order accuracy of the scheme, rapid convergence is observed, not only for the upstream rarefaction and downstream shock, but also for the internal contact discontinuity. A surprising behaviour of the solutions is seen more downstream. Originating from the upstream upper layer, a spurious liquid mound overrides the developing wavefront and travels on top of the downstream lower layer ahead of the shock. This pinched-off feature forms in the early stages of the computations. It is then smeared out and eventually nearly vanishes for the converged solution at long times. This feature was first observed by Chen *et al.* (submitted), who interpreted it as a computational flaw and found that it could be suppressed by adding a moderate amount of friction between the two layers. Rather than artificially damp it through friction, here this feature is let free to evolve naturally. This is because it constitutes the precursor of an interesting solution behaviour observed further below for the case of different densities $\rho_2 \neq \rho_1$.

In Fig. 3.10, a profile corresponding to $t\sqrt{gH}/\Delta x = 2300$ (very long time *t*, or very small step Δx) is compared to the analytical solution. While the two solutions show good overall agreement, two puzzling features are observed (for clarity, they are magnified by a factor of 5 in the figure insets). Firstly, a residue of the spurious wave identified earlier is seen at the downstream end of the profile. One notices that this spurious perturbation does not vanish completely, but rather survives as a solitary wave propagating at constant speed. This feature will later be linked to the fourth degree of freedom of the two-layer model. The formation of the second puzzling feature, located just downstream of the contact discontinuity, is more difficult to interpret. It turns out to be associated with a local loss of hyperbolicity of the two-layer equations in that region. This is illustrated in Fig. 3.10b, which shows the eigenvalues corresponding to the profiles of Fig. 3.10a. The region in which the puzzling behaviour is observed is seen to exhibit conjugate non-zero imaginary parts associated with the two internal eigenvalues (see the figure inset, magnified by a factor 10). Although the two layer code is applied here to a degenerate case for which the eigenvalues should remain real, loss of hyperbolicity does locally affect the computations. Fortunately, this effect is rather limited, and does not significantly corrupt the calculated profiles. The imaginary component of the celerities is also smaller than their real counterpart by more than one order of magnitude.

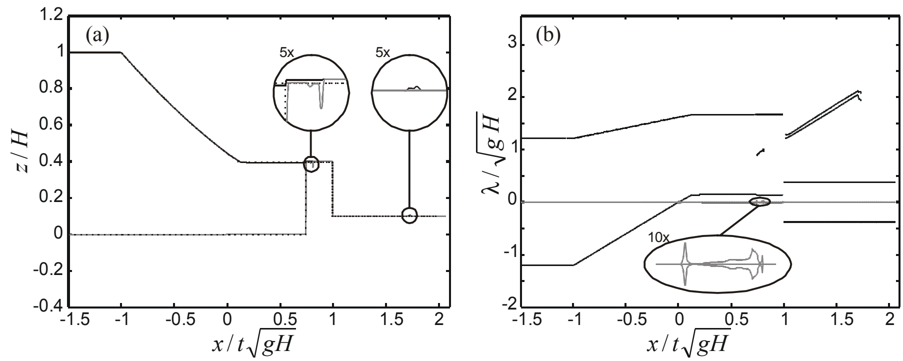

Figure 3.10. Puzzling features observed for the computations of a coloured dam-break close to convergence: a) flow profiles; b) eigenvalues: real part (black) and imaginary part (grey).

4.2. Ritter asymptotes

For a single layer dam-break wave propagating over an initially dry bed, the Stoker solution is well-known to reduce to the Ritter solution. Only the rarefaction wave remains, and it follows from (3.46) that the depth profile becomes

$$h(x,t) = \frac{4H}{9}\left\{1 - \frac{x/t}{2\sqrt{gH}}\right\}^2, \quad -\sqrt{gH} \le \frac{x}{t} \le 2\sqrt{gH}\,. \tag{3.48}$$

Here one considers two-layer dambreak waves for which $\rho_2 \ne \rho_1$ and starting from initial conditions of the form

$$x<0: \begin{pmatrix} h_1 \\ h_2 \\ u_1 \\ u_2 \end{pmatrix} = \begin{pmatrix} h_{1L} \\ h_{2L} \\ u_{1L} \\ u_{2L} \end{pmatrix} = \begin{pmatrix} H \\ \eta \\ 0 \\ 0 \end{pmatrix}, \quad x>0: \begin{pmatrix} h_1 \\ h_2 \\ u_1 \\ u_2 \end{pmatrix} = \begin{pmatrix} h_{1R} \\ h_{2R} \\ u_{1R} \\ u_{2R} \end{pmatrix} = \begin{pmatrix} 0 \\ \eta \\ 0 \\ 0 \end{pmatrix}, \tag{3.49}$$

i.e. the initial depths of the lower liquid layer are the same on both sides of the dam, $h_{2L} = h_{2R} = \eta$, while the upper layer has initial depths $h_{1L} = H$ to the left and $h_{1R} = 0$ to the right. Initial conditions of this type will be used later to simulate the dambreak waves over granular beds observed in the experiments.

Starting from the above initial conditions, two-layer dambreak waves can be expected to converge towards the Ritter solution in two limiting cases. First, for a given depth η of the lower layer, Ritter behaviour is expected for the upper layer when $\rho_1 / \rho_2 \to 0$. As the density ratio approaches zero, the lower layer becomes increasingly heavier than the upper layer, and should eventually remain motionless underneath the propagating wave of lighter liquid. Secondly, for a given density ratio $0 < \rho_1 / \rho_2 < 1$, the upper layer should again behave like the Ritter wave in the limit $\eta / H \to 0$ when the depth of the lower layer vanishes. The aim of the present section is to contrast the behaviour of the two-layer solutions in these limiting cases with their behaviour in more generic conditions.

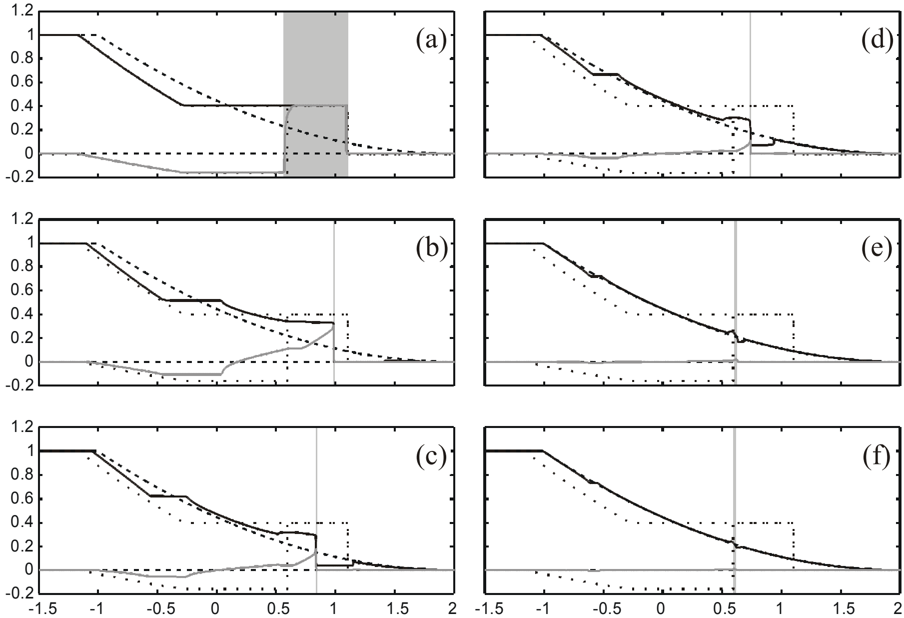

Figure 3.11. Nearly converged numerical results for the dam-break of a light fluid over a heavier fluid of increasing density ρ_2, (a)-(f) for a density ratio $\rho_1/\rho_2 = 1$, 0.5, 0.2, 0.1 0.02 and 0.01 respectively. Analytical results provided in the background for the Stoker solution ($\rho_1/\rho_2 = 1$) in dotted line and for the Ritter solution ($\rho_1/\rho_2 \to 0$) in dashed line. Grey vertical stripes highlight the reaches where complex eigenvalues appear in the numerical simulations. Dimensionless plots: vertical axis: height z / H, horizontal axis: dimensionless position $x / t\sqrt{gH}$.

Results for the case of decreasing density ratios are presented in Fig. 3.11. The profiles are shown in dimensionless form, and correspond to the following conditions: $\eta / H = 0.357$ and $t\sqrt{gH} / \Delta x = 1500$. The density ratios examined are $\rho_1/\rho_2 = 1$, $\frac{1}{2}$, $\frac{1}{5}$, $\frac{1}{10}$, $\frac{1}{50}$ and $\frac{1}{100}$, starting far away from the Ritter asymptote and gradually moving towards this limit. The lowest density ratios are explored here only for the sake of probing the asymptotic behaviour of the two-layer model, since it is clear that such ratios are not encountered for natural liquids nor granular materials. The computed profiles shown on the upper left panel (Fig. 3.11a) are for two layers of identical density $\rho_1/\rho_2 = 1$, and closely approximate a Stoker solution similar to the one of the previous section. The imaginary band inside which the internal eigenvalues become complex is highlighted as a greyed vertical stripe, and corresponds here to the whole reach separating the internal contact discontinuity from the bore. As previously outlined, this is the region in which the two-velocity model departs from the single-velocity model and leads to non-vanishing velocity differences between the layers. Various changes can be observed as the density ratio ρ_1/ρ_2 decreases. First, the mobility of the lower layer decreases. Second, the initially sharp contact discontinuity evolves into a smoother profile which likely corresponds to a rarefaction wave (Fig. 3.11b). Third, whereas for identical densities the front region is composed exclusively of liquid from the lower layer, as the density ratio decreases the bore becomes a mixed zone in which both light and dense liquids are present. Fourth, the extent of the imaginary band narrows to a very thin slice surrounding the bore. What precisely occurs across this region will be discussed in Section 5.2. Finally, for very low density ratios (Fig. 3.11f), the relative inertia of the lower layer becomes so large that it virtually behaves as a rigid solid body. The upper layer then adopts the smooth wave profile corresponding to the Ritter solution. The panels of

Figure 3.11 thus document the full range of behaviour exhibited by two-layer dambreak waves when going from identical densities $\rho_1/\rho_2 = 1$ to a vanishing density ratio $\rho_1/\rho_2 \to 0$. While the Stoker and Ritter profiles retrieved at the two limits are well-known, profiles in the intermediate range do not seem to have been systematically examined before.

The evolving profiles observed when varying the density ratio provide a number of insights into the behaviour of the two-layer model. For identical densities, the velocities of the two layers remain identical ($u_2 = u_1 = u$), hence one of the degrees of freedom of the system is suppressed. By contrast, when the density ratio decreases, all four degrees of freedom associated with the four evolution variables h_1, h_2, u_1, u_2 become activated. For a Riemann problem involving a hyperbolic system, one would expect a wave structure composed of four identifiable waves interleaved with a set of uniform regions (three internal constant states in addition to the two outer constant states associated with the initial conditions left and right of the dam).

A self-similar wave structure of this kind is indeed suggested by Fig. 3.11b and the subsequent panels. The first internal constant state can be identified upstream of the contact discontinuity for the extended Stoker solution of Fig. 3.11a. In Fig. 3.11b, this constant state is now displaced upstream, moving to abscissas in the approximate range $-0.5 \le x/t\sqrt{gH} \le 0$. The contact discontinuity itself has turned into a rarefaction wave extending over abscissas in the approximate range $0 \le x/t\sqrt{gH} \le 0.6$. Meanwhile the second constant state of the extended Stoker solution (downstream of the contact discontinuity) has narrowed to the approximate range $0.6 \le x/t\sqrt{gH} \le 0.7$. The forward shock of the Stoker solution is further seen to evolve into a wave of a mixed type, or *compound wave* (Leveque, 2002), involving a combination of a rarefaction and a shock. In addition, a fourth wave is seen to develop more downstream, over the approximate range $1.5 \le x/t\sqrt{gH} \le 2$. This wave is only slightly visible in Fig. 3.11b, but becomes more conspicuous in Fig. 3.11c and the subsequent panels. This wave is strikingly reminiscent of the spurious forward feature observed in Section 4.1 for the case of a “coloured” dam-break wave with layers of identical densities. The sequence of plots shown on Fig. 3.11 makes it clear that it is associated with the fourth degree of freedom of the two-layer system. Strikingly, this feature converges towards the smooth tip of the Ritter profile as $\rho_1/\rho_2 \to 0$, and its downstream edge is observed to move at speed $u_1 = 2\sqrt{gH}$ regardless of the density ratio. It is thus proposed to refer to this wave as the "Ritter pinch-off".

This peculiar “pinch-off” feature consists in a fast wave of light fluid propagating over the heavy fluid without hardly perturbing it. It appears to converge numerically towards a stable configuration only when ρ_1/ρ_2 is small enough. For the case of Fig. 3.10 ($\rho_1 = \rho_2$), and also for the case of density ratios close to 1 (as for the pearls and PVC material that will be explored in Section 5.2), a pinch-off forms initially but then smears out as the numerical solution converges. For these cases, the main wavefront is always composed of heavy fluid only. One is thus tempted to state a necessary condition for the existence of a stable Ritter pinch-off such as the one observed in Fig. 3.11c, i.e. that the main wavefront be of a mixed type, composed of both light and heavy fluid. Indeed, for the initial pinch-off to converge towards a stable self-similar profile, dilating in space at a constant rate without smearing out, it requires a continuous supply of additional light fluid. This contribution may only be supplied from the upper reaches of the wave if (i) the depth of light fluid at the main wavefront is non-zero, and

(ii) the velocity of the light fluid in that region is greater than the velocity of the wavefront itself. In Fig. 3.12, such flow and velocity profiles are plotted for two density ratios $\rho_1/\rho_2 = 0.77$ and 0.2. In the first case, the wavefront is saturated in heavy fluid and no pinch-off appears. In the second, the main front, located at $x/t\sqrt{gH} \approx 0.8$, is of a mixed type. At this point, the light-fluid velocity is larger than the speed of the propagating wavefront, and a constant flux of light fluid overruns it and nourishes the foremost portion of the wave, comprising a thin uniform flow region (from $x/t\sqrt{gH} \approx 0.8$ to 1.2) and a stable Ritter pinch-off (at $x/t\sqrt{gH} > 1.2$).

The second way in which the Ritter asymptote can be approached is to progressively reduce the thickness of the lower layer of denser liquid, while maintaining the density ratio constant. A sequence of converged profiles of this kind is presented in Fig. 3.13 for a density ratio $\rho_1/\rho_2 = 1/2$, and

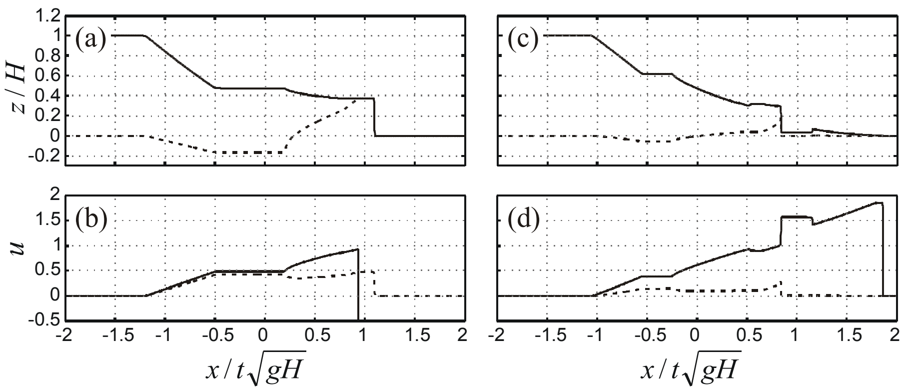

Figure 3.12. Condition of emergence of a Ritter pinch-off. (a) converged flow profile for a density ratio $\rho_1/\rho_2 = 0.77$; (b) layer velocity profiles for $\rho_1/\rho_2 = 0.77$; (c) and (d) flow and velocity profiles for a density ratio $\rho_1/\rho_2 = 0.2$. Solid line refer to the layer of light fluid, dashed line to the layer of heavy fluid.

relative thickness of the lower layer given respectively by $\eta / H = 0.357$, 0.0286, 0.0029 and 0.0003. Computations are again obtained for $t\sqrt{gH} / \Delta x = 1500$. Again, a satisfactory convergence towards the Ritter solution is observed, and the regions highlighted in grey of partly imaginary eigenvalues stay confined to very thin bands. The depth of the denser liquid is seen to significantly affect the overall behaviour of the dam-break wave. This observation will be exploited further below in Section 5.2, when comparing two-layer flow computations with the experimental dam-break waves over granular beds.

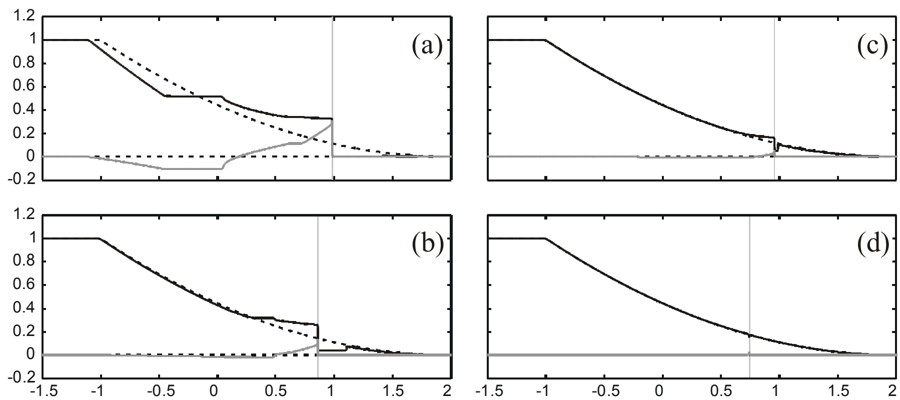

Figure 3.13. Nearly converged numerical results for the dam-break of a light fluid over a layer of a heavier fluid with decreasing initial thickness η, (a)-(d) for initial depth ratios $\eta / H = 0.357$, 0.0286, 0.0029 and 0.0003 respectively. Density ratio $\rho_1/\rho_2 = 1/2$. Analytical results are provided in the background for the Ritter solution ($\eta \to 0$) in dashed line. Grey vertical stripes highlight the reaches where complex eigenvalues appear in the numerical simulations. Dimensionless plots: vertical axis z / H, horizontal axis $x / t\sqrt{gH}$.

4.3. Comparison with two layer/single velocity solutions

Further insights can be gained by comparing two-layer computations with a reduced "two layer/single velocity" formulation for which analytical solutions are available. This reduced formulation is obtained by constraining the velocities of the two layers to stay equal to each other, even when the density ratio is not equal to unity. In that case, setting $u_2 = u_1 = u$ and combining equations (3.21) and (3.20) into a single momentum equation, one obtains the following system of three equations:

$$\frac{\partial h_1}{\partial t} + \frac{\partial (h_1 u_1)}{\partial x} = 0, \quad \frac{\partial h_2}{\partial t} + \frac{\partial (h_2 u_2)}{\partial x} = 0, \tag{3.50}$$

$$\begin{aligned} &\frac{\partial}{\partial t}\{(\rho_1 h_1 + \rho_2 h_2)u\} \\ &+ \frac{\partial}{\partial x}\{(\rho_1 h_1 + \rho_2 h_2)u^2 + \tfrac{1}{2}\rho_1 g (h_1 + h_2)^2 + \tfrac{1}{2}(\rho_2 - \rho_1) g h_2^2\} = 0 \end{aligned} . \tag{3.51}$$

As shown by Capart (2000), these equations are hyperbolic and have a relatively simple eigenstructure that can be written explicitly. In particular, the three eigenvalues are given by

$$\lambda_{\text{ext}}^{\pm} = u \pm c, \quad \lambda_{\text{int}} = u \tag{3.52}$$

where the celerity c becomes

$$c = \sqrt{\frac{\rho_1 g h_1^2 + 2\rho_1 g h_1 h_2 + \rho_2 g h_2^2}{\rho_1 h_1 + \rho_2 h_2}} . \tag{3.53}$$

Here the aim is to compare two-layer solutions starting from initial conditions of the form (3.49) with solutions of reduced equations (3.50)-(3.51) starting from the equivalent initial conditions

$$x<0: \begin{pmatrix} h_1 \\ h_2 \\ u \end{pmatrix} = \begin{pmatrix} h_{1L} \\ h_{2L} \\ u_L \end{pmatrix} = \begin{pmatrix} H \\ \eta \\ 0 \end{pmatrix}, \quad x>0: \begin{pmatrix} h_1 \\ h_2 \\ u \end{pmatrix} = \begin{pmatrix} h_{1R} \\ h_{2R} \\ u_R \end{pmatrix} = \begin{pmatrix} 0 \\ \eta \\ 0 \end{pmatrix}. \quad (3.54)$$

It was recently observed by Capart (see Ke, 2005) that the reduced equations can be solved analytically by further extending the Stoker solution described earlier for the case $\rho_2 = \rho_1$. The extended solution is characterized by the same wave structure as the Stoker solution with colour advection: an upstream rarefaction, a contact discontinuity, and a shock. Each of these waves differs slightly from the case of identical density, however. The rarefaction profile becomes governed by

$$u - c = x/t, \quad u + 2c = 2c_{\mathrm{L}}, \quad \frac{h_2}{h_1 + h_2} = \frac{h_{2L}}{h_{1L} + h_{2L}}, \quad (3.55)$$

which take the same form as the earlier relations (3.46), except that the celerity c is now given by the revised formula (3.53), and that the depth ratio $h_2/(h_1 + h_2)$ furnishes an additional Riemann invariant that must be taken into account. Across the contact discontinuity, the following relations apply

$$u_{CL} = u_{CR}, \quad P_{CL} = P_{CR} \quad (3.56)$$

where $P = ½\rho_1 g(h_1 + h_2)^2 + ½(\rho_2 - \rho_1)gh_2^2$ is the depth-integrated pressure thrust, and where the two subscripts CL and CR denote states to the left and to the right of the contact discontinuity, both in the central region of the dambreak wave. Just like the colour case ($\rho_2 = \rho_1$), the velocity u is continuous across the contact wave (which itself propagates at the same speed as the liquid), and the depth ratios (or colours) on both sides are arbitrary. When $\rho_2 \neq \rho_1$, however, density effects cause the free surface profile to become discontinuous. Finally the usual compatibility relations apply across the shock.

Full two-layer computations are compared with the reduced analytical solutions in Fig. 3.14. The conditions chosen are $\eta / H = 0.357$ and $t\sqrt{gH} / \Delta x = 1500$, and the different panels show results for the following values of the density ratio: $\rho_1/\rho_2 = 1$, 0.975, 0.77 and 0.5. For completeness, results are shown in Fig. 3.14a for layers of identical densities, even though this corresponds to the colour case which has been discussed already. The other three density ratios roughly correspond to the three granular materials that will be investigated in Section 5.2.

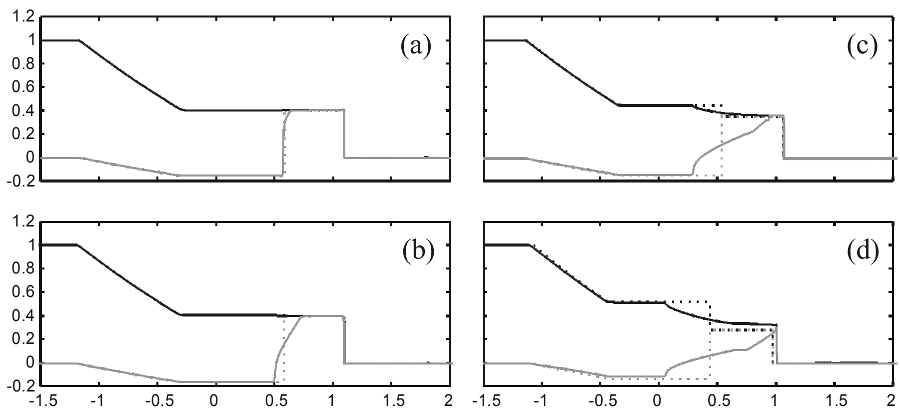

Figure 3.14. Comparisons of two-layer single-velocity analytical results (dotted lines) and full two-layer converged numerical results (solid lines), (a)-(d) for density ratios $\rho_1/\rho_2 = 1$, 0.98, 0.77 and 0.5, respectively (roughly corresponding to water and the three granular materials exploited hereafter: pearls, PVC and sand). Dimensionless plots: vertical axis z / H, horizontal axis $x / t\sqrt{gH}$.

When moving to density ratios lower than one (Fig. 3.14b and followings), the most patent disparity between single-velocity analytical profiles and two-velocity computed profiles lies in the behaviour of the internal interface separating regions of light and dense fluids. While the single velocity profiles preserve a sharp contact discontinuity, the profiles pertaining to the two-velocity formulation show a much more gradual transition in the form of a rarefaction wave. This is very clear even on Fig. 3.14b, corresponding to a density contrast of only 2.5 %. For the lower density ratios depicted in Fig. 3.14c and 3.14d, the rarefaction wave is seen to spread over a longer distance. On the other hand, on both sides of this rarefaction, the two internal constant states of the computed profiles are relatively well captured by the single-velocity analytical solutions. This is especially true on Fig. 3.14b and Fig. 3.14c, i.e. cases for which the wavefront is fully composed of dense fluid only. For the lower density ratio $\rho_1/\rho_2 = 0.5$(Fig. 3.14d), the computed wavefront becomes of a mixed type, and the nearby internal constant state, displaced more upstream in the rarefaction, is characterized by distinct levels of the lower and upper fluids.

5. Comparison with experiments

In the previous section, the two-layer shallow-water computational model has been validated against analytical solutions for a range of idealised dam-break configurations. In the present section simulations are compared with dam-break experiments. In a first stage, the “coloured” liquid dam-break experiments of Janosi *et al.*, introduced in Section 2.2, are again considered. The two-layer flow behaviour of dam-break waves over granular beds is then investigated by comparing simulations with dam-break experiments for three different granular densities. The observed discrepancies are discussed and weighted against deviations observed for the pure liquid experiments. In particular, the influence of the granular density is discussed and related to bed mobility and effective fluid-like thickness of the granular layer. Discussions about the hyperbolic domains and critical stability flow states yield plausible indications for explaining the emergence of antidune-like bedforms as the ones depicted in Section 2.2.

5.1. Comparison of theory and colour dam-break experiments

The experiments of Janosi et al., presented first in Fig. 3.4, consisted in the release of an upstream layer of 15 cm of pure water over a downstream layer of 1.5 cm of coloured water. Simulations for this configuration, using the above model with two layers of identical densities, were performed on a channel extending one meter on both sides of the gate, and with space steps $\Delta x = 1$ mm. Results are presented in Fig. 3.15, where computed profiles are plotted as thick lines superimposed on the greyed flow regions digitised from the experimental images.

Fig. 3.15a reveals a clear difference in behaviour during the initial formation of the wavefront. The experimental wavefront is formed progressively after the emergence and collapse of the mushroom-like and plunging structures discussed in Section 2.2. On the contrary, the shape of the computed wavefront is formed quasi instantaneously and the wave structure simply evolves as a self-similar profile. As a consequence, the computed wavefront is initially far ahead of its experimental counterpart, but the discrepancy reduces in time, as seen at later instants in Figs. 3.15f and 3.15g. The initial gap between wavefront velocities might also partly be ascribed to the relative uncertainty on the precise time of gate removal of the Janosi *et al.* experiments, given the limited frame rate of the employed digital camera.

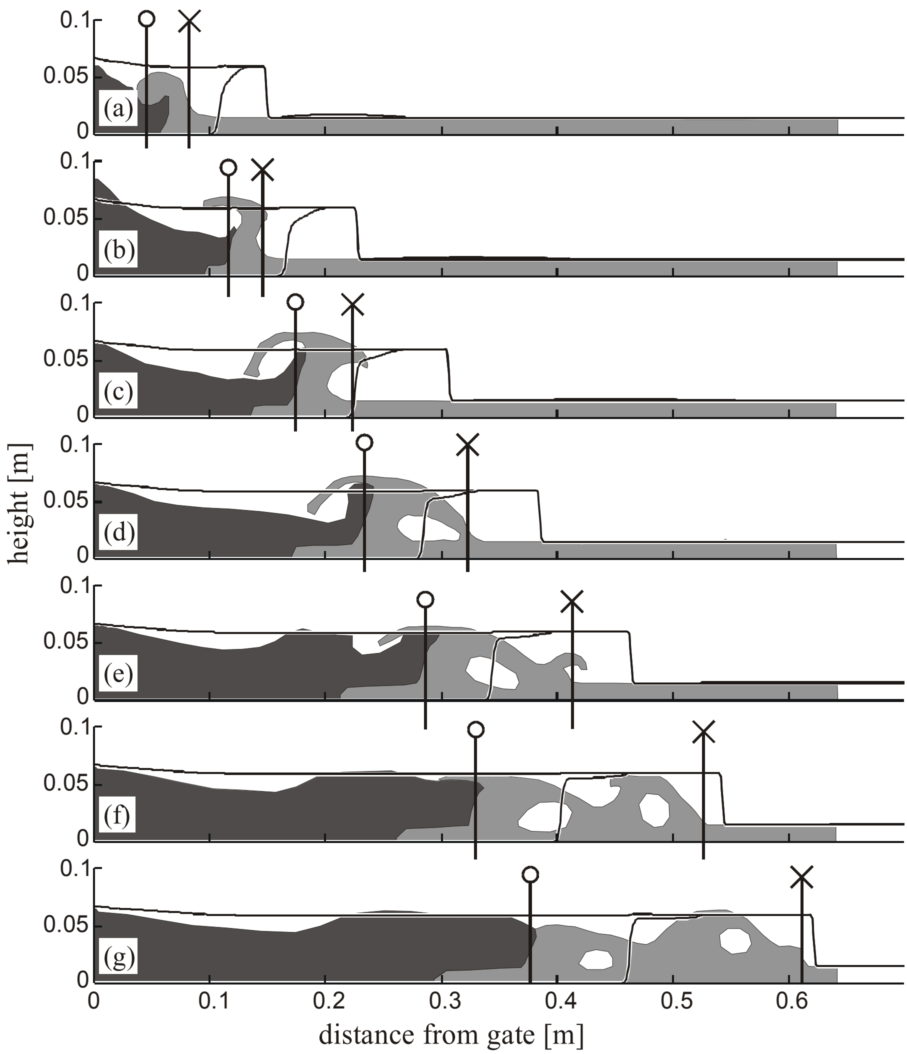

Figure 3.15. Comparison of numerical results for layers of identical densities $\rho_1 = \rho_2$ with the experiments by Janosi *et al.* (2004, Fig. 14) at $t = 0.131$, 0.196, 0.261, 0.327, 0.392, 0.457 and 0.522 s respectively. Circle- and cross-marks identify approximate positions of experimental feature-points: internal contact discontinuity and wavefront.

Observed and computed positions of the internal "colour" contact discontinuity, on the contrary, exhibit an initial difference that does not diminish at later instants. Moderate mixing at the interface between the transparent and coloured regions could noticeably enlarge the dark flow region and partially explain the difference. Both the positions of the observed wavefront (╳) and internal discontinuity (○) are indicated as characteristic feature-points on Fig. 3.15. Despite the significant discrepancies in these two representative horizontal celerities, the height of the water level at the inner constant state of the numerical profiles is remarkably consistent with experimental observations.

In order to investigate the effect of the downstream fluid depth on the celerity and shape of the wave, with the intention of relating it to the density of the granular material for the experiments over granular beds presented in the next section, the same feature points are plotted in Fig. 3.16 on a second series of profiles derived from Janosi *et al.* experiments. The profiles all correspond approximately to the same instant $t \approx 0.6$ s and refer to a constant initial depth $h_u = 15$ cm of pure water in the upstream reservoir, but differ in the depth h_d of ambient coloured water downstream of the gate, respectively equal to $h_d = 0.5$, 1.5, 3.0, 5.8 and 7.0 cm. Positioning of the feature-points is delicate and endowed with some degree of subjectivity, especially for the cases of a larger downstream depth for which the wavefront is not sharp. Analytical profiles of the two-layer model, derived by using the procedure described in Section 4.1, are superimposed as thick lines on the images. Deviations from the experimental profiles are substantial for the positions of the discontinuities, but again the levels of the inner constant states are in good agreement.

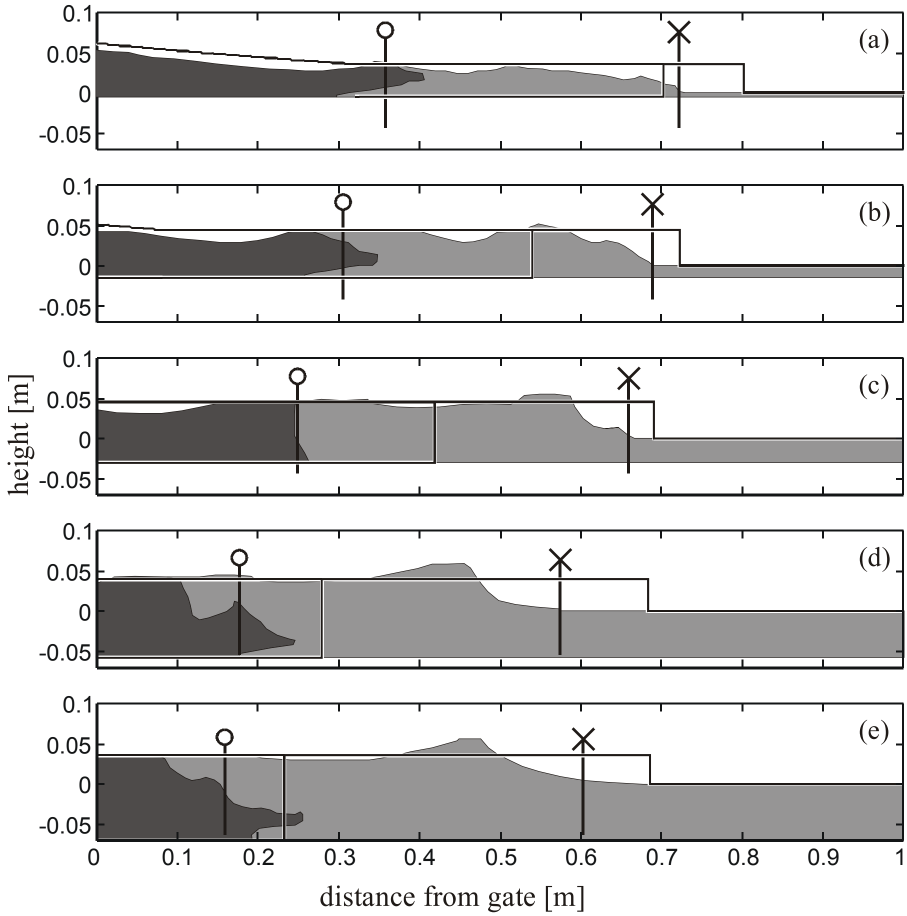

Figure 3.16. Comparison of numerical results for layers of identical densities $\rho_1 = \rho_2$ with the experiments by Janosi *et al.* (2004, Fig. 15) at $t \approx 0.6$ s for a downstream coloured layer of varying depth, $h_d = 5$, 15, 30, 58 an 70 mm respectively. Approximate positions of experimental feature-points as circle- and cross-marks.

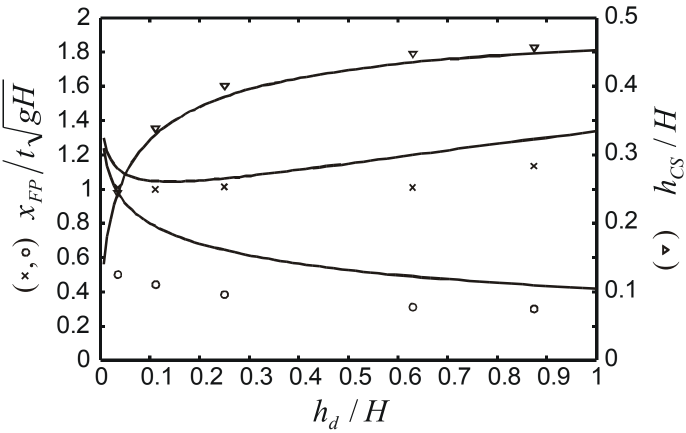

Figure 3.17. Evolution of theoretical (solid lines) and Janosi *et al.* experimental feature-points for coloured dam-breaks with distinct dimensionless depth ratios $h_d / H = h_d /(h_u - h_d)$. Dimensionless positions of the experimental wavefront ($\times$) and contact discontinuity ($\circ$) on the left vertical axis; height of the internal constant state ($\triangledown$) on the right vertical axis. Solid lines feature the theoretical evolution as given by analytical solutions.

These observations are summarized in Fig. 3.17, presenting the evolution of both the experimental and theoretical feature-points for increasing depths of the downstream coloured region. Dimensionless depth ratios on the horizontal axis are expressed as the ratio between the downstream depth h_d and the reference depth H, the latter as previously defined and equal in the present context to the depth difference between upstream and downstream regions, $H = h_u - h_d$. The same ratio will later be used to substantiate the two-fluid analogy of the dam-break waves over granular beds, considering an effective “fluidised” depth of granular material. The dimensionless positions of the wavefront ($\times$) and the contact discontinuity ($\circ$) are scaled with the length factor $t\sqrt{gH}$ on the left vertical axis. The height of the internal constant state ($\triangledown$) is made dimensionless by scaling with the reference depth H on the right vertical axis. One may observe that both the positions of the wavefront ($\times$) and of the contact discontinuity ($\circ$) are poorly reproduced by the theory. The sensitivity to changes in the downstream depth ratio is rather limited, and the evolution of the wavefront position is non-monotonic. In contrast, the predicted level of the inner constant state represents a robust indicator of the actual observed value (∇), with a good sensitivity across the investigated range and a remarkable agreement with experimental measurements.

5.2. Comparison of computations and liquid-granular dambreak experiments

The analogy between the experimental dam-break waves over granular beds presented in Chapter 2, and the two-layer flow model depicted in Section 3, is now evaluated. The solid-like saturated granular bed will be regarded as an equivalent layer h_s of a fluid with the same bulk density. The thickness of this "fluidised" granular layer is expected to depend upon the density of the granular assembly, ρ_s, and on the initial water depth in the reservoir of the failed dam, H. Two-layer flow simulations have been conducted for three different density ratios. The first two refer to the coarse sand and the PVC pellets used for the experiments presented in Section 2. Their specific densities are $\rho_{M,Sand}$ = 2680 and $\rho_{M,PVC}$ = 1580 kg/m³, so that the density ratios between the equivalent "granular fluid" and water are ρ_s/ρ_w $= \varepsilon + (1-\varepsilon)\rho_M/\rho_w \approx$ 2.0 and 1.3 respectively, for an approximate porosity $\varepsilon \approx 0.4$, assumed constant. The third density ratio investigated is that of the artificial pearls used in the pioneering experiments of Capart and Young (1998). These particles are much lighter, with a specific density ρ_M = 1048 kg/m³, i.e. density ratio $\rho_s/\rho_w \approx 1.03$, and diameter $d = 6.1$ mm.

Given the known geometry of the experiments and assigned values of density ratios, the sole parameter that remains to be prescribed is the thickness h_s of the fluidised bed layer that acts as the lower layer of the two-fluid system, over which the granular material is assumed to behave as a fluid. The effective depth ratio $\eta = h_s / H$ is left as a tuning parameter, to be adjusted to provide a best possible agreement with characteristic feature-points of the experimental profiles. As was observed for the coloured experiments (Fig. 3.17), the positions of the wavefront and internal contact discontinuity are mediocre indicators in this regard. The first is tainted with ambiguities in the gate opening time and with the near-field effects occurring at the first stages of wave development. Its evolution with the effective depth ratio is rather flat and non-monotonic. The second suffers from the same drawbacks, and is not well defined in the case of density contrasts between the two-layers, as it was seen in Section 4.2 to evolve into a smooth rarefaction. On the contrary, the level of the inner constant state was seen to be in remarkable agreement for the coloured dam-break experiments. It shows a monotonic evolution for growing effective depth ratios, with a pronounced sensitivity in the region of low depth ratios, as is expected for granular equivalents. It does not vanish or degenerate in the case of density contrasts, and was therefore chosen as the target value for the estimation of the effective depth ratio to be used in the simulations. From basic physical considerations, the value of η is supposed to decrease for denser granular materials, i.e. increasing values of the ratio ρ_s / ρ_w. It may thus be expected that $\eta_{Pearls} > \eta_{PVC} > \eta_{Sand}$. Given the crude approximations of bed porosity, η was tuned moderately, and after a few tests raw values were chosen as: $\eta_{Pearls} = 1/4$, $\eta_{PVC} = 1/10$, and $\eta_{Sand} = 1/35$.

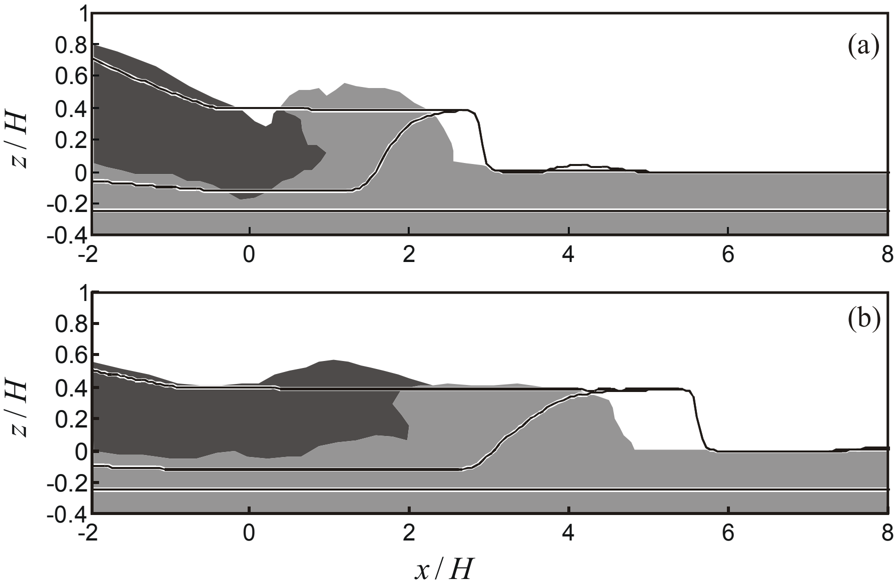

Figure 3.18. Comparison of numerical results (density ratio $\rho_s/\rho_w = 1.03$ and depth ratio $\eta = 1/4$) with the experiments by Capart and Young (1998) for a granular bed made of light pearls, at times (a) $t =$ 0.29 s and (b) $t =$ 0.55 s. Dimensionless plots.

Comparisons for the lowest granular density, corresponding to the artificial pearls of the experiments by Capart and Young (1998), are shown in Fig. 3.18. The initial water depth in the reservoir is $H = 10$ cm, and with $\eta_{Pearls} = 1/4$, the initial thickness of the "granular fluid" layer extending on both sides of the dam is 2.5 cm. Experimental profiles at 0.29 s and 0.55 s were kindly provided by the authors. They refer to dimensionless instants $t\sqrt{g/H} =$ 1.81 and 3.44, thus still pertaining to relatively early stages of the wave development. The dark grey and light grey regions on the images refer respectively to clear water and granular-rich region. No distinction is made between the moving grains and the static bed. The three simulated interfaces are superimposed as solid lines. The lowest horizontal line represents the postulated fixed boundary between fluidised and solid-like granular regions. Fig. 3.18 reveals that the simulated wavefront is substantially in advance. This was already observed for the "colour" experiments of Janosi *et al.* (Fig 3.15). In the present case, it results partly from the overestimation of the positive external eigenvalue. This is due to the crude assumption of complete fluidisation of the effective granular depth, even in the downstream region yet unaffected by the wave. Despite this translation, the computed and observed water profiles are in reasonably good agreement, within margins of accuracy similar to those observed for the "colour" experiments. The shape and height of the wavefront, saturated in moving grains, is correctly reproduced. More particular to this case of different densities, the spreading of the internal discontinuity into a rarefaction wave is well modelled. The Ritter "pinch-off" feature ahead of the wavefront is negligibly small.

Results for the intermediate density of the PVC pellets are shown in Fig. 3.19. The initial water depth upstream of the gate is $H = 25$ cm. The granular bed is assumed fluidised over a thickness of 2.5 cm, i.e. $\eta_{PVC} = 1/10$. The four selected profiles correspond to dimensionless instants $t\sqrt{g/H} =$ 1, 3, 6 and 9, thus the wave development is seen on pretty longer time scales than for the artificial pearls tests. Again, an almost vanishing behaviour of the computed Ritter pinch-off is observed at the foremost extremity of the wave. Used as an indicator for the estimation of η, the level of the inner constant state in the vicinity of the failed dam is correctly captured, and so is the upstream rarefaction, where solid transport is practically nonexistent. On the downstream side, the correspondence between the observed and modelled behaviour is less good. The formation and celerity of the simulated bore is in reasonably good agreement with observations, but its height is largely overestimated. Again, this is due to the requirement of the two-layer model to set in motion the full depth of the postulated fluidised bed layer, whereas the observed wavefront only mobilizes a very thin layer of grains upon its passage. Lastly, in Section 4.2 it was observed that the most significant alteration of the flow, when moving from equal densities and single velocity to lower density ratios and distinct layer velocities, was the evolution of the internal discontinuous "colour" interface into a smooth rarefaction wave. This is clearly observed both

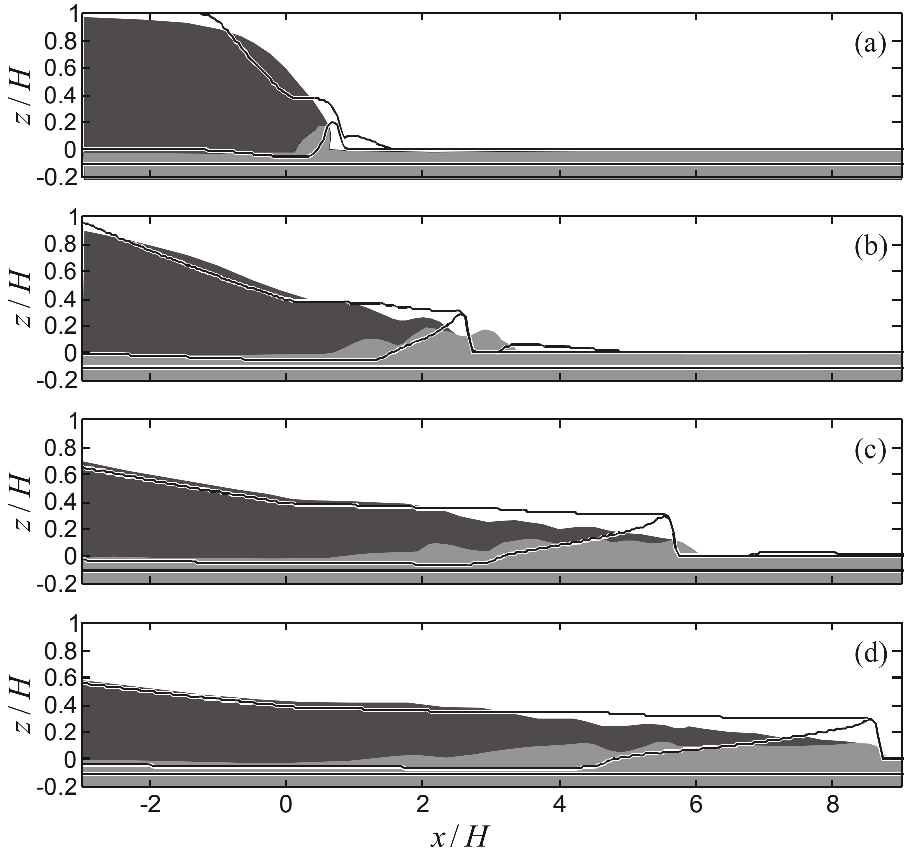

Figure 3.19. Comparison of numerical results ($\rho_s / \rho_w = 1.3,\ \eta = 1/10$) with the PVC experiments, at dimensionless times $t / t_0 = 1$, 3, 6 and 9.

during the experiments and on the simulated profiles of Fig. 3.19. In particular, the two points of detachment of the saturated granular zone, just behind the bore, are at very close locations.

The third granular material is coarse sand. Results are presented in Fig. 3.20. In this case, the initial water depth in the upstream reservoir is 35 cm. This natural material being much heavier than the two artificial analogues analysed previously, the effective depth ratio is much lower. A value of η_{Sand} =1/35 was adopted, i.e. a fluidised granular layer of 1 cm. Profiles are shown at the same dimensionless instants as for the PVC tests, i.e. $t\sqrt{g/H}$ = 1, 3, 6 and 9. Whereas the agreement between simulated and observed levels is reasonable in the upstream reach, the same does not hold at the wavefront. The position of the latter is completely missed out. The simulated bore is located way behind the observed front. On the other hand, the Ritter pinch-off has now a significant magnitude and does not vanish with time. Strikingly, the computed water level profile within that Ritter pinch-off roughly corresponds to the observed one.

The peculiar behaviour of the Ritter pinch-off may be better grasped by looking to the two critical stability Froude numbers delimiting the domain inside which imaginary eigenvalues of the two-layer model are found. Using the procedure that allowed to construct Fig. 3.6 by computing analytically the discriminant of the characteristic polynomial, one may obtain the two longitudinal profiles of the lower and upper stability Froude numbers. The two resulting curves are plotted in Fig. 3.21 for the converged self-similar profile corresponding to the sand tests of Fig. 3.20. They form a band inside which strict hyperbolicity is lost. The actual profile of the two-layer stability Froude number $Fr^{\Delta} = (u_1 - u_2)/\sqrt{g(h_1 + h_2)}$ is plotted as a solid line.

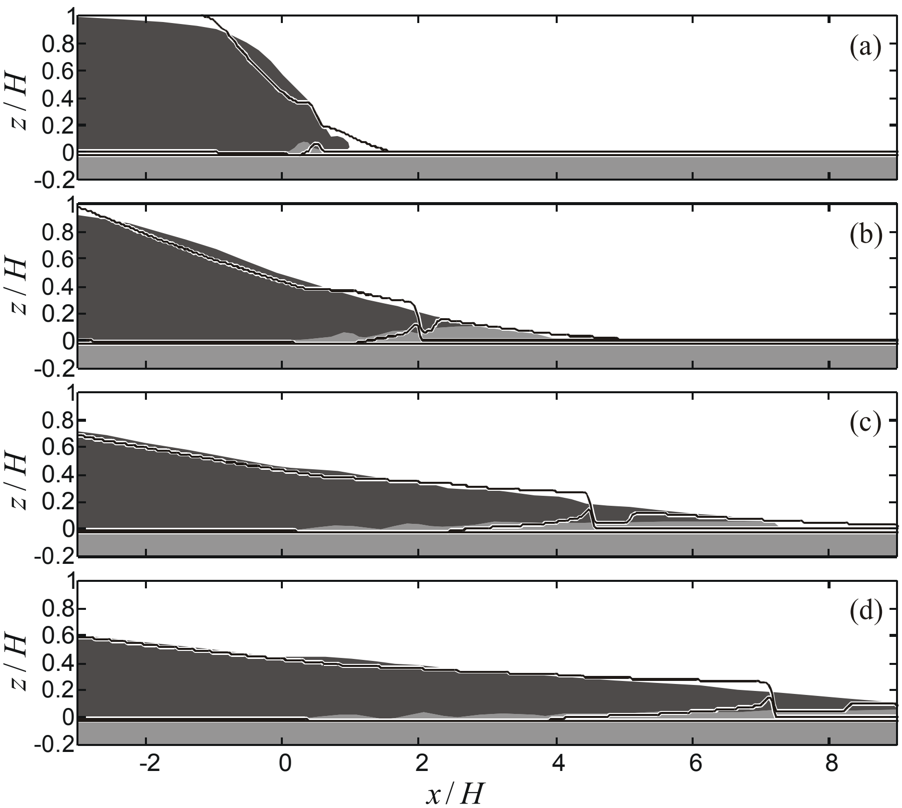

Figure 3.20. Comparison of numerical results ($\rho_s / \rho_w = 2,\ \eta = 1/35$) with the sand experiments, at dimensionless times $t / t_0 = 1$, 3, 6 and 9.

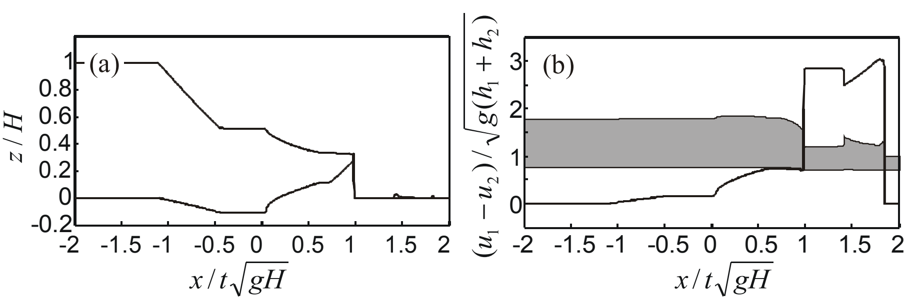

Figure 3.21. Numerical results for the sand test: (a) converged flow profile; (b) profile of the stability Froude number $Fr^{\Delta} = (u_1 - u_2) / \sqrt{g(h_1 + h_2)}$ (solid line) and band with complex internal eigenvalues (grey region).

Two fascinating features are observed. Firstly, while the actual Froude profile is always located outside of the non-hyperbolic band, it is seen to jump across this band at the position of the main wavefront, switching from the lower stable region upstream of the front to the upper stable region within the Ritter pinch-off and intermediate uniform state. The wave seems to behave as if it was striving to remain in the hyperbolic domain and converge towards a stable Riemann solution. The transition for the converged solution of Fig. 3.21 is found very sharp. In the numerical computations, however, the transition is spread over some numerical cells that are thus located within the non-hyperbolic band, explaining the thin vertical stripes of imaginary eigenvalues observed e.g. in Fig. 3.11. The second peculiar feature observed in Fig. 3.21 lies in the region situated just upstream of the bore. Before abruptly jumping to the upper stable region, the Froude profile is seen to come very close to the lower stability Froude number over a substantial portion of the internal rarefaction. The flow in that region is thus very near instability. For the case of the PVC tests, the computed Froude numbers in that region were found to slightly enter the imaginary band before jumping to the upper region. Looking back to the PVC profiles of Fig. 3.19, one is tempted to regard this nearly unstable region as a region favourable to the emergence of instabilities at the interface between the two fluid layers, materialised in the present context as the antidunes-like bedforms observed more clearly in Fig. 3.4.

5.3. Elementary wave structures and characteristic paths

In Section 4.2 it was anticipated that, for the Riemann-type initial conditions as the dam-break configurations that were explored, the system of two-layer shallow-water equations should lead to self-similar solutions comprising a series of four elementary waves (shocks or rarefactions, or combinations of the two) separated by three internal constant states. Numerical simulations were carried out towards convergence and the results indeed suggested a structure of this kind.

Here, in order to further clarify the wave structure, one seeks to draw in an *x*-*t* plane the characteristic rays associated to each of the four eigenvalues of the system. Physically, they express the propagation of information related to each considered eigenvalue in the system. Different configurations of these rays are possible: (i) within constant flow states, such rays should consist of parallel straight lines for any eigenvalue; (ii) within a rarefaction wave associated to eigenvalue λ_i, the rays for λ_i should consist of a diverging fan of straight lines radiating from the origin, while the rays associated to $\lambda_{j \neq i}$ may cross the rarefaction and adopt a curvature; (iii) in the vicinity of a shock associated with eigenvalue λ_i, the rays for λ_i should converge towards the shock; (iv) according to Leveque (2002, Chapter 16), additional configurations are possible in some special cases, e.g. for equations of the mixed type "which lose hyperbolicity over some relatively small regions of space"; configuration of characteristic rays within these regions may consist of a combination of a rarefaction and a shock, the associated rays thus converging only on one side towards the shock.

The characteristic rays were derived for the three configurations of previous section, i.e. dam-break waves over a granular bed of light pearls, PVC pellets and sand. They may be drawn efficiently from the numerical simulations in the following steps: (i) obtain a well-defined numerical solution by pursuing the simulations until approaching convergence of the self-similar profile; (ii) compute profiles of the four eigenvalues based on this converged numerical solution; (iii) extend this solution backwards at short times according to self-similarity; (iv) grow a bundle of characteristic rays for each eigenvalue, starting from $t = 0$ and adopting a local slope in the x-t plane, given by the associated eigenvalue at that point.

Such plots are given in Figs. 3.22, 3.23 and 3.24, along with the converged flow profile and eigenvalues, for the cases of light pearls, PVC and sand, respectively. The converged numerical results of the upper-left panels reveal sharp profiles, where constant states appear remarkably and separate the non-uniform regions associated with each wave. These regions are highlighted in colours that are reported in the subsequent figure panels, depending on the characteristic(s) to which they seem to pertain.

The profiles for the cases of light pearls and PVC are peculiar, in that the wavefront is saturated in “heavy fluid” (i.e. moving sediments). In the constant state region just upstream of the wavefront, the two internal eigenvalues (coloured in pink and blue) are seen to coincide, and consequently also the associated characteristic rays. A demonstration of what exactly occurs in this region goes beyond the scope of the present thesis, but it seems that due to this degeneration of the characteristics, the fourth degree of freedom of the full system is inhibited, and so is the wave associated to that characteristic in the solution. In Section 4.2, it was shown that the wave associated to the fourth degree of freedom of the system is this peculiar feature that was called “Ritter pinch-off”. At the time (see page 3-33) it was also stated that a physical “Ritter pinch-off” may only exist if the main wavefront is of a mixed type, composed of both light and heavy fluid. This is consistent with what is observed on the panels (a) of Figs. 3.22 and 3.23: beyond the wavefront, at the foremost extremity of the wave (region coloured in green), the perturbations to the initial flow configuration are imperceptible. Though, the figures show perturbed characteristic rays in that region. Those are believed to be associated to a flaw in the numerical simulations, already identified in Section 4.1 and creating a fast spurious wave at the initial instants. This spurious wave, although having a depth vanishing with time, affects the characteristic rays in a durable way.

The behaviour for the case of the sand bed is depicted in Fig. 3.24. The wavefront is now of a mixed type, and as a result the Ritter pinch-off does not vanish. Although still very weak, it is visible ahead of the wavefront on Fig. 3.24a. The four characteristics plotted in Fig. 3.24b are now everywhere distinct, and the characteristic rays plotted in the subsequent panels reveal a four-waves structure. Tough, the behaviour of the waves associated with λ_3 and λ_4 (coloured red and green) is yet not fully understood. It seems that the first one has evolved into a *compound wave* in the sense of Leveque (2002), composed of both a rarefaction and a shock. Its precise characterisation, however, goes beyond the scope of the thesis and is left for further work.

6. Conclusions

Based on a qualitative comparison of dam-break experiments over granular beds with two-fluids coloured dam-break experiments taken from the literature, a two-layer shallow-flow model was introduced and motivated, where the layers have distinct densities and are allowed to flow at distinct velocities. The resulting set of governing equations has been derived based on the least action principle of mechanical systems, and essential properties of the equations have been highlighted, among others the intrinsically non-conservative formulation and, more importantly, the possible loss of

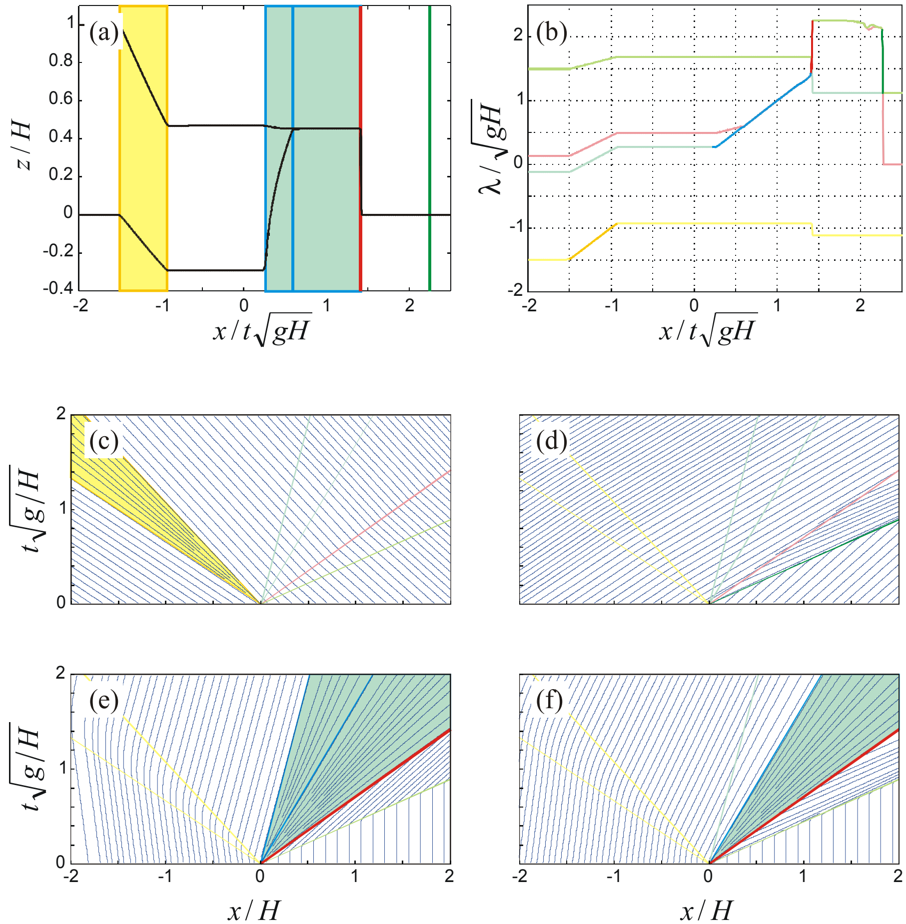

Figure 3.22. Wave structure associated to the bed made of light pearls. (a) converged self-similar flow profile; (b) profiles of eigenvalues $\lambda_1 < \lambda_2 < \lambda_3 < \lambda_4$; (c) characteristic rays associated with λ_1; (d) λ_4-rays; (e) λ_2-rays; (f) λ_3-rays. All plots made dimensionless.

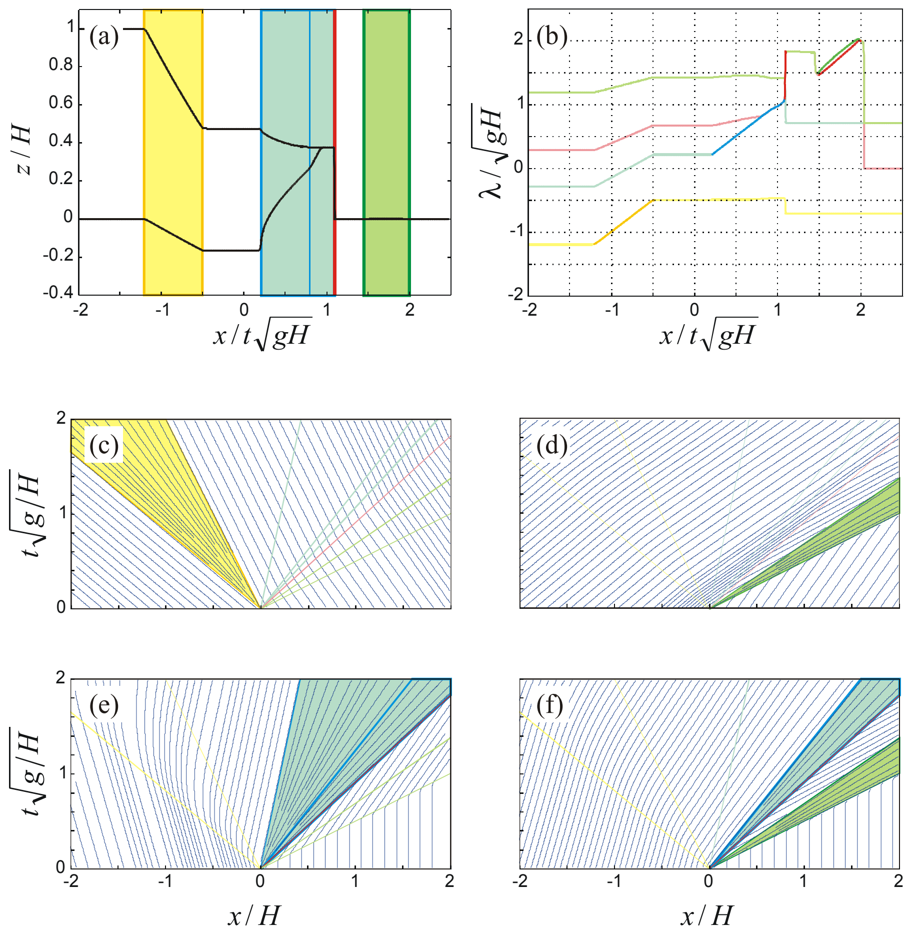

Figure 3.23. Wave structure associated to the bed made of PVC. (a) converged self-similar flow profile; (b) profiles of eigenvalues $\lambda_1 < \lambda_2 < \lambda_3 < \lambda_4$; (c) characteristic rays associated with λ_1; (d) λ_4-rays; (e) λ_2-rays; (f) λ_3-rays. All plots made dimensionless.

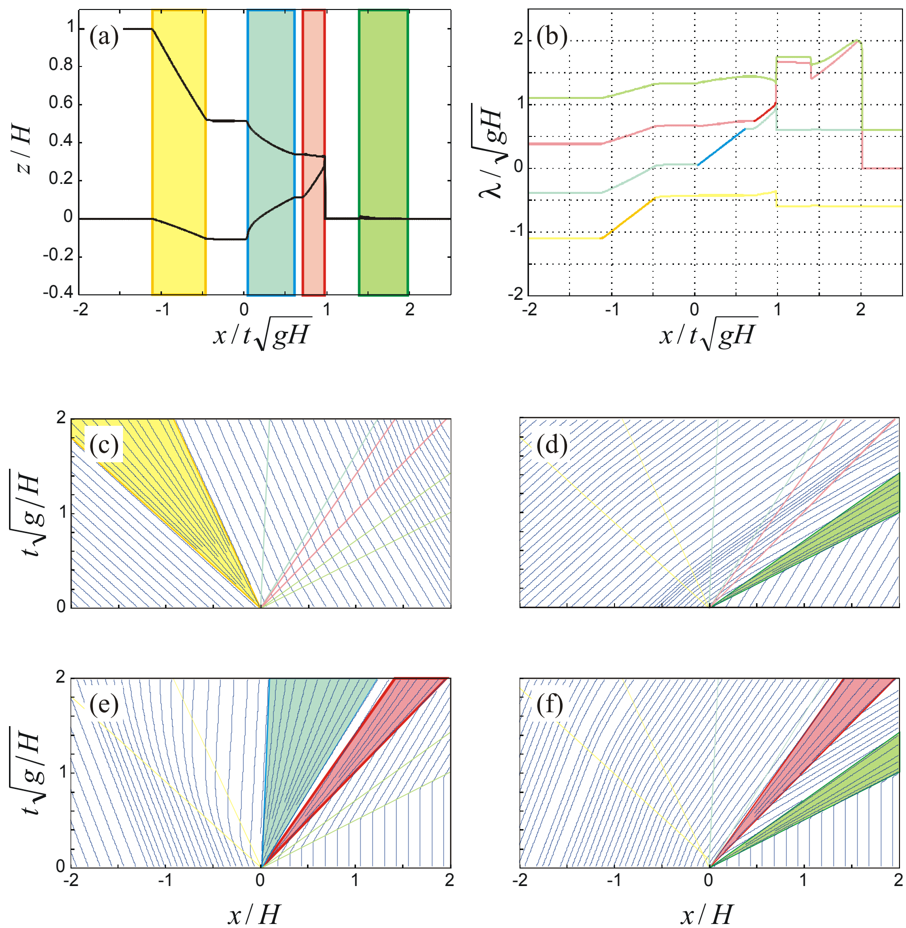

Figure 3.24. Wave structure associated to the bed made of sand. (a) converged self-similar flow profile; (b) profiles of eigenvalues $\lambda_1 < \lambda_2 < \lambda_3 < \lambda_4$; (c) characteristic rays associated with λ_1; (d) λ_4-rays; (e) λ_2-rays; (f) λ_3-rays. All plots made dimensionless.

hyperbolicity. Numerical computations were performed, using a second-order accurate numerical scheme, to characterise the behaviour of the system for dam-break type initial conditions. Validation of the model against limiting cases with analytical solutions, and its detailed inspection for the general case, permitted to gain insights into the implications of the density and of the distinct layer velocities on the observed structures of shallow dam-break waves over granular beds.

In this chapter the two-fluids analogy was pushed to its limits by considering the granular bed as an equivalent "granular fluid", completely and permanently fluidised over a certain predefined bed thickness. Comparisons with the experiments yielded interesting observations. In the range of a moderate density difference between the two layers, the analogy may explain the flattening of the internal discontinuity into a rarefaction, the appearance of a saturated or of a mixed wavefront, the proneness for emergence of instabilities. But the analogy breaks down for lower density ratios ρ_w/ρ_s, corresponding to heavier granular materials: if the concept of a predefined effective fluidised layer leads to a reasonable approximation in the vicinity of the dam, it does not provide a correct representation near the wavefront. In reality, an additional mechanism has to be incorporated in the description, which governs the phase transition of the granular material, passing from a solid-like behaviour in the static bed to a fluid-like behaviour in the layer of mobilised sediments. This transition should be based on the local balance of entraining and resistive forces acting on the grains, rather than on an *a priori* postulated thickness of a fluidised layer. The extension of the above two-layer shallow-flow model with the inclusion of a physically-based criterion for the solid/fluid transition of granular material lies precisely at the core of the next chapter of the thesis.

Chapter 4
Erosion and deposition, and the effects of granular dilatancy on dam-break induced sheet flow

"Without attempting anything like a complete dynamical theory ...
I would point out the existence of a singular fundamental property of ...
granular media, I have called "dilatancy"

O. Reynolds, *Phil. Mag.* **20**, 467 (1885).

1. Introduction

In the previous chapter a shallow-water model for two-layer stratified flows with a density contrast was presented. Its behaviour for dam-break flows was investigated on cases that involve the sudden release of a mass of "light" fluid over a uniform substrate of a "heavier" fluid extending on both sides of the idealised dam. An analogy with dam-break waves propagating over granular beds was suggested, by considering the bottom granular layer as a "heavy" fluid with its proper density. By contrasting model simulations with results obtained for two layers having the same density, valuable insights were gained into the implications of the density contrast on the observed behaviour of the dam-break wave. Though, clear limitations of this highly simplified approach were also identified: (i) the granular layer was assumed to be instantaneously and totally fluidised over a certain bed thickness, regardless of its movement or immobility; (ii) no clear physical argument was available for the predetermination of the thickness of this layer; (iii) no interactions between this fluidised layer and the below granular bed were accounted for; (iv) the layers were completely immiscible and frictionless. The major limitation of that approach is thus that the dynamical effects resulting from the entrainment of granular material and its incorporation into the flow are thoroughly disregarded.

In order to improve the description, one needs to properly account for the difference in behaviour between the granular bed, behaving as a solid, and the moving sediment mixture, behaving as a fluid, and to provide a mechanism for the transition from one behaviour to the other, materialised as erosion or deposition. Doing so, besides the sharp interface separating the water layer from the sediment transport layer, a second evolving interface is introduced, separating this moving granular layer from the underlying static bed. A sharp view of this interface will also be adopted, and it will be regarded as a phase interface across which the granular material undergoes a phase transition from a solid-like to a fluid-like behaviour.

One major benefit of the proposed description, as opposed to former proposals, is to account for the effect of granular dilatancy associated with erosion. It relies upon the postulate that the mobilisation of bed material is associated with an expansion of the granular matrix so that the volumetric sediment concentration in the moving layer is lower than in the static bed.

Whereas the previous chapter focused on the horizontal structure of transient two-layer shallow flows propagating over a rigid bottom boundary, the present chapter will thus seek to address the vertical structure of geomorphic flows in interaction with a loose bottom boundary. The proposed description is first motivated on the basis of experimental observations in Section 2, and its implications on the flow dynamics are discussed. Then, in Section 3, the description is formalised into a set of equations governing the "vertical" flow structure. At first, for sake of clarity but without loss of generality, the derivation is performed by assuming uniform flow conditions. In a second step, a combination with the "horizontal" flow structure derived in the previous chapter will provide a complete formulation for two-layer geomorphic flows in unsteady, non-uniform conditions. Section 4 presents the adopted numerical scheme. Section 5 is then devoted to a scrutinized analysis of the model behaviour. Among others, model parameters are classified and model accuracy and stability is investigated. In order to further motivate the impact of granular dilatancy, one quantifies the relative importance of friction and granular dilatancy as two mechanisms of coupling between the clear-water and moving sediments layer. In Section 6 model simulations are faced with the experiments presented in Chapter 2. Finally, Section 7 shows that this coupling mechanism resulting from granular dilatancy is sufficient to generate erosion and create a stable sheet-flow layer even in the absence of any friction at the interface. A reduced set of homogeneous equations is obtained. Being homogeneous, the reduced system conforms the conditions for the existence of self-similar solutions characterised by a Riemann structure.

2. The vertical flow structure

2.1. Imaging observations

Small-scale laboratory dam-break experiments were presented in Chapter 2. At the time the analysis restricted to general observations of the flood wave. Here more detailed experimental observations are presented, and key features of the flow are pinpointed that will lead to the identification of an idealised vertical structure.

2.1.1. A layered flow structure...

Figure 4.1a shows a typical mosaic image of the dam-break experiments introduced in Chapter 2. Two sharp characteristic lines are clearly identified and separate distinct flow regions. The first is the water free surface. The second is the upper limit of the granular material, and features a very sharp transition between a sediment-rich layer and a pure water layer. In order to further discriminate distinct flow regions, one must add some information to the image, representing the flow dynamics. A simple way to do this is to construct a differentiated image, subtracting pixel by pixel the image from an image taken at a nearby instant. Fig. 4.1b is obtained in this way, by subtracting the image of Fig. 4.1a from the image at 1/100 s later, then taking the absolute value and slightly enhancing the image look-up table. Doing so, regions of constant pixel values appear black. This is the case of the immobile granular bed, and of the ambient air. The vast majority of the pure water flow region appears black as well, as it is characterised by uniformly dark pixels except in zones where small entrapped air bubbles or impurities are found. On the contrary, the zone of moving grains appears much brighter. The transition between this bright region and the upper and lower dark regions is found to be quite abrupt again. Whereas its upper limit was already clearly visible in Fig. 4.1a, its lower limit features a third sharp interface of the flow. It separates the region of moving grains from the static bed, and thus constitutes the loose bottom boundary of the flow. For a better visualisation, the rectangular insets of Figs. 4.1a and 4.1b are magnified in Figs. 4.2a and 4.2b. All together, the observations support an idealised layered structure as the one sketched in Fig. 4.2c: the flow will be regarded as a superposition of three distinct shallow layers, each having homogeneous properties: (i) a pure water layer with a free surface on top, (ii) a transport layer made of a dense mixture of water and moving grains, and (iii) a motionless granular bed below. The movement of the lower interface results from erosion or deposition. The displacements of the other two interfaces are governed by a combination of spatial gradients in the horizontal flow components and of the potential vertical exchanges between the layers. Note that the thickness of individual layers may become zero in special cases. This may happen for the layer of moving sediments in the absence of sediment transport, but also for the clear water layer in case of fully developed debris-flow conditions, like is observed in the vicinity of the wavefront in Fig. 4.1a.

Overall, such an idealisation is believed to be a reasonable approximation of flow conditions in which the sediments move as a dense contact load, with negligible suspended transport in the upper layer. Conditions ranging from mild bed load to intense sheet flow should be covered. From now on, the moving sediments layer will be referred as the sheet-flow layer.

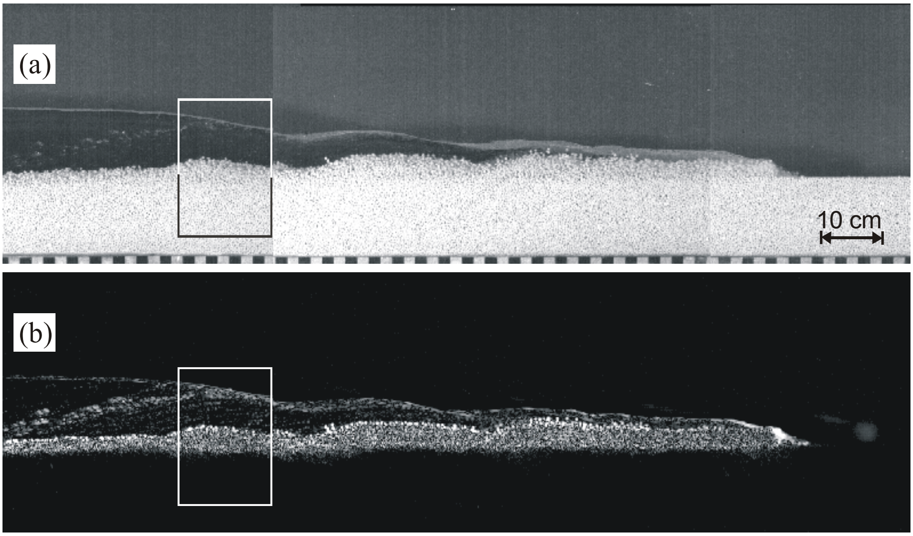

Figure 4.1. Experimental flow mosaic assembled from different runs. (a) mosaic image; (b) differentiated image obtained by subtracting pixel-by-pixel two successive images

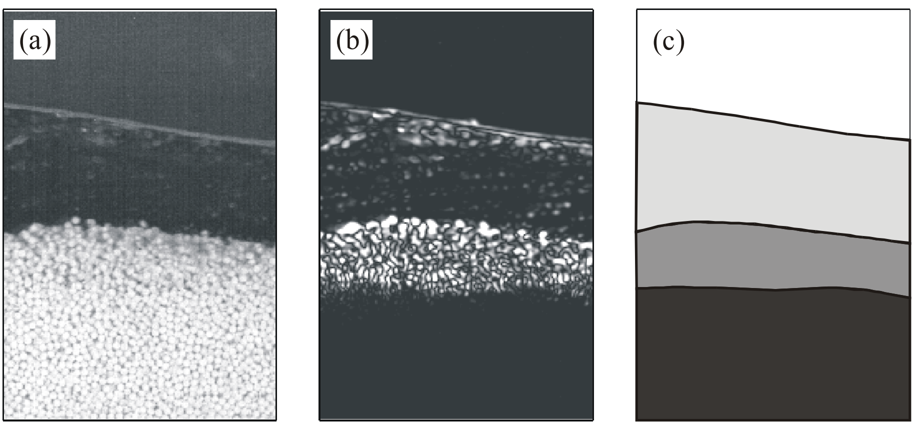

Figure 4.2. Layered flow structure, visualised in zooms on the rectangle insets of Fig. 4.1. (a) mosaic image; (b) differentiated image; (c) idealised layered vertical flow structure.

2.1.2. ... with distinct velocities in the two flowing layers ...

In accordance with the shallow-water approximation, depth-averaged velocities are considered in each layer. In Fig. 4.3 imaging techniques are utilised to characterise the actual velocity profiles observed in the dam-break experiments. Specially designed imaging algorithms were used to track at the same time the movements of the PVC pellets in the granular region, and the movements of “pliolite” neutrally-buoyant tracers dispersed in the water layer (see Chapter 2 for some details on the techniques). Results are highlighted in Fig. 4.3b and 4.3c for the two rectangular regions visible on the typical mosaic image of Fig. 4.3a. The left panels show a zoom on the considered regions. The identified centroids of PVC particles and pliolite tracers are indicated in the middle-left panels, in red and blue respectively. Correspondence with particle positions obtained at the next image delivered the displacement vectors shown on the middle-right panels. Even if some particles could not be paired and if a few vectors are manifestly incorrect, the vectors give a reasonable estimate of the displacement field. To obtain a better estimate of the velocity profile, the procedure is repeated over 20 successive frames (corresponding to a time interval of 0.1 s around the image of Fig. 4.3a) and the results are averaged and interpolated over the entire depth. The resulting profiles are plotted on the left panels, superimposed on the three flow regions as identified in the previous section: the static bed, the sheet-flow, and the clear water.

Several observations can be made. Firstly, the velocity in the clear water region is nearly constant throughout the depth. Secondly, as expected the velocity vanishes in the bed region. Thirdly, the velocities in the sheet-flow layer are not equal to those of the clear water layer. Their evolution is more gradual and they adopt a roughly linear profile, starting from zero near the bed interface and increasing when approaching the upper interface of the layer. In its immediate vicinity the velocities in the sediment-rich and clear water regions are very similar, but it may not be deduced from the observations that the profile is really continuous there.

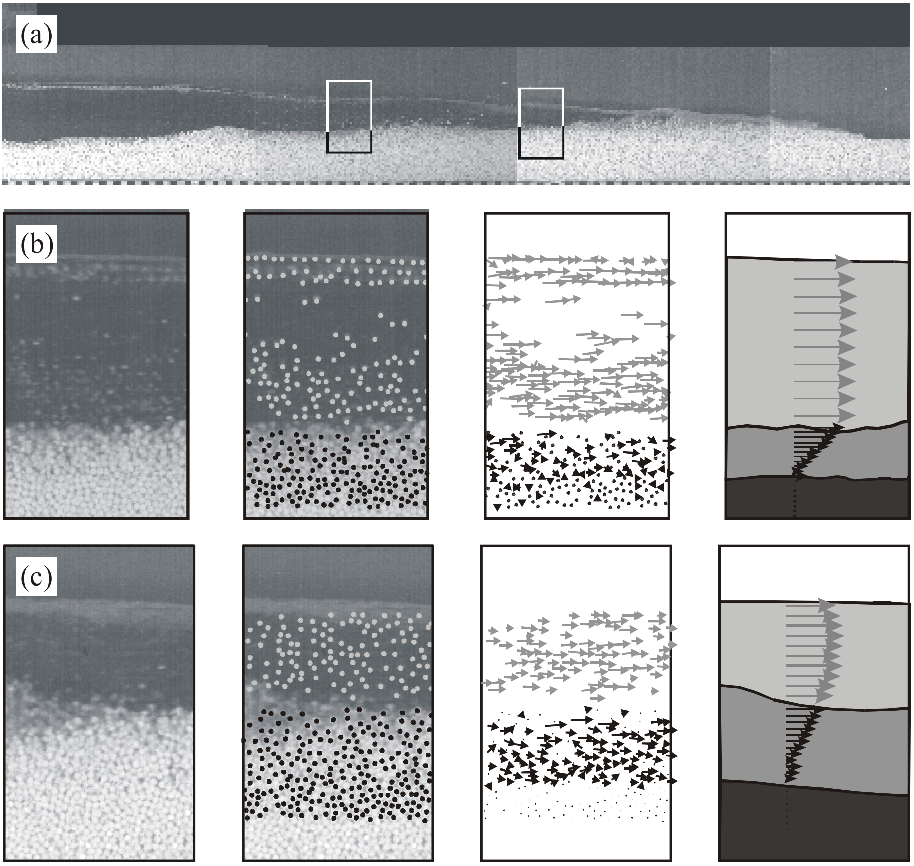

Figure 4.3. Distinct layer velocities. (a) flow mosaic; (b) and (c) from left to right: zooms on the two rectangle insets of (a); identified positions of bed sediments (black) and Pliolite® tracers (grey); displacements between two successive frames; interpolated velocity profile obtained by averaging velocity vectors over 20 successive frames (i.e. 0.1 s)

Overall, the above observations support the necessity to allow the two flowing layers to have distinct velocities. An idealised piecewise constant profile is adopted, in which the individual profile in each layer is replaced by a depth-averaged value. Within the sheet-flow layer, any velocity difference between the grains and interstitial water is neglected. Typically, the velocities in the water layer will be larger than in the layer of moving sediments. However, no predetermined relation between the two layer velocities will be postulated a-priori. They will constitute two degrees of freedom of the flow, whose evolution will be imposed by the governing equations for conservation of mass and longitudinal momentum.

2.1.3. ... and distinct sediment concentrations in the two granular layers ...

To complete the vertical flow structure, the evolution of the granular concentration c_s in the sheet-flow layer should be prescribed. A possibility is to regard it as an evolving variable (Ferreira *et al.*, 2003). One would then need an additional governing equation and closure law. An alternative is to consider that it is roughly equal to the concentration prevailing in the static bed underneath, i.e. $c_s = c_b$ (Capart, 2000; Fraccarollo and Capart, 2002). However, the mobilisation of granular material requires to set the grains apart to some extent to let them move. This should result in a vertical expansion of the granular matrix, a phenomenon described by Reynolds (1885) as granular dilatancy. In order to quantify this effect in the present context, one will again rely on experimental observations.

Figure 4.4 shows a typical sequence of flow snapshots for the PVC pellets, spanning from 0 to 2 s after gate removal, with the three typical flow regions emphasised in distinct grey scales. As the wavefront has not passed the downstream extremity of the image, and if the negligible amount of sediments supplied through the very thin sheet-flow layer at the upstream extremity of the image is disregarded, the amount of granular material present in the visible region is constant throughout the sequence. For each snapshot the area of the static bed A_b and the area of the sheet-flow layer A_s are computed. Results are presented in Fig. 4.5a. Circular symbols (○) stand for the difference in bed area compared to the initial area, $A_b - A_b^0$. The deficit corresponds to the eroded material. The triangular symbols (△) correspond to the difference in total granular area (bed + sheet-flow), i.e. $A_s + A_b - A_b^0$. Non-zero values are obtained, which means that the sheet-flow area does not balance the deficit in bed area. The difference results from a reduced sediment concentration in the moving layer. This reduction is quantified in Fig. 4.5b by computing the bulk concentration in the sheet-flow layer c_s (□) such that the amount of eroded material within $A_b - A_b^0$ balance exactly the amount of transported material within A_s. The concentration inside the static bed was measured separately by analysing bed samples taken *in situ*, and amounted to $c_b = 0.58$ (○ in Fig. 4.5b). Much lower values are observed in the moving layer. However, despite the large range of transport intensities ranging from the mild bed load in the upstream reaches to the debris flow near the wavefront, values stay confined in a remarkably narrow range from $c_s \approx 0.21$ to 0.25.

Comforted by these observations, the sediment concentration in the sheet-flow layer c_s, while distinct from the bed concentration c_b, is assumed to remain constant over time. For the PVC experiments, a value of $c_s = 0.22$ will be adopted. Using the ratio c_s/c_b as a correction for the sheet-flow area, values of $A_b - A_b^0 + A_s\, c_s/c_b$, plotted as square symbols (□) in Fig. 4.5a, are very close from zero.

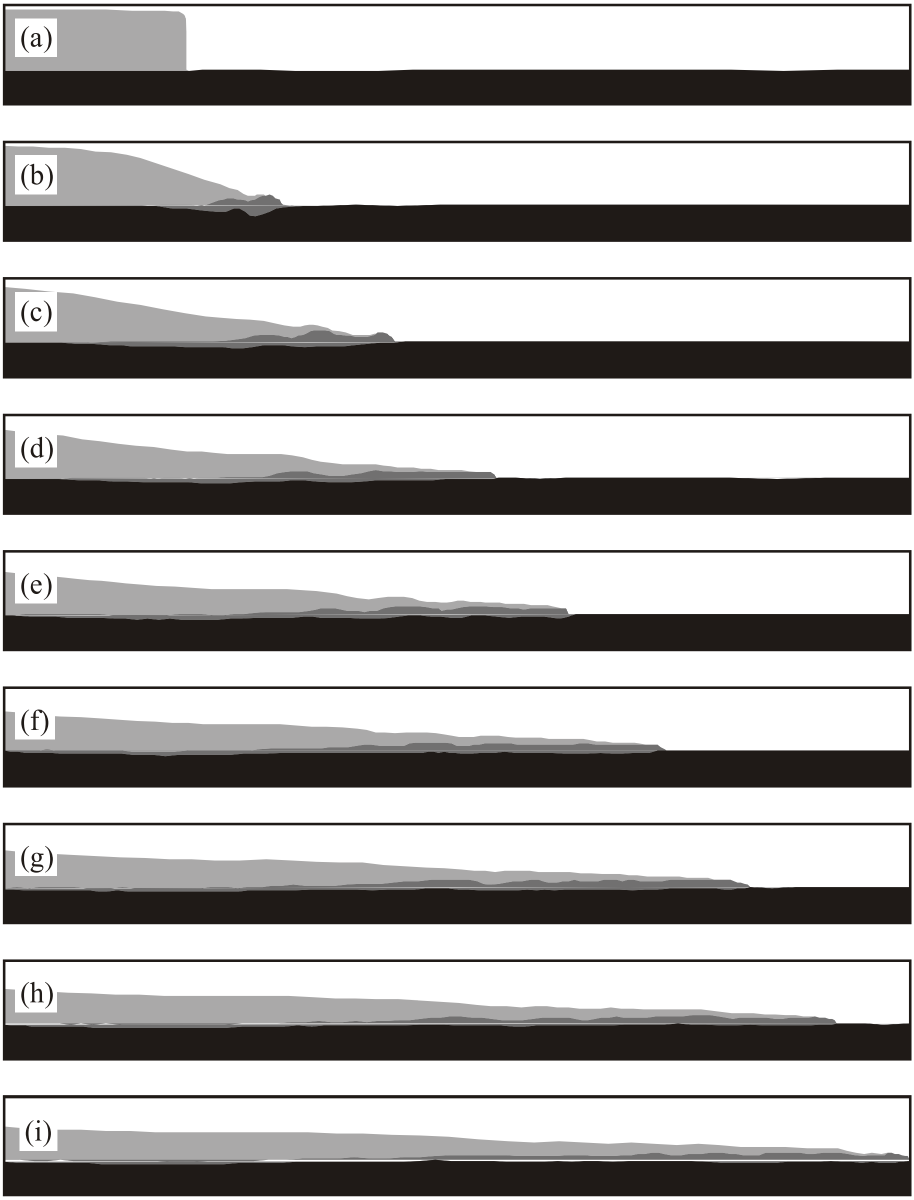

Figure 4.4. Sequence of flow snapshots for the experiment with a flat PVC bed and $H = 25$ cm, spanning from 0 to 2 s after gate removal, with the three typical flow regions emphasised in distinct grey scales.

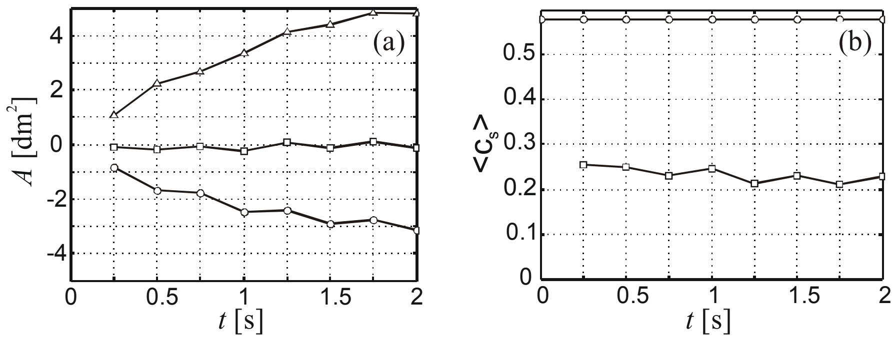

Figure 4.5. Effects of granular dilatancy on the snapshots of Fig. 4.4. (a) balances of bed and sheet-flow layer areas: (○) eroded material $A_b - A_b^0$; (△) difference in total granular area $A_b - A_b^0 + A_s$; (□) correction accounting for granular dilatancy, $A_b - A_b^0 + A_s\, c_s / c_b$ with $c_s = 0.22$; (b) actual evolution of the averaged granular concentration: (○) in the static bed, $c_b = 0.58$; (□) in the sheet-flow layer, c_s.

The above observations were based on experiments performed with PVC pellets; however, the same conclusions were drawn from the analysis of experiments performed with natural sand.

2.2. Consequences on the flow dynamics

In Fig. 4.6, the postulated vertical flow structure motivated by the experimental observations of previous section is considered: a static granular bed of density ρ_b extending at level $z^{(b)}$; a sediment transport layer of depth h_s and horizontal velocity u_s, with a granular concentration $c_s < c_b$, thus yielding a layer density $\rho_s < \rho_b$; and a pure water layer of depth h_w and horizontal velocity u_w. The three layers are considered homogeneous, and are separated by sharp interfaces $\Gamma^{(b)}$, $\Gamma^{(s)}$ and $\Gamma^{(w)}$. Here, as in Chapter 3 and throughout the thesis, subscripts are used to denote layer variables whereas superscripts refer to interface variables. The proposed

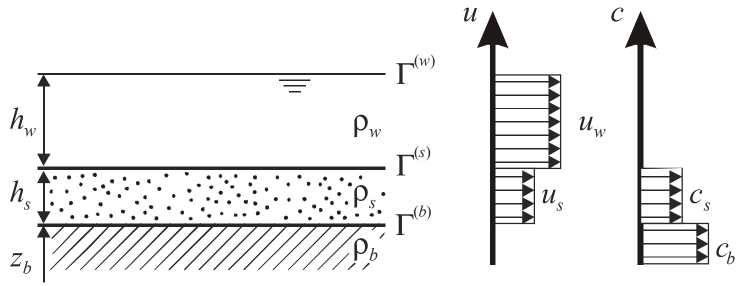

Figure 4.6. Sketch of the postulated idealised vertical flow structure

description of Fig. 4.6 builds up on an earlier modelling approach (Capart, 2000), and adopts a similar layered structure, but relaxes a number of simplifying assumptions: the flowing layers are allowed to flow at distinct velocities, and the solid concentration in the sheet-flow layer is considered lower than its value in the static bed. The implications of this new set of phenomenological assumptions on the flow dynamics are now investigated.

Assuming equal velocities in the two layers imposes a movement of the sheet-flow layer that remains fully locked to that of the water layer. On the contrary, allowing $u_s \neq u_b$ means that one or more coupling mechanisms are required to drive the sheet-flow layer. The first is the pressure thrust due to the surface gradient, acting both on the water and on the grains. This was essentially the sole coupling mechanism present in the simplified immiscible two-layer model discussed in Chapter 3. The second is due to the frictional shear stresses at the interface between the clear water and sheet-flow layer. Those two mechanisms are independent of the relation between c_s and c_b. Below it is demonstrated that a third important coupling mechanism derives precisely from the effect of granular dilatancy.

Accounting for granular dilatancy by allowing $c_s \neq c_b$ has several implications. Beyond its pure volumetric effect (layer thickening) identified in Section 2.1.3., dilatancy may affect the dynamics of the flow in several ways, enumerated here and discussed more in details below: 1) pore pressure relaxation effects; 2) suspension; 3) capillary effects; 4) vertical mass and momentum exchanges between the layers.

Pore pressure relaxation effects result from the non-immediate adaptation of the solid concentration from c_b to c_s. For bed material to be entrained, the grains have to expand in the vertical direction. To counterbalance the movement of the grains, the expansion requires a flux of water relative to the grains. This flux is hindered by the finite permeability of the bed. Capart (2004) showed that permeability thus act as a delaying mechanism for erosion by increasing the resisting effective stress on the grains. In the present context, only bed material with a large permeability combined with relatively small sheet-flow layer thickness is considered, and thus this effect is assumed negligible.

A significant dilatation of the granular material may result in much lower rates of inter-particle contacts and collisions within the upper portion of the transport layer. As a result, the mode of transport of the grains changes, and suspension may occur. Suspension is governed by different mechanisms such as turbulent friction, that are not accounted for in the description. While it may not be intractable to incorporate in the description of the upper clear water layer a concentration in suspended particles with some adequate closure relation for the estimation of the suspended discharge, suspension was almost not noticed in the present dam-break experiments. For the coarse material that was investigated, the threshold for suspension was not attained. This phenomenon is thus not considered.

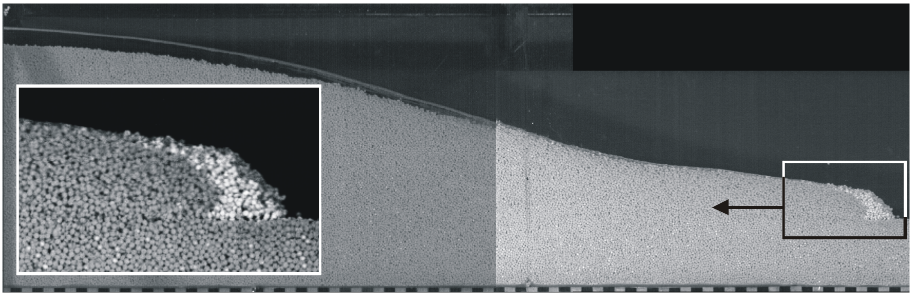

Figure 4.7. de-saturated wavefront on a flow snapshot at $t = 0.6$ s for the PVC experiment involving an upstream reservoir nearly filled with sediments (configuration of Fig. 2.8e). The dry region at the wave forefront appears much brighter on the image (rectangular inset).

As a result of dilatation, the thickness of the sheet-flow layer may grow substantially and at a point almost fill the entire flow depth. What happens next appears to be strongly influenced by capillary effects. A further thickening or dilatation of the sheet-flow layer would tend to de-saturate the upper grains. Indeed, a peculiar dam-break experiment, carried out with an upstream reservoir initially almost entirely filled with sediments, was seen to temporarily create a dry wavefront as a result of granular dilatancy combined with a very intense transport rate. An illustration of this wavefront is shown in Fig. 4.7, where the de-saturated wavefront appears much brighter than the saturated wave. But in order to emerge the grains, the forces tending to further increase the sheet-flow thickness should first overcome the surface tension at the free surface. At the scale of laboratory experiments, in which the height of capillary rise in the granular material may be of the same order of magnitude as the height of the dam-break wavefront, such an effect is not negligible. To account adequately for capillary effects may appear as a tricky complication. However, it might have only the limited role of preventing de-saturation of the granular medium at the wavefront. Indeed, except for the very peculiar case of Fig. 4.7, real de-saturation of the wavefront was not observed. Though, in many cases the wavefront was entirely filled with moving grains, and the precise observation of the water surface suggested small menisci surrounding grains at the point of emerging. In the next section a simple physical framework is proposed to account for this limited effect of capillarity.

The last implication of granular dilatancy represent the key novel feature of the description. It consists in the mass and momentum exchanges induced between the two flowing layers. When erosion takes place, the mobilised bed material undergoes a transition from solid-like to fluid-like behaviour. At the same time, in order to integrate the sheet-flow layer, the fluidised granular material dilates from a volume concentration c_b to c_s. By virtue of simple volume conservation, this requires a supply of water to counterbalance the increase in pore volumes. This volume of water will be supplied by the above clear water layer, and it is assumed that this transfer takes place instantaneously, which amounts to assume an infinite permeability of the sheet-flow layer. The opposite takes place in case of deposition. The deposited granular material leaves a surplus of water in the sheet-flow layer, which is transferred back into the clear water layer. The implications of these mass transfers of water are made clear when the associated momentum transfers are considered. Since the layer velocities are not equal, the transferred water endowed with the velocity of its initial layer ends up in a layer with a different velocity, and the momentum of the layers should be modified accordingly.

Globally, since in general larger water velocities than sheet-flow velocities may be expected, the water exchanges at $\Gamma^{(s)}$ will tend to accelerate the sheet-flow layer in case of erosion (to see whether this will actually happen so, however, exchanges at the bed interface $\Gamma^{(s)}$ should also be considered), and in any way to decelerate the clear water layer in case of deposition. Doing so, they act precisely so as to restore some coupling mechanism between the two layers. As will be shown in Section 7 this allows the emergence and driving of a sheet-flow layer even in the absence of frictional shear stresses, an argument that is not met when $c_s = c_b$ is assumed. This will constitute an important pre-requisite when trying to prove the existence of self-similar exact solutions of the resulting governing equations.

3. Extended shallow flow description

A two-layer shallow-water model is to be developed, that is based on the layered vertical flow structure described previously. For the sake of simplicity but without loss of generality, governing equations for the conservation of mass and longitudinal momentum are derived by considering "transient uniform" flow conditions and a horizontal bed (Capart, 2004). Such idealised conditions may for example be pictured by considering an infinitely long channel, with uniform flow conditions such that the flow variables h_w, h_s, u_w, u_s are everywhere equal. Even in this situation, the flow might not be in equilibrium with the bed, so that erosion or deposition may result (consider e.g. a fast pure-water flow on a easily erodible sediment bed). Given that flow variables are everywhere identical, this geomorphic evolution will process at exactly the same rate at all sections along the channel. After a small time step, a new flow situation is attained, distinct from the previous one due to vertical interaction between the bed and flowing layers, but still constituting a uniform flow in the sense that flow variables are equal all along the channel. The flow thus evolves as a succession of uniform states.

Such "transient uniform" flow conditions may appear tricky and artificial. However, they allow to derive the vertical flow structure associated with erosion and deposition more clearly. Doing so, the terms associated with the spatial gradients of the flow variables are suppressed, and the focus is set on the terms related to the vertical exchanges discussed in the previous section. Then, the terms of the horizontal flow structure, described by the model of Chapter 3, and the bed slope terms, are re-incorporated to form a complete description.

3.1. Unsteady uniform flow with interfacial transfer

The physical laws for conservation of mass and longitudinal momentum are now applied to the physical system shown in Fig. 4.8. Transient uniform flow is assumed throughout the flow depth, so that net changes of mass and momentum result only from vertical exchanges between the layers, through frictional and geomorphic interactions.

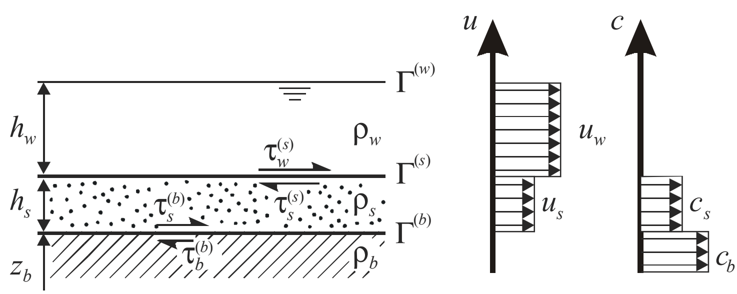

Figure 4.8. Sketch of vertical flow structure for pseudo-uniform conditions.

A procedure similar to the one described by Fraccarollo and Capart (2002) is followed by applying Reynolds transport theorem to the balance of mass and horizontal momentum on an arbitrary control volume Ω. In the present context, as opposed to their derivation, the exchanges occur across layers of distinct densities, and thus conservation of mass further needs to be distinguished from conservation of volume. The three equations write:

$$\frac{\partial}{\partial t}\int_{\Omega} \mathrm{d}\Omega + \int_{\Gamma} (\mathbf{u}-\mathbf{v})\cdot\mathbf{n}\,\mathrm{d}\Gamma = 0 \tag{4.1}$$

$$\frac{\partial}{\partial t}\int_{\Omega} \rho\,\mathrm{d}\Omega + \int_{\Gamma} \rho(\mathbf{u}-\mathbf{v})\cdot\mathbf{n}\,\mathrm{d}\Gamma = 0 \tag{4.2}$$

$$\frac{\partial}{\partial t}\int_{\Omega} \rho\mathbf{u}_x\,\mathrm{d}\Omega + \int_{\Gamma} \rho\mathbf{u}_x((\mathbf{u}-\mathbf{v})\cdot\mathbf{n})\mathrm{d}\Gamma = \int_{\Omega} \rho\,\mathbf{g}_x\,\mathrm{d}\Omega + \int_{\Gamma} [\boldsymbol{\sigma}\cdot\mathbf{n}]_x\,\mathrm{d}\Gamma \tag{4.3}$$

where ρ = mass density, $\mathbf{u}$ = material velocity, $\mathbf{v}$ = celerity of non-material boundary Γ, $\mathbf{n}$ = outward unit normal to Γ, $\boldsymbol{\sigma}$ = stress tensor and $\mathbf{g}$ = oriented acceleration of gravity. Equations (4.1) and (4.2) are scalar equations. Equation (4.3) is normally a vector equation, but only its horizontal component is here considered, governing the evolution of horizontal flow momentum.

The volume flux density e, the mass flux density i, and the horizontal momentum flux density j across control surface Γ are defined as

$$e = (\mathbf{u}-\mathbf{v})\cdot\mathbf{n} \tag{4.4}$$

$$i = \rho(\mathbf{u}-\mathbf{v})\cdot\mathbf{n} \tag{4.5}$$

$$j = \rho\mathbf{u}_x((\mathbf{u}-\mathbf{v})\cdot\mathbf{n}) - [\boldsymbol{\sigma}\cdot\mathbf{n}]_x \tag{4.6}$$

The integral equations (4.1), (4.2), and (4.3) are applied successively from top to bottom over the rectangular control volumes corresponding to the water layer of depth h_w, the sheet-flow layer of depth h_s and the static bed at level $z^{(b)}$. Given that uniform flow is assumed, the fluxes across the left and right vertical boundaries of the control volumes balance exactly, and integration over Γ resumes to the integration over the layer interfaces $\Gamma^{(w)}, \Gamma^{(s)}$ and $\Gamma^{(b)}$. Since the interfaces are horizontal, the acceleration of gravity has no component in the direction of longitudinal momentum and the first term on the right-hand side of (4.3) is zero.

The following equations are thus obtained for the continuity of clear-water layer, sheet-flow layer, and bed material (in terms of volume and mass, respectively), and for the momentum of water layer and sheet-flow layer:

$$\frac{\partial h_w}{\partial t} = -e^{(w)} + e^{(s)} \tag{4.7}$$

$$\frac{\partial h_s}{\partial t} = -e^{(s)} + e^{(b)} \tag{4.8}$$

$$\frac{\partial z^{(b)}}{\partial t} = -e^{(b)} \tag{4.9}$$

$$\frac{\partial}{\partial t}(\rho_w h_w) = -i^{(w)} + i^{(s)} \tag{4.10}$$

$$\frac{\partial}{\partial t}(\rho_s h_s) = -i^{(s)} + i^{(b)} \tag{4.11}$$

$$\frac{\partial}{\partial t}\left(\rho_b z^{(b)}\right) = -i^{(b)} \tag{4.12}$$

$$\frac{\partial}{\partial t}(\rho_w h_w u_w) = -j^{(w)} + j^{(s)} \tag{4.13}$$

$$\frac{\partial}{\partial t}(\rho_s h_s u_s) = -j^{(s)} + j^{(b)} \tag{4.14}$$

in which subscripts *w*, *s* and *b* stand for layer variables, while the superscripts (*w*), (*s*) and (*b*) refer to interface variables. *e*, *i* and *j* with superscripts denote the volume, mass and horizontal momentum flux densities across the discontinuous layer interfaces $\Gamma^{(w)}, \Gamma^{(s)}$ and $\Gamma^{(b)}$. They are considered positive when oriented downwards. The layer densities are

$\rho_s = c_s\,\rho_M + (1-c_s)\,\rho_w$ and $\rho_b = c_b\,\rho_M + (1-c_b)\,\rho_w$, with ρ_M being the specific density of the granular particles.

Interface $\Gamma^{(w)}$ is a "no-flux" boundary, so that $e^{(w)} = i^{(w)} = j^{(w)} = 0$. Summation of equations (3.1), (4.8) and (4.9) implies that $\partial z^{(w)}/\partial t = 0$, or in other words that the level of the water surface $z^{(w)}$ is not affected by vertical exchanges occurring at internal interfaces $\Gamma^{(s)}$ and $\Gamma^{(b)}$. Combining (3.1) with (4.10) and (4.9) with (4.12) gives relations between volume and mass fluxes

$$i^{(s)} = \rho_w e^{(s)} \quad \text{and} \quad i^{(b)} = \rho_b e^{(b)}$$

so that (4.8) and (4.11) together yield a compatibility constraint between the movement of interfaces $\Gamma^{(s)}$ and $\Gamma^{(b)}$:

$$e^{(s)} = -\frac{\rho_b - \rho_s}{\rho_s - \rho_w} e^{(b)} \tag{4.15}$$

The movement of interface $\Gamma^{(s)}$ is not free. It is tied to the evolution of the bed interface $\Gamma^{(b)}$ so as to preserve constant densities of the flow layers. Also observed from (4.15) is that $e^{(b)}$ and $e^{(s)}$ always have opposite signs. A downward movement of $\Gamma^{(b)}$, associated with mobilisation of bed sediments through erosion, requires a dilatation of the eroded material, initially at a density ρ_b, to reach the sheet-flow density ρ_s. An upward movement of $\Gamma^{(s)}$ results, aimed at transferring just the required amount of water to fill the increase of pore volumes created by the dilatation.

To ensure that the description is consistent, one must still guarantee that volume, mass and horizontal momentum is conserved across the discontinuities $\Gamma^{(w)}, \Gamma^{(s)}$ and $\Gamma^{(b)}$. This leads additional relations known as jump conditions (Chapman, 2000). They state that the flux densities i and j experienced on both sides of the discontinuous interfaces are to be identical.

Using (4.5) and (4.4), equalling mass flux densities $i_s^{(b)}$ and $i_b^{(b)}$ on both sides of the bed interface $\Gamma^{(b)}$ requires

$$\rho_s\left(u_{sn}+e^{(b)}\right)=\rho_b\left(u_{bn}+e^{(b)}\right)$$

where u with subscript n denote the vertical component of layer velocity, i.e. in the direction orthogonal to the interface. They are assumed positive when oriented upwards. As the bed is immobile, $\mathbf{u}_b=0$ and thus also $u_{bn}=u_b=0$. The vertical velocity of material within the transport layer is obtained:

$$u_{sn}=\frac{\rho_b-\rho_s}{\rho_s}e^{(b)} \tag{4.16}$$

This vertical layer velocity does not correspond either to the vertical movements of the grains dilating along the vertical, or to the vertical celerity of the water moving in the opposite direction to counterbalance the dilatation, but constitutes an average material velocity which derives simply from a mass conservation argument between layers of distinct but homogeneous densities.

At interface $\Gamma^{(s)}$, the relation reads

$$\rho_s\left(u_{sn}+e^{(s)}\right)=\rho_w\left(u_{wn}+e^{(s)}\right)$$

Since the water surface $\Gamma^{(w)}$ is invariant under uniform conditions ($dz^{(w)}/dt=\partial z^{(w)}/\partial t=0$), the vertical velocity in the water layer is zero, $u_{wn}=0$, and

$$u_{sn}=-\frac{\rho_s-\rho_w}{\rho_s}e^{(s)} \tag{4.17}$$

which is consistent with (4.16) and (4.15), but is redundant and does not bring additional information.

A similar development is performed for the momentum flux densities (4.6). At interface $\Gamma^{(b)}$, equalling $j_s^{(b)}$ and $j_b^{(b)}$ yields

$$\rho_s u_s \left(u_{sn} + e^{(b)}\right) - \tau_s^{(b)} = \rho_b u_b \left(u_{bn} + e^{(b)}\right) - \tau_b^{(b)}$$

Again, $u_b = u_{bn} = 0$ and, using (4.16), the relation reduces to

$$e^{(b)} = \frac{1}{\rho_b\, u_s}\left(\tau_s^{(b)} - \tau_b^{(b)}\right) \tag{4.18}$$

This constitutes a Rankine-Hugoniot type argument that preserves the conservation of longitudinal momentum across the bed discontinuity. It is similar to the interface relation obtained by Fraccarollo and Capart (2002), and expresses the erosion/deposition rate $e^{(b)}$ as a function of the velocity jump u_s across the bed interface, and of the difference between the shear stresses on both sides: the entraining shear stress $\tau_s^{(b)}$ in the fluid-like sheet-flow layer Ω_s and the resistive shear stress $\tau_b^{(b)}$ in the solid-like bed.

In the same way, the momentum flux density across interface $\Gamma^{(s)}$ should also be single-valued. Compatibility between lower estimate $j_s^{(s)}$ and upper estimate $j_w^{(s)}$ requires that

$$\rho_s u_s \left(u_{sn} + e^{(s)}\right) - \tau_s^{(s)} = \rho_w u_w \left(u_{wn} + e^{(s)}\right) - \tau_w^{(s)}$$

Using (4.17) and given that $u_{wn} = 0$, another interface relation is obtained, relating the vertical movement of interface $\Gamma^{(s)}$ to a difference in shear stresses:

$$e^{(s)} = \frac{1}{\rho_w\left(u_w - u_s\right)}\left(\tau_w^{(s)} - \tau_s^{(s)}\right) \tag{4.19}$$

Note the similarity between (4.18) and (4.19). In the latter case, the velocity jump experienced across the interface is $u_w - u_s$.

Summarising the above developments, the set of governing equations for the conservation of mass and momentum may be obtained by expanding the fluxes on the right-hand sides of (3.1)- (4.9) and (4.13)-(4.14). Recall that, $\Gamma^{(w)}$ being a no-flux interface, $e^{(w)} = j^{(w)} = 0$. Given that interface relations (4.18) and (4.19) ensure that the fluxes $j = \rho u e - \sigma \cdot \mathbf{n}$ at each interface $\Gamma^{(s)}$ and $\Gamma^{(b)}$ are single-valued, they may be equally evaluated based on variables on both sides, i.e.,

$$j^{(s)} = \begin{cases} \rho_w u_w e^{(s)} - \tau_w^{(s)} \\ \rho_w u_s e^{(s)} - \tau_s^{(s)} \end{cases}$$
$$j^{(b)} = \begin{cases} \rho_b u_b e^{(b)} - \tau_b^{(b)} = -\tau_b^{(b)} \\ \rho_b u_s e^{(b)} - \tau_s^{(b)} \end{cases} \tag{4.20}$$

Using (4.20), the complete set of governing equations may be written as:

$$\frac{\partial h_w}{\partial t} = e^{(s)} \tag{4.21}$$

$$\frac{\partial h_s}{\partial t} = e^{(b)} - e^{(s)} \tag{4.22}$$

$$\frac{\partial z^{(b)}}{\partial t} = -e^{(b)} \tag{4.23}$$

$$\frac{\partial \left(h_w u_w\right)}{\partial t} = u_w e^{(s)} - \frac{\tau_w^{(s)}}{\rho_w} \tag{4.24}$$

$$\frac{\partial \left(h_s u_s\right)}{\partial t} = -\frac{\rho_w}{\rho_s} u_w e^{(s)} + \frac{\tau_w^{(s)}}{\rho_s} - \frac{\tau_b^{(b)}}{\rho_s} \tag{4.25}$$

complemented by interface relations (4.18) and (4.19). The above system is written based on the first estimates of j in (4.20), i.e. in terms of $\tau_w^{(s)}$ and $\tau_b^{(b)}$, but an alternate formulation could be written based on the second estimates. The two formulations are mathematically strictly equivalent. However, when designing a computational strategy to solve the system in distinct successive steps, in Section 4, one formulation will lead to a natural partition of numerical operators for the case of erosion ($e^{(b)} > 0$), and the other for the case of deposition ($e^{(b)} < 0$). More details will be given in Section 4.

3.2. Shear and normal stresses functions

Closure of the system (4.21)-(4.25) still requires to specify constitutive equations for the shear stresses at interfaces $\Gamma^{(s)}$ and $\Gamma^{(b)}$. Four distinct shear stresses were introduced: two of them, $\tau_b^{(b)}$ and $\tau_s^{(b)}$, govern the evolution of the bed interface as dictated by the shock relation (4.18). The other two, $\tau_s^{(s)}$ and $\tau_w^{(s)}$, are related through the shock relation (4.19). But interfaces $\Gamma^{(b)}$ and $\Gamma^{(s)}$ do not evolve freely and independently. Their respective displacements $e^{(b)}$ and $e^{(s)}$ are constrained by (4.15). One may see the water exchanges produced by the displacement of $\Gamma^{(s)}$ as an immediate response to bed evolution, counterbalancing the apparent change of density that would otherwise result from dilatation/contraction of the bed material in case of erosion/deposition. As a consequence, one needs to specify closure relations for three of the four shear stresses only. The fourth shear stress may be derived from (4.15), (4.18) and (4.19).

For shear stresses in the fluid region at the top face of both interfaces, $\tau_s^{(b)}$ and $\tau_w^{(s)}$, constitutive laws similar to those postulated by Fraccarollo and Capart (2002) are adopted, extended to the case of different layer densities and velocities. These are Chezy-type relations expressing that the shear stresses have a quadratic dependence on the velocity slip at the interface:

$$\tau_s^{(b)} = C^{(b)}\, \rho_s\, u_s^2 \,\mathrm{sgn}(u_s) \tag{4.26}$$

$$\tau_w^{(s)} = C^{(s)}\, \rho_w\, (u_w - u_s)^2 \,\mathrm{sgn}(u_w - u_s) \tag{4.27}$$

where $C^{(b)}$ and $C^{(s)}$ are dimensionless friction coefficients.

At the bed, interface $\Gamma^{(b)}$ constitutes a "phase change" discontinuity, across which the bed material undergoes a transition between solid-like and fluid-like behaviour (Capart, 2000). Viewed from below, the interface constitutes a shear surface. Along such a failure plane, the shear stress $\tau_b^{(b)}$ may be related to Terzaghi's effective normal stress $\sigma'^{(b)}$ through the Coulomb law, describing the stress state at failure for a rigid granular assembly:

$$\tau_b^{(b)} = \left(\tau_{bc} + \sigma'^{(b)} \tan\varphi\right) \mathrm{sgn}(u_s) \tag{4.28}$$

where τ_{bc} is a critical yield stress, $\tan\varphi$ is the friction angle, and $\mathrm{sgn}(u_s)$ must be introduced to ensure that $\tau_b^{(b)}$ is always a resistive stress, oriented against the sheet-flow.

By virtue of conservation, the total stress $\sigma_b^{(b)}$ in the bed just beneath the interface, in a direction normal to it, is equal to the pressure exerted on the bed by the flow, hence $\sigma_b^{(b)} = \sigma_s^{(b)} = \sigma^{(b)}$. The latter pressure was assumed hydrostatic, so that

$$\sigma^{(b)} = \rho_w\, g\, h_w + \rho_s\, g\, h_s \tag{4.29}$$

In extracting the effective stress taken over by the grains $\sigma'^{(b)}$, one must first evaluate the pore water pressure $p_w^{(b)}$. In case of a substantial thickness of the pure water layer overlying it, the transport layer is completely submerged, and under the hydrostatic assumption the pore water pressure at the bed is essentially $p_w^{(b)} = \rho_w\, g\left(h_w + h_s\right)$. When the thickness of the transport layer h_s increases, however, it may come to the point that its upper boundary almost reaches the water surface. This was seen in Section 2 to occur in the region close to the wavefront for the granular dam-break experiments under study. Further increase of the transport layer would lead to partial de-saturation of some grains and create a dry plug of granular material overlying the flow. Analogue features are indeed observed in nature at mountainous debris-flow snouts. Yet for de-saturation to actually take place, the growing transport layer must first overcome the capillary pressure. When the thickness of the water layer decreases below the height of capillary rise, the water pressure at the free surface will start to turn negative. The deficit is transferred to the grains, who will bear a greater portion of the total stress. The resulting increase of the effective normal stress $\sigma'^{(b)}$ at the bed, will act as a slow-down mechanism for further erosion, through a substantial increase of the resistive shear stress $\tau_b^{(b)}$.

In order to investigate the relative importance of capillary action at the wavefront, a typical case is considered, representative of the experiments with PVC pellets presented in Chapter 2. Raw estimations of the height of capillary rise for that material within static assemblies were obtained by means of a “tulip” test, leading values ranging between 5 and 15 mm. Slightly lower values are expected for the more dilute dispersions within the sheet-flow layer. Given the specific density of PVC $\rho_M = 1560$ kg/m³, and assuming an upper bound for the solid concentration in the transport layer near the front $c_s = 0.5$, the bulk density of the layer is $\rho_s = 1560 \cdot 0.5 + 1000 \cdot 0.5 = 1280$ kg/m³. For a typical height of the saturated wavefront $h_s = 20$ mm, the effective stress at the bed, without accounting for the capillary supplement, is $\sigma'^{(b)} = \left(\rho_s - \rho_w\right) g\, h_s \approx 55\ \mathrm{N}$.

This corresponds to about 5 mm of water pressure, which is the same order of magnitude as the capillary rise. This confirms that accounting for capillary effects while estimating the effective normal stress at the bed is not something odd and marginal, but that it may significantly affect the erosive power of dense liquid-granular flows at laboratory scales. For the same material, capillarity was found as an important parameter for determining effective granular stresses in steady uniform debris flows involving a partially emerged plug of desaturated grains (Armanini et al., 2005).

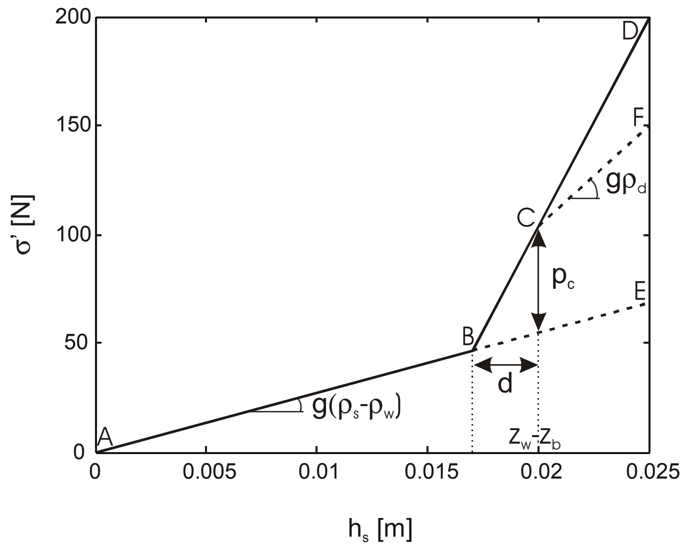

Figure 4.9. Effect of capillarity on effective granular stress experienced at the bed.

The capillary effects are accounted through a modified model for the evaluation of $\sigma'^{(b)}$. Figure 4.9 illustrates the concept by plotting $\sigma'^{(b)}$ as a function of the thickness of the transport layer, for a constant water level $z^{(w)}$ and bed level $z^{(b)}$. Numerical values are taken from the above example, with a grain diameter d = 3 mm and capillary rise p_c = 5 mm. For low values of h_s (indicated by segment A-B on Fig. 4.9), capillarity does not intervene and $\sigma'^{(b)} = (\rho_s - \rho_w) g\, h_s$. When the thickness of the pure water layer vanishes, at $h_s = z^{(w)} - z^{(b)}$, capillarity has fully developed and the effective stress is supplemented by capillary pressure p_c (point C on Fig. 4.9). In fact, the mobilisation of capillary pressure is not instantaneous. It is assumed that a gradual transition takes place over a height of one grain diameter *d*, indicated by the segment B-C on Fig. 4.9. For higher values of h_s, desaturation occurs and the supplement in effective stress corresponds to the weight of the dry grains $\Delta\sigma'^{(b)} = \rho_d\, g\, \Delta h_s$, with ρ_d being the density of the desaturated granular layer (segment C-F on Fig. 4.9). While it may be possible to account explicitly for the possible emergence of such a desaturated layer, it was not considered in the present two-layer model introduced above. Instead, an extension of segment B-C is considered for higher values of h_s (segment B-C-D on Fig. 4.9). Accordingly, a general expression for $\sigma'^{(b)}$ may thus be written as follows:

$$\sigma'^{(b)} = (\rho_s - \rho_w) g\, h_s + \max(d - h_w, 0)\, \rho_w g\, h_c / d \tag{4.30}$$

This consists in presuming that the effect of capillarity will always be sufficient to prevent desaturation to occur at any time. Even if it might not extend straightforwardly to real scales and natural material, the scale and granular material of the experiments currently under study tend to confirm this simplification. The assumption will be verified *a posteriori* in the simulations carried out in the next sections, by verifying that $h_w > 0$ even near the wavefront.

3.3. Dissipation of mechanical energy

Equations (4.21)-(4.25) have been obtained by imposing conservation of mass and balance of longitudinal momentum in a two-layer system constrained by the vertical structure introduced in Section 2. In order to guarantee a physical behaviour, the system should also obey an essential principle: the dissipation of mechanical energy. It imposes that the mechanisms governing the flow may only act so as to preserve or dissipate energy. A mechanism that would lead to an increase of the flow energy would violate the second law of thermodynamics, and should be proscribed. In the absence of non-conservative external forces acting on the system, the constraint for dissipation of mechanical energy is the following:

$$\frac{d}{dt}\left(T+U\right)\leq 0 \tag{4.31}$$

where T is the kinetic energy and U the potential energy. Below this constraint is applied to the system described by(4.21)-(4.25), by extending a reasoning initially proposed by Capart (2004) for a simpler set of equations. The derivation is somewhat tedious, but the results will prove especially useful when designing well-posed algorithms as will be shown in Section 4.1.

The kinetic energy, per unit surface in the horizontal plane, is

$$T = \int_0^{z^{(w)}} \tfrac{1}{2} m(z)\, u^2(z)\, dz = \tfrac{1}{2}\rho_w h_w u_w^2 + \tfrac{1}{2}\rho_s h_s u_s^2 \tag{4.32}$$

The potential energy, again per unit surface in the horizontal plane, is defined relative to a reference level $z = 0 < z^{(b)}$:

$$\begin{aligned} U &= \int_0^{z^{(w)}} m(z)\, g\, z\, dz = \left[\tfrac{1}{2}\rho_b g\, z^2\right]_0^{z^{(b)}} + \left[\tfrac{1}{2}\rho_s g\, z^2\right]_{z^{(b)}}^{z^{(s)}} + \left[\tfrac{1}{2}\rho_w g\, z^2\right]_{z^{(s)}}^{z^{(w)}} \\ &= \tfrac{1}{2}\rho_b g\, z^{(b)2} + \left(\rho_w g\, h_w + \rho_s g\, h_s\right) z^{(b)} + \tfrac{1}{2}\rho_s g\, h_s^2 + \rho_w g\, h_w h_s + \tfrac{1}{2}\rho_w g\, h_w^2 \end{aligned} \tag{4.33}$$

The derivative of mechanical energy may be written as a function of the derivatives of the primary variables $h_w, h_s, z^{(b)}, h_w u_w, h_s u_s$:

$$\begin{aligned}\frac{d}{dt}\left(T+U\right) &= \rho_w u_w \frac{d(h_w u_w)}{dt} + \rho_s u_s \frac{d(h_s u_s)}{dt} \\ &+ \rho_w\left(g\,h_w - \tfrac{1}{2}u_w^2 + g\,h_s + g\,z^{(b)}\right)\frac{dh_w}{dt} \\ &+ \rho_s\left(g\,h_s - \tfrac{1}{2}u_s^2 + \rho_w/\rho_s\; g\,h_w + g\,z^{(b)}\right)\frac{dh_s}{dt} \\ &+ \left(\rho_w g\,h_w + \rho_s g\,h_s + \rho_b g\,z^{(b)}\right)\frac{dz^{(b)}}{dt}\end{aligned} \tag{4.34}$$

This is a linear combination of the right-hand sides of equations (4.21)-(4.25). These may thus be replaced in (4.34) by the corresponding left-hand sides, and one obtains a relation without spatial derivatives in the right-hand side, but function of the parameters governing the evolution of the system: interface velocities $e^{(b)}$ and $e^{(s)}$ and shear stresses $\tau_w^{(s)}$ and $\tau_b^{(b)}$. The relation may then be further worked out. Invoking interface relations (4.15), (4.18) and (4.19), and after some laborious work, a surprisingly simple criterion is obtained for the dissipation of energy:

$$\frac{d}{dt}\left(T+U\right) = -\tfrac{1}{2}\left(\tau_s^{(b)}+\tau_b^{(b)}\right)u_s - \tfrac{1}{2}\left(\tau_w^{(s)}+\tau_s^{(s)}\right)\left(u_w-u_s\right) + \left(\rho_b-\rho_s\right)g\,h_s e^{(b)} \le 0 \tag{4.35}$$

Three terms are identified. The first two terms indicate that the dissipation of energy is proportional to the arithmetic mean of the shear stresses on both sides of the discontinuous interfaces $\Gamma^{(b)}$ and $\Gamma^{(s)}$, multiplied by the jump in horizontal velocity across those interfaces, $u_s - u_b = u_s$ and $u_w - u_s$ respectively. To ensure that those terms are negative and correspond to energy dissipation in (4.35), it suffices that the corresponding shear stresses be defined positive in the direction opposite to the flow in the faster moving layer of the interface. This amounts to state that they should be resistive shear stresses, a quite natural consideration. The third term is more delicate, and deserves further attention. In case of deposition, $e^{(b)} < 0$ by definition, and the third term in (4.35) is always negative, and corresponds to energy dissipation. In case of erosion however, $e^{(b)} > 0$, and the term is always positive. It thus constitutes an apparent violation of the second law of thermodynamics, as a mechanism introducing additional energy in the system. In order to explain this apparently non-physical behaviour, it is first interesting to consider two special cases: if the more restrictive assumptions of Fraccarollo and Capart (2002) are retained, i.e. identical flow velocities $u_w = u_s = u_m$ and identical granular layer densities $\rho_s = \rho_b$, the second and third terms of (4.35) are zero, and the relation reduces to its first term, in accordance with the result previously obtained by Capart (2002):

$$\frac{d}{dt}(T+U) = -\tfrac{1}{2}\left(\tau_s^{(b)} + \tau_b^{(b)}\right)u_m \leq 0 \tag{4.36}$$

which is trivially verified. If then only the assumption on the velocities is relaxed by allowing $u_w \neq u_s$, the third term is still zero. Following (4.15), $e^{(s)} = 0$ and, invoking (4.19), the shear stresses at $\Gamma^{(s)}$ must thus be identical, $\tau_w^{(s)} = \tau_s^{(s)}$, so that the relation is

$$\frac{d}{dt}(T+U) = -\tfrac{1}{2}\left(\tau_s^{(b)} + \tau_b^{(b)}\right)u_s - \tau_w^{(s)}\left(u_w - u_s\right) \leq 0 \tag{4.37}$$

which is also trivially verified. In those two cases, the energy dissipation may be fully cast into functions of the shear stresses only, because the exchanges across interface $\Gamma^{(b)}$ occur between layers having the same density. The third term in (4.35) thus results from the relaxation of the assumption of identical granular layer densities. It comes as a result of the dilatation of the granular material associated with erosion, and founds a physical interpretation by invoking (4.15) to express it as a function of $e^{(s)}$:

$$\left(\rho_b - \rho_s\right) g\, h_s\, e^{(b)} = -\left(\rho_s - \rho_w\right) g\, h_s\, e^{(s)} \tag{4.38}$$

Since $e^{(s)} < 0$ in case of erosion, the apparent gain of mechanical energy thus follows from the raising of interface $\Gamma^{(s)}$, and is equal to the potential energy gained by the raising grains within the thin layer that undergoes a density change from ρ_w to ρ_s. Though, the second and third terms of (4.35) are intimately related through (4.19), and they both pertain to a single physical mechanism. The apparent gain (4.38), generated by distinct shear stresses on both sides of the interface, is largely counterbalanced by the dissipative work performed by the same shear stresses. All together, the dissipative constraint (4.35) was found to be verified in all the computations performed, as will be shown in the next sections.

3.4. Non-uniform shallow-flow theory

For sake of clarity and conciseness, the vertical structure of the flow, governed by the set of geomorphic equations (4.21)-(4.25), has been derived under the assumption of uniform flow, by which spatial gradient terms are all zero. In order to deal with non-uniform dam-break flows, one obviously needs to model the horizontal flow structure, introduce the spatial gradient terms on the left hand side of the equations, and collect the various terms into a complete formulation. Shallow water equations for an immiscible two-layer system with a density contrast have been derived in Chapter 3 by using Hamilton's principle of least action, and were discussed in light of the possible wave structures associated to two-fluid dam-break waves on horizontal beds.

The equations of continuity for the water layer and for the transport layer, along with the equations for the conservation of longitudinal momentum within the two layers, are:

$$\frac{\partial h_w}{\partial t}+\frac{\partial(h_w u_w)}{\partial x}=0 \tag{4.39}$$

$$\frac{\partial h_s}{\partial t}+\frac{\partial(h_s u_s)}{\partial x}=0 \tag{4.40}$$

$$\frac{\partial(h_w u_w)}{\partial t}+\frac{\partial}{\partial x}\left(h_w u_w^2+\frac{g h_w^2}{2}\right)+g h_w \frac{\partial\left(z^{(b)}+h_s\right)}{\partial x}=0 \tag{4.41}$$

$$\frac{\partial(h_s u_s)}{\partial t}+\frac{\partial}{\partial x}\left(h_s u_s^2+\frac{g h_s^2}{2}\right)+g h_s\left(\frac{\partial z^{(b)}}{\partial x}+\frac{\rho_w}{\rho_s}\frac{\partial h_w}{\partial x}\right)=0 \tag{4.42}$$

As compared to the equations derived in Chapter 3, an additional term has been introduced in each of the momentum equations to account for the non-horizontal profiles of the bed surface $z^{(b)}$. They extend straightforwardly from the classical term for a sloping bed in the single-layer shallow-water equations (see e.g. Soares Frazão, 2002). One notes that the momentum equations may not be written in full conservation form. Besides the usual term associated with bed slope $\partial z^{(b)}/\partial x$, non-conservative terms are associated with the pressure thrust acting on the sloping interface $\Gamma^{(s)}$, producing momentum exchanges between the two layers.

The complete set of unsteady non-uniform geomorphic equations are obtained by merging the set of equations (4.21)-(4.25), governing the vertical exchanges, with equations (4.39)-(4.42), governing the flow propagation in the longitudinal direction. In the end, one obtains:

$$\frac{\partial h_w}{\partial t} + \frac{\partial (h_w u_w)}{\partial x} = e^{(s)} \tag{4.43}$$

$$\frac{\partial h_s}{\partial t} + \frac{\partial (h_s u_s)}{\partial x} = e^{(b)} - e^{(s)} \tag{4.44}$$

$$\frac{\partial z^{(b)}}{\partial t} = -e^{(b)} \tag{4.45}$$

$$\frac{\partial (h_w u_w)}{\partial t} + \frac{\partial}{\partial x}\left(h_w u_w^2 + \frac{g h_w^2}{2} \right) + g h_w \frac{\partial \left(z^{(b)} + h_s \right)}{\partial x} = u_w e^{(s)} - \frac{\tau_w^{(s)}}{\rho_w} \tag{4.46}$$

$$\begin{aligned} &\frac{\partial (h_s u_s)}{\partial t} + \frac{\partial}{\partial x}\left(h_s u_s^2 + \frac{g h_s^2}{2} \right) + g h_s \left(\frac{\partial z^{(b)}}{\partial x} + \frac{\rho_w}{\rho_s} \frac{\partial h_w}{\partial x} \right) \\ &\qquad = -\frac{\rho_w}{\rho_s} u_w e^{(s)} + \frac{\tau_w^{(s)}}{\rho_s} - \frac{\tau_b^{(b)}}{\rho_s} \end{aligned} \tag{4.47}$$

complemented by morphodynamic interface relations:

$$e^{(b)} = \frac{1}{\rho_b \left| u_s \right|} \left(\tau_s^{(b)} - \tau_b^{(b)} \right) \tag{4.48}$$

$$e^{(s)} = -\frac{\rho_b - \rho_s}{\rho_s - \rho_w} e^{(b)} \tag{4.49}$$

and closure relations (4.26)-(4.28) for the shear stresses $\tau_s^{(b)}$, $\tau_w^{(s)}$ and $\tau_b^{(b)}$.

4. Computational scheme

The system (4.43)-(4.47) may be written in the compact vector form

$$\frac{\partial \mathbf{U}}{\partial t} + \mathbf{A}(\mathbf{U})\frac{\partial \mathbf{U}}{\partial x} = \mathbf{S}(\mathbf{U}) \tag{4.50}$$

with the vector of variables

$$\mathbf{U} = \begin{bmatrix} h_w \\ h_s \\ z^{(b)} \\ h_w u_w \\ h_s u_s \end{bmatrix}, \tag{4.51}$$

the coefficient matrix

$$\mathbf{A}(\mathbf{U}) = \begin{bmatrix} 0 & 0 & 0 & 1 & 0 \\ 0 & 0 & 0 & 0 & 1 \\ 0 & 0 & 0 & 0 & 0 \\ -u_w^2 + gh_w & gh_w & gh_w & 2u_w & 0 \\ gh_s \dfrac{\rho_w}{\rho_s} & -u_s^2 + gh_s & gh_s & 0 & 2u_s \end{bmatrix}, \tag{4.52}$$

and the vector of source terms

$$\mathbf{S}(\mathbf{U}) = \begin{bmatrix} e^{(s)} \\ e^{(b)} - e^{(s)} \\ -e^{(b)} \\ u_w e^{(s)} - \dfrac{\tau_w^{(s)}}{\rho_w} \\ -\dfrac{\rho_w}{\rho_s} u_w e^{(s)} + \dfrac{\tau_w^{(s)}}{\rho_s} - \dfrac{\tau_b^{(b)}}{\rho_s} \end{bmatrix}, \tag{4.53}$$

For solving system (4.50) an operator splitting methodology is adopted, and the integration is performed in two steps. The first considers the homogeneous system obtained when removing the source terms, i.e.

$$\frac{\partial \mathbf{U}}{\partial t}+\mathbf{A}(\mathbf{U})\frac{\partial \mathbf{U}}{\partial x}=0\,. \tag{4.54}$$

The integration procedure will closely reproduce the numerical scheme introduced in Chapter 3. The second step integrates the source terms vector by solving

$$\frac{\partial \mathbf{U}}{\partial t}=\mathbf{S}(\mathbf{U})\,. \tag{4.55}$$

It is more specific and should be performed with care. This is why the focus is first set below on the details of its treatment. In the subsequent section, a brief description is made on how the hyperbolic operator is dealt with, and how to the splitting of operators is handled when extending the scheme to second-order accuracy.

4.1. Source operators

4.1.1. Source operator splitting

The complete source operator $\mathbf{S}(\mathbf{U})$ may not be easily integrated in a single step. Instead, using once more a splitting approach, it may again be split in various components that are more easily integrated separately. When doing so however, one has to be extremely careful at keeping the computations stable, and at ensuring a physical sense to each of the individual operators. This will especially be the case for the highly transient erosional dam-break waves under study, because the source terms are computationally stiff and have a significant impact on the flow dynamics. In particular, the mechanisms included in the source vector $\mathbf{S}(\mathbf{U})$ may act only as mechanisms for the dissipation of mechanical energy contained within the system. One should thus ensure that energy is either preserved or dissipated by each of the operators.

The components of the source vector $\mathbf{S}(\mathbf{U})$ may be broadly divided in two categories: friction and geomorphic changes. Friction induces diffusive exchanges of momentum between the layers flowing at distinct velocities, but does not affect the depth of the layers. Geomorphic changes are associated with interfaces displacements $e^{(b)}$ and $e^{(s)}$, and provoke both mass and momentum transfers. One would thus like to split the source vector in two components:

$$\mathbf{S}(\mathbf{U}) = \mathbf{S}_{\mathbf{F}}(\mathbf{U}) + \mathbf{S}_{\mathbf{G}}(\mathbf{U}), \tag{4.56}$$

where $\mathbf{S}_{\mathbf{F}}(\mathbf{U})$ and $\mathbf{S}_{\mathbf{G}}(\mathbf{U})$ are frictional and geomorphic components, and then solve the two corresponding source operators in sequence. Doing so, the geomorphic operator will take over the transfers of mass across the interfaces, and the "convective" transfers of momentum. Convective transfers stand for the transfer of momentum that is directly connected to the transfer of mass (convective momentum transfer = mass transfer * velocity of the transferred mass). The frictional source operator will account for the diffusive transfers of momentum, occurring in the absence of mass transfers. It will further be divided in two components, $\mathbf{S}_{\mathbf{F}}(\mathbf{U}) = \mathbf{S}_{\mathbf{F}}^{(s)}(\mathbf{U}) + \mathbf{S}_{\mathbf{F}}^{(b)}(\mathbf{U})$, representative of friction at interfaces $\Gamma^{(s)}$ and $\Gamma^{(b)}$ respectively.

The division of momentum exchanges in "convective" and "diffusive" transfers should be made in such a way that energy dissipation is guaranteed for each operator taken separately. Therefore, one should distinguish between the cases of erosion ($e^{(b)} > 0$ implying $\tau_s^{(b)} > \tau_b^{(b)}$) and deposition

($e^{(b)} < 0$ implying $\tau_s^{(b)} < \tau_b^{(b)}$). The source vector $\mathbf{S}(\mathbf{U})$ should be written differently for the two cases:

$$\mathbf{S}(\mathbf{U}) = \begin{bmatrix} e^{(s)} \\ e^{(b)} - e^{(s)} \\ -e^{(b)} \\ u_w e^{(s)} - \dfrac{\tau_w^{(s)}}{\rho_w} \\ -\dfrac{\rho_w}{\rho_s} u_w e^{(s)} + \dfrac{\tau_w^{(s)}}{\rho_s} - \dfrac{\tau_b^{(b)}}{\rho_s} + 0 \end{bmatrix} \text{ in case of erosion, } (\tau_s^{(b)} \geq \tau_b^{(b)}) \tag{4.57}$$

$$\mathbf{S}(\mathbf{U}) = \begin{bmatrix} e^{(s)} \\ e^{(b)} - e^{(s)} \\ -e^{(b)} \\ u_s e^{(s)} - \dfrac{\tau_s^{(s)}}{\rho_w} \\ -\dfrac{\rho_w}{\rho_s} u_s e^{(s)} + \dfrac{\tau_s^{(s)}}{\rho_s} - \dfrac{\tau_s^{(b)}}{\rho_s} + \dfrac{\rho_b}{\rho_s} u_s e^{(b)} \end{bmatrix} \text{ in case of deposition, } (\tau_s^{(b)} < \tau_b^{(b)}) \tag{4.58}$$

Invoking interface relations (4.18) and (4.19), it may be checked that the above two expressions are in fact identical (see Section 3.1). However they form a convenient basis for the splitting of source operators into its various components $\mathbf{S_G}(\mathbf{U})$, $\mathbf{S_F^{(s)}}(\mathbf{U})$ and $\mathbf{S_F^{(b)}}(\mathbf{U})$, by explicitly partitioning the momentum transfers in convective and diffusive components. The various components of (4.57) and (4.58) found a natural physical interpretation. The first three elements are directly related to mass transfers. The fourth element represent the change of longitudinal momentum in the clear water layer, and has two terms: (1) the first term represents the convective transfer associated with mass transfer $e^{(s)}$; in case of erosion, the loss of momentum associated with water leaving the layer at velocity u_w; in case of deposition, the gain of momentum associated with water integrating the layer at velocity u_s; (2) the second term accounts for the diffusive transfer due to friction at the interface, and depends on $\tau_w^{(s)}$ or $\tau_s^{(s)}$ respectively to ensure compatibility of the full source vector with (4.53). Finally, the last elements of (4.57) and (4.58) are the change of momentum within the sheet-flow layer, as a result of convective and diffusive momentum transfers across the upper (first two terms) and lower (last two terms) interfaces. One notices that the mass exchange with the bed is not associated with any convective momentum transfer in the case of erosion. The bed velocity is indeed zero and the eroded material does not convey additional momentum in the sheet-flow layer. The overall distinction between the cases of erosion and deposition is illustrated in Fig. 4.10. Table 4.1 summarises the adopted splitting technique for the three elementary source operators.

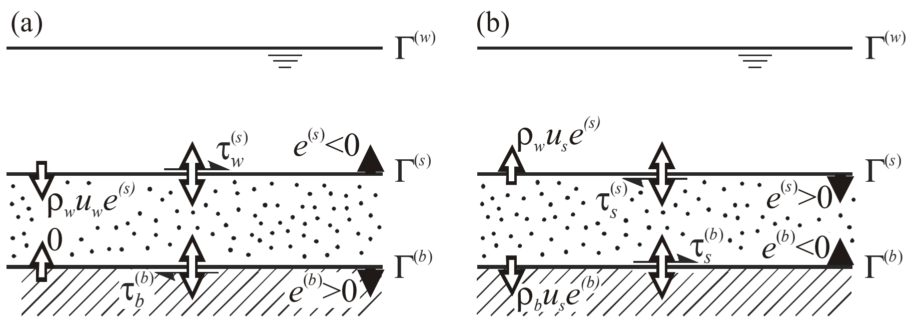

Figure 4.10. Mass and momentum transfers associated with the source terms. (a) erosion; (b) deposition. Black arrows: mass transfers; white single arrows: “convective” momentum transfers resulting from bed level changes and granular dilatancy; white double arrows: “diffusive” momentum transfers resulting from friction at the interfaces.

Table 4.1. Adequate partitioning of the geomorphic and frictional source operators for the case of erosion and deposition.

	Erosion: $\tau_s^{(b)} \geq \tau_b^{(b)}$, $e^{(b)} > 0$, $e^{(s)} < 0$	Deposition: $\tau_s^{(b)} < \tau_b^{(b)}$, $e^{(b)} < 0$, $e^{(s)} > 0$
Geomorphic operator $\mathbf{S_G}(\mathbf{U})$	$\mathbf{S_G}(\mathbf{U}) = \begin{bmatrix} e^{(s)} \\ e^{(b)} - e^{(s)} \\ -e^{(b)} \\ u_w e^{(s)} \\ -\dfrac{\rho_w}{\rho_s} u_w e^{(s)} \end{bmatrix}$	$\mathbf{S_G}(\mathbf{U}) = \begin{bmatrix} e^{(s)} \\ e^{(b)} - e^{(s)} \\ -e^{(b)} \\ u_s e^{(s)} \\ -\dfrac{\rho_w}{\rho_s} u_s e^{(s)} + \dfrac{\rho_b}{\rho_s} u_s e^{(b)} \end{bmatrix}$
Friction at $\Gamma^{(s)}$ $\mathbf{S_F^{(s)}}(\mathbf{U})$,	$\mathbf{S_F^{(s)}}(\mathbf{U}) = \begin{bmatrix} 0 \\ 0 \\ 0 \\ -\dfrac{\tau_w^{(s)}}{\rho_w} \\ +\dfrac{\tau_w^{(s)}}{\rho_s} \end{bmatrix}$	$\mathbf{S_F^{(s)}}(\mathbf{U}) = \begin{bmatrix} 0 \\ 0 \\ 0 \\ -\dfrac{\tau_s^{(s)}}{\rho_w} \\ +\dfrac{\tau_s^{(s)}}{\rho_s} \end{bmatrix}$
Friction at $\Gamma^{(b)}$ $\mathbf{S_F^{(b)}}(\mathbf{U})$	$\mathbf{S_F^{(b)}}(\mathbf{U}) = \begin{bmatrix} 0 \\ 0 \\ 0 \\ 0 \\ -\dfrac{\tau_b^{(b)}}{\rho_s} \end{bmatrix}$	$\mathbf{S_F^{(s)}}(\mathbf{U}) = \begin{bmatrix} 0 \\ 0 \\ 0 \\ 0 \\ -\dfrac{\tau_s^{(b)}}{\rho_s} \end{bmatrix}$

4.1.2. Integration procedure

Using the splitting methodology described above, it may be checked that each operator is associated with energy dissipation. The inspection of model behaviour carried out in Section 5.4 will present energy plots that show the fraction of energy dissipation generated by each operator.

The general integration procedure to solve $\partial \mathbf{U}/\partial t = \mathbf{S}(\mathbf{U})$ from $\mathbf{U}(t_i)$ to $\mathbf{U}(t_{i+1}) = \mathbf{U}(t_i + \Delta t)$ is to solve the individual source operators in sequence, with the following three steps:

$$\begin{aligned}\mathbf{U}^{(1)} &= \mathbf{U}(t_i) + \mathbf{S}_{\mathbf{F}}^{(s)}(\mathbf{U})\,\Delta t \\ \mathbf{U}^{(2)} &= \mathbf{U}^{(1)} + \mathbf{S}_{\mathbf{F}}^{(b)}(\mathbf{U})\Delta t \\ \mathbf{U}(t_{i+1}) &= \mathbf{U}^{(2)} + \mathbf{S}_{\mathbf{G}}(\mathbf{U})\,\Delta t\end{aligned} \tag{4.59}$$

For each operator, a robust method is to seek to obtain a number of homogeneous equations by appropriate combinations of the system of equations to be solved. This furnishes a number of invariants $\mathbf{W}$, i.e. combinations of variables that are not affected by that operator. These "source" invariants are invariants of the source system (4.55) only, and thus they are not invariants of the complete non-uniform system (4.50). For example, a first source invariant may yet be derived independently of the considered source operator. It is the water surface level, obtained by summing up the three first source equations:

$$\frac{\partial z^{(w)}}{\partial t} = \frac{\partial}{\partial t}\left(z^{(b)} + h_s + h_w\right) = -e^{(b)} + e^{(b)} - e^{(s)} + e^{(s)} = 0 \tag{4.60}$$

It is clear that the water surface level is not an invariant of the full system (4.50) and is likely to evolve with the flow. But (4.60) simply states that $z^{(w)}$, being an invariant of (4.55), is not affected by the source operators.

The other invariants are specific to the considered operator. By appropriate change of variables, the system of equations for each operator may be reduced to a principal scalar equation, function only of a single principal variable ω and of the operator invariants $\mathbf{W}$:

$$\frac{\partial \omega}{\partial t} = f(\omega, \mathbf{W}) \tag{4.61}$$

This principal equation is more easily integrated. Finally, when this scalar equation has been solved and the principal variable updated, the other updated primitive variables may be retrieved from the operator invariants and the updated principal variable.

For the integration of (4.61), implicit and explicit schemes offer two alternatives. An implicit backward Euler scheme would be preferable, because it is unconditionally stable whatever the time step of the computations. In this case, the right-hand side of (4.61) is to be evaluated at the new time step, and the discretised equation becomes:

$$\frac{\omega^{\Delta} - \omega}{\Delta t} = f\left(\omega^{\Delta}, \mathbf{W}\right) \tag{4.62}$$

where, here and in the following paragraphs, a superscript Δ denotes an updated variable. In the best cases, (4.62) yields a quadratic polynomial in ω^{Δ}. Depending on the particular expressions for the invariants $\mathbf{W}$, however, it may lead to a quartic polynomial that is more cumbersome to solve, requiring an iterative procedure and special care to ensure convergence to the sole physical root of the quartic polynomial.

On the contrary, an explicit forward Euler scheme is much more easy to implement and is computationally less expensive. It amounts to evaluating the right-hand side of (4.61) at the initial time of the computational step, resulting in the discretised equation

$$\frac{\omega^{\Delta} - \omega}{\Delta t} = f(\omega, \mathbf{W}) \tag{4.63}$$

which may be integrated in a straightforward manner.

To discriminate between explicit and implicit schemes, the two alternatives were implemented for the case where the capillary effect on $\tau_b^{(b)}$ is neglected. In fact no significant differences at all were observed for the present erosional dam-break wave simulations. This may be due to the highly transient character of the wave, and due to the small computational time steps that are imposed by the Courant-Friedrichs-Levy (CFL) condition on the flow propagation algorithm. An implicit version was found more delicate to implement when accounting for the capillary effect discussed in Section 3.2. Comforted by the above analysis, the simpler and faster explicit scheme was adopted, and consequently in (4.59) the operators $\mathbf{S}_{\mathbf{F}}^{(s)}(\mathbf{U})$, $\mathbf{S}_{\mathbf{F}}^{(b)}(\mathbf{U})$ and $\mathbf{S}_{\mathbf{G}}(\mathbf{U})$ are evaluated explicitly, at $\mathbf{U}(t_i)$, $\mathbf{U}^{(1)}$ and $\mathbf{U}^{(2)}$ respectively. When resorting to an explicit scheme, the derivation of operator invariants is not strictly required, as in fact the whole right-hand side of (4.63) is considered invariant. However, when discussing the integration procedure particularised to each operator in the next sub-sections, the invariants for each operator will be established. Their derivation is interesting in itself, and gives physical insights into the respective implications of the source operators on the flow dynamics. In addition, doing so, a possible future extension of the scheme to an implicit treatment will be facilitated.

4.1.3. Friction at $\Gamma^{(s)}$

The friction operator at $\Gamma^{(s)}$ is the only source operator for which no distinction should be made between erosion and deposition. Indeed, discussion in Section 3.2 shows that only one of the two shear stresses $\tau_w^{(s)}$ and $\tau_s^{(s)}$ may be given a constitutive relation, since the movement of interface $\Gamma^{(s)}$ is not governed by the difference in shear stresses, but rather by the movement of $\Gamma^{(b)}$ through (4.49). The two formulations of $\mathbf{S}_{\mathbf{F}}^{(s)}(\mathbf{U})$ in Table 4.1 are thus exactly equivalent. The system of equations to be solved is

$$\begin{gathered}\frac{\partial h_w}{\partial t}=0 \quad , \quad \frac{\partial h_s}{\partial t}=0 \quad , \quad \frac{\partial z^{(b)}}{\partial t}=0 \quad , \\ \frac{\partial (h_w u_w)}{\partial t}=\frac{-\tau_w^{(s)}}{\rho_w} \quad , \quad \frac{\partial (h_s u_s)}{\partial t}=\frac{\tau_w^{(s)}}{\rho_s}\end{gathered} \tag{4.64a-e}$$

Three invariants for this operator are directly obtained from the first three source equations: h_w, h_s and $z^{(b)}$. As one would expect, friction only alters the layer velocities. Summation of the last two equations (4.64d-e) multiplied by the respective layer densities yields

$$\frac{\partial}{\partial t}\left(\rho_w h_w u_w + \rho_s h_s u_s\right)=0 \tag{4.65}$$

Thus, the operator preserves the total flow momentum $\Pi=\rho_w h_w u_w+\rho_s h_s u_s$. The principal equation is obtained by dividing (4.64d) by h_w and (4.64e) by h_s, then subtracting the two to obtain an equation in the relative velocity of both layers:

$$\begin{aligned}\frac{\partial}{\partial t}\left(u_w-u_s\right)&=\frac{-\tau_w^{(s)}}{\rho_w}\,\frac{\rho_w/\rho_s\, h_w+h_s}{h_w h_s} \\ &=-C^{(s)}\left(u_w-u_s\right)^2\operatorname{sgn}\left(u_w-u_s\right)\frac{\rho_w/\rho_s\, h_w+h_s}{h_w h_s}\end{aligned} \tag{4.66}$$

Defining $u_r = u_w - u_s$ and integrating in the explicit Euler scheme yield the updated relative velocity u_r^Δ:

$$u_r^\Delta = u_r - \Delta t\, C^{(s)} u_r^2 \,\mathrm{sgn}(u_r) \frac{\rho_w/\rho_s\, h_w + h_s}{h_w h_s} \tag{4.67}$$

The updated layer velocities are then derived from the unchanged flow momentum, $\Pi^\Delta = \Pi$:

$$u_w^\Delta = \left(\frac{\Pi}{\rho_w} + \frac{\rho_s}{\rho_w} h_s u_r^\Delta \right) \Bigg/ \left(h_w + \frac{\rho_s}{\rho_w} h_s \right) \tag{4.68}$$

$$u_s^\Delta = u_w^\Delta - u_r^\Delta \tag{4.69}$$

Finally, two exceptions are considered for vanishing thickness of the layers. Firstly, when the depth of the sheet-flow layer is negligibly small (in practice, when $h_s < h_{\min}$, with $h_{\min}$ a predefined minimal depth, typically 10^{-6} times a characteristic depth of the flow), the layer velocities are not updated, $u_s^\Delta = u_s$ and $u_w^\Delta = u_w$. Secondly, when the depth of the clear-water layer is below that threshold ($h_w < h_{\min}$), the velocity of the clear-water layer is set equal to that of the sheet-flow layer, $u_w^\Delta = u_s$.

4.1.4. Friction at $\Gamma^{(b)}$

The set of equations to be solved is:

$$\frac{\partial h_w}{\partial t} = 0 \quad , \quad \frac{\partial h_s}{\partial t} = 0 \quad , \quad \frac{\partial z^{(b)}}{\partial t} = 0 \quad , \quad \frac{\partial (h_w u_w)}{\partial t} = 0$$

$$\begin{cases} \dfrac{\partial u_s}{\partial t} = -\dfrac{\tau_b^{(b)}}{\rho_s h_s} & \text{if} \quad \tau_s^{(b)} > \tau_b^{(b)} \qquad (\text{erosion}) \\ \dfrac{\partial u_s}{\partial t} = -\dfrac{\tau_s^{(b)}}{\rho_s h_s} & \text{if} \quad \tau_s^{(b)} < \tau_b^{(b)} \qquad (\text{deposition}) \end{cases} \tag{4.70}$$

The first four equations state four invariants: the bed level, the layer depths and clear-water layer velocity. For solving the remaining principal equation in u_s, one should distinguish between erosion and deposition. The updated sheet-flow layer velocity is

$$\begin{cases} u_s^{\Delta} = u_s - \Delta t \, \dfrac{\tau_b^{(b)}}{\rho_s h_s} & \text{if} \quad \tau_s^{(b)} > \tau_b^{(b)} \qquad (\text{erosion}) \\ u_s^{\Delta} = u_s - \Delta t \, \dfrac{\tau_s^{(b)}}{\rho_s h_s} & \text{if} \quad \tau_s^{(b)} < \tau_b^{(b)} \qquad (\text{deposition}) \end{cases} \tag{4.71}$$

where, in accordance to an explicit treatment, the shear stresses are evaluated using (4.28) and (4.26) based on the initial variables.

4.1.5. Erosional geomorphic exchanges

The cases of erosion and deposition are again treated separately. The set of equations to be solved in the case of erosion is:

$$\begin{aligned} &\frac{\partial h_w}{\partial t} = e^{(s)} \quad , \quad \frac{\partial h_s}{\partial t} = e^{(b)} - e^{(s)} \quad , \quad \frac{\partial z^{(b)}}{\partial t} = -e^{(b)} \\ &\frac{\partial (h_w u_w)}{\partial t} = u_w e^{(s)} \quad , \quad \frac{\partial (h_s u_s)}{\partial t} = -\frac{\rho_w}{\rho_s} u_w e^{(s)} \end{aligned} \tag{4.72a-e}$$

Subtracting u_w times (4.72a) from (4.72d) yields

$$h_w \frac{\partial (u_w)}{\partial t} = \frac{\partial (h_w u_w)}{\partial t} - u_w \frac{\partial (h_w)}{\partial t} = u_w e^{(s)} - u_w e^{(s)} = 0 \, , \tag{4.73}$$

so that the clear-water layer velocity is an invariant of the erosional geomorphic operator. This is indeed suggested in Fig. 4.10. The convective momentum transfer at $\Gamma^{(s)}$ is directed from the water layer towards the sheet-flow layer, and the loss of momentum for the water layer results directly from the equivalent loss of mass, so that overall the layer velocity is preserved. The second invariant is less trivial, and may be found by first invoking the compatibility relation (4.49) to write (4.72b) in terms of $e^{(s)}$ only :

$$\frac{\partial(h_s)}{\partial t} = e^{(b)} - e^{(s)} = -\frac{\rho_b - \rho_w}{\rho_b - \rho_s} e^{(s)} , \tag{4.74}$$

By using this to extract $e^{(s)}$, (4.72a-e) becomes:

$$\frac{\partial(h_s u_s)}{\partial t} = \frac{\rho_w}{\rho_s} \frac{\rho_b - \rho_s}{\rho_b - \rho_w} u_w \frac{\partial h_s}{\partial t} , \tag{4.75}$$

Putting all the terms in the left-hand side gives the invariant:

$$\frac{\partial}{\partial t}\left[h_s \left(u_s - \frac{\rho_w}{\rho_s} \frac{\rho_b - \rho_s}{\rho_b - \rho_w} u_w \right) \right] = 0 , \tag{4.76}$$

The invariant expression contained within the [] brackets is denoted Ψ.

Using (4.49) again but in the reverse order, (4.72b) may be written only in terms of $e^{(b)}$,

$$\frac{\partial(h_s)}{\partial t} = e^{(b)} - e^{(s)} = \frac{\rho_b - \rho_w}{\rho_s - \rho_w} e^{(b)} , \tag{4.77}$$

and then solved with the classical explicit Euler scheme to yield the updated depth of the sheet-flow layer. $e^{(b)}$ is given by (4.48) based on initial variables only:

$$h_s^{\Delta} = h_s + \Delta t \, \frac{\rho_b - \rho_w}{\rho_s - \rho_w} \frac{1}{\rho_b u_s} \left(\tau_s^{(b)} - \tau_b^{(b)} \right), \tag{4.78}$$

The updated clear-water layer depth is obtained by using

$$\frac{\partial(h_w)}{\partial t} = e^{(s)} = -\frac{\rho_b - \rho_s}{\rho_b - \rho_w} \frac{\partial h_s}{\partial t} , \tag{4.79}$$

and thus

$$h_w^\Delta = h_w - \frac{\rho_b - \rho_s}{\rho_b - \rho_w}\left(h_s^\Delta - h_s\right), \tag{4.80}$$

Finally, the updated sheet-flow layer velocity is retrieved from the invariant quantity Ψ :

$$u_s^\Delta = \frac{\Psi}{h_s^\Delta} + \frac{\rho_w}{\rho_s}\frac{\rho_b - \rho_s}{\rho_b - \rho_w}u_w, \tag{4.81}$$

An exception should be considered when the thickness of the water layer vanishes as a result of the dilatation of the sheet-flow layer. In particular, the thickness may not become negative. When the updated depth $h_w^\Delta < h_{\min}$ (again $h_{\min}$ is a predefined minimal depth, typically 10^{-6} times a characteristic depth of the flow), $h_w^\Delta = h_{\min}$ is imposed and the other variables h_s^Δ and u_s^Δ are adapted accordingly.

4.1.6. Depositional geomorphic exchanges

The set of equations to be solved is in this case are

$$\begin{gathered}\frac{\partial h_w}{\partial t} = e^{(s)} \quad , \quad \frac{\partial h_s}{\partial t} = e^{(b)} - e^{(s)} \quad , \quad \frac{\partial z^{(b)}}{\partial t} = -e^{(b)} \\ \frac{\partial (h_w u_w)}{\partial t} = u_s e^{(s)} \quad , \quad \frac{\partial (h_s u_s)}{\partial t} = -\frac{\rho_w}{\rho_s}u_s e^{(s)} + \frac{\rho_b}{\rho_s}u_s e^{(b)}\end{gathered} \tag{4.82a-e}$$

Subtracting u_s times (4.82b) from (4.82e), and using (4.49) to express $e^{(b)}$ as a function of $e^{(s)}$, results in

$$h_s\frac{\partial u_s}{\partial t} = \frac{\partial (h_s u_s)}{\partial t} - u_s\frac{\partial h_s}{\partial t} = u_s e^{(s)}\frac{\rho_s - \rho_w}{\rho_s} + u_s e^{(b)}\frac{\rho_b - \rho_s}{\rho_s} = 0\,. \tag{4.83}$$

Here, as illustrated in Fig. 4.10, all the convective momentum transfers are directed outwards of the sheet-flow layer, so that the velocity of the latter is preserved and constitutes an invariant. Equation (4.82b) may thus be integrated straightforwardly with the explicit Euler relation:

$$h_s^{\Delta} = h_s + \Delta t \, \frac{\rho_b - \rho_w}{\rho_s - \rho_w} \frac{1}{\rho_b u_s} \left(\tau_s^{(b)} - \tau_b^{(b)} \right), \tag{4.84}$$

Then, the updated clear-water layer depth is

$$h_w^{\Delta} = h_w - \frac{\rho_b - \rho_s}{\rho_b - \rho_w} \left(h_s^{\Delta} - h_s \right), \tag{4.85}$$

and velocity

$$u_w^{\Delta} = u_s + \frac{h_w}{h_w^{\Delta}} \left(u_w - u_s \right). \tag{4.86}$$

4.2. Hyperbolic operator

In the previous section, the focus was set on the source operators, materializing erosion or deposition by vertical mass and momentum exchanges between the layers. They were dealt with first because they constitute the key novel elements of the proposed layered description. The remainder of system (4.50) describes the longitudinal propagation of the two flowing layers, and accounts for the horizontal mass and momentum exchanges between neighbouring computational cells as a result of spatial gradients in the flow variables:

$$\frac{\partial \mathbf{U}}{\partial t} = -\mathbf{A}(\mathbf{U}) \frac{\partial \mathbf{U}}{\partial x} \tag{4.87}$$

where $\mathbf{U}$ and $\mathbf{A}(\mathbf{U})$ are as introduced in (4.51) and (4.52). The resulting numerical operator is usually referred to as the hyperbolic operator. In fact it is essentially the same as the two-layer shallow-water solver introduced in Chapter 3, and since the same numerical scheme is used, the developments are note replicated. The sole difference lies in the fact that in Chapter 3, a flat horizontal bottom surface was assumed. Here, as a result of erosion and depositional exchanges, the bed profile may evolve and the actual topography should be considered. To account for the pressure thrusts acting on a sloping bed with local gradient $\partial z^{(b)} / \partial x$, additional terms appear in the momentum equations. Those are the terms corresponding to the third column of $\mathbf{A}(\mathbf{U})$. They are non-conservative in nature, and present similarities with the terms related to the pressure interaction between the two layers (see Chapter 3, Section 3.3). They are treated in the same way, i.e. as lateralised corrections to the numerical fluxes evaluated using the HLL scheme. More details on this so-called LHLL scheme may be found in Chen *et al.* (submitted) in the framework of a first-order implementation. The present code relies on a second-order extension as described by Capart and Young (2002), and briefly introduced in Chapter 3, Section 3.3. The reader may refer to those publications for more details. For a first-order accurate version of the model, the hyperbolic and source operators are simply solved in sequence at each time step. For the second-order version, the hyperbolic operator is solved using a predictor-corrector time-stepping procedure. The integration of the source terms is thus performed in two steps, each accounting for a half time step: one before the predictor step, one after the corrector step.

Overall, the complete numerical code was build upon an existing code initially developed by H. Capart at National Taiwan University for a distinct set of equations (Capart and Young, 2002; Chen *et al.*, submitted), and kindly made available for the present work.

5. Model behaviour

Before validating the description by comparing simulations with the laboratory experiments, the general behaviour of the proposed model is investigated first: the choice of model parameters and their sensitivity, the implications of the presence of source terms on the observed wave structure, the numerical accuracy and the characterisation of model instabilities.

5.1. Model parameters

In the system (4.43)-(4.49) complemented with closures (4.26)-(4.28) and (4.30), a total of ten model parameters are found: $g, \rho_w, \rho_s, \rho_b, \tan\varphi, \tau_c^{(b)}$, $h_c, d, C^{(b)}, C^{(s)}$. They can be subdivided into four different categories depending on how they are evaluated: universal constants, independent measurements, experimental observations, and calibration parameters.

The first category includes universal constants: the acceleration of gravity, $g = 9.81$ m/s², and the density of pure water, $\rho_w = 1000$ kg/m³.

The second category includes soil parameters that may be measured through standardised tests of the soil mechanics, thus independently of the dam-break experiments: the bulk density of the saturated granular bed, ρ_b, is measured by analysing bed samples taken in situ with small cylindrical annuli; the soil friction angle, $\tan\varphi$, was deduced from the angle of repose of loosely poured heaps; the particle diameter d is taken as the average diameter d_{50} for granular material with variable grain size and shape ; the height of capillary rise h_c was estimated with a “tulip” test for static assemblies, however the effective capillary pressure in the sheet-flow layer is expected to be lower due to the lower solid concentration ($\rho_s < \rho_b$), and the estimation from the tulip test should be considered as an upper bound.

The third category consist in parameters that are evaluated based on experimental measurements. This is the case of the postulated constant density of the sheet-flow layer, ρ_s. It derives from the average volumetric solid concentration c_s in the layer, evaluated based on balances of bed volumes like explained in Section 2.1.3. This is a measured average value, based on one experiment for each granular material and then taken as a constant value throughout the experiments. For sheet-flow regimes, Nnadi and Wilson (1992) expect the average volumetric solid concentration c_s to be in the range of 1/2 of the solid concentration c_b in the static bed, a ratio similar to the imaging estimations based on balances of layer volumes. Concentration profiles within laboratory fluid-granular flows obtained with stereoscopic imaging techniques (Spinewine *et al.*, 2003) revealed similar orders of magnitude.

The last category features parameters that may not easily be deduced from independent measurements: the dimensionless friction coefficients $C^{(s)}$ and $C^{(b)}$, and the critical bed shear stress $\tau_c^{(b)}$. They are left as adjustable calibration parameters. However, the order of magnitudes for those parameters may be obtained by facing the model with a classical sediment transport formula under uniform-flow equilibrium conditions on a uniformly sloping bed. The spatial gradients of the complete system then reduce to a constant bed slope $\partial z^{(b)} / \partial x = -S_0$, and equilibrium transport imposes $\tau_b^{(b)} = \tau_s^{(b)}$. Under such assumptions, Savary (see Zech *et al.*, 2005) has shown that the reduced system of equations leads to a relationship between on the one hand parameters $C^{(s)}$ and $C^{(b)}$ and on the other hand the equilibrium volumetric solid discharge per unit width, $q_s = c_s h_s u_s$. If the latter is constant, evaluated either experimentally or from an adequate empirical predictor, a set of unique values for parameters $C^{(s)}$ and $C^{(b)}$

may be obtained. When q_s varies, however, the relationship is non-linear and parameters $C^{(s)}$ and $C^{(b)}$ are affected. Since the model assumes constant values, the above procedure may thus only furnish an order of magnitude that can guide us in the choice of adequate values of the parameters used in the simulations, which are allowed to slightly depart from those equilibrium values. The last parameter, $\tau_c^{(b)}$, may be related to the initiation of motion. For the erosional dam-break experiments under study, the effect of initiation of motion was deemed negligible, and it was simply considered that $\tau_c^{(b)}=0$.

Table 4.2 summarises parameter values considered in all the simulations. Note that the only adjusted parameters, $C^{(b)}$, $C^{(s)}$, $\tau_c^{(b)}$ and h_c, are taken as equal for the cases of PVC and sand beds. Thus, the PVC and sand simulations only differ in parameters that were precisely measured with independent characterisation tests of the material, the most determinant being the specific density of the sediment particles.

5.2. General observations

A typical time sequence of simulated profiles is shown in Fig. 4.11. It corresponds to a granular bed made of PVC pellets, and an initial depth of water in the upstream reservoir of 25 cm. This case is used as a prototype for all the analysis of the next sub-sections. Profiles on Fig. 4.11 are given at 0.5 s intervals, and were computed with the parameters of Table 4.2, spatial steps $\Delta x = 2$ cm, a Courant number $Cr = 0.5$ like elsewhere in the thesis, and first-order accuracy. One may observe the downstream propagation of the dam-break wave, and the gradual mobilisation of the sheet-flow layer. Near the wavefront the sheet-flow is seen to cover almost the entire flow depth, as was observed in the experiments. It is interesting to compare qualitatively

Table 4.2 : Values of model parameters for the simulations

Symbol	Description	Units	PVC value	Sand value	(Source)
Universal constants					
g	Acceleration of gravity	[m/s²]	9.81		[–]
ρ_w	Clear-water layer density	[kg/m³]	1000		[–]
Material properties					
ρ_M	Specific granular density	[kg/m³]	1580	2680	measured
c_b	Bed granular concentration	[–]	0.58	0.53	measured
ρ_b	Bed layer bulk density	[kg/m³]	1336.4	1890.4	$= c_b \rho_M + (1 - c_b)\rho_w$
φ	Friction angle	[°]	38	30	measured
d	Particle diameter	[mm]	3.92	1.82	measured
c_s	Sheet-flow granular concentration	[–]	0.22		imaging estimate
ρ_s	Sheet-flow layer bulk density	[kg/m³]	1127.6	1369.6	$= c_s \rho_M + (1 - c_s)\rho_w$
Shear-stresses parameters					
$C^{(b)}$	Friction coefficient at $\Gamma^{(b)}$	[–]	0.04		adjusted
$C^{(s)}$	Friction coefficient at $\Gamma^{(s)}$	[–]	0.005		adjusted
$\tau_c^{(b)}$	Critical bed shear	[N/m]	0		assumed
h_c	Capillary rise	[mm]	10		estimated
Numerical parameters					
Cr	CFL constant	[–]	0.5		[–]

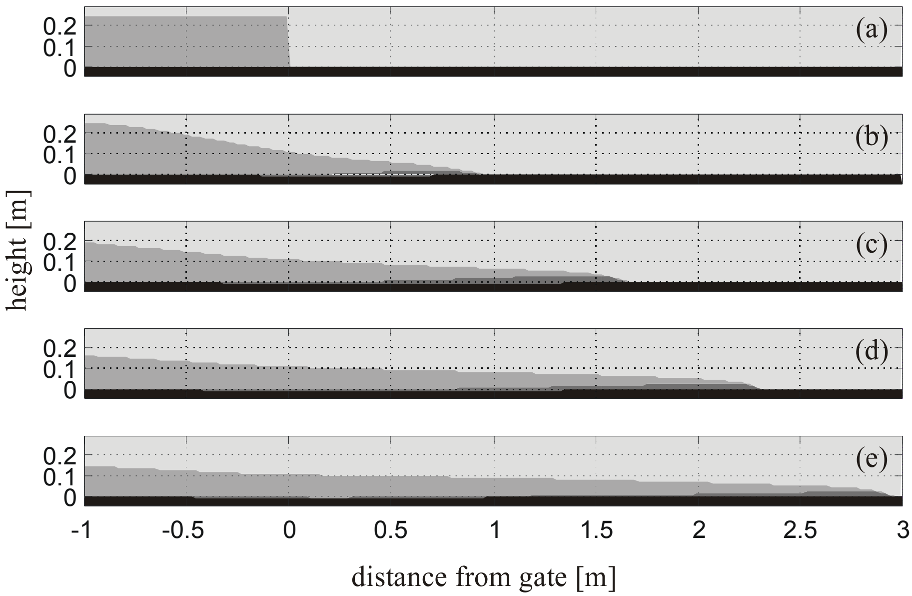

Figure 4.11. Time sequence of computed profiles (PVC, flat bed, $H = 25$ cm) at $t = 0$, 0.5, 1, 1.5 and 2 s. Greyed regions, from light to dark, refer to water, sheet-flow and bed layers respectively.

the profiles of Fig. 4.11 with the profiles of Fig. 3.11, obtained in Chapter 3, using the simplified two-layer model in which the granular layer was assumed completely and permanently fluidised. The major difference is that the fluidisation of granular material is now modelled rather then postulated. Another major dissimilarity is the disappearance of the curious pinched-off feature that was observed previously to move rapidly ahead of the wavefront. This could indeed be expected, as the pinch-off was seen to be associated with very large velocity difference between the two layers. Friction along $\Gamma^{(s)}$, that is now accounted for and is function of the square of the velocity difference, will naturally tend to prevent this feature to detach from the main wavefront.

The profiles of Fig. 4.11 may be analysed further by arranging them in non-dimensional form according to Froude similarity, as in Fig. 4.12, where the vertical scale is also stretched to enhance visibility. This reveals one more fundamental difference with the simulated profiles of Chapter 3. The profiles do not collapse on a single curve, which means that self-similarity of the solution is lost. Several mechanisms included in the source terms are responsible for this phenomenon: the inertial effects causing non-equilibrium sediment transport, the capillary effects near the wavefront, and the friction along the two interfaces $\Gamma^{(s)}$ and $\Gamma^{(b)}$. These mechanisms act at different time scales, and their implications on the flow development are distinct. Non-equilibrium effects are most significant in the near-field (Fig. 4.12a), and result in a gradual mobilisation of the bed material. Capillarity has only a local influence in the vicinity of the wavefront, which will be discussed later. Friction has the most apparent impacts in the far field (Fig. 4.12b): slowing down of the wavefront, swelling of the water profile behind the front, and reduction of the sheet-flow layer thickness. Later in Section 7, it will be shown that within an intermediate range of time scales, for which equilibrium transport may be assumed and friction may be neglected, geomorphic exchanges do not violate Froude scaling and may still preserve self-similarity of the solution.

In the far-field of the wave development (see the profile at $t = 2$ s in Fig. 4.12b), the bed exhibits a non-monotonous profile with distinct zones: substantial scouring behind the wavefront, followed by partial re-deposition of bed material (in the region of $x/t\sqrt{gH} \approx 0.5$), and a developing scour hole just downstream of the failed dam ($x >\approx 0$).

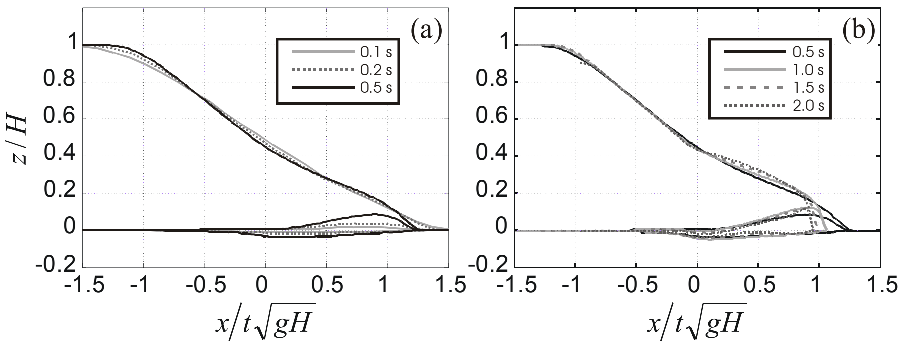

Figure 4.12. Self-similar plots of the computed profiles of Fig. 4.11, with exaggerated vertical scale. (a) near-field: $t = 0.1$, 0.2 and 0.5 s; (b) far-field: $t = 0.5$, 1.0, 1.5 and 2.0 s.

5.3. Numerical accuracy and instabilities

Numerical tests have been performed to investigate the differences between the first-order and second-order accurate simulations, and the model convergence for decreasing computational steps Δx. Figure 4.13 compares the first- and second-order accurate simulations at two instants, for the same test case as in the previous figures, with discretisation $\Delta x = 2$ cm. Differences are hardly noticeable. As expected, the second-order profiles enhance the flow discontinuities. They exhibit a sharper wavefront and a cusped profile in the vicinity of the failed dam, but the overall behaviour is largely similar to the first-order results (note that the vertical scale is stretched by a factor 5 in Fig. 4.13).

Simulations presented in Fig. 4.14 correspond to a computational mesh refined by a factor 4 as compared to Fig. 4.13, thus with discretisation $\Delta x = 5$ mm. The refined first-order profiles closely reproduce the unrefined second-order profiles of Fig. 4.13. However, the computational cost (in terms of CPU time) associated with the mesh refinement is largely superior

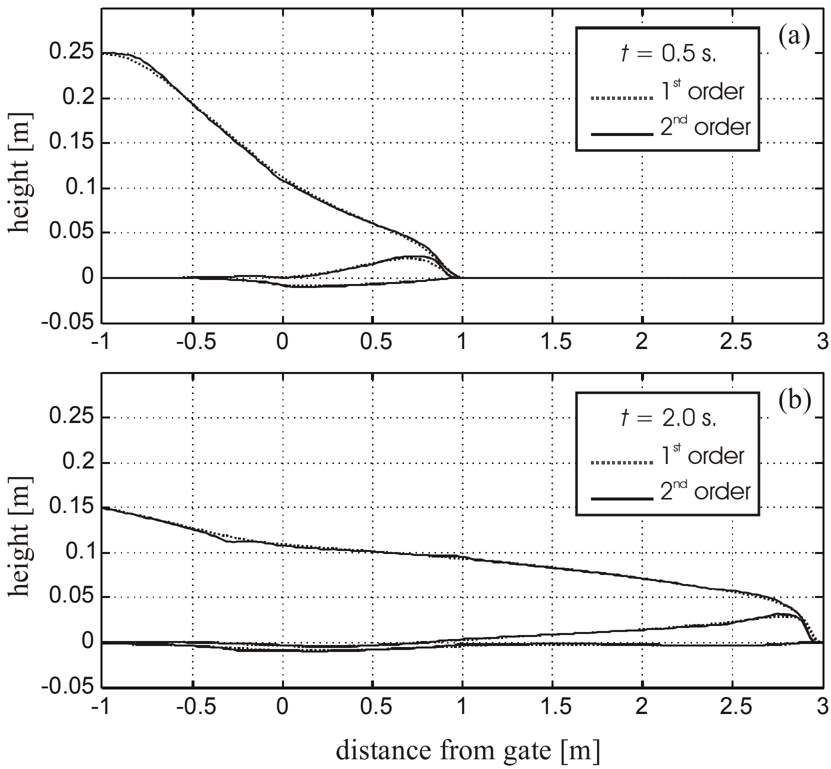

Figure 4.13. Comparisons of computed results at 1st order and 2nd order accuracy at mesh size $\Delta x = 2$ cm: (a) $t = 0.5$ s; (b) $t = 2.0$ s.

to that of the second-order extension, making the latter a preferable alternative. Another flaw of the mesh refinement is made clear in Fig. 4.14 for the second-order profiles, and consists in the emergence of instabilities at the interface between the clear-water and the sheet-flow layer. These instabilities first appear at some location behind the wavefront (Fig. 4.14a), and then develop into a regular train of oscillations across the whole length of the internal rarefaction (Fig. 4.14b, from $x \approx 0.5$ m till the wavefront). The shape and ratio of horizontal and vertical length scales of the oscillations are better visualised in the Figure inset, where the axis are

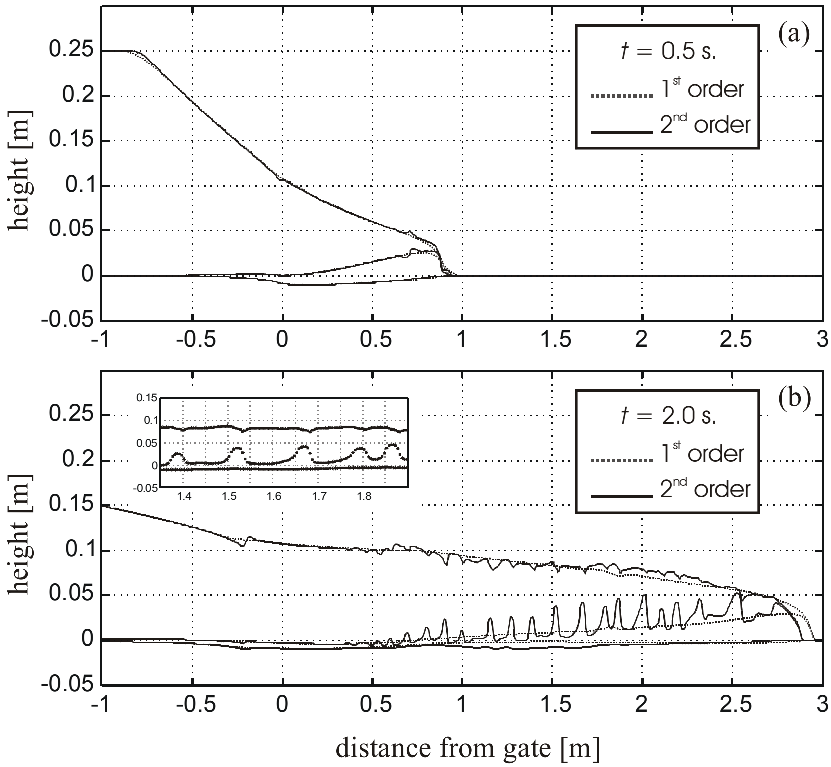

Figure 4.14. 1st and 2nd order computations on a refined mesh ($\Delta x = 5$ mm): (a) $t = 0.5$ s; (b) $t = 2.0$ s. Distorted vertical scale, except in inset of (b)

undistorted. The wavelength of a single oscillation spans over many computational cells (approximately 25), with a relatively smooth rising edge and a sharper falling edge. Corresponding oscillations are reproduced at the free surface. They have a much smaller magnitude but approximately the same wavelength as the sheet-flow oscillations, though with a small lag.

Apparently, the oscillations stay confined to the internal rarefaction separating the upstream region with low thickness of the sheet-flow layer, from the downstream region where the sheet-flow invades the whole flow depth. In the simulations of Chapter 3, Section 5.2 (see Fig. 3.21) it was observed that this is precisely the reach where the stability Froude number, $Fr^{\Delta} = (u_w - u_s)/\sqrt{g(h_w + h_s)}$, comes very close to the critical value for onset of instabilities associated with the loss of hyperbolicity of the homogeneous two-layer equations. In Fig. 4.15, the actual profiles of this stability Froude number are plotted versus the unstable bands inside which hyperbolicity of the homogeneous system is lost. In Fig. 4.15a, the profile of the standard second-order simulation approaches the unstable region, but remains smoothly outside of it. For the refined mesh, in Fig. 4.15b, oscillations occur even if the profile, though approaching it, stays outside of the unstable band. It thus seems that instabilities may emerge even outside of the unstable region corresponding to the homogeneous equations. The appearance of unstable numerical modes for very fine meshes is a classical drawback of higher-order numerical schemes. While the matter would certainly require further attention and a scrutinized inspection, in the present context, it is believed that (i) the instabilities are initiated numerically at mesh size, due to mesh refinement that encourage the development of unstable numerical modes associated with small wavelengths, but that (ii) the amplification of these instabilities and their development into pseudo-stable oscillations is governed by physical processes. In this regard, friction (shear) has initially a destabilizing effect, while the density contrast has a stabilizing effect that prevent the oscillations from growing indefinitely. This is in qualitative agreement with the description by Drazin and Reid (1981), who explain on physical grounds the processes governing the evolution of instabilities in stratified shear flows. The emergence of stable oscillations in the framework of a two-layer model for fluid-granular flows was first observed by Capart and Young (2002). At the time they did not insist on the mechanisms for the emergence and for the stabilization of these oscillations.

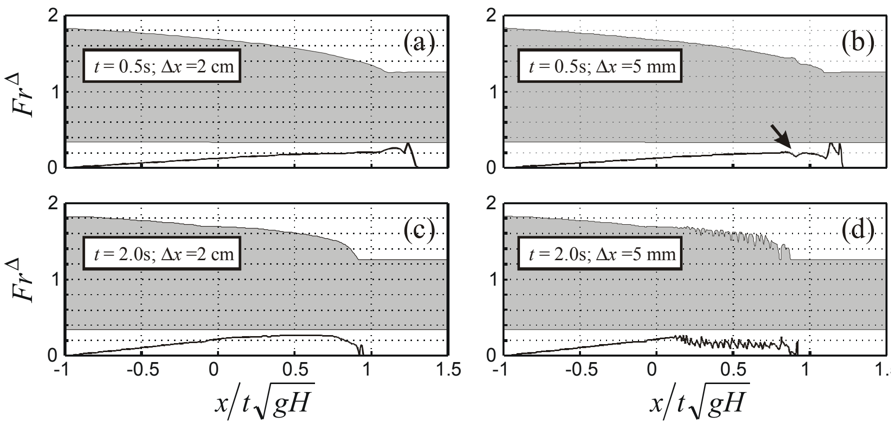

Figure 4.15. Stability Froude profiles (solid lines) for 2nd order accurate simulations, and bands of partial loss of hyperbolicity (grey regions).

While the oscillations of Fig. 4.14 are reminiscent of the antidune-like bedforms observed in the experiments, these should be handled with care and the matter should rather be considered as an interesting perspective worthy of further research. In the simulations, and in particular when comparing the model to the experiments in Section 6, the mesh refinement will thus be limited to prevent the emergence of these instabilities.

5.4. Dissipation of mechanical energy

In terms of energy, the breaking of a dam mainly involves the transformation of potential energy, stored in the reservoir upstream of the failed dam, into kinetic energy of the flood wave, while some energy is dissipated in the process. This is illustrated in Fig. 4.16. The evolution of potential and kinetic energies, integrated over the entire flume length, are plotted versus time for the same test case as discussed above (a dam-break wave initiated by the release of a 25 cm layer of clear water over a bed of PVC pellets, modelled at second-order accuracy). The sum of both is the total mechanical energy of

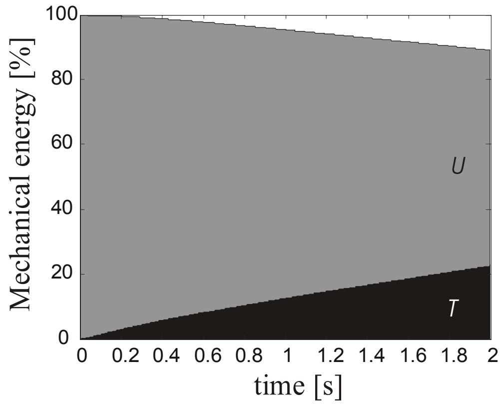

Figure 4.16. Evolution of mechanical energy in the simulations (PVC, flat bed, $H = 25$ cm, 2nd order): potential energy U (grey), kinetic energy T (black), and energy dissipation (white).

the flow. The triangular-shaped region left above the two coloured regions thus corresponds to the dissipated energy, which is analysed in details below.

In Section 3.3 a global mathematical relation was derived, constraining the flood wave to dissipate mechanical energy. This is a physical constraint, known as the second law of thermodynamics. Numerically, in Section 4.1.1, it was stipulated that a robust treatment of the source terms should also ensure that energy is either preserved or dissipated by each of the individual numerical operators derived from an operator splitting approach. System (4.50) features two classes of processes: the "hyperbolic" operator, governing the horizontal propagation of a two-layer flow as introduced in Chapter 3, and the "source" operators, governing the vertical exchanges of mass and momentum between layers as a result of friction and geomorphic exchanges. In the absence of dissipation, the hyperbolic operator should theoretically preserve flow energy. However, numerical rounding errors may cause spurious energy dissipation, depending on the accuracy of the selected

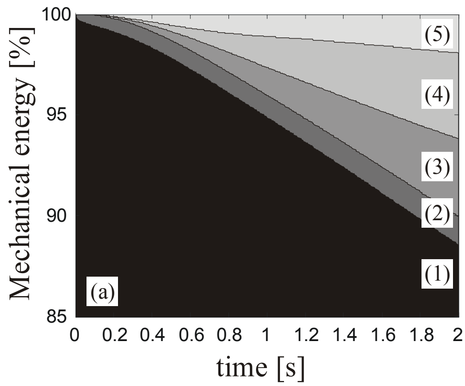

Figure 4.17. Contribution of the various operators to energy dissipation for (a) 1st order; (b) 2nd order simulations. From dark grey to light grey: (1) mechanical energy, $T+U$; energy losses associated with (2) hyperbolic operator; (3) friction operator $\mathbf{S}_{\mathbf{F}}^{(s)}(\mathbf{U})$; (4) friction operator $\mathbf{S}_{\mathbf{F}}^{(b)}(\mathbf{U})$; (5) geomorphic operator $\mathbf{S}_{\mathbf{G}}(\mathbf{U})$.

numerical scheme. Globally, the source operators were seen in Section 3.3 to be compatible with energy dissipation. Here it is checked that energy is individually dissipated by each source operator: friction between the flowing layers along $\Gamma^{(s)}$, friction along the bed interface $\Gamma^{(b)}$, and geomorphic action of erosion and deposition. The respective contributions of each process to the global energy loss, in the near-field and in the far-field, are highlighted.

This is illustrated in Fig. 4.17, featuring time lines of the mechanical energy similar to the ones of the previous figure, and for the same test case. The left panel corresponds to a first-order simulation, and the right panel to a second-order simulation. The lower grey region indicates the decreasing mechanical energy left available in the system. The four coloured stripes overlying it correspond to the energy losses caused respectively by the hyperbolic operator and by the three source operators. Several observations can be made. Firstly, the energy losses associated to the four stripes are strictly positive. A trivial observation is also that the sum of mechanical energy and of the four stripes features a horizontal line, which simply means that the energy balance is consistent. Secondly, the energy loss of the hyperbolic operator is not zero, but is materialised by a band of approximately constant thickness on Fig. 4.17. The related numerical dissipation is thus mainly caused at the very first instants of wave formation, and does hardly grow later on. In the right panel, it is substantially reduced with second-order accuracy. Thirdly, the energy losses of the three source operators are of the same order of magnitude. The effect of geomorphic action is predominant in the near-field (until $t \approx 0.4$ s), whereas the effect of friction is more significant in the mid- and far-field.

5.5. Effect of granular dilatancy

One of the implications of granular dilatancy on the flow dynamics, as identified in Section 2.2, is the generation of clear-water transfers at interface $\Gamma^{(s)}$. Those are required to counterbalance the surplus or deficit in pore volumes within the sediment grains, enduring dilatation or contraction as they are eroded or deposited. The related transfers of flow momentum provide, in case of erosion, an additional driving force for the sheet-flow layer.

In order to quantify the implications of granular dilatancy, in Fig. 4.18 model simulations for the sand test are obtained for three sets of parameters. The profiles of Fig. 4.18a reproduce the results obtained with the parameters as given in Table 4.2, thus accounting for granular dilatancy with $c_b = 0.53$ and $c_s = 0.22$. The profiles of Fig. 4.18b are obtained when setting $c_s = c_b$, thus turning off the effects of granular dilatancy. Two major differences are observed: first, the modelled wavefront is much faster than observed; second, bed erosion and thickness of the sheet-flow layer are largely underestimated. In fact, turning off granular dilatancy suppress the major coupling mechanism between the two flow layers. The sheet-flow may not be driven any more by the supply of fast-moving clear-water transferred from the upper layer. The sole mechanism still available for its acceleration is friction at the interface $\Gamma^{(s)}$.

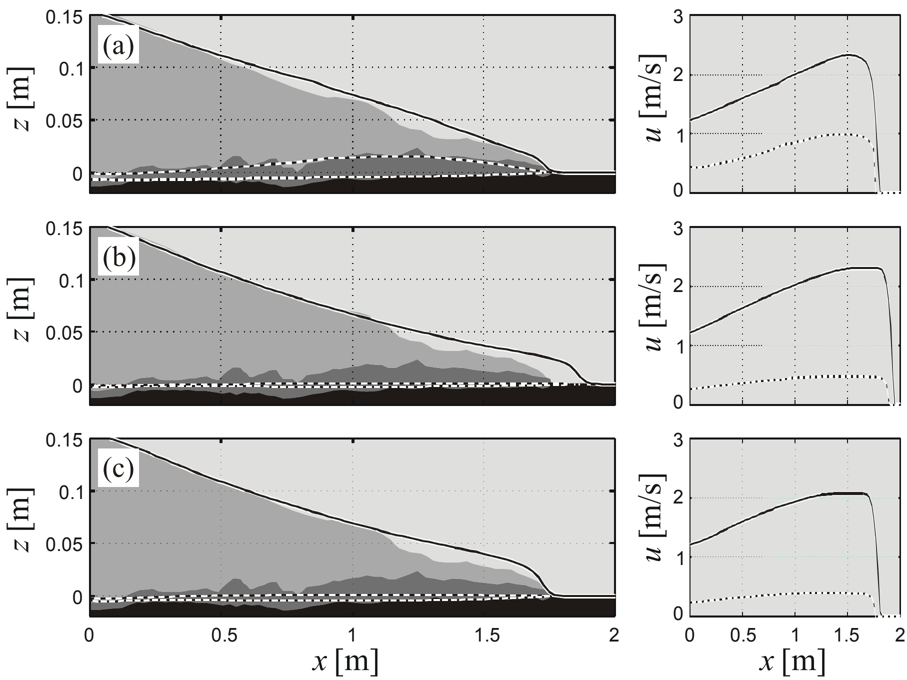

Figure 4.18. Implications of granular dilatancy. Comparisons of flow profiles (left) and layer velocities (right) for three different configurations: (a) $c_s \neq c_b$, with model parameters given in Table 4.2; (b) $c_s = c_b$, with other parameters as in Table 4.2; (c) $c_s = c_b$, but with a substantial increase of friction parameters $C^{(s)}$ and $C^{(b)}$. ($t = 0.75$ s, sand bed, $H = 35$cm, experimental profiles as shaded grey regions in the background, vertical scale of the flow profiles distorted by a factor 4)

One alternative to rectify the simulations of Fig. 4.18b while still forcing $c_s = c_b$ is to increase substantially the friction parameters. The simulations of Fig. 4.18c are obtained for dimensionless friction coefficients $C^{(s)}$ and $C^{(b)}$ that were adjusted so as to restore a correct positioning of the wavefront. Values $C^{(s)} = 0.01$ and $C^{(b)} = 0.1$ correspond to about 2.5 times the values of Table 4.2. If a reasonable agreement is obtained with the experiment, this alternative has an important drawback: it substitutes the role of friction to the role of granular dilatancy. While the latter vanish in conditions of uniform flow and equilibrium transport, friction does not. Consequently, artificially large values of friction adjusted for highly transient dam-break flows may lead non-realistic predictions of sediment-transport rates in uniform flow conditions.

Overall, the best agreement between simulations and observations is obtained for the case of Fig. 4.18a. For this case, the velocity profiles plotted in the right panel suggest a ratio between depth-averaged velocities u_s / u_w roughly equal to 0.4 (whereas $u_s / u_w \approx 0.15$ in Figs. 4.18b and 4.18c), a value in qualitative agreement with the experimental observations of Fig. 4.3.

5.6. Effect of capillarity

In Section 3.2, it was indicated that when the sheet-flow layer invades the entire flow depth, capillary forces at the free surface may have a substantial effect on Terzaghi's effective normal stress at the bed, at least at the reduced scale of laboratory experiments. Near the saturated wavefront, the increase of normal stress due to capillarity was seen to be potentially of the same order of magnitude as the submerged weight of granular particles within the sheet-flow layer. A simplified correction to the resistive shear stress $\tau_b^{(b)}$

(4.28) was proposed in (4.30), by which capillary pressure is assumed to develop progressively over a thickness of one grain diameter below the free surface (see Fig. 4.9), and assuming that this correction is enough to prevent partial de-saturation at the wavefront.

All of the above simulations and figures of Section 5 have been constructed with values of capillary pressure and grain diameter as in Table 4.2. The simulations shown in Fig. 4.19 compare the same test case with results obtained by not considering the effect of capillarity. Simulation time is $t = 2$ s. As expected, capillarity only intervenes near the wavefront (Fig. 4.19a), where the remaining thickness of the clear-water layer vanishes, but in that region its influence is surprisingly significant (Fig. 4.19b and c).

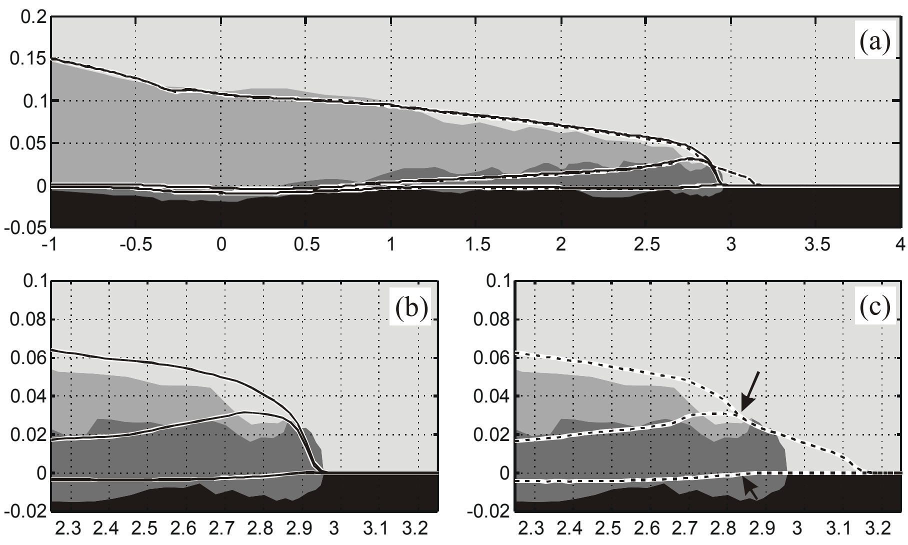

Figure 4.19. Effect of capillarity at the wavefront (PVC, flat bed, $H = 25$ cm, $t = 2$ s): comparison of simulations with (——) and without (------) effect of capillarity. Experimental observations as greyed regions in the background. (a) general view; (b) and (c) closer views on the wavefront.

In the absence of capillary action, the top of the sheet-flow layer at the wavefront quickly reaches the water free surface. A “contact point” occurs, that separates regions of finite and zero clear-water thickness. Downstream of this contact point, erosion is prevented in the model since the top layer can not provide the necessary clear water for the dilatation of the bed material. As a result, the granular slurry behaves as if it was propagating on a rigid substrate. It is not slowed down by incorporation of additional bed material, and rapidly moves forward, in such a way that the wavefront adopts the peculiar profile of Fig. 4.19c. When capillarity is accounted for (Fig. 4.19b), the shape of the bore is sharper and more regular. Luckily, it is also more consistent with the shape of the experimental wavefront. Erosion behind the bore is slowed down by the capillary forces that increase the resistive bed shear stress. Here as for all the cases that were investigated, capillary action was sufficient to prevent the occurrence of the peculiar behaviour of Fig. 4.19c.

6. Comparison of model and experiments

Model simulations are compared with the experiments for the three distinct configurations sketched in Fig. 4.20a-c. Configurations (**a**) and (**b**) feature the same initial conditions, with 35 cm of water in the upstream reservoir, but differ in the granular material constituting the bed, i.e. sand and PVC respectively. Configurations (**b**) and (**c**) compare results obtained with PVC for two different depths of clear-water in the reservoir, 35 cm and 25 cm respectively.

Comparisons of simulated and observed profiles for the three configurations at selected times are shown in Figs. 4.21, 4.22 and 4.23, respectively. Experimental profiles are drawn as shaded regions of different grey scales.

The computed profiles are superimposed as solid lines. On each figure the vertical scale has been distorted by a factor of 2, for viewing purposes.

The simulated profiles depicted in Fig. 4.21 for the sand bed compare very well with the experimental observations. Only the first profile at $t = 0.25$ s shows substantial deviations in position of the wavefront, thickness of the sheet-flow layer and curvature of the free surface, that may be due to violations of the shallow-water assumptions. Non-hydrostatic pressure distributions, combined with the non-instantaneous gate release, make the observed profiles deviate locally from the shallow-water predictions.

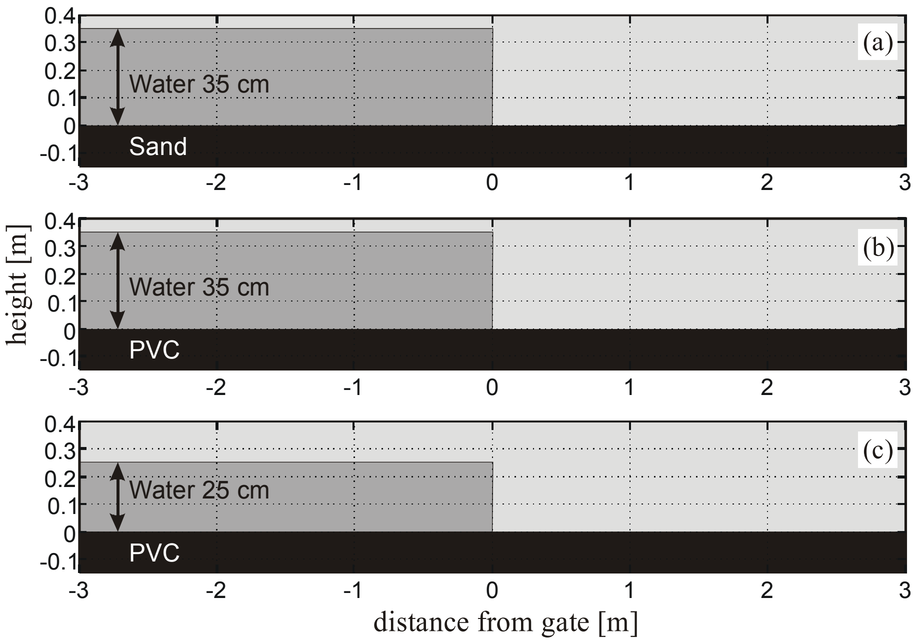

Figure 4.20. Sketch of the three experimental configurations that are faced with numerical results in the next figures.

Such effects are not limited to the present case of moveable beds, since similar discrepancies were also observed for pure liquid dam-break experiments on rigid beds (Janosi *et al.*, 2004; Stansby *et al.*, 1998). However, efforts paid for a careful gate design were not vain, and the experimental conditions are getting closer to the idealisation of an instantaneous gate release assumed in the simulations. At later times, the agreement between the simulations and the observations is much better. Both the free surface profile, wavefront celerity, bed scour and sheet-flow thickness are satisfactorily reproduced.

Comparisons for the case of a lighter bed of PVC with identical initial test conditions are reported in Fig. 4.22. The granular bed at $t = 0.25$ s shows a very peculiar profile, attributable to the massive soil movement initiated by the gate release. The process is that of a plastic soil failure, and has nothing to do with the mechanisms of sheet-flow entrainment postulated in the description. In fact the granular movements in that layer are very slow, and consist mainly in small rearrangements of the grains, without significantly affecting the formation of the dam-break wave. At later times, again, the correspondence between the observed and simulated waves is good. As compared to the sand tests of Fig. 4.21, the thickness of the sheet-flow layer is substantially larger, and the celerity of the wavefront substantially reduced. Note that these results for sand and PVC are obtained for identical values of the two adjustable friction coefficients (see Table 4.2). Thus, the simulations differ only in granular material properties (mainly density and repose angle), that were measured independently of the experiments.

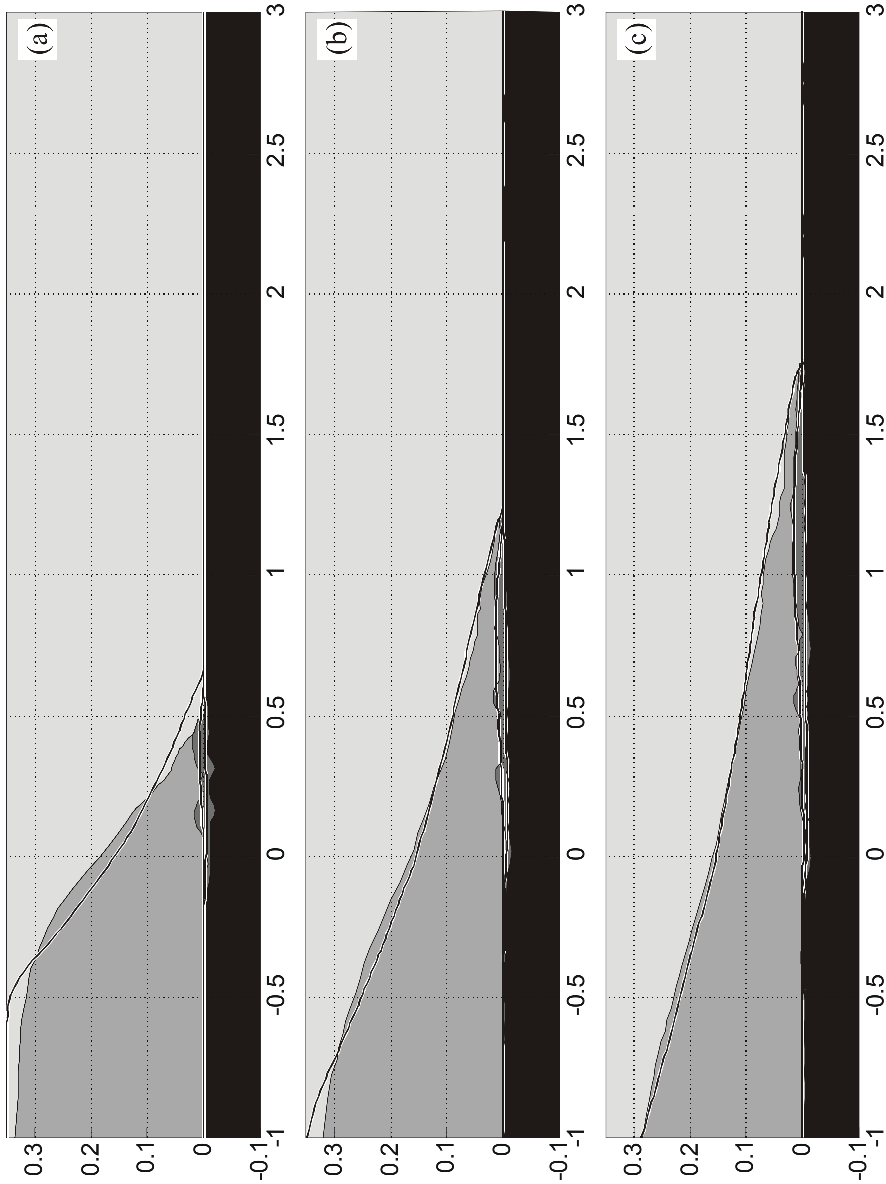

Figure 4.21. (2 pages) Comparisons of numerical profiles (solid lines) and experimental observations (shaded regions) for the configuration of Fig. 4.20a (sand, flat bed, $H = 35$ cm). Times $t = 0.25, 0.5, 0.75, 1,$

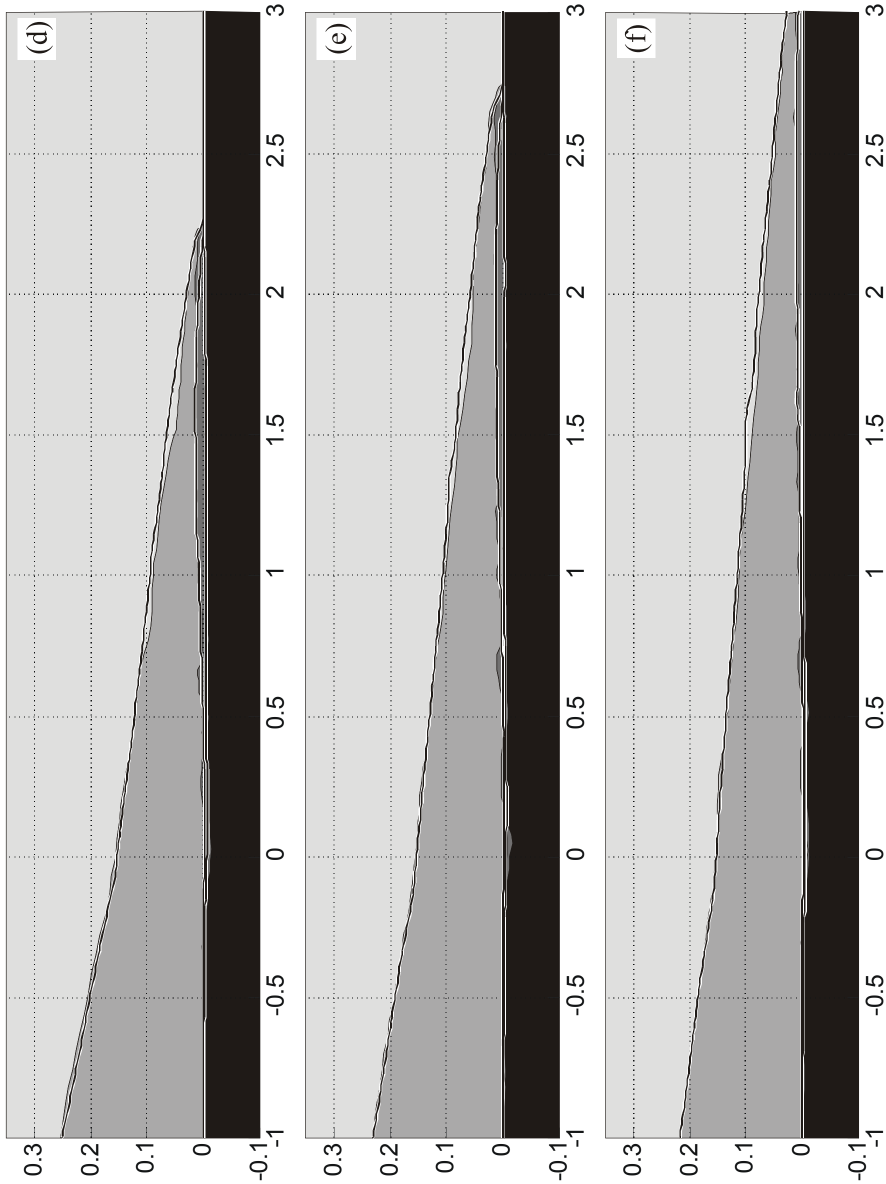

1.25, 1.5, 1.75, and 2 s. Dimensions are in meters, vertical scale is distorted by a factor of 2.

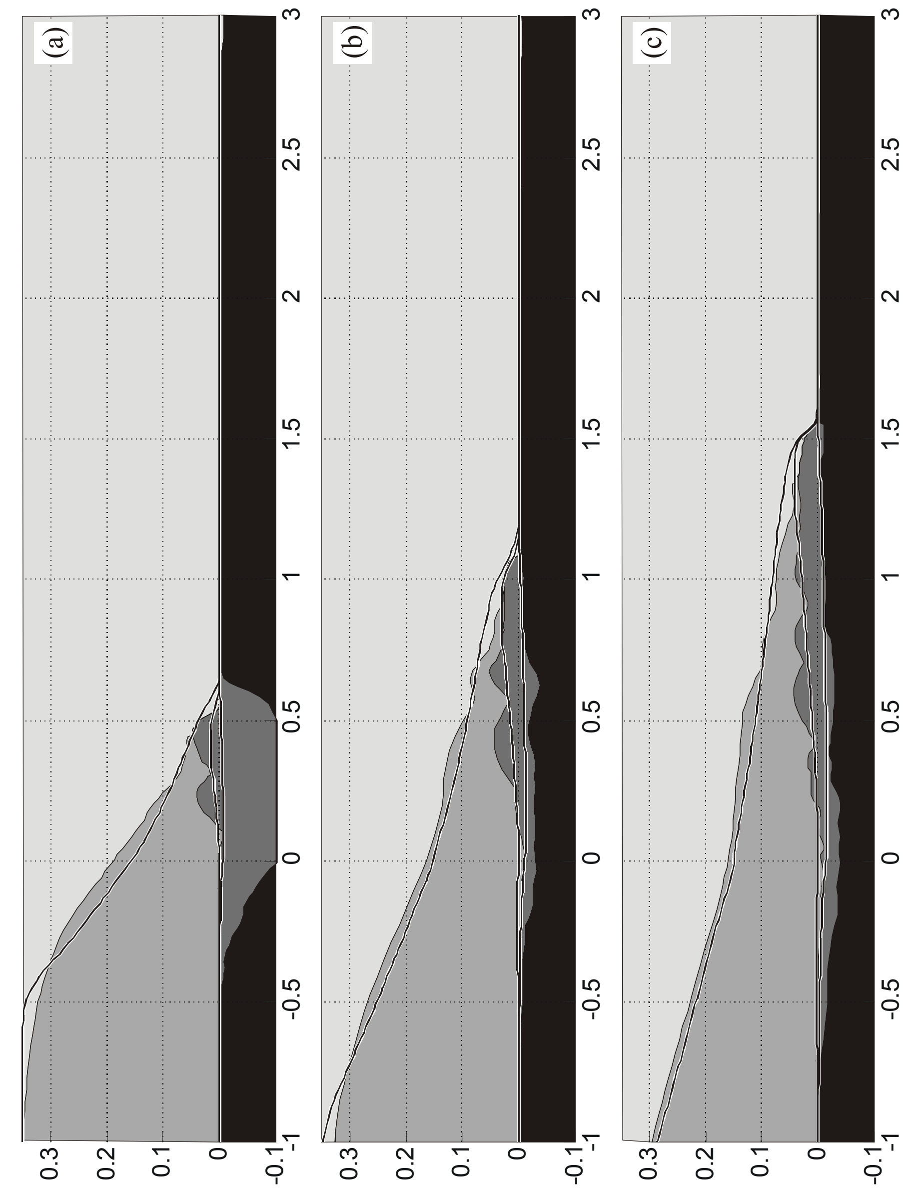

Figure 4.22. (2 pages) Comparisons of numerical profiles (solid lines) and experimental observations (shaded regions) for the configuration of Fig. 4.20b (PVC, flat bed, $H = 35$ cm). Times $t = 0.25$, 0.5, 0.75, 1,

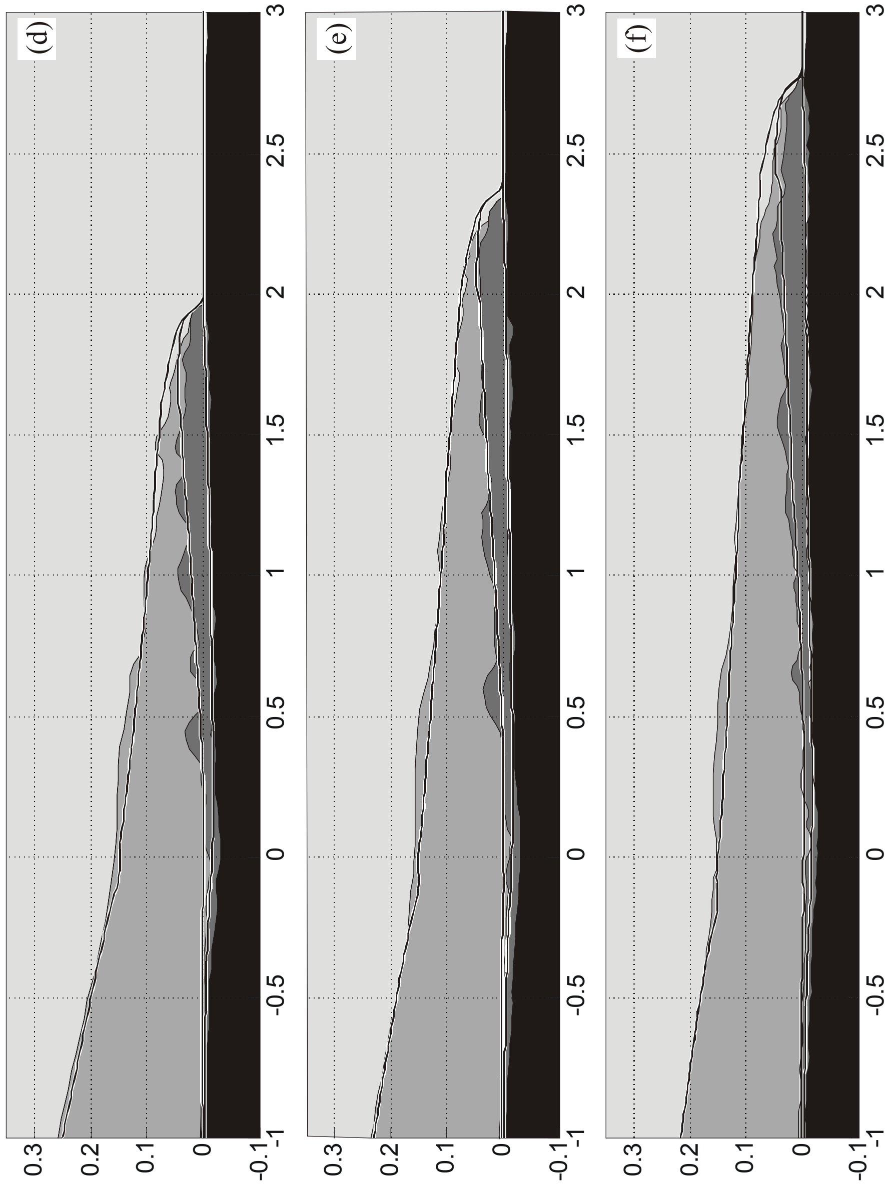

1.25, 1.5, 1.75, and 2 s. Dimensions are in meters, vertical scale is distorted by a factor of 2.

Observations for the PVC tests further indicate the typical in-phase oscillations of the sheet-flow layer and free surface, that were discussed previously in sections 5.3. In the simulations, the emergence of these instabilities was hampered by limiting mesh refinement, but convergence tests at second-order accuracy have shown that similar oscillations can emerge numerically and grow on the basis of physical processes to reach pseudo-stable configurations. Encouragingly, the non-oscillating simulated interfaces of Fig. 4.22 provide reasonable comparisons with the observed undulating profiles. The behaviour of the observed wavefront, quickly filled up with moving grains but showing no signs of grain de-saturation, comforts the simplified model to account for capillary forces.

Figure 4.23 plots comparisons for the same PVC bed but with a lower depth of water in the upstream reservoir. The agreement between observed and simulated flows is comparable to that of Fig. 4.22. The resemblance is further enhanced in Fig. 4.24 where dimensionless profiles are obtained by scaling the vertical axis with the initial depth $z' = z/h_{w,0}$ and the horizontal axis according to Froude similarity, $x' = x/(t\sqrt{g\, h_{w,0}})$. The profiles pertaining to the two cases are plotted at the same dimensionless time $t = 7.94\, t_0$, with $t_0 = \sqrt{h_{w,0}/g}$. This corresponds to $t = 1.5$ s for the 35 cm test and to $t = 1.27$ s for the 25 cm test. The resemblance suggests that the mechanisms responsible for breaking the Froude self-similarity, identified in Section 5.2, do not depend on the initial depth $h_{w,0}$.

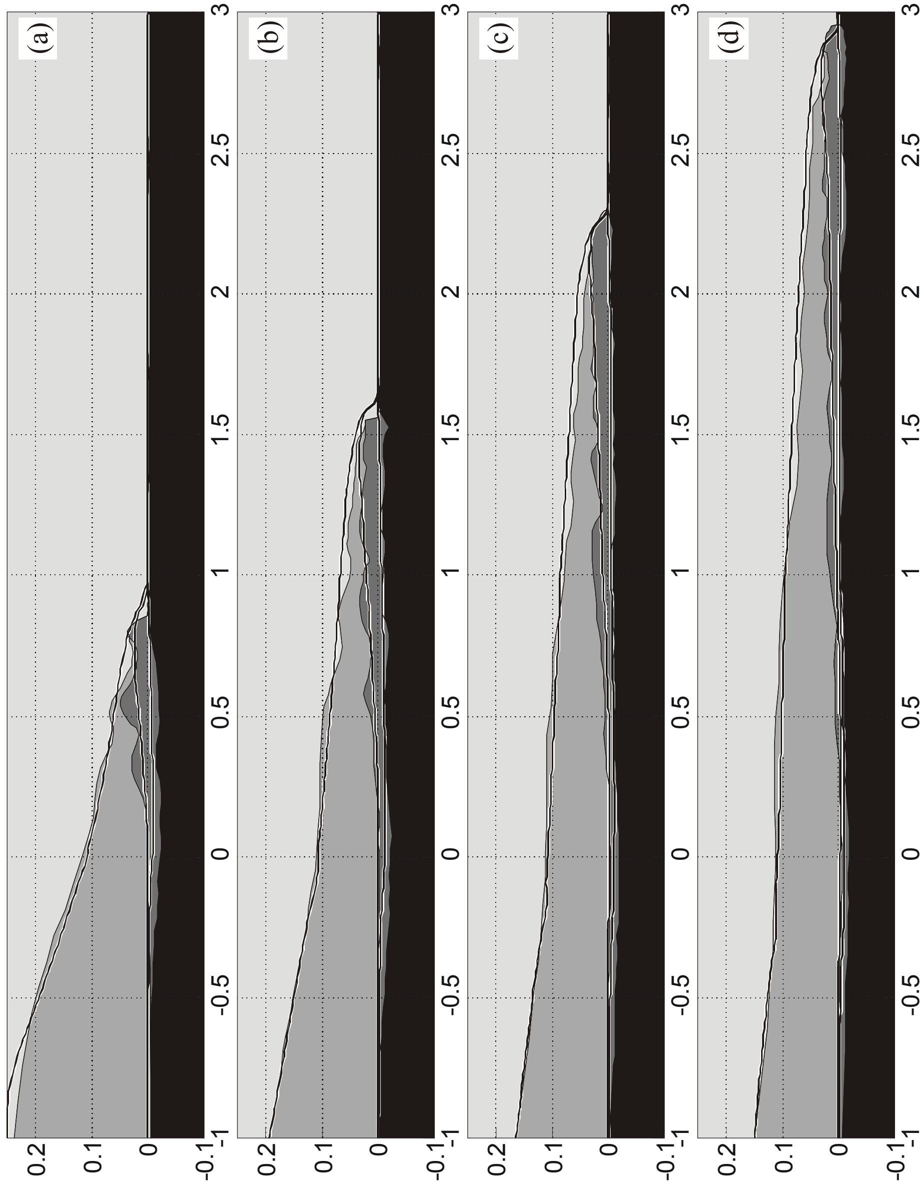

Figure 4.23. Comparisons of numerical profiles (solid lines) and experimental observations (shaded regions) for the configuration of Fig. 4.20c (PVC, flat bed, $H = 25$ cm). Times $t = 0.5$, 1, 1.5 and 2 s. Dimensions are in meters, vertical scale is distorted by a factor of 2.

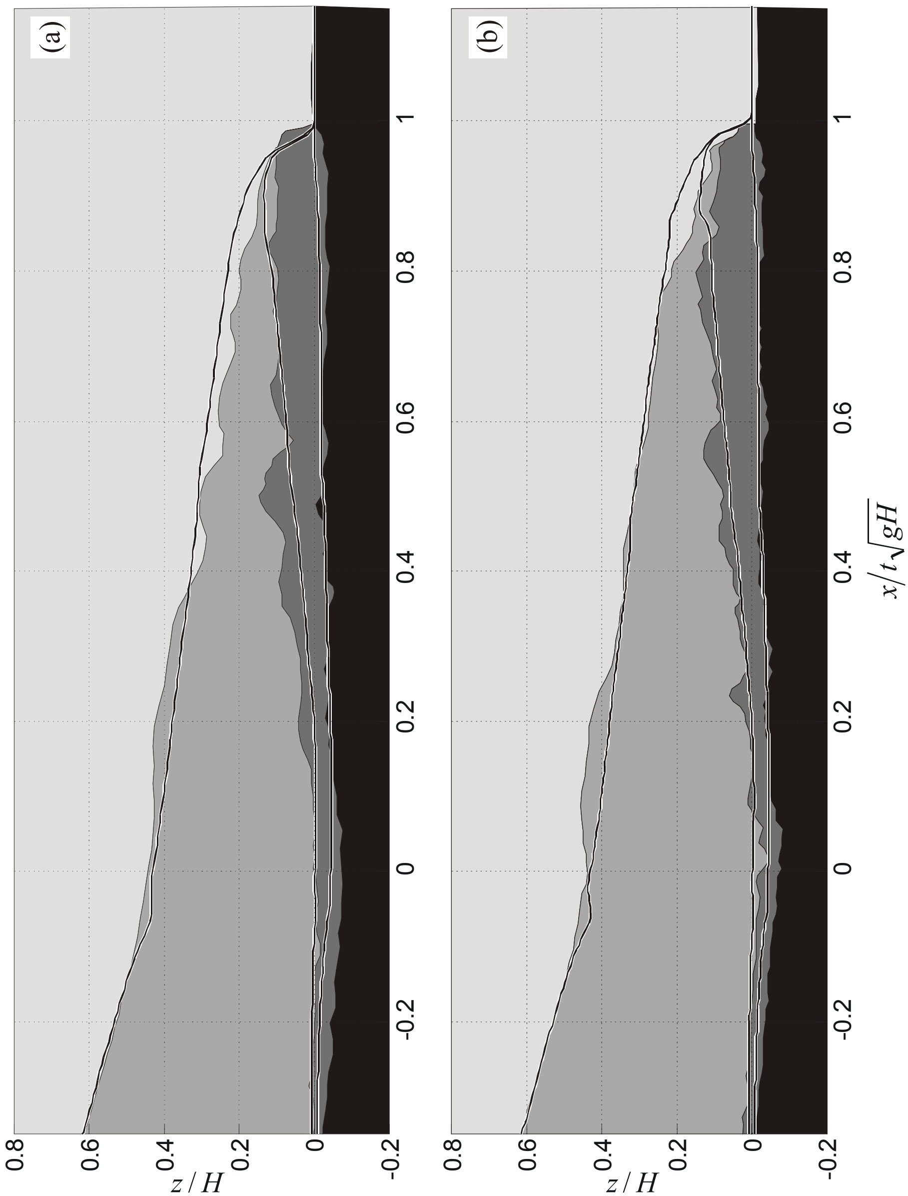

Figure 4.24. Comparisons of PVC profiles with different water depths: (a) $H = 25$ cm; (b) $H = 35$ cm. Numerical profiles (solid lines) and experimental observations (shaded regions) plotted in dimensionless form at the same dimensionless time $t/\sqrt{H/g} = 7.94$

7. Reduced theory with Riemann description and self-similar wave structure

The purpose of this last section is to show that one further advantage of the proposed description is that, under certain additional assumptions, it is amenable to a homogeneous system for which a Riemann-type exact solution should be available. Such exact solutions of the equations are interesting numerically, because they provide benchmarks for the validation of numerical models, and physically, because they allow to gain insight into the nature of the various waves that form the solution.

In Chapter 3, the two-layer shallow-water equations were introduced, governing the propagation of a two-layer system with distinct densities and velocities over a rigid bed. It was shown that the system, in the absence of frictional or geomorphic source terms, was homogeneous, and thus compatible with a Riemann description, provided that the region of loss of hyperbolicity is avoided. Instead of building up an analytical solution that was beyond the scope of the thesis, numerical simulations were performed, at second-order accuracy on very refined numerical meshes, and the numerical solutions were indeed seen to converge to self-similar profiles presenting a series of simple waves separated by constant states.

Departing from the rigid bed assumption, Fraccarollo and Capart (2002) have shown that a two-layer system accounting for erosion and deposition may still be amenable to a Riemann description, provided that two flow mechanisms are disregarded: non-equilibrium sediment transport processes, and friction. Since these processes act respectively in the near-field and in the far-field, there may exist an intermediate range of wave evolution for which the assumption could hold. Within this range, they have derived exact self-similar profiles for erosional dam-break waves. However, they relied on a simpler flow structure than the one that is postulated in the present work (Section 3). Most importantly, they assumed a single flow velocity throughout the flow depth, thus equalling the flow velocity in the sheet-flow layer and in the clear-water layer.

Capart and Young (2002) first proposed a geomorphic two-layer model with distinct layer velocities, but with equal solid concentrations in the bed and sheet-flow. Under this set of assumptions, the only mechanism for the emergence and acceleration of the sheet-flow layer was friction between the two layers (interface $\Gamma^{(s)}$). Such a description is thus not compatible with a Riemann description. In the absence of friction, there is no more any coupling mechanism between the two layers, whereas the description by Fraccarollo and Capart (2002) consisted in a full coupling of velocity between the two flow layers ($u_w = u_s = u$). With distinct velocities and in the absence of friction, no erosion can thus be generated when starting from a sheet-flow layer of zero thickness.

In the present context, it is argued that accounting for distinct concentrations in the bed and sheet-flow regions provides precisely such a coupling between the two layers, and in this way restores the existence of Riemann-type solutions. The coupling mechanism is induced by granular dilatancy, that generates exchanges of water and momentum between the clear-water and sheet-flow layers. As the sheet-flow thickens through erosion, it also incorporates fast-moving water from the above layer, affecting the velocity of the sheet-flow layer that can further grow towards an equilibrium.

This will be demonstrated in successive steps, by first resorting again to uniform flow conditions and turning off the frictional shear stress terms.

Under these conditions, invariant quantities will be identified, and it will be verified that the sheet-flow layer can still emerge and reach a stable equilibrium value. Assuming that the sediment transport adapts instantaneously to the flow conditions amounts to state that the sheet-flow thickness and velocity adapt instantaneously so as to ensure that $\tau_b^{(b)} = \tau_s^{(b)}$ at any time, yielding an additional relation between equilibrium sheet-flow variables $u_s^{(eq)}$ and $h_s^{(eq)}$. Reduced equations are obtained in the form of a homogeneous system of four conservation equations, in which gradient terms are reintroduced. Finally, instead of a complete analytical approach, a modified version of the numerical code is used, that incorporates a relaxation equation for the equilibrium sediment transport. The behaviour of this model for a very small relaxation time is analysed.

7.1. Unsteady uniform invariants

In the absence of frictional source terms, the system of equations (4.21)-(4.25) obtained when assuming unsteady uniform flow conditions reduces to:

$$\frac{\partial h_w}{\partial t} = e^{(s)} \tag{4.88}$$

$$\frac{\partial h_s}{\partial t} = e^{(b)} - e^{(s)} \tag{4.89}$$

$$\frac{\partial z^{(b)}}{\partial t} = -e^{(b)} \tag{4.90}$$

$$\frac{\partial (h_w u_w)}{\partial t} = u^{INV} e^{(s)} \tag{4.91}$$

$$\frac{\partial (h_s u_s)}{\partial t} = -\frac{\rho_w}{\rho_s} u^{INV} e^{(s)} \tag{4.92}$$

where $u^{INV} = u_w$ in case of erosion and $u^{INV} = u_s$ in case of deposition. In the below development only eroding flows are considered (erosion occurs until the equilibrium sediment transport is reached, and then the equilibrium is maintained), and thus $u^{INV} = u_w$. To consider a depositional behaviour, a different approach than the one described below should be adopted.

A number of physical quantities are preserved by system (4.88)-(4.92). They may be obtained by the following linear combinations:

$$(4.88)+(4.89)+(4.90) \Rightarrow \quad \frac{\partial}{\partial t}\left[z^{(b)} + h_s + h_w\right] = 0 \qquad (4.93)$$

$$(4.91) - u_w\ (4.88) \Rightarrow \quad \frac{\partial}{\partial t}\left[u_w\right] = 0 \qquad (4.94)$$

$$\rho_w (4.91) + \rho_s (4.92) \Rightarrow \quad \frac{\partial}{\partial t}\left[\rho_w h_w u_w + \rho_s h_s u_s\right] = 0 \qquad (4.95)$$

$$(4.88) + \frac{\rho_b - \rho_s}{\rho_b - \rho_w}(4.89) \Rightarrow \frac{\partial}{\partial t}\left[h_w + \frac{\rho_b - \rho_s}{\rho_b - \rho_w} h_s\right] = 0 \qquad (4.96)$$

where (4.15) was also invoked to derive (4.96).

The four system invariants are thus: the level of the flow free surface, the total flow momentum, the velocity of the clear-water layer, and an equivalent flow depth, that would correspond to the depth of the clear-water layer if the densities ρ_b and ρ_s were equal.

7.2. Equilibrium transport asymptote

Let us consider the initial unsteady uniform flow conditions sketched in Fig. 4.25a, with a clear water layer of depth h_w^0, and no sediment transport. For the existence of a non-trivial solution to system (4.88)-(4.92), there should also exist a corresponding configuration as the one sketched in

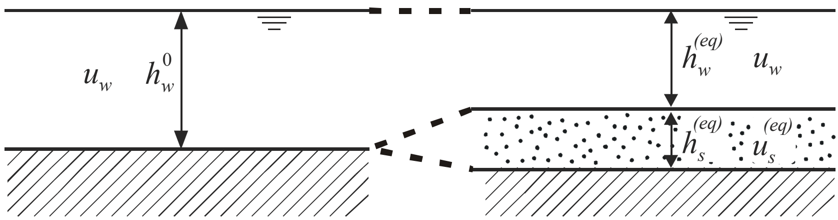

Figure 4.25. Possibility of emergence of a stable sheet-flow layer in the absence of friction, under an equilibrium transport assumption.

Fig. 4.25b, with a non-zero sheet-flow layer of depth $h_s^{(eq)}$ and velocity $u_s^{(eq)}$ that preserve the above invariants.

Expressing the invariance of (4.96) between the two configurations yields:

$$h_w^0 - h_w^{(eq)} = \frac{\rho_b - \rho_s}{\rho_b - \rho_w} h_s^{(eq)} \tag{4.97}$$

and the invariance of the total flow momentum (4.95):

$$\rho_w (h_w^0 - h_w^{(eq)}) u_w = \rho_s \, h_s^{(eq)} \, u_s^{(eq)} \tag{4.98}$$

For the target situation of Fig. 4.25b, the equilibrium assumption on the sediment transport requires that the situation will evolve so as to equate the two shear stresses on both sides of the bed interface. Indeed, a residual difference in shear stress would induce further erosion or deposition until equilibrium is attained. With shear stresses functions (4.26) and (4.28), and neglecting the effects of capillarity and critical bed shear, imposing $\tau_s^{(b)} = \tau_b^{(b)}$ yields an additional relation between the sheet-flow variables $h_s^{(eq)}$ and $u_s^{(eq)}$:

$$\rho_s C^{(b)} {u_s^{(eq)}}^2 = (\rho_s - \rho_w) \, g \, h_s^{(eq)} \tan\varphi \tag{4.99}$$

Defining the dimensionless constant

$$\mu = \frac{\rho_s}{\rho_s - \rho_w} \frac{C^{(b)}}{\tan \varphi}, \tag{4.100}$$

the expression reduces to

$$h_s^{(eq)} = \frac{\mu}{g} u_s^{(eq)2}. \tag{4.101}$$

This relation resembles a classical sediment transport formula, and expresses the equilibrium sediment transport capacity ($\propto h_s^{(eq)} u_s^{(eq)}$) as a function of a flow velocity to the third power. Using (4.97) to suppress the factor $(h_w^0 - h_w^{(eq)})$, and incorporating the equilibrium relation (4.101), the constraint of flow momentum conservation (4.98) can be further elaborated into the following expression:

$$u_s^{(eq)2} \frac{\mu}{g} \left[u_s^{(eq)} - \kappa u_w \right] = 0 \tag{4.102}$$

in which

$$\kappa = \frac{\rho_w}{\rho_s} \frac{\rho_b - \rho_s}{\rho_b - \rho_w} \tag{4.103}$$

is a second dimensionless constant. Besides the trivial solution $u_s^{(eq)} = 0$ corresponding to a status quo of the first configuration (Fig. 4.25a) with no sediment-transport, another solution exists, with the development of a stable sheet-flow layer of the type of Fig. 4.25b, characterised by the following values for equilibrium velocity and depth:

$$u_s^{(eq)} = \kappa u_w \tag{4.104}$$

$$h_s^{(eq)} = \frac{\mu}{g} u_s^{(eq)2} \tag{4.105}$$

One may also observe that in case of $\rho_s = \rho_b$, the constant κ equals zero, and the only solution to (4.102) is the trivial solution $u_s^{(eq)} = 0$. This explains why such a description (Capart and Young, 2002) does not allow the emergence of a sheet-flow layer in the absence of friction. In other words, accounting for granular dilatancy by allowing $\rho_s < \rho_b$ provides a mechanism to supply flow momentum to the eroding grains and allow erosion and sediment transport to take place even in the absence of friction between the two flow layers.

For sake of clarity, the above development assumed that the initial situation was that of a pure water flow with no active sheet-flow layer. Let us now consider the situation of a two-layer flow whose sheet-flow layer was in equilibrium at a time t_i, and assume that the layer variables (depth and velocity) have been perturbed (Fig. 4.26a). This may happen due to other flow mechanisms, and, in the event, due to the spatial gradient terms responsible for the horizontal flow propagation. In order to restore an equilibrium consistent with the adjusted flow variables at time t_{i+1}, one must again find a configuration of the type of Fig. 4.26b that preserves the erosional invariants (4.93)-(4.96). By conducting a similar reasoning than the one performed to obtain (4.104) for the simpler picture of Fig. 4.25, a relation for the equilibrium sheet-flow velocity may be obtained, in the form of a cubic equation:

$$u_s^{(eq)^3} + a_1\, u_s^{(eq)^2} + a_2\, u_s^{(eq)} + a_3 = 0 \qquad (4.106)$$

with coefficients:

$$a_1 = -\kappa u_w \quad , \quad a_2 = 0 \quad , \quad a_3 = -h_s \frac{g}{\mu}\left(u_s - \kappa u_w\right) \qquad (4.107)$$

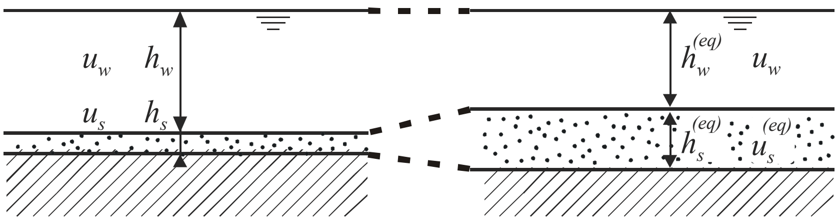

Figure 4.26. Restoration of an equilibrium sheet-flow layer from an arbitrary initial situation.

It may be checked that the relation reduces to (4.104) when the initial sheet-flow thickness h_s equals zero.

7.3. Reduction to homogeneous system

Under the assumption of an instantaneous adaptation towards equilibrium, the system (4.88)-(4.92) may be recast in terms of the four erosional invariants (4.93)-(4.96). To complete the description, the spatial gradient terms of the complete system (4.43)-(4.47) may also be re-introduced. After some rearrangement the following system is obtained:

$$\frac{\partial E_1}{\partial t} + \frac{\partial}{\partial x}\left(h_w u_w + h_s u_s\right) = 0 \tag{4.108}$$

$$\begin{aligned} &\frac{\partial E_2}{\partial t} + \frac{\partial}{\partial x}\left(\rho_w h_w \left(u_w^2 + \tfrac{1}{2} g h_w\right) + \rho_s h_s \left(u_s^2 + \tfrac{1}{2} g h_s\right)\right) \\ &\quad + \left(\rho_w g h_w + \rho_s g h_s\right)\frac{\partial z^{(b)}}{\partial x} + \rho_w g \frac{\partial (h_w h_s)}{\partial x} = 0 \end{aligned} \tag{4.109}$$

$$\frac{\partial E_3}{\partial t} + u_w \frac{\partial u_w}{\partial x} + \frac{\partial}{\partial x}\left(z^{(b)} + h_s + h_w\right) = 0 \tag{4.110}$$

$$\frac{\partial E_4}{\partial t} + \frac{\partial}{\partial x}\left(h_w u_w + \frac{\rho_b - \rho_s}{\rho_b - \rho_w} h_s u_s\right) = 0 \tag{4.111}$$

$$h_s = h_s^{(eq)} = \frac{\mu}{g} u_s^2 \tag{4.112}$$

where $\mathbf{E} = [E_1 \quad E_2 \quad E_3 \quad E_4]$ stand for the four invariants of the unsteady uniform system:

$$E_1 = z^{(b)} + h_s + h_w, \qquad E_2 = \rho_w h_w u_w + \rho_s h_s u_s,$$

$$E_3 = u_w, \qquad E_4 = h_w + \frac{\rho_b - \rho_s}{\rho_b - \rho_w} h_s \tag{4.113}$$

This constitutes a system of four conservation equations, complemented by an equilibrium relation for the sheet-flow layer. Compared to the full set of governing equations (4.43)-(4.47) endowed with five degrees of freedom, the equilibrium assumption thus removes one degree of freedom of the system, by constraining the sheet-flow variables h_s and u_s to stay locked together through (4.112).

A very important property of system (4.108)-(4.111) is that it is homogeneous, i.e. all the right-hand terms are zero, and the left-hand terms contain only time derivatives of the erosional invariants and spatial gradients. As such, any uniform flow state (with zero spatial gradients) is a valid solution provided that it satisfies the equilibrium constraint (4.112). For dam-break type initial conditions, solving (4.108)-(4.111) constitutes a Riemann problem, expected to produce self-similar solutions consisting in a series of uniform states separated by *n* simple waves (shocks or rarefactions, n being the number of degrees of freedom). It should theoretically be tractable by means of semi-analytical techniques, consisting in the explicit integration of Riemann invariants across each wave.

7.4. Computational solutions in the limit of equilibrium transport

If this Riemann problem could be solved analytically, exact analytical solutions for the dam-break problem would be available, extending the analytical solution that Fraccarollo and Capart (2002) derived for the simpler case when $u_s = u_w$ and $\rho_s = \rho_b$ are assumed. However, the derivation of such exact solutions seems largely out of reach in the framework of the present thesis.

Instead, numerical computations are used, relying on a modified version of the numerical code used to produce the comparisons of Section 6. Simply, the friction source operators $\mathbf{S}_\mathbf{F}^{(s)}(\mathbf{U})$ and $\mathbf{S}_\mathbf{F}^{(b)}(\mathbf{U})$ are turned off, and the geomorphic operator $\mathbf{S}_\mathbf{G}(\mathbf{U})$ is replaced by:

$$\frac{\partial h_s}{\partial t} = \frac{1}{\varepsilon}\left(h_s^{(eq)} - h_s\right) \tag{4.114}$$

This is a classical relaxation equation, in which the sheet-flow thickness is assumed to approache asymptotically the equilibrium value according to the relaxation time ε. The limit of equilibrium transport is achieved for very small values of the relaxation parameter ε.

The relaxed geomorphic operator is solved in the following successive steps: (i) obtain $u_s^{(eq)}$ by solving analytically the cubic equation (4.106); (ii) obtain the corresponding equilibrium depth $h_s^{(eq)}$ with (4.105); (iii) solve (4.114) for the updated depth h_s' with an implicit Euler scheme, and (iv) retrieve the other updated variables u_s', h_w' from the operator invariants, and $u_w' = u_w$.

No exhaustive evaluation of the model behaviour and emerging wave structures was performed at this exploratory stage. Though, test simulations were carried out for the typical case of the PVC dam-break experiments, with the following parameters:

- *Initial conditions*: 35 cm of clear-water in the upstream reservoir, a flat granular bed, and a uniform layer of 4 mm of water in the downstream reach;
- *Material properties*: specific density $\rho_M = 1580$ kg/m³, solid concentrations $c_b = 0.58$ and $c_s = 0.22$, corresponding to layer densities $\rho_s = 1128$ kg/m³ and $\rho_b = 1336$ kg/m³, $\varphi = 38°$ and a dimensionless constant $\mu = 2.25$.
- *Numerical parameters*: relaxation parameter $\varepsilon = 0.001$, Courant number $Cr = 0.5$, $\Delta x = 2$ cm, first-order accuracy;

The above parameters are similar to those of Table 4.2 that led to the results of Fig. 4.22, except for two aspects: the adoption of a small downstream layer of water $h_w = 4$ mm, and the new parameter μ. The first was required as a necessary band-aid to avoid de-saturation to occur near the wavefront. It plays a role similar to the capillary effects that were introduced in the full model. The second characterises the equilibrium transport asymptote, and was kept as an adjustable parameter.

Figure 4.27a compares experimental and "equilibrium" numerical profiles at $t = 0.75$ s. The agreement is surprisingly good, given the simplified model. As was explained above, in the absence of any friction at the interfaces, the only mechanism responsible for initiating and driving the sheet-flow layer is the granular dilatancy. The latter is quite efficient in this regard, as seen also on the simulated velocity profiles along the wave plotted in Fig. 4.27b, in solid line for u_w and in dashed line for u_s. Note that here the ratio between u_w and u_s comes out as a model output, rather than being prescribed from an empirical closure law. This is an important strength of a full two-layer approach, which does not make any *a priori* assumption on the profile of layer-averaged velocities.

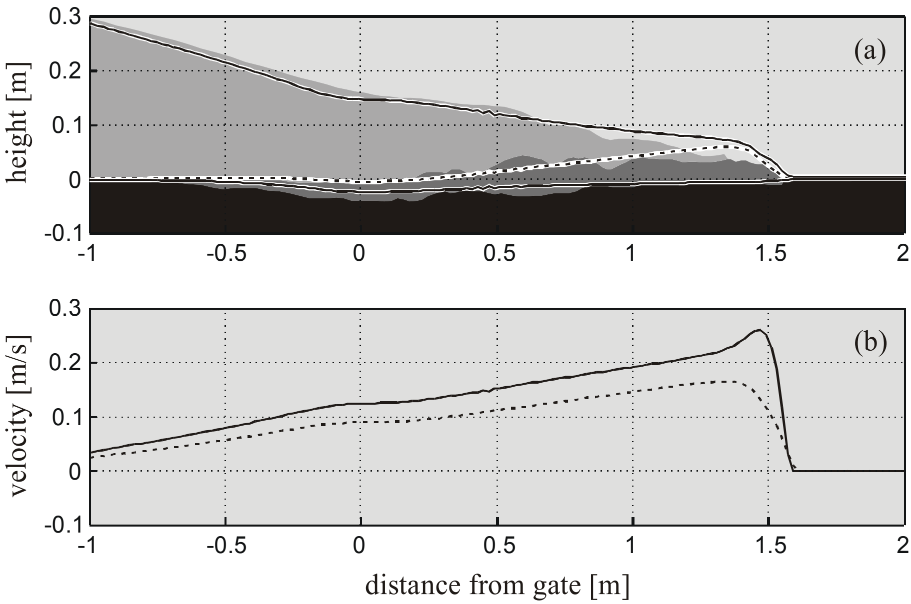

Figure 4.27. Comparisons of "equilibrium" simulations with experiments (PVC, flat bed, $H = 35$ cm, $t = 0.75$ s). (a) simulated flow profiles (solid and dashed lines) and experimental observations (shaded regions); (b) simulated flow velocities in the water (——) and sheet-flow (------) layers.

Chapter 5
Behaviour in case of a discontinuous bed profile: a slope failure mechanism for the fluidisation of unstable bed steps

1. Introduction

As well for the motivation as for the validation of the proposed description, the two previous chapters (3 and 4) relied on experimental dam-break waves propagating over a flat granular bed extending on both sides of the dam. In Chapter 2 other configurations were explored in the experimental campaign, involving an initial discontinuity of the bed profile across the dam section. Such configurations were seen to behave differently, with a pronounced modification, in the very first instants of wave formation, of the bed profile in the immediate vicinity of the discontinuity. In this chapter the behaviour of the model is investigated for such cases. In particular, to reproduce satisfactorily the observed behaviour, it will be necessary to incorporate an additional mechanism in the description, accounting for the initial reshaping of the bed discontinuity that has more to do with soil mechanics than with flow-induced sediment erosion. A simple slope failure criterion is used, that was proposed initially for lateral bank erosion of erodible channels (Spinewine, Capart, *et al.* 2002), in the framework of a two-layer model with equal concentrations in the bed and transport layers. Here it is applied in the longitudinal direction to the failure of unstable bed steps, and different alternatives for implementation are discussed, that come out when extending it to a model with distinct concentrations in the two granular layers. The resulting simulations are faced against their equivalents obtained without this additional mechanism, and against the experiments.

2. Experimental observations

Five experimental configurations explored in Chapter 2 contained a discontinuity of sediment level at the dam, Δz_b, that was defined as positive if the upstream bed level is higher than its downstream counterpart. They were performed with an initial water table maintained at a constant level $z_0^{(w)} = 35$ cm above the downstream sediment level, taken as a reference. The initial depth of the upstream clear water layer is thus $h_{w,0} = z_0^{(w)} - \Delta z_b$. One configuration involved an upward step $\Delta z_b =$ -5 cm, two involved a downward step of height $\Delta z_b = +5$ cm and +10 cm, the latter being also reproduced with a simultaneous layer of clear water of the same height (10 cm) in the downstream reach. Finally, a last configuration involved a downward bed step such that the upstream reservoir is almost entirely filled with sediments; it will not be considered here, as it pertains to a different class of flow, closer to a landslide than to a fluid flow.

The initial formation of the wave is illustrated for the case of a bed step on the basis of the configuration with $\Delta z_b = +10$ cm. The panels of Fig. 5.1 show selected snapshots of the flow at instants immediately following the release of the gate, $t = [0\ \ 0.05\ \ 0.10\ \ 0.15]$ s. On each frame, grain trajectories, reconstructed over a few successive frames (5 frames, or 1/40 s) with the Voronoï imaging techniques (see Chapter 2), are superimposed as red segments. They give an idea of the deformation rate within the granular matrix.

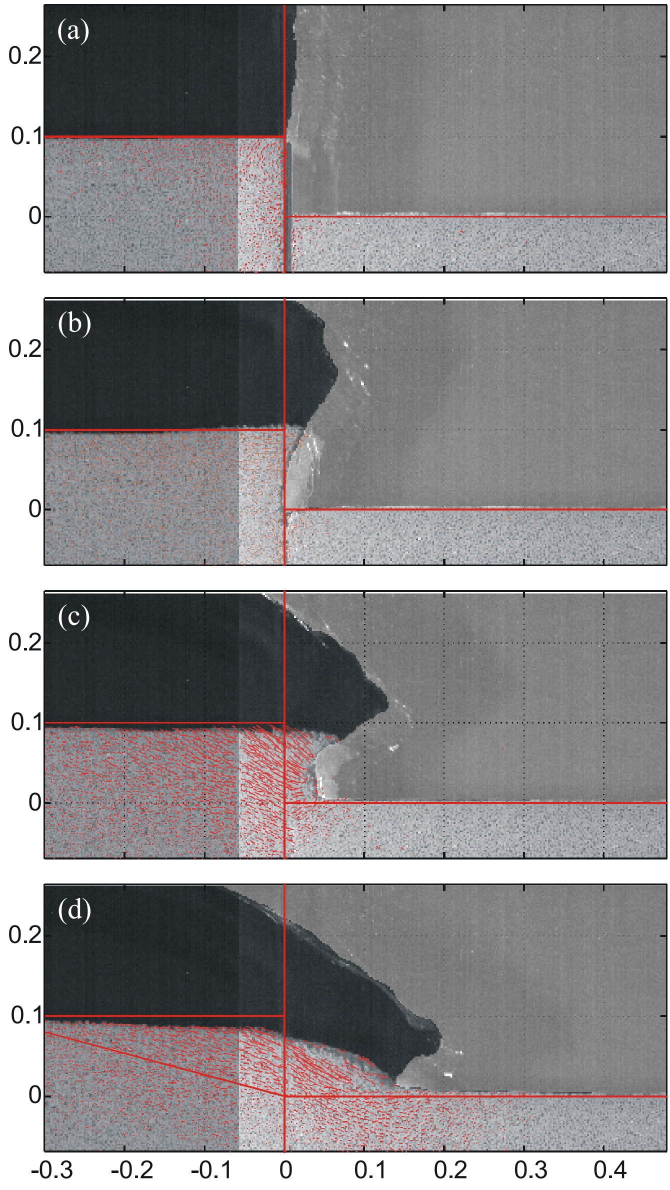

Figure 5.1. Flow snapshots immediately after gate drop-down, at $t = 0$, 0.05, 0.1 and 0.15 s respectively. Initial PVC bed configuration is indicated on each panel as dashed lines. Grain trajectories over 1/40 s in superimposition. Dimensions are in meters.

It is clearly observed in Fig. 5.1 that the bed step does not remain in place as a rigid body. Instead, a substantial portion of the bed is mobilised in the first instants. In Fig. 5.1a, it is observed that near the upper corner of the bed step, the grains are slightly lifted upwards and to the right. It results in a swelling of the bed step visible in Fig. 5.1b. This swelling releases somewhat the sustained inter-particle contacts that prevailed in the solid-like granular bed, allowing sediments to move more freely. Later on (Fig. 5.1c), the bed step further plunges downstream, following the movement of the collapsing water body. The moving region of the bed covers the whole bed step and even a lower portion in the vicinity of the gate. Grain velocities have increased substantially, and trajectories are predominantly oriented in the lower-right direction. In the upper reach, the level of the granular bed has dropped, as opposed to the swelling observed initially in the preceding panel. In Fig. 5.1d, the collapsing bed step has reached the downstream bed level, which is shoved below and forward due to the impact. This results in a curved movement of the downstream bed along a spoon-shaped failure surface. Upstream, the drop of the bed profile has continued, and the moving region of the bed still encompasses a large portion of the step, roughly wedge-shaped as delimitated by the thick oblique line sketched on Fig. 5.1d.

All these massive soil movements may not be explained solely by the erosional action of flow-induced shear stresses. Geotechnical considerations must be invoked. Geotechnical instability is induced by the unstable vertical face of the bed discontinuity, and fluidisation of the unstable bed region is facilitated by the sudden decrease of effective stresses due to the rapid draw-down of the water table, able to fluidise the grains.

As a consequence of geotechnical instability and fluidisation, the bed discontinuity rapidly evolves in a much smoother profile. In turn, it may be expected that the alteration of the bed geometry will affect the hydrodynamics of the dam-break wave. Any predictive numerical model seeking to simulate adequately the propagation of the wave and the evolution of the bed should thus incorporate somehow a mechanism to account for this initial failure. The need for such a mechanism is illustrated in Fig. 5.2, where experimental observations, for the same experiment as above but at two later instants, are compared with numerical simulations obtained with the two-layer shallow water model presented previously. In Chapter 4, the model was successfully validated for a flat bed profile, but Fig. 5.2 shows a very different picture. If the agreement is relatively satisfactory in the region of the wavefront, the simulation largely fails to reproduce the observed behaviour in the other regions: (i) in the vicinity of the gate, the simulated bed step remains steep and is only gradually eroded by the flow. A control section rapidly develops above the step, that determines the discharge. The downstream flow is much more rapid and able to erode the bed more actively, so that a deep scour hole forms in that region, which is not present in the experiments; (ii) due to the control section upstream, the discharge released from the reservoir is underestimated, and consequently the water profile throughout the downstream reach is lower than observed.

This makes it clear that the sole action of flow-induced erosion is insufficient to explain the reshaping of the bed discontinuity at the first instants. Geotechnical considerations must be invoked. A simple criterion is proposed below, first developed in the context of lateral bank erosion of erodible valleys but easily adapted for the present purpose.

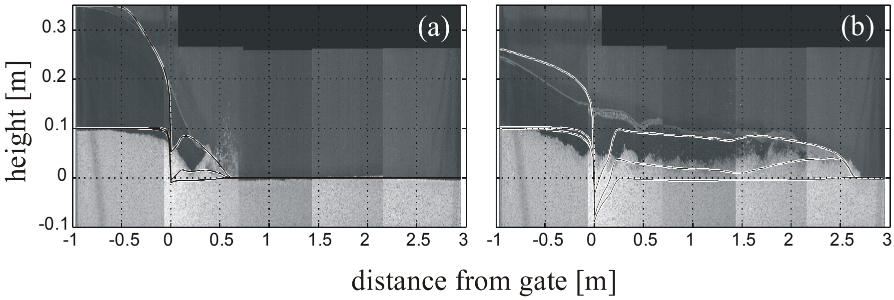

Figure 5.2. Simulated flow profiles in the absence of any bed step failure mechanism, faced against mosaic images for the same experimental configuration as Fig. 5.1, at (a) $t = 0.25$ s and (b) $t = 1.5$ s. Dimensions in meters, vertical scale exaggerated by a factor 5.

3. A slope failure mechanism derived from bank erosion studies

The erosive power of the dam-break waves explored so far was restricted to the modifications of the longitudinal bed profile, in an experimental channel whose lateral boundaries were constrained. Actual dam-break floods, however, can significantly rework the morphology of erodible valleys (Lapointe *et al.*, 1998; Brooks and Lawrence, 1999). They exert their geomorphic action not only on the bed of the valley, but also on its flanks: the bankline itself may retreat severely under the attack of surging waters. Observations in the laboratory (Goncette and Spinewine, 1998; Jonard and Le Grelle, 2001) indicate that the bankline retreat proceeds in a sequence of discrete block failures. Destabilised chunks of banks collapse and slump into the channel, before dissolving into the stream. The overall impact of the flood is then determined by a strong interaction between in-channel and bank processes.

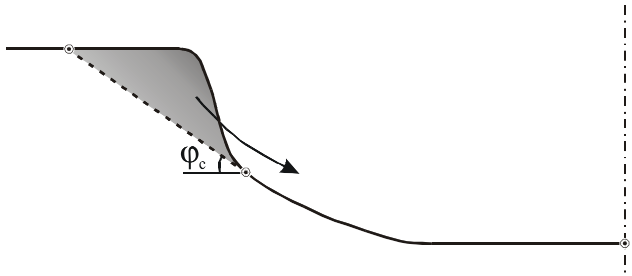

Figure 5.3. Principle of a discrete mass failure triggered by slope instability

In a previous work (Spinewine, Capart, *et al.*, 2002), a relatively simple criterion to account for discrete bank failure events due to geotechnical instability was proposed. A similar concept is utilised for the initial bed failure of stepped-bed dam-break experiments. The basic idea is illustrated in Fig. 5.3. The stability of the bank is characterised by a critical repose angle, and a block failure is triggered whenever the local slope of the bank exceeds a critical repose angle. The failed material, situated above the failure surface, is incorporated in the flow as additional sediment material available for transport. In Spinewine *et al.* (2002), the mechanism was further refined by (i) distinguishing a *critical* angle, at which failure is initiated, and a *residual* angle, delimiting the actual extent of failure and the adopted profile after failure; and (ii) considering distinct stability angles for submerged and emerged regions of the bank. Such refinements have proven useful when simulating lateral widening of erodible channels.

Our present context of a longitudinal bed failure in the vicinity of the dam differs substantially from the context of lateral bank failures. Tough, the same simple criterion (without the four-angles refinement) may be used to account for the mass failure of the bed step observed at the first instants. Furthermore, it is conveniently incorporated in a two-layer flow model. If one assumes that the failed bed material is instantaneously fluidised, it may be simply transferred into the sheet-flow layer, so that its subsequent movement is then taken over by the two-layer flow algorithm.

When fluidising the bed material into the sheet-flow layer, however, one must be especially careful at respecting the postulated flow structure with constant layer densities. In Chapter 4, granular dilatancy was considered as a mechanism responsible for the reduction of granular concentration in the sheet-flow layer as compared to the static bed. The description was simplified by assuming piecewise constant profiles of the solid concentration, with a representative value for the bed, and a lower representative value for the sheet-flow layer. Thus, the failed bed material from geotechnical instability, if incorporated in the sheet-flow layer, must evolve from a bed density ρ_b to a sheet-flow density ρ_s . In order to ensure mass conservation in the system, the sheet-flow layer must thus dilate, and add a volume of water to counterbalance the expansion of the granular matrix. The overall process was previously explained in details in Chapter 4, Section 2.2.

4. Possible alternatives for practical implementation

In this context, several alternatives are possible to distribute the volume of the failed material resulting from the geotechnical instability of the bed step. They are summarised in Fig. 5.4. The first panel recalls the initial situation of the bed step. Fig. 5.4b illustrates the failure surface and the fluidisation of the bed material situated in the triangular region above it. However, in the case of the model with distinct concentrations, the sole incorporation of this triangular region in the sheet-flow layer as such would violate mass conservation, for the reason explained above, and is not acceptable.

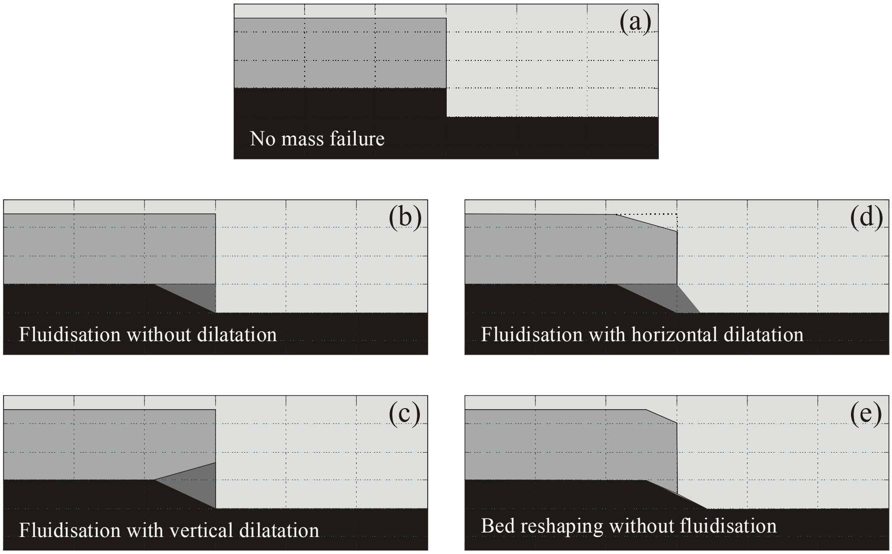

Figure 5.4. Various alternatives for implementing a mechanism for mass failure of the bed discontinuity.

A method that would account correctly for granular dilatation is the one sketched in Fig. 5.4c. At each location, i.e. at each computational cell of the numerical model, the top level of the sheet-flow layer is raised so as to ensure mass conservation of sediments according to the evolving density. This is performed using exactly the same principles as the ones described in Chapter 4 (Section 4.1.5.), for flow-induced erosion. This results in the creation of the inverse triangular region visible on top of the sheet-flow layer. The advantage of this method is precisely that it is local and involves no horizontal displacement of material, but only in-cell transfers of material between the three layers. It does not rely on any predefined shape of the bed profile, and thus allows to account not only for the failure of the initial bed step at the gate, but for any unstable portion of the bed profile that may appear at any instant of the simulation, an argument that could be significant when applying the model to real valleys with a complex topography: at every time step (or every few time steps to limit the associated computational cost), the computational domain may thus be surveyed for unstable bed slopes. Failure toes are identified, and the failed material is expanded vertically within each cell affected. In the process of vertical expansion, one should also account for the transfer of momentum between the two flowing layers, just as one had been doing for the flow-induced erosion process considered in Chapter 4 (Section 4.1.5.).

The method of Fig. 5.4c has nevertheless one prominent drawback, that may be explained in terms of energy. The vertical dilatation of the fluidised bed material induces a vertical redistribution of weight as the grains, heavier than water, are lifted upwards. This causes an increase of the total potential flow energy. In the case of gradual flow-induced erosion, this gain of potential energy is limited, and largely counterbalanced by a loss of kinetic energy of the sheet-flow layer, due to the inertia of the eroded grains, leaving the static bed with no initial velocity (see Chapter 4, Section 3.3). But in contrast, for the failure of the bed discontinuity at the first time step, (i) the volume of fluidised material is much more significant, and so is the related gain of potential energy; (ii) the flow has not started yet, so that the dilatation does not induce any loss of flow kinetic energy. The method of Fig. 5.4c thus violates the physical constraint that any mechanical system may evolve only so as to preserve or dissipate energy.

In fact, the vertical dilatation of the grains does not occur instantaneously. Rather, the failed material is initially fluidised without change of solid concentration, as if it simply experienced a phase change from a solid-like to a fluid-like behaviour (Capart, 2000). The concentration in the sheet-flow layer then gradually adapts towards a local equilibrium value corresponding to the flow conditions. Figure 5.5 motivates this description experimentally by plotting the time evolution of the average granular concentration within the sheet-flow layer, again for the same initial configuration with a bed step $\Delta z_b = +10$ cm. As in Chapter 4 (Section 2.1.3.), estimates of concentration are obtained by balancing the areas of the bed and sheet-flow layers, considering that the total mass of sediments within the field of view is constant. Starting from a value close to the one of the static bed, the concentration slowly diminish towards a value similar to the one observed for the flat bed configuration (see Fig. 4.5 in Chapter 4). Accounting for this observed behaviour with the current flow description is simply not possible. It would require to consider the concentration as an evolving variable, which is believed to bring many additional complications in the theoretical framework and would require additional closure laws without necessarily leading to substantial improvements. Instead, the gradual adaptation of concentration is disregarded, considered as a temporary phenomenon.

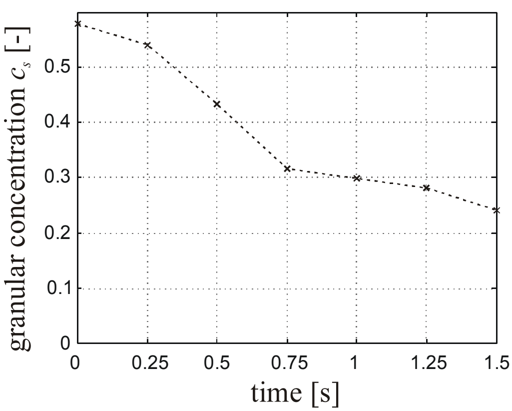

Figure 5.5. Evolution of wave-averaged granular concentration in the moving sediments region, for the same experimental configuration as Fig. 5.1.

Coming back to the failure of the initial bed step, the increase of potential energy associated with the solution of Fig. 5.4c is more and more pronounced as the difference between layer densities ρ_b and ρ_s is significant. Two special corrections are possible to counter this unphysical increase of energy. The first is to displace the dilating grains horizontally instead of vertically. The solution described in Fig. 5.4d is obtained, where the upper triangle of fluidised material above the initial bed level is transferred just downstream of the dam. To ensure conservation of water, a small triangle of water must then also be subtracted from the reservoir. This configuration may appear as a kitchen recipe, somewhat artificial, but is in fact much closer to the actual behaviour observed in the experiments (see Fig. 5.1d). It has also the advantage of verifying the energy inequality constraint, the global potential energy of the system being reduced.

Fig. 5.4e is a last alternative, where the initial failure of the bed step is viewed solely as a local reshaping of the bed profile, no sediment being actually fluidised and transferred to the sheet-flow layer. An advantage of this alternative is that it does not explicitly requires a two-layer flow description, and may thus be implemented also with most classical morphodynamic codes based on a flow model coupled with an external sediment-transport routine. However, at least for the PVC tests it does not replicate the sustained mobilisation of the grains that was observed in the experiments (Fig. 5.1).

5. Comparisons

There is no clear physical argument indicating which of the above mechanisms should be selected as appropriate for modelling, each having advantages and drawbacks, and representing only a facet of the actual behaviour. If the difference in concentration between the two granular layers considered in the model is substantial, the methods of Figs. 5.4b and 5.4c should preferably be rejected, as (i) the first violates mass conservation in the system; (ii) the second involves an instantaneous dilatation of the fluidised material along the vertical that was not observed experimentally, and violates the energy constraint. The observations of Fig. 5.1 for the PVC bed in the near field tend to support the method of Fig. 5.4d, with a horizontal dilatation, but there is no evidence that the same would hold for the heavier sand, which could be more prone to redeposit very quickly at a smoother angle after the initial failure, thus conforming the method of Fig. 5.4e. Also the initial configuration may influence the mode of failure. For example, in the presence of an initial layer of water downstream of the dam, the stability of the bed step is increased, so that real sustained fluidisation may be prevented.

Instead of claiming a priori one mechanism as universally preferable, the different alternatives were thus all implemented numerically (except the non-conservative method of Fig. 5.4b which was rejected), and here one compares the various model simulations with experiments. At first, the reference configuration of Fig. 5.1 is again considered, i.e. a PVC bed with a step $\Delta z_b = +10$ cm. The experiment allowed to illustrate the failure mode of the bed discontinuity in the near field. Here the implications of the initial failure mode on the model behaviour in the far field are studied. In a second stage, model simulations are faced with other experimental configurations. The purpose is not to present extensive comparisons for all the configurations, and hence only a few selected results are shown. Results for the other bed configurations did not bring substantial new findings. For all the simulations reported hereafter, model parameters are essentially the same as the ones that were used throughout Chapter 4 (see Table 4.2). The sole additional parameter is the representative failure angle of the bed step. A value of 15° was adopted, taken from the visual observations of Fig. 5.1.

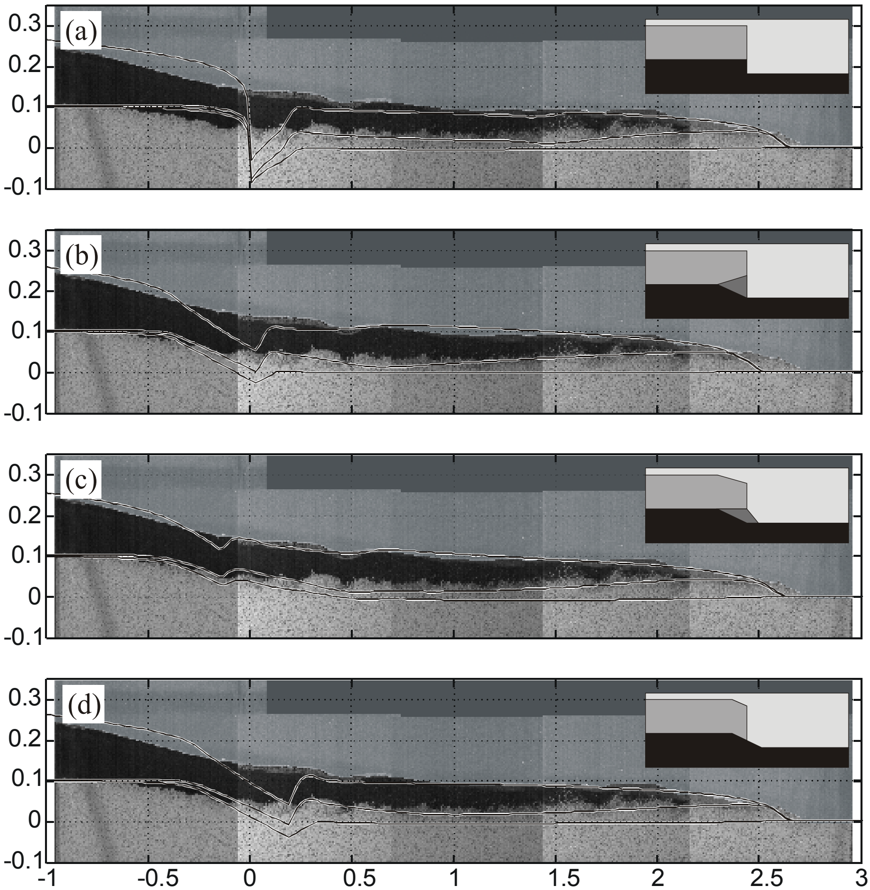

Figure 5.6. Implication of the simulated mode of failure on the wave behaviour in the far-field (PVC, downward bed step of 10 cm, $H = 35$ cm, $t = 1.5$ s); (a) no mass failure; (b) fluidisation with vertical dilatation; (c) fluidisation with horizontal dilatation; dimensions in meters, vertical scale stretched by a factor 2.

Figure 5.6 compares the various alternatives for the reference case (a PVC bed with a step $\Delta z_b = +10$ cm) at instant $t = 1.5$ s. Figure insets indicate the considered failure mechanism, the first panel thus reproducing the profiles obtained with the standard model. All the failure modes lead similar results near the wavefront, and are in relatively good agreement with the experiments in that region. In the vicinity of the gate, the methods of vertical fluidisation (Fig. 5.6b) and bed tilting (Fig. 5.6d) preserve a steep bed slope at the residual bed step, whereas the experimental wave has flattened out more the bed profile. They lead both to the emergence of a spurious scour hole, though to a less extent than on Fig. 5.6a. The best agreement is obtained for the case of horizontal fluidisation (Fig. 5.6c). The latter was already identified as the most realistic mode of failure in the near field. As compared to Fig. 5.6a, it yields also substantial improvements in the far field in terms of water profile all along the downstream reach.

Figure 5.7 features an equivalent comparison of alternatives for the case of a sand bed, at instant $t = 1.25$ s. In contrast to the PVC observations, the methods that account for a sustained fluidisation of the bed step lead the worst agreement: they significantly underestimate the celerity of the wavefront and overestimate water levels in the downstream reach. The best concordance is here obtained for the simple tilting of the bed (Fig. 5.7d).

Although the bed step is completely reshaped at the initial instants as a result of geotechnical instability, it looks as if the failed bed material could not be fluidised for a sustained period by the rushing waters. Density, in this regard, certainly provides the major argument for the difference in behaviour between sand and PVC experiments. The larger grain size and roundness of the PVC pellets may also explain their greater proneness to fluidisation.

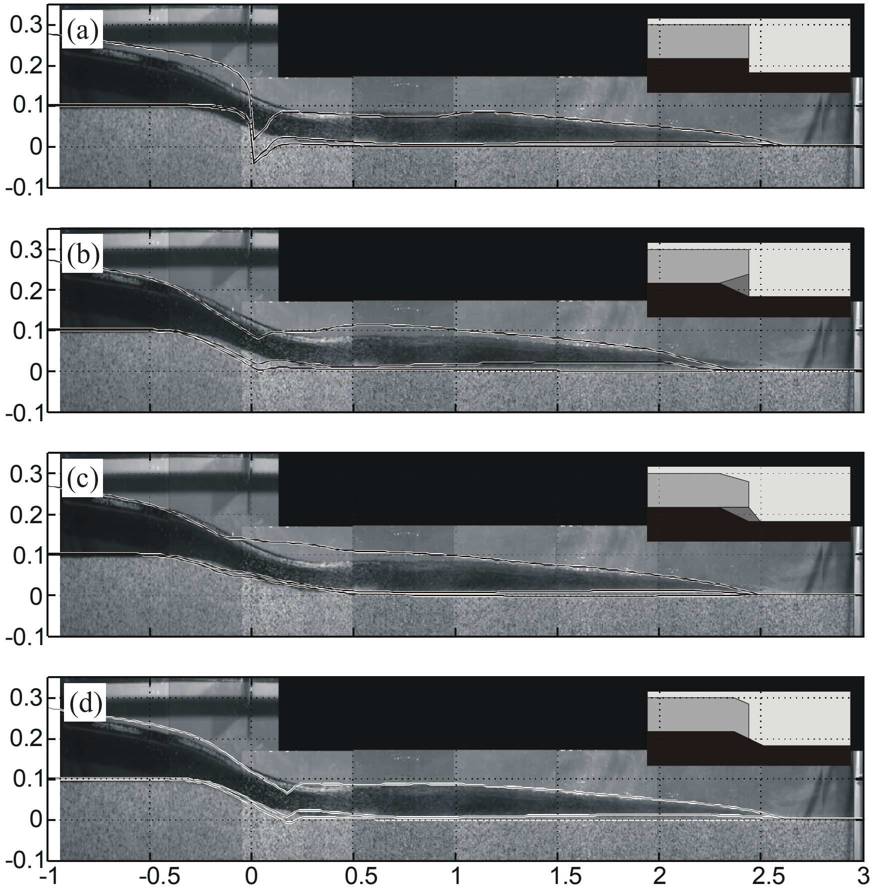

Figure 5.7. Implication of the simulated mode of failure on the wave behaviour in the far-field (Sand, downward bed step of 10 cm, $H = 35$ cm, $t = 1.5$ s); dimensions in meters, vertical scale stretched by a factor 2, mode of failure in the insets as in Fig. 5.4.

The other bed configurations that were reproduced experimentally (see Chapter 2), with a lower bed step or an upward bed step, were also faced with simulations, leading observations and conclusions similar to the case discussed above. To complete the description, results for the configuration

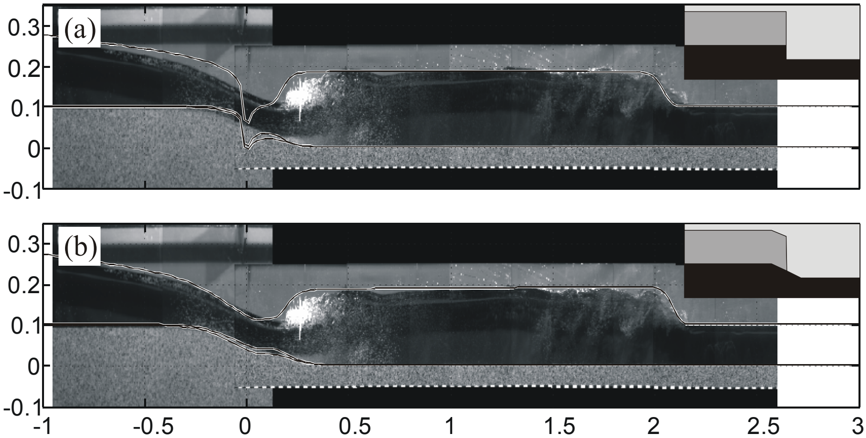

Figure 5.8. Comparisons of simulated profiles and experimental images in the case of a downward bed step combined with a downstream water layer. (a) simulations without any failure mechanism; (b) with initial reshaping of the bed step. Time $t = 1.25$ s, dimensions in meters, vertical scale stretched by a factor 2.

involving a downstream layer of water, which is a more particular case, are presented in Fig. 5.8. The sand bed is taken as an example, with the failure mode of bed tilting. The agreement of simulated profiles with the experimental mosaic is surprisingly good.

In fact the intensity of bed modifications for this configuration is much lower, the presence of water downstream generating a hydraulic jump, under which all the sediments transported from around and upstream the bed step redeposit as the flow velocities drop abruptly.

6. Conclusions

The near-field behaviour of experimental dam-break waves was investigated for configurations involving an initial discontinuity of the bed profile across the dam. In the first instants, massive soil movements were found to occur in the vicinity of the discontinuity, whose cause is to be found in geotechnical instability rather than flow-induced sediment entrainment. In turn, this initial alteration of the bed profile is susceptible of affecting the overall wave behaviour in the long term, and not only in the immediate vicinity of the dam, comforting the need to account for such effects in the simulations. A simple mechanism was proposed, based on a principle of a critical slope angle initially set up for modelling lateral bank erosion of erodible valleys. Different methods for implementing the approach in the context of the two-layer flow model were discussed. They were compared with the experiments for two distinct configurations and for the two bed materials. They provided significant improvements as compared to results obtained without any such failure mechanism. Although, no clear evidence was found to discriminate between the method consisting in a real fluidisation of the bed step, and the method relying simply on a local tilting of the bed profile without fluidisation; the first yielding best results for the light PVC bed and the second for the heavier sand bed.

Chapter 6
Conclusions

Geomorphic floods induced by the failure of a dam or flood-defence structure may trigger large modifications of the downstream channel bed and banks. The presence of large sediments and boulders in the rushing waters, usually not transported by normal floods, may increase its destructive power against infrastructure; fine sediments may be transported over long distances and create widespread deposition in wider and flatter areas, which are more densely populated and used. Overall, in terms of damages to mankind and infrastructure, the sedimentological impacts of such floods may be much larger than the impacts of the flooding itself.

Traditional alluvial morphodynamic models, based on pure hydrodynamic flood routing scheme combined with a "passive" sediment transport module, seem inappropriate to predict geomorphic bed evolution adequately during highly transient floods having intense and non-uniform sediment transport.

Previous authors (Capart, 2000; Fraccarollo and Capart, 2002) have shown that it is crucial in this regard to account for the sediment inertia. They proposed to describe the flow as having a sharp layered structure, composed of a clear-water layer and a moving sediment layer, the latter interacting with the sediment bed substrate. They adopted a discontinuous view of the evolving bed profile, in which erosion or deposition results from a downward or upward displacement of the interface separating the solid-like bed from the fluid-like moving sediment mixture. A similar strategy was adopted in the present work.

To address the issue and investigate the mechanisms of geomorphic evolution and sediment transport in such conditions, idealised laboratory experiments were presented in Chapter 2. A dedicated flume, and the benefit of the experience gained in previous series of dam-break experiments in the laboratory, permitted to attain test conditions that approach best the idealization of an instantaneous dam collapse. High-speed digital imaging through the flume sidewalls combined with particle tracking imaging algorithms furnished a detailed visualization of the flow field both in the water and within the sediment transport layer. It was experimentally observed that: (i) as compared to a rising gate system, a lowering gate induces less perturbations to the flow and to the sediment bed during the withdrawal; (ii) in the short-time near field of wave formation and propagation, plunging breakers are generated, similar to the ones observed for pure liquid waves; (iii) the observations for the class of sediments that were investigated confirm a layered flow structure with sharp interfaces separating the distinct flow regions; (iv) the longitudinal flow velocity is not constant throughout the flow depth. Rather, observations suggest a roughly linear evolution within the sediment transport layer, and a nearly constant value in the clear-water layer; (v) the average bulk sediment concentration in the transport layer is significantly lower than that in the bed, but is nearly constant in time. Through a wide range of transport intensities, it remained within a narrow range around 0.25; (vi) sediment transport is much more intense for lower granular densities. Dam-break waves over lighter sediment beds are also more prone to generate in-phase undulations of the free-surface and bed profiles, that are reminiscent of the antidune bedforms of alluvial channels in supercritical regime; (vii) tests performed with the same bed configuration but different water levels in the upstream reservoir scaled surprisingly well with Froude similarity; (viii) for configurations involving an initial discontinuity in bed levels across the dam, failure of the bed step and massive soil movements were observed in its vicinity at the first instants, resulting in a significant reshaping of the bed profile.

Based on experimental observations, a theoretical framework is proposed for the simulation of dam-break induced geomorphic floods with a multi-layer shallow-water approach. Departing from the idealized flow structure of Capart (2000) and Fraccarollo and Capart (2002), it is shown that a number of assumptions may be relaxed without making the resulting description intractable, but yielding new insights into the mechanisms of sediment erosion and bulking into the flow. In particular, two major extensions have been examined, which allow the two flowing layers to move at distinct velocities, and consider the effect of granular dilatancy associated with erosion.

The first extension was examined in Chapter 3. The two-layer shallow water equations with a density contrast, which are well-known, have been incorporated in a numerical model whose behaviour was scrutinized for dam-break flows, involving the release of a mass of "light" fluid over a substrate of "heavy" fluid, leading to some observations that do not seem to have been examined systematically before. It is observed that: (i) the two-layer shallow water equations may be elegantly derived from Hamilton's principle of least-action; (ii) hyperbolicity of the system of equations is not guaranteed for a range of velocity difference between the two shallow layers. Loss of hyperbolicity stays confined to relatively narrow bands, whose limits depend on the density ratio and on the depth ratio between "light" and "heavy" fluid layers; (iii) flow conditions moving close to or inside the non-hyperbolic region may possibly result in instabilities emerging at the interface between the layers; (iv) model simulations converge well towards analytical solutions available for degenerate cases with equal layer densities ($\rho_1 = \rho_2$) or equal layer velocities ($u_1 = u_2$ but $\rho_1 \neq \rho_2$); (v) while a sharp contact discontinuity between regions of light fluid and heavy fluid is found for those two degenerate cases, converged numerical simulations obtained for the general case ($\rho_1 \neq \rho_2$ and $u_1 \neq u_2$) reveal a more gradual transition in the form of a rarefaction wave; (vi) while the limits $\rho_1 / \rho_2 = 1$ and $\rho_1 / \rho_2 = 0$ correspond respectively to the well-known Stoker and Ritter solutions, results obtained in the intermediate range of density ratios suggest a series of solutions that do not seem to have been observed yet, composed of four distinct waves; (vii) the fastest wave is observed ahead of the main wavefront, and closely reproduces the tip of the Ritter wavefront observed for $\rho_1 / \rho_2 = 0$. It is proposed to refer to this peculiar wave as the "Ritter pinch-off"; (viii) a Ritter pinch-off may exist only for density ratios sufficiently lower than 1, when the main wavefront becomes of a mixed type, composed of both light and heavy fluids; (ix) stability Froude numbers within the main wave and the Ritter pinch-off are situated on the two opposite sides of the band characterizing loss of hyperbolicity, and the transition was found to occur sharply across the position of the main wavefront; (x) simulations obtained with this simplified two-layer model are in a relatively good agreement with dam-break experiments over movable beds in case of very light sediments, but completely fail to simulate adequately the case of a bed composed of heavier sediments.

The second extension was examined in Chapter 4, in which the two-layer model was supplemented with a vertical flow structure that governs the exchanges of mass and momentum between the layers as a result of erosion or deposition. The main contribution of the proposed description was to account for granular dilatancy associated with erosion, by considering a solid concentration in the transport layer which is lower than in the bed. Granular dilatancy was found to have several implications on the flow dynamics, the most prominent being to generate a strong mechanism of coupling between the transport layer and the clear-water layer: transfers of water occur across the interface separating the two, and are required to counterbalance the deficit of interstitial water generated in the transport layer due to the dilating sediments. The description has been formalised into a set of governing equations, and some specificities of the numerical implementation were presented. The behaviour of the model and the influence of its parameters was studied, and simulations have been compared with the experiments. It is observed that: (i) comparisons between experiments and simulations with the full model gave very good agreement, in terms of wavefront celerity, free surface profile, bed scour, thickness of sediment transport layer, and, qualitatively, ratio between velocity in each layer. This was obtained for the sand bed and for the PVC bed by using a single set of adjusted model parameters, the simulations thus only differing in terms of sediment density and diameter; (ii) mechanical energy is dissipated both by friction and by geomorphic exchanges. Energy dissipation from geomorphic exchanges was found most significant in the near field, while friction predominates at later times; (iii) when not considering granular dilatancy, friction between the layers must be artificially increased in order to retrieve a satisfactory behaviour; such friction parameters may not provide reliable estimates of sediment transport under uniform flow conditions, and do not lead a realistic ratio between velocities in the clear-water and sediment transport layers under dam-break conditions; (iv) capillary forces may have a significant influence in the region of the wavefront when the latter becomes fully saturated in moving grains. They may prevent de-saturation of the wavefront to occur; their incorporation in the model yielded a better agreement with experiments in that region; (v) when performing simulations with second-order accuracy on very fine meshes, oscillations were generated along the internal rarefaction just upstream of the wavefront. Instead of amplifying, the oscillations then evolved into a regular train of undulations. Although some degree of relation is possible with the potential loss of hyperbolicity and stability condition of two-layer flows as identified in Chapter 3, no straightforward relationship between physical and numerical undulations could be proven; (vi) when neglecting friction and considering that sediment transport adapts instantaneously towards equilibrium, a reduced set of equations may be obtain in the form of a homogeneous system, thus associated with a Riemann structure.

In Chapter 5 the behaviour of the laboratory dam-break waves was investigated for the cases where the bed profile exhibits a level discontinuity across the dam. Several simple mechanisms are proposed, based on geotechnical considerations to account for the mass failure of the bed step observed at the first instants. The incorporation of this additional mechanism in the model was seen to significantly improve the agreement between simulations and observations in the neighbourhood of the dam.

Ultimately, one possible direction for further work is stressed. Recently, the model was extended to two horizontal dimensions. This 2D extension relies on an unstructured triangular mesh and solves the 1D Riemann problems in the direction orthogonal to every cell face. The architecture of the code is built on the skeleton of a one-layer model on a fixed bed, developed by V. Guinot at Université Montpellier II (Guinot, 2003), that was kindly made

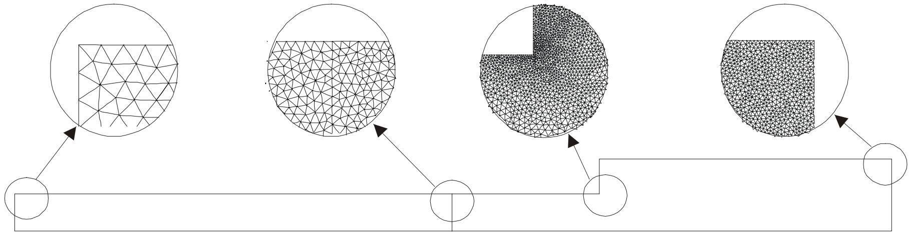

Figure **6**.1. The triangular computational mesh used in the 2D computations.

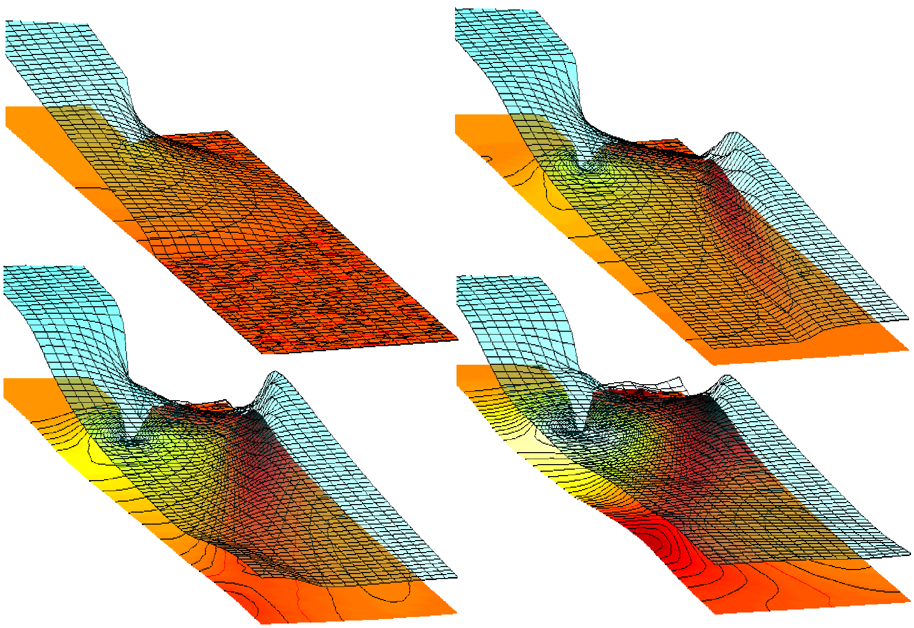

Figure **6**.2**a-d**. Simulated flow snapshots at times $t = 1,2,3$ and 5 seconds, respectively. The bed topography is shown through the translucent water surface, with depth contours every 1 mm.

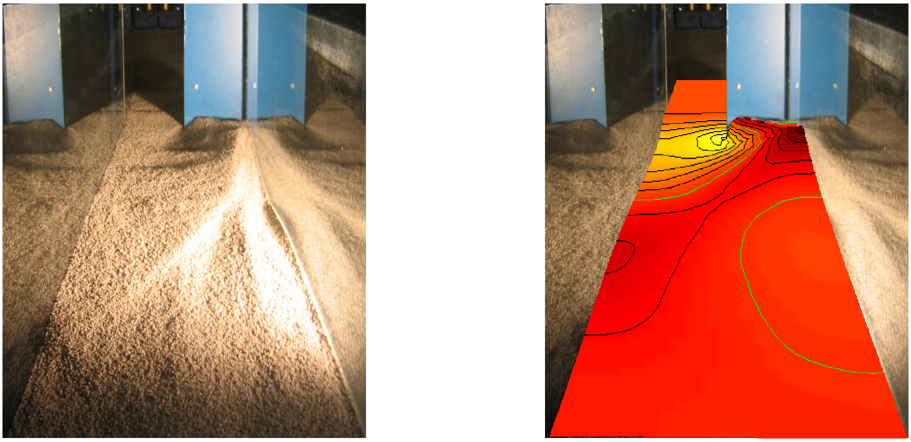

Figure **6**.3. Left: Downstream photograph of the final bed topography. Flow was from top to bottom. Right: simulated bed profile in superposition, with depth contours every 4 mm.

available for the present work. Preliminary results were obtained by applying the 2D model to the case of a sudden channel enlargement. For comparison, laboratory experiments were performed in collaboration with a student investigator (Silva, 2004) in the same flume as the one designed for the experiments described in chapter 2, but with the adjusted configuration of Fig. 2.4, with a sudden asymmetric enlargement at one meter downstream of the gate. The triangular mesh used for the 2D simulation is shown in Fig. 6.1, and was generated using the Gmsh package (Geuzaine & Remacle, http://www.geuz.org/gmsh/), with local mesh refinement in the neighbourhood of the inner corner at the sudden enlargement. Fig. 6.2 shows some snapshots of the simulated flow, and Fig. 6.3 qualitatively compares the modelled final bed topography with a picture of the experiment.

Once the 2D model is validated against idealized laboratory situations, the final objective is to apply it to the real scale on natural topography. Owing to the large amount of data available for the pre-flood and post-flood conditions, the case study of the failure of the Ha! Ha! Lake in the Saguenay region of Quebec in 1996 (Brooks and Lawrence, 1999; Capart, Spinewine *et al.* 2003) will seem a legitimate candidate in this regard.

References

ABBOTT M.B. 1979 *Computational Hydraulics*. London: Pitman.

ARMANINI A., CAPART H., FRACCAROLLO L., LARCHER M. 2005 Rheological stratification in experimental free-surface flows of granular-liquid mixtures. *J. Fluid Mech.* **532**, 269-319

ARMI L. 1986 The hydraulics of two flowing layers of different densities. *J. Fluid Mech.* **163**, 27

ARTALE V., LEVI D. 1988 Solitary waves in straits. In *Nonlinear Evolutions*. J.J. Leon (ed). World Scientific

AUDUSSE E. 2005 A multilayer Saint-Venant model: Derivation and numerical validation. *Discrete and continuous dynamical systems-Series B* **5**(2), 189–214

BELLAL M., SPINEWINE B., SAVARY C., ZECH Y. 2003 Morphological evolution of steep-sloped river beds in the presence of a hydraulic jump: experimental study. *Proc. 30th IAHR Congress*, Thessaloniki, Greece, August 25-31, Vol C-II pp. 133–140

BENITO G., GRODEK T., ENZEL Y. 1998 The geomorphic and hydrologic impacts of the catastrophic failure of flood-control dams during the 1996-Biescas flood (Central Pyrenees, Spain). *Z. Geomorph.* **42**, 417–437

BROOKS G.R., LAWRENCE D.E. 1999 The drainage of the Lake Ha!Ha! reservoir and downstream geomorphic impacts along Ha!Ha! River, Saguenay area, Quebec, Canada. *Geomorphology* **28**(1-2), 141–168

CAPART H. 2000 *Dam-break induced geomorphic flows and the transition from solid- to fluid-like behaviour across evolving interfaces*. PhD thesis, Université catholique de Louvain.

CAPART H. 2002 *A mathematical theory of shallow geomorphological flows*. Lecture notes, National Taiwan University.

CAPART H. 2004 *Shallow Flow*. Lecture notes, National Taiwan University.

CAPART H., SPINEWINE B., YOUNG D.L., ZECH Y., BROOKS G.R., LECLERC M., SECRETAN Y. 2003 The 1996 Lake Ha! Ha! breakout flood, Québec: proposed test case for geomorphic flood models. in EC Contract EVG1-CT-2001-00037 IMPACT *Investigation of Extreme Flood Processes and Uncertainty*, Proc. 3rd project workshop, Louvain-la-Neuve, Belgium.

CAPART H., YOUNG D.L. 1998 Formation of a jump by the dam-break wave over a granular bed. *J. Fluid Mech.* **372**, 165–187

CAPART H., YOUNG D.L. 2002 Two-layer shallow water computations of torrential geomorphic flows. *River Flow 2002, Proc. 1st IAHR Int. Conf. on Fluvial Hydraulics*, Louvain-la-Neuve, Belgium, Bousmar D. & Zech Y.(eds). Balkema: pp. 1003–1012

CAPART H., YOUNG D.L., ZECH Y. 2002 Voronoï imaging methods for the measurement of granular flows. *Exp. Fluids* **32**, 121–135

CHAPMAN C.J. 2000 *High Speed Flow.* Cambridge University Press.

CHEN S.C., PENG S.H., CAPART H. 200X Two-layer shallow water computation of mud flow intrusions into quiescent water. Submitted to *J. Hydr. Res.*

CHEN Y.H., SIMONS D.B. 1979 An experimental investigation of hydraulic and geomorphic changes in an alluvial channel induced by failure of a dam. *Water Resources Research* **15**, 1183–1188

CUSHMAN-ROISIN B. 1994 *Introduction to Geophysical Fluid Dynamics.* Prentice Hall.

DOUXCHAMPS D., DEVRIENDT D., CAPART H., CRAEYE C., MACQ B., ZECH Y. 2005 Stereoscopic and velocimetric reconstructions of the free surface topography of antidune flows. *Exp. Fluids*, in press (published online 15 June 2005)

DOUXCHAMPS D., SPINEWINE B., CAPART H., MACQ B., ZECH Y. 2003 Particle-based imaging methods for the characterisation of complex fluid flows. *Proc. BSMEE European Workshop Photomec'02*, Louvain-la-Neuve, Belgium.

DRAZIN P.G., REID W.H. 1981 *Hydrodynamic stability.* Cambridge University Press.

FERREIRA R.M.L., LEAL J.G.A.B., CARDOSO A.H., ALMEIDA A.B. 2003 Sediment transport by dam-break flows. A conceptual framework drawn from the theories for rapid granular flows. *In* EC Contract EVG1-CT-2001-00037 IMPACT *Investigation of Extreme Flood Processes and Uncertainty*, Proc. 3rd project workshop, Louvain-la-Neuve, Belgium.

FRACCAROLLO L., CAPART H. 2002 Riemann wave description of erosional dam-break flows. *J. Fluid Mech.* **461**, 183–228

FRACCAROLLO L., CAPART H., ZECH Y. 2002 A Godunov method for the computation of erosional shallow-water transients. *Int. J. Num. Meth. Fluids* **41**, 951–976

GALLINO G.L., PIERSON T.C. 1985 Pollalie Creek debris flow and subsequent dam-break flood of 1980, East Fork Hood River Basin, Oregon. *U. S. Geological Survey Water Supply Paper* 2273, 22 pages

GLADSTONE C., RITCHIE L.J., SPARKS R.S.J., WOODS A.W. 2004 An experimental investigation of density-stratified inertial gravity currents. *Sedimentology* **51**, 767–789

GONCETTE L., SPINEWINE B. 1998 *Intégration d'un mécanisme d'érosion des berges dans un modèle d'évolution morphologique d'une rivière*. MEng thesis, Université catholique de Louvain (in French), unpublished.

GRAY J.M.N.T., TAI Y.C., NOELLE S. 2003 Shock waves, dead zones and particle-free regions in rapid granular free-surface flows. *J. Fluid Mech.* **491**, 161–181

GUINOT V. 2003 *Godunov-type schemes: An introduction for engineers*. Elsevier.

GULER M., EDIL T.B., BOSSCHER P.J. 1999 Measurement of particle movement in granular soils using image analysis. *J. Comp. Civ. Eng.* **13**, 116–122

HAMPTON M.A. 1996 Submarine landslides. *Reviews of Geophysics* **34**(1), 33–59

HARTEN A., LAX P.D., VAN LEER B. 1983 On upstream differencing and Godunov-type schemes for hyperbolic conservation laws. *SIAM Review* **25**, 35–61

IVERSON R.M. 1997 The physics of debris flows. *Reviews of Geophysics* **35**(3), 245–296

JÄHNE B. 1995 *Digital Image Processing*. Springer.

JANOSI I.M., DOMINIQUE JAN, GABOR SZABO K., TAMAS TEL 2004 Turbulent drag reduction in dam-break flows. *Exp. Fluids* **37**, 219–229

JARRET R.D., COSTA J.E. 1993 Hydrology and geomorphology, 1982 Lawn Lake dam failure, Colorado. in *Ecological Effects of the Lawn Lake Flood of 1982, Rocky Mountain National Park: Scientific Monograph*. McCutchen, H.E., Herrmann, Raymond, and Stevens, D.R. (eds.), NPS/NRROMO/NRSM-93/21, USDI, National Park Service, 1–17.

JONARD F.D., LE GRELLE N. 2001 *Evolution morphologique d'un chenal à fond et berges érodables en écoulement transitoire: modélisations numérique et expérimentale dans le cas d'une rupture de barrage*. MEng thesis, Université catholique de Louvain (in French), unpublished.

KE W.-T. 2005 *Self-similar build-up of sediment deltas over rigid slopes*. MSc thesis, National Taiwan University.

KERSHAW J.A., CLAQUE J.J., EVANS S.G. 2005 Geomorphic and sedimentological signature of a two-phase outburst flood from moraine-dammed Queen Bess Lake, British Columbia, Canada. *Earth Surface Processes and Landforms* **30**(1), 1–25

LAJEUNESSE E., MOGNIER J.B., HOMSY, G.M. 200X Granular slumping on a horizontal surface. *Physics of Fluids*, submitted.

LAPOINTE M.F., SECRETAN Y., DRISCOLL S.N., BERGERON N., LECLERC M. 1998 Response of the Ha! Ha! River to the flood of July 1996 in the Saguenay Region of Quebec: Large-scale avulsion in a glaciated valley. *Water Resources Research* **34**(9), 2383–2392

LARCHER M. 2002 *Vertical structure of high-concentration liquid-granular flows*. PhD thesis, University of Padova, Italy.

LARCHER M., SPINEWINE B., FRACCAROLLO L., ARMANINI A. 2005 Segregation in binary mixtures. *Geophysical Research Abstracts* **7**, 09511.

LAWRENCE G.A. 1990 On the hydraulics of Boussinesq and non-Bousinesq two-layer flows. *J. Fluid Mech.* **215**, 457–480

LEAL J.G.A.B., FERREIRA R.M.L., CARDOSO A.H. 2002 Dam-break waves on movable bed. *River Flow 2002, Proc. 1st IAHR Int. Conf. on Fluvial Hydraulics*, Louvain-la-Neuve, Belgium, Bousmar D. & Zech Y.(eds). Balkema: pp. 981–990

LE GRELLE N., SPINEWINE B., SOARES FRAZAO S., ZECH Y. 2004 Non-intrusive imaging measurements of the morphological evolution of a channel during a dam-break flow. *Proc. River Flow 2004, 2nd IAHR Int. Conf. on Fluvial Hydraulics*, Napoli, Italy, June 23-25. Balkema: pp. 977–983

LEVEQUE R.J. 2002 *Finite Volume Methods for Hyperbolic Problems.* Cambridge University Press.

LONG, R.R. 1956 Long waves in a two-fluid system. *J. Met.* **13**, 70

MCELWAINE J., NISHIMURA K. 2001 Ping-pong ball avalanche experiments. *Annals of Glaciology* **32**, 241–250

NNADI F.N., WILSON K.C. 1992 Motion of contact-load particles at high shear stress. *J. Hydr. Engrg.* **118**, 1670–1684

NSOM B. 2002 Horizontal Viscous dam-break flow: experiments and theory. *J. Hydr. Engrg.* **128**(5), 543–546

OKABE A., BOOTS B., SUGIHARA K. 1992 *Spatial Tesselations: Concepts and Applications of Voronoï Diagrams*. Wiley.

PERNG, T.H., CAPART H., CHOU H.T. 200X Granular motions and patterns in slow uniform flows driven by an inclined conveyor belt. *Granular Matter*, accepted.

REYNOLDS O. 1885 On the dilatancy of media composed of rigid particles in contact with experimental illustrations. *Philos. Mag.* **20**, 469–481

ROBERTS M.J., TWEED F.S., RUSSEL A.J., KNUDSEN Ó., HARRIS T.D. 2003 Hydrologic and geomorphic effects of temporary ice-dammed lake formation during jökulhlaups. *Earth Surface Processes and Landforms,* **28**(7), 723–737

SHIN J.O., DALZIEL S.B., LINDEN P.F. 2004 Gravity currents produced by lock exchange. *J. Fluid Mech.* **521**, 1–34

SILVA P. 2004 *Rupture de barrages. Caractérisation de l'écoulement en conséquence d'un élargissement brusque en aval de l'écluse.* Travail Final d'Etudes. Instituto Superior Tecnico (in French), unpublished.

SIMPSON J.E. 1987 *Gravity currents. In the Environment and the Laboratory.* Ellis Horwood Series in Environmental Science.

SOARES FRAZÃO S. 2002 *Dam-break induced flows in complex topographies. Theoretical, numerical and experimental approaches*. PhD thesis, Université catholique de Louvain.

SOARES FRAZAO S., NOEL B., SPINEWINE B., ZECH Y. 2003 The isolated building test case : results from the IMPACT benchmark. *In* EC Contract EVG1-CT-2001-00037 IMPACT *Investigation of Extreme Flood Processes and Uncertainty*, Proc. 3rd project workshop, Louvain-la-Neuve, Belgium.

SOARES FRAZAO S., SPINEWINE B., ZECH Y. 2001 Digital-imaging velocity measurements and numerical modelling of a dam-break flow through a 90° bend. *Proc. 29th IAHR Congress*, Beijing, China, September 16-21, pp. 240–245

SOLER SALLES R. 2000 *Estudio experimental de flujos con sedimento hiper-concentrados mediante el uso de técnicas de imágenes digitales. Aplicación a rotura de presas y avalanchas*. MEng thesis, Universidad Politécnica de Cataluña (in Spanish), unpublished.

SPINEWINE B. 2005 Two-layer shallow water modelling of fast geomorphic flows and experimental validation on idealised laboratory dam-break waves. *Proc. XXXI IAHR Congress, J.F.K. Student Paper Competition. Seoul*

SPINEWINE B., CAPART H., ZECH Y. 2000 Stereoscopic imaging measurements of solid concentrations in dense granular flows. *Proc. 10th International Conference on Transport & Sedimentation of Solid Particles*, Wroclaw, Poland, pp. 497–509

SPINEWINE B., CAPART H., LARCHER M., ZECH Y. 2003 Three-dimensional Voronoï imaging methods for the measurement of near-wall particulate flows. *Exp. Fluids* **34**(2), 227–241

SPINEWINE B., CAPART H., LE GRELLE N., SOARES FRAZÃO S., ZECH Y. 2002 Experiments and computations of bankline retreat due to geomorphic dam-break floods. *River Flow 2002, Proc. 1st IAHR Int. Conf. on Fluvial Hydraulics*, Louvain-la-Neuve, Belgium, Bousmar D. & Zech Y.(eds). Balkema: pp. 651–661

SPINEWINE B., CAPART H., ZECH Y. 2002 Three-dimensional Voronoï imaging methods for the simultaneous measurement of velocities and concentrations in dense particulate flows. *Proc. HMEM 2002, joint IAHR & ASCE Conference on Hydraulic Measurements & Experimental Methods*, Estes Park, Colorado, USA.

SPINEWINE B., DELOBBE A., ELSLANDER L., ZECH Y. 2004 Experimental investigation of the breach growth process in sand dikes. *River Flow 2004, Proc. 2nd IAHR Int. Conf. on Fluvial Hydraulics*, Napoli, Italy, June 23-25. Balkema: pp. 983–993

SPINEWINE B., ZECH Y. 2001 Digital imaging characterisation of a granular hopper flow. *Proc. Partec 2001, International Congress for Particle Technology*, Nürnberg, Germany.

SPINEWINE B., ZECH Y. 2002 Dam-break waves over movable beds: a “flat bed” test case. *In* EC Contract EVG1-CT-2001-00037 IMPACT *Investigation of Extreme Flood Processes and Uncertainty*, Proc. 2nd project workshop, Mo-i-Rana, Norway.

STANSBY P.K., CHEGINI A., BARNES T.C.D. 1998 The initial stages of dam-break flow. *J. Fluid Mech.* **374**, 407–424

SUTHERLAND B.R. 2002 Interfacial gravity currents. I. Mixing and entrainment. *Physics of Fluids* **14**(7), 2244–2254

TSORNG S.J., CAPART H., LAI J.S., YOUNG D.L. 200X Three-dimensional tracking of the long time trajectories of suspended particles in a lid-driven cavity flow. *Exp. Fluids*, submitted

VAN GOETHEM J.L., VILLERS L. 2000 *Modélisation du transport solide associé à l'onde de rupture d'un barrage: développement d'un schéma numérique aux volumes finis et analyse de mesures expérimentales par techniques d'imagerie digitale*. MEng thesis, Université catholique de Louvain (in French), unpublished.

VAN LEER B. 1977 Towards the ultimate conservative difference scheme IV. A new approach to numerical convection. *J. Comput. Phys.* **23**, 276–299

VEBER P., DAHL J., HERMANSSON R. 1997 Study of the phenomena affecting the accuracy of a video-based particle tracking velocimetry technique. *Exp Fluids* **22**, 482–488

WAYTHOMAS C.F. 2001 Formation and failure of volcanic debris dams in the Chakachatna River valley associated with eruptions of the Spurr volcanic complex, Alaska. *Geomorphology* **39**, 111–129

ZECH Y., SOARES FRAZÃO S., SPINEWINE B., BELLAL M., SAVARY C. 2005 The morphodynamics of super- and transcritical flow. *Proc. RCEM 2005 Int. Conf. on River, Coastal and Estuarine Morphodynamics*

ZHU D.Z., LAWRENCE G.A. 2001 Holmboe's instability in exchange flows. *J. Fluid Mech.* **429**, 391–409

Appendix I.

Three-dimensional Voronoï imaging methods for the measurement of near-wall particulate flows

This appendix furnishes the abstract of the publication referenced as:

SPINEWINE B., CAPART H., LARCHER M., ZECH Y. 2003 Three-dimensional Voronoï imaging methods for the measurement of near-wall particulate flows. *Exp. Fluids* **34**(2), 227–241

The full paper is available at http://dx.doi.org/10.1007/s00348-002-0550-4

Abstract A set of stereoscopic imaging techniques is proposed for the measurement of rapidly flowing dispersions of opaque particles observed near a transparent wall. The methods exploit projective geometry and the Voronoï diagram. They rely on purely geometrical principles to reconstruct 3D particle positions, concentrations, and velocities. The methods are able to handle position and motion ambiguities, as well as particle-occlusion effects, difficulties that are common in the case of dense dispersions of many identical particles. Fluidization cell experiments allow validation of the concentration estimates. A mature debris-flow experimental run is then chosen to test the particle-tracking algorithm The Voronoï stereo methods are found to perform well in both cases, and to present significant advantages over monocular imaging measurements.

Appendix III. Exact analytical expressions for the eigenvalues and determinant of two-layer shallow-water equations with a density contrast

This appendix briefly outlines a procedure to obtain exact expressions for the eigenvalues of the two-layer shallow-water equations introduced in Chapter 3. An analytical expression for the determinant is also given, which allowed to characterize precisely the range of flow conditions for which strict hyperbolicity of the two-layer system is lost, leading to partly imaginary eigenvalues (see Chapter 3, Fig. 3.6). The derivation closely reproduces that presented in Lawrence (1990). The reader may refer to that publication and to Armi (1986) and Artale and Levy (1988) for additional details.

The governing equations for a two-layer shallow-water system with a density contrast on a horizontal bed are given by:

$$\frac{\partial h_1}{\partial t}+\frac{\partial (h_1 u_1)}{\partial x}=0\,, \tag{AIII.1}$$

$$\frac{\partial h_2}{\partial t}+\frac{\partial (h_2 u_2)}{\partial x}=0\,, \tag{AIII.2}$$

$$\frac{\partial (h_1 u_1)}{\partial t}+\frac{\partial}{\partial x}\left(h_1 u_1^2+\frac{g h_1^2}{2}\right)+g h_1\frac{\partial h_2}{\partial x}=0 \tag{AIII.3}$$

$$\frac{\partial (h_2 u_2)}{\partial t}+\frac{\partial}{\partial x}\left(h_2 u_2^2+\frac{g h_2^2}{2}\right)+g h_2\frac{\rho_1}{\rho_2}\frac{\partial h_1}{\partial x}=0 \tag{AIII.4}$$

They may be written in the vector form

$$\frac{\partial \mathbf{U}}{\partial t}+\mathbf{A}(\mathbf{U})\frac{\partial \mathbf{U}}{\partial x}=0 \tag{AIII.5}$$

where vector **U** and coefficient matrix **A** are given by

$$\mathbf{U}=\begin{bmatrix} h_1 \\ h_2 \\ h_1 u_1 \\ h_2 u_2 \end{bmatrix},\quad \mathbf{A}(\mathbf{U})=\begin{bmatrix} 0 & 0 & 1 & 0 \\ 0 & 0 & 0 & 1 \\ -u_1^2+g h_1 & g h_1 & 2u_1 & 0 \\ g h_2\dfrac{\rho_1}{\rho_2} & -u_2^2+g h_2 & 0 & 2u_2 \end{bmatrix}. \tag{AIII.6}$$

This constitutes a homogeneous system of first order quasi-linear equations, the behaviour of which is well-known to be controlled by the eigenstructure of matrix **A**. The eigenvalues are the roots of equation

$$\det\left(\mathbf{A}-\lambda\mathbf{I}\right)=0\,. \tag{AIII.7}$$

Developing the determinant yields the characteristic polynomial

$$\{(\lambda-u_1)^2-g h_1\}\{(\lambda-u_2)^2-g h_2\}-\frac{\rho_1}{\rho_2}g^2 h_1 h_2=0\,. \tag{AIII.8}$$

which may be solved analytically with the below procedure.

The following quantities are defined:

- total flow depth h: $h = h_1 + h_2$
- depth ratio α. This ratio is zero when one of the layer vanishes, and equal to unity when the flow depth is equally partitioned between the two layers, i.e. $h_1 = h_2 = h/2$:

$$\alpha = 4h_1 h_2 / h^2$$

- arithmetic mean velocity $\bar{u}$: $\bar{u} = \frac{1}{2}(u_1 + u_2)$
- "hat" velocity $\hat{u}$. This corresponds to the internal "convective" velocity of two-layer flows under a Boussinesq approximation, i.e. when $\rho_1 \approx \rho_2$:

$$\hat{u} = (u_1 h_2 + u_2 h_1)/h$$

- relative density difference ε: $\varepsilon = \dfrac{\rho_2 - \rho_1}{\rho_2}$
- reduced gravity g': $g' = \varepsilon\, g$
- Densimetric Froude numbers of the individual layers F_1, F_2:

$$F_i = \frac{u_i}{\sqrt{g' h_i}}, \quad i = 1, 2$$

- composite Froude number $G : G^2 = F_1^2 + F_2^2 - \varepsilon F_1^2 F_2^2$
- stability Froude number $F_\Delta : F_\Delta^2 = \dfrac{(u_2 - u_1)^2}{g' h}$

Various "Froude" numbers are so defined. The stability Froude number F_Δ governs the stability of the two-layer system to long waves (Long, 1956). As discussed in Chapter 3, partly imaginary internal eigenvalues are encountered when it exceeds a threshold value $F_\Delta^2 > (F_\Delta^2)_{\text{crit}}$ (see Fig. 3.6), so that it governs the hyperbolicity of the two-layer shallow-water equations. The composite Froude number G may determine the overall criticality of two-layer flows. For a precise determination of flow criticality in terms of external waves (barotropic) and internal waves (baroclinic), one should however distinguish between internal Froude number F_I and external Froude number F_E. For the general case involving a density contrast, simple algebraic expressions for those Froude numbers are not available. They will be calculated as a side-product of the below derivation of the eigenvalues.

With the above definitions, the characteristic polynomial (3.26) may be rewritten:

$$\sum_{m=0}^{4} a_m \, \lambda_m = 0 \tag{AIII.9}$$

where $a_0 = u_1^2 u_2^2 - g h_1 u_2^2 - g h_2 u_1^2 + g\, g' h_1 h_2 = g\, g' h_1 h_2 \left(1 - G^2\right)$

$$a_1 = -4 u_1 u_2 \overline{u} + 2 g\, h\, \hat{u}$$

$$a_2 = 4 \overline{u}^2 + 2 u_1 u_2 - g\, h$$

$$a_3 = -4 \overline{u}$$

$$a_4 = 1$$

The first step of the solution procedure is reduce (AIII.9) by making a substitution of variables, considering an observer moving at the arithmetic mean velocity $\bar{u}$, i.e. $\lambda = y + \bar{u}$, yielding the reduced quartic equation:

$$y^4 + d\,y^2 + e\,y + f = 0 \tag{AIII.10}$$

where $d = \frac{1}{2} g\,h \left(2 + \varepsilon\,F_\Delta^2\right)$

$e = 2\,g\,h\left(\hat{u} - \bar{u}\right)$

$f = \left(\frac{1}{4} g\,h\right)^2 \left(4\varepsilon\left(\alpha - F_\Delta^2\right) + \varepsilon^2 F_\Delta^4\right)$

The four solutions of the reduced quartic equation are

$$\begin{aligned} y_1 &= \xi\, z_1^{1/2} + z_2^{1/2} + z_3^{1/2} \\ y_2 &= -\xi\, z_1^{1/2} - z_2^{1/2} + z_3^{1/2} \\ y_3 &= -\xi\, z_1^{1/2} + z_2^{1/2} - z_3^{1/2} \\ y_4 &= \xi\, z_1^{1/2} - z_2^{1/2} - z_3^{1/2} \end{aligned} \tag{AIII.11a-d}$$

where $\xi = \operatorname{sgn}(u_2 - u_1)$, and z_1, z_2, z_3 are the solutions of the normalized cubic equation:

$$z^3 + r\,z^2 + s\,z + t = 0 \tag{AIII.12}$$

where $r = -(\frac{1}{4} g\,h)(2 + \varepsilon\,F_\Delta^2)$

$s = (\frac{1}{4} g\,h)^2 \left(1 + \varepsilon\,(2\,F_\Delta^2 - \alpha)\right)$

$t = -\varepsilon\,(\frac{1}{4} g\,h)^3\,(1 - \alpha)\,F_\Delta^2$

The solutions of this normalized cubic resolvent depend on the value of its discriminant:

$$D_z = \prod_{i<j;\, i,j=1}^{4} (z_i - z_j)^2 = (\tfrac{1}{3}p)^3 + (\tfrac{1}{2}q)^2 \qquad \text{(AIII.13)}$$

where $p = \frac{1}{3}(3s - r^2)$

$q = \frac{1}{27}(2r^3 - 9rs + 27t)$

The sign of this discriminant is also the sign of the discriminant of the original characteristic polynomial

$$D_\lambda = \prod_{i<j;\, i,j=1}^{4} (\lambda_i - \lambda_j)^2 \,, \qquad \text{(AIII.14)}$$

If $D \le 0$, all roots are real. If $D > 0$, two of them become complex conjugate. An analytical expression for this discriminant is given by:

$$D_z = -\frac{\alpha\varepsilon(\frac{1}{4}gh)^6}{108}\left(\beta + (1 - F_\Delta^2)\sum_{n=0}^{3} b_n \varepsilon^n\right), \qquad \text{(AIII.15)}$$

with $b_0 = 4$

$b_1 = (27\alpha - 12)F_\Delta^2 - 9\alpha$

$b_2 = 12F_\Delta^4 - 18\alpha F_\Delta^2$

$b_3 = -4F_\Delta^6$

$\beta = \alpha\varepsilon\left(1 + 2\varepsilon(2\alpha - F_\Delta^2) + \varepsilon^2 F_\Delta^4\right),$

indicating that the value of the discriminant is a function only of the three dimensionless parameters α, ε and F_Δ^2. This observation allowed to span the regions of partly imaginary eigenvalues as a function of these parameters, however rearranged differently (see Fig. 3.6).

If $D \le 0$, the roots of the normalized cubic resolvent are:

$$z_n = 2\gamma \cos(\tfrac{1}{3}\phi + \tfrac{2}{3}n\pi) - \tfrac{1}{3}r \qquad (n = 1...3) \tag{AIII.16}$$

where $$\gamma = \left(-\frac{p}{3}\right)^{1/2}, \quad \cos\phi = -\frac{q}{2\gamma^3}, \quad \sin\phi = \frac{(-D)^{1/2}}{\gamma^3},$$

$$p = -\frac{(\tfrac{1}{4} g\, h)^2}{3}\left(1 + \varepsilon(3\alpha - 2F_\Delta^2) + \varepsilon^2 F_\Delta^4\right), \text{ and}$$

$$q = \frac{(\tfrac{1}{4} g\, h)^3}{27}\left(2 + \varepsilon(27\alpha F_\Delta^2 - 18\alpha - 6F_\Delta^2) + \varepsilon^2(6F_\Delta^4 - 9\alpha F_\Delta^2) - 2\varepsilon^3 F_\Delta^6\right)$$

Once they are obtained, the four exact real solutions of the original quartic characteristic polynomial are retrieved as:

$$\lambda_{1,4} = \overline{u} + \xi\, z_1^{1/2} \pm (z_3^{1/2} + z_2^{1/2}) \tag{AIII.17}$$

$$\lambda_{2,3} = \overline{u} - \xi\, z_1^{1/2} \pm (z_3^{1/2} - z_2^{1/2}) \tag{AIII.18}$$

where again $\xi = \operatorname{sgn}(u_2 - u_1)$.

If $D > 0$, z_1 remains real, but z_2 and z_3 are complex conjugate. Being conjugate, the combination $(z_3^{0.5} + z_2^{0.5})$ remains real also, so that the external eigenvalues $\lambda_{1,4}$ are always real. On the contrary, the combination $(z_3^{0.5} - z_2^{0.5})$ is purely imaginary, leading to internal eigenvalues $\lambda_{2,3}$ that are complex conjugate.

For single-layer shallow flows, it is well known that the two characteristic velocities are given by $\lambda = u \pm c$, with $c = \sqrt{g\,h}$, and criticality of the flow is governed by the Froude number $Fr = u/c$. By analogy, in (AIII.17) and (AIII.18), $\overline{u} \pm \xi\, z_1^{0.5}$ represents the "convective" velocity, and $(z_3^{0.5} \pm z_2^{0.5})$ the "phase" speeds, of respectively external (free surface) and internal (interfacial) wave motions. As a side-product of the above derivation, dividing convective velocities by phase speeds, one obtains the two Froude numbers governing criticality of two-layer flows in terms of external waves and internal waves:

$$F_E = \frac{\overline{u} + \xi\, z_1^{1/2}}{z_3^{1/2} + z_2^{1/2}} \tag{AIII.19}$$

$$F_I = \frac{\overline{u} - \xi\, z_1^{1/2}}{z_3^{1/2} - z_2^{1/2}} \tag{AIII.20}$$

Achevé d’imprimer sur les presses de l’imprimerie CIACO
(Louvain-la-Neuve, Belgique, tél +32.10.47.55.35)
Décembre 2005

Université catholique de Louvain
Faculté des sciences appliquées
Département architecture, urbanisme, génie civil et environnemental
Unité de génie civil et environnemental

Place du Levant 1, 1348 Louvain-la-Neuve (Belgique)
Tél. 32 (0) 10 47 21 23 – fax 32 (0) 10 47 21 79
E-mail spinewine@gmail.com - spinewine@gce.ucl.ac.be - zech@gce.ucl.ac.be
http://www.gce.ucl.ac.be

In case of exceptional floods induced by the failure of a dam, huge amounts of sediments may be eroded. This results in large-scale modifications of the valley morphology and may drastically increase the resulting damages.
The objective of the research is to advance the understanding of sediment transport under dam-break flows. For such highly erosive and transient floods, it is crucial to account explicitly for sediment inertia, and therefore traditional "clear-water" modelling approaches are largely inappropriate. The present approach relies on a two-layer idealisation of the flow behaviour. Separating a clear-water flow region from the underlying sediment bed, the transported sediments are confined in a flow layer of finite thickness, endowed with its proper inertia, density and velocity. The thesis also pinpoints granular dilatancy as an essential mechanism of interaction between the layers. When passing from a solid-like to a fluid-like behaviour as they are entrained by the flow, the eroded sediment grains dilate along the vertical, and this generates vertical exchanges of mass and momentum that should be accounted for.
The thesis proceeds first with experimental investigations. Laboratory dam-break waves are reproduced in a dedicated flume, exploring different bed configurations and sediment densities. Imaging observations are used to support the proposed phenomenological description of the flow. Within a shallow-water framework, theoretical and numerical endeavours are then developed to investigate the implications on the flow dynamics of the two essential contributions of the proposed description, i.e. the two-layer flow behaviour, and the effects of granular dilatancy.

Benoit Spinewine is born in Brussels, Belgium, on November 2nd, 1974. Civil Engineer (Université catholique de Louvain, 1998), he spent one year as a research assistant at the Unesco-IHE Institute for water education, Delft, The Netherlands. Back in Belgium, he benefited from a First-Université fellowship and developed 3D digital imaging techniques for fluid-granular flows. Since November 2001, he is a PhD student funded by the Fonds pour la recherche dans l'industrie et l'agriculture, Belgium, and the fonds spécial pour la recherche, Université catholique de Louvain.

The content of the present thesis obtained the J.F. Kennedy award at the student paper competition during the XXXI Congress of the International Association of Hydraulic Engineering and Research in Seoul, September 2005.